Doctoral theses at NTNU, 2020:246

Nikolai Helth Gaukås

Lead-Free Ferroelectric KNN Films for Biomedical Applications

Doctoral thesis

Nikolai Helth Gaukås

ISBN 978-82-326-4840-5 (printed ver.)
ISBN 978-82-326-4841-2 (electronic ver.)
ISSN 1503-8181

NTNU
Norwegian University of Science and Technology

NTNU
Norwegian University of Science and Technology
Thesis for the Degree of
Philosophiae Doctor
Faculty of Natural Sciences
Department of Materials Science and Engineering

Doctoral theses at NTNU, 2020:246

NTNU

Nikolai Helth Gaukås

Lead-Free Ferroelectric KNN Films for Biomedical Applications

Thesis for the Degree of Philosophiae Doctor

Trondheim, September 2020

Norwegian University of Science and Technology
Faculty of Natural Sciences
Department of Materials Science and Engineering

NTNU
Norwegian University of
Science and Technology

NTNU
Norwegian University of Science and Technology

Thesis for the Degree of Philosophiae Doctor

Faculty of Natural Sciences
Department of Materials Science and Engineering

ISBN 978-82-326-4840-5 (printed ver.)
ISBN 978-82-326-4841-2 (electronic ver.)
ISSN 1503-8181

Doctoral theses at NTNU, 2020:246

Printed by NTNU Grafisk senter

Preface

This thesis has been submitted to the Norwegian University of Science and Technology (NTNU) in partial fulfillment of the requirements for the academic degree of Philosophiae Doctor.

The work described herein has been performed at NTNU between August 2016 and July 2020, including a 5.5 months stay with the Laboratory of Molecular Neuroscience and Dementia at The University of Sydney (USYD) from October 2019 to March 2020. The work has been supervised by Professor Tor Grande (main advisor), Professor Mari-Ann Einarsrud (co-advisor) and Associate Professor Julia Glaum (co-advisor) at the Functional Materials and Materials Chemistry Research Group (FACET), Department of Materials Science and Engineering (DMSE), NTNU.

The project has been funded by the Research Council of Norway (NFR) as part of the strategic project “Environmental friendly piezoelectric materials for sensors, actuators and implants in medical technology” (NFR project no. 250184) and via NTNU NanoLab through the Norwegian Micro-and Nano-Fabrication Facility, NorFab, project number 245963/F50.

All experimental work has been performed by the author, with the exception of the following. The thin film characterization using TEM in Paper I was

performed by Andreas Toresen and Randi Holmestad (Deptartment of Physics, NTNU). Interdigitated electrode deposition in Paper I and Ti^{4+}-solution preparation in Paper II were performed by Trygve M. Ræder (FACET, NTNU). $BaTiO_3$-solution preparation and thin film characterization using reflectance IR spectroscopy in Manuscript I were performed by Kristine Bakken (FACET, NTNU). Imaging of immunostained cells using confocal microscopy in Manuscript II was performed by Anishchal Pratap (Laboratory of Molecular Neuroscience and Dementia, USYD). The contact angle measurments in Manuscript II were performed by Johannes Ofstad (DMSE, NTNU). The AFM measurments in Manuscript II were performed by Viviann Hole (FACET, NTNU).

Parts of this thesis have been published or prepared for publication, and these scientific papers and manuscripts are included in the appendices. A list of the papers and manuscripts, and a summary of the contributions provided in each work, is provided in the following.

The following scientific papers and manuscripts are included in this dissertation

Paper I: **N. H. Gaukås**, S. M. Dale, T. M. Ræder, A. Toresen, R. Holmestad, J. Glaum, M.-A. Einarsrud, T. Grande. *Controlling Phase Purity and Texture of $K_{0.5}Na_{0.5}NbO_3$ Thin Films by Aqueous Chemical Solution Deposition*, Materials **2019**, 12, 2042.

Contributions: N.H.G., M.-A.E. and T.G. conceived and designed the experiments; N.H.G. and S.M.D. synthesized the powders and thin films and performed SEM and XRD on the thin films; N.H.G. performed XRD, TGA-MS and FTIR on the powders; A.T. and R.H. performed TEM; N.H.G. and T.M.R. performed the ferroelectric measurements; N.H.G., A.T., R.H., J.G., M.-A.E. and T.G. analyzed the data; N.H.G. and T.G. wrote the paper with inputs from all the authors.

Paper II: **N. H. Gaukås**, J. Glaum, M.-A. Einarsrud, T. Grande. *Ferroelectric and dielectric properties of Ca^{2+}-doped and Ca^{2+}–Ti^{4+} co-doped $K_{0.5}Na_{0.5}NbO_3$ thin films*, J. Mater. Chem. C **2020**, 8, 5102-5111.

Contributions: N.H.G., J.G. and T.G. conceived and designed the experiments; N.H.G. synthesized the powders and thin films and performed XRD and SEM; N.H.G. and J.G. performed dielectric characterization; N.H.G., J.G., M.-A.E. and T.G. analyzed the data; N.H.G. and T.G. wrote the paper with input from all the authors.

Manuscript I: **N. H. Gaukås**, R. H. Klaussen, E. Khomyakova, J. Glaum, M.-A. Einarsrud, T. Grande. *Preparation of flexible piezoelectric $K_{0.5}Na_{0.5}NbO_3$ thin films*.

Contributions: N.H.G., E.K., M.-A.E and T.G. conceived and designed the experiments; N.H.G. and R.H.K. synthesized and characterized the thin films; N.H.G., R.H.K., J.G., M.-A.E. and T.G. analyzed the data; N.H.G. and T.G. wrote the paper with input from all the authors.

Manuscript II: **N. H. Gaukås**, Q.-S. Huynh, A. A. Pratap, M.-A. Einarsrud, T. Grande, R. M. D. Holsinger, J. Glaum. *In vitro biocompatibility of piezoelectric $K_{0.5}Na_{0.5}NbO_3$ thin films on platinized silicon substrates*.

Contributions: N.H.G., Q.S.H., R.M.D.H. and J.G. conceived and designed the experiments; N.H.G. synthesized the thin films and performed SEM and XRD on the thin films; N.H.G. and Q.S.H. cultured cells, performed the proliferation assays and imaged the cells with SEM; N.H.G., Q.S.H. and A.A.P. stained the cells; A.A.P. imaged the cells with confocal microscope; all authors analyzed the data; N.H.G., T.G. and J.G. wrote the paper with input from all the authors.

The following scientific paper is not included in this dissertation

K.-N. Pham, **N. H. Gaukås**, M. Morozov, T. Tybell, P. E. Vullum, T. Grande, M.-A. Einarsrud. *Epitaxial $K_{0.5}Na_{0.5}NbO_3$ thin films by aqueous chemical solution deposition*, R. Soc. open sci. **2019**, 6, 180989.

Contributions: K.-N.P., T.G. and M.-A.E. conceived and designed the experiments; P.E.V. performed the TEM experiments; K.-N.P. and M.M. performed the electrical measurements; K.-N.P performed the synthesis experiments; K.-N.P., T.T., T.G. and M.-A.E. analysed the data; K.-N.P., N.H.G. and M.-A.E. wrote the paper with inputs from all the authors.

Nikolai Helth GAUKÅS
Trondheim
July 2020

Acknowledgements

The making of a PhD involves not only an optimistic and determined novice. Behind every PhD is a crowd of shepherds, collaborators, supporters and friends. I would like to take this opportunity to express my gratitude to all of the people who have helped me during my time as a PhD candidate.

First and foremost, I would like to express my highest gratitude to my main advisor, Tor, for our time together. Thank you for sharing your wisdom, for guiding and supporting me, and for always staying positive. You have been a wonderful supervisor. I also have to give many thanks to my excellent co-supervisors. Mari-Ann, thank you for giving me the chance to do a PhD on this project and for always believing in me. I have really enjoyed collaborating with you these past years, either it being on my research project, TMT4130 or Arne Martin's science-themed birthday party. Julia, thank you for always having the time to answer my endless stream of simple and difficult questions. You are excellent at listening to and valuing your students' ideas and thoughts, and I hope this is a skill you never leave behind. Lucky are the future students that will have you as their supervisor.

From October 2019 to March 2020 I visited Dr. Damian Holsinger's research group at the Laboratory of Molecular Neuroscience and Dementia at The University of Sydney, Australia, and I am very grateful for this opportunity. I would like

to thank Dr. Holsinger for taking me in as one of his own and for giving a blunt chemist as myself the opportunity to learn the fine art of working with cells. To Anish, Carol and Susan, thank you so much for not only being superb colleagues, but for also being the very best of friends. A special thanks goes to Dr. Philip Boughton for finding time for me and my project in your hectic life.

The brilliant master students associated with the project, Silje Marie Dale, Ragnhild Hyllnes Klaussen and Andreas Toresen, have my highest appreciation for their valuable contributions. Thanks to Dr. Evgeniya Khomyakova for your ideas and your humor. I am also grateful for the fruitful collaboration with Per Martin Rørvik, Tor Olav Sunde, Henrik Ræder, Marit Synnøve Sæverud Stange and the other people from SINTEF in Oslo.

This thesis would not have been possible without the help and support from the technical staff at the Department of Materials Science and Engineering and at NTNU NanoLab. Thank you all. I also want to thank all the PhD candidates and postdocs I have worked alongside with the last four years. A special thanks goes to my office mates Mikalai, Kara and Magnus. You're the best. Thanks to Trond for convincing me to do a PhD and for being a good friend along the way.

Finally, I would like to thank my family and friends for love and support through these four years. Thanks to Håkon and Thea for the fancy dinners and hiking trips to Skjellbreia. Thanks to Kristoffer for all the phone calls and vacations over the years. Thanks to my parents for supporting me, and my brother for believing in me.

Summary

Ferroelectric materials are utilized in a wide range of different electronic devices throughout our modern society, including all kinds of consumer electronics, ultrasound equipment, minimally invasive surgical tools and intersatellite communication devices, just to name a few. The crave for ferroelectric materials is due to their excellent piezoelectric properties. Piezoelectric materials can passively "translate" between the mechanical world of us humans and the electronic world we are increasingly surrounding us with. As such, these materials can be used as sensors, actuators and energy harvesters. A major advantage of these materials over alternative systems is their conservation of functionality with scaling down to the nanometer range. This makes the ferroelectric materials attractive as components in micro-electromechanical systems (MEMS), and especially in MEMS technology for medical implantation due to the strict size restrictions *in vivo*. One of the main challenges in the field of ferroelectric materials is to develop lead-free alternatives to the state-of-the-art ferroelectric materials, the lead-titanate-zirconates (PZTs). This work was therefore concerned with the development of lead-free piezoelectric films for biomedical applications based on the ferroelectric material potassium sodium niobate ($K_{0.5}Na_{0.5}NbO_3$, KNN). The principle goal of the project was to develop an aqueous wet chemical processing route to KNN films with properties appropriate for medical applications.

The first part of the thesis was focused on the development of an aqueous synthesis platform to phase pure KNN thin films. Two water-based precursor solutions were investigated, prepared from the combination of alkali metal nitrates and either oxalic acid (KNN-Ox) or malic acid (KNN-MA) complexed niobium as cation precursors. The decomposition process of these precursor solutions during film pyrolysis was demonstrated to be crucial for promoting nucleation of KNN and suppressing the formation of secondary phases. By combining thermal analysis, X-ray diffraction and infrared spectroscopy on powders prepared by drying and calcining the precursor solutions, it was shown that the decomposition temperature could be manipulated by the solution chemistry and processing conditions. Based on the analysis of the powder processing, a processing route to phase pure KNN films on single crystal $SrTiO_3$ substrates was developed. Transmission electron microscopy and X-ray diffraction was applied to investigate the microstructure of the KNN films, and the films were shown to have a columnar microstructure with out-of-plane texturing. A correlation between the thermal processing and the observed film texture was discussed.

Compositional engineering of the KNN films was further targeted with the aim of improving the ferroelectric properties. Ca^{2+} doping and Ca^{2+}-Ti^{4+} co-doping ($CaTiO_3$ doping) was implemented in the aqueous processing route developed in the first part of the thesis. Platinized silicon (SiPt) substrates were used since Si-based substrates are more relevant for integration in electronic applications. It was demonstrated that the dopants were dissolved into the KNN crystal lattice and the ferroelectric properties of the doped KNN films were significantly improved relative to the undoped KNN films. Doping was observed to promote ferroelectric switching, resulting in films with remnant polarizations of 6.37 ± 0.47 and $7.40 \pm 0.09\,\mu C\,cm^{-1}$ for the Ca^{2+} and $CaTiO_3$ doped films, respectively. A high dielectric permittivity (1800-3200) was observed for all three compositions of the films.

Fabrication of piezoelectric oxide films on flexible supports allows for high-performing microelectromechanical system (MEMS) devices with minimal loss of functionality due to mechanical clamping. Motivated by this, a wet chemical processing route to flexible KNN films on polymer supports was explored. The synthesis involved a lift-off procedure using ZnO as a release layer for the flex-

ible KNN film. X-ray diffraction and infrared spectroscopy were used to investigate the phase composition of the different oxide layers during the processing of the films, and introduction of a $BaTiO_3$ buffer layer was shown to mitigate the formation of secondary phases in the KNN film grown directly on ZnO. Microstructural investigation using scanning electron microscopy revealed that the mechanical integrity of the flexible KNN film was greatly improved by the addition of a platinum bottom electrode between the film and PDMS support. A proof-of-concept for a complete aqueous processing route of a flexible KNN film was demonstrated, and future development possibilities for the preparation of flexible lead-free ferroelectric films were discussed.

In the final part of the thesis, *in vitro* cytotoxicity assays were performed to evaluate the biocompatibility of the KNN films with living cells. Undoped and $CaTiO_3$ doped KNN films on SiPt substrates were tested using three different cell lines. The cells were grown on the films for up to 10 days, and cell morphology, viability and proliferation were assessed using scanning electron microscopy, immunofluorescence microscopy and spectrophotometry. The results from the *in vitro* experiments showed that proliferation rates for the cells grown on the KNN thin films were equally high or higher than those on glass control samples, and no cytotoxic effect from either the films or the substrate was observed. The results demonstrated that the KNN films prepared in this thesis are very promising candidates for components in implantable medical devices.

To summarize this work, an aqueous synthesis platform to phase pure ferroelectric KNN films was established, and the processing route was demonstrated to be compatible with compositional alterations and the use of both rigid and flexible substrates. *In vitro* biocompatibility of the films with cells was also demonstrated. These results highlight the potency of aqueous chemistry as an environmentally friendly and cost-effective tool in oxide film fabrication. New ideas and techniques regarding processing of films on polymeric supports were also introduced and explored, and this part of the project is suggested to hold great potential for further exploitation. Finally, this thesis demonstrates the potential of KNN films as components in implantable medical devices.

Populærvitenskapelig sammendrag

Piezoelektriske materialer kan konvertere elektriske signaler til mekaniske signaler og vice versa, uten å kreve ekstra tilførsel av energi i prosessen. Klem på et piezoelektrisk materiale, og du får ut ren elektrisk energi. Sett strøm på materialet, og det spiller Ariana Grande og Tsjajkovskij. På grunn av denne utrolig nyttige egenskapen har de piezoelektriske materialene sakte, men sikkert blitt en fast del av hverdagen vår. Tenk baderomsvekter, klokker, smarttelefoner, barneleker og printere. Siden disse materialene kan lage strøm av bevegelse forskes det også på bruk av disse materialene til implanterbar elektronikk. Se for deg en pacemaker som aldri trenger å bytte batteri, eller en liten dings du kan plassere under huden som 24/7 passer på at du er frisk, begge støttet av en piezoelektrisk strømfabrikk som lager strøm av naturlige bevegelser fra kroppen din. Det beste og mest populære piezoelektriske materialet på markedet i dag er bly-zirkonat-titanat, forkortet PZT. Som navnet tilsier inneholder dette materialet det giftige tungmetallet bly, og det jobbes iherdig med å utvikle alternative materialer til PZT. Et av de mest lovende blyfrie piezoelektriske materialene er kalium-natrium-niobat, forkortet KNN. Denne doktorgraden har hatt som mål å utvikle tynne prøver (filmer) av KNN for bruk innen helse og medisin.

Denne doktorgraden kan deles inn i fire deler. I den første delen beskrives utviklingen av en ny metode for å lage KNN-filmer. En miljøvennlig kjemisk løsning basert på vann ble brukt til å lage KNN-filmer på overflaten av énkrystaller av strontium-titanat (STO). Den kjemiske løsningen måtte modifiseres slik at det ikke dannet seg uønskede biprodukter i KNN-filmene under produksjonen. Dette ble oppnådd ved å bruke eplesyre til å stabilisere ionene i den kjemiske løsningen i stedet for oksalsyre, da eplesyre forbrennes ved en høyere temperatur enn oksalsyre og derfor forhindrer dannelsen av biprodukter under varmebehandlingen.

I den andre delen av doktorgraden ble eplesyre-løsningen utviklet i del 1 anvendt til å lage KNN-filmer på silisium-brikker med platinabelegg (SiPt), siden silisium er standarden i elektronikk-industrien. Små mengder (0.5 %) med kalsium og titan ble tilsatt KNN-filmene for å forbedre de piezoelektriske egenskapene til filmene. Testing av filmene viste at KNN-filmene med både kalsium og titan hadde de beste egenskapene, etterfulgt av KNN-filmene som kun ble tilsatt kalsium. KNN-filmer uten kalsium og titan hadde de dårligste egenskapene.

Den tredje delen av prosjektet utforsket en metode for å lage KNN-filmer på fleksible materialer (f.eks. polymerer), siden slike materialer vil dempe de piezoelektriske egenskapene til KNN-filmene minst mulig. Myke/fleksible materialer tåler som oftest ikke de høye temperaturene man trenger for å lage KNN-filmer (>500 °C), så metoden som ble utviklet innebar å først lage KNN-filmene på SiPt-brikker og så flytte de over til et fleksibelt materiale. Dette ble gjort ved å påføre et lag med sinkoksid mellom SiPt-brikkene og KNN-filmene. Etter at KNN-filmene var laget ved 700 °C ble det fleksible materialet poly-dimetyl-siloksan (PDMS) limt oppå KNN-filmene. Så ble sinkoksid-laget mellom KNN-filmene og SiPt-brikkene etset bort med eddiksyre, slik at KNN-filmer med PDMS ble løsnet fra SiPt-brikkene. Denne metoden viste seg å fungere bra, og metoden har potensiale for å kunne benyttes til å lage mange typer filmer på fleksible materialer.

I den siste delen av doktorgraden ble giftigheten til KNN-filmene testet på celler ved University of Sydney i Australia. Vanlige KNN-filmer og KNN-filmer med 0.5 % kalsium og titan ble testet mot to typer celler, bindevevs-produserende

fibroblast-celler og nervestøttevevs-produserende gliaceller. Cellene ble grodd på toppen av KNN-filmene over flere dager, og cellenes form/fasong, levedyktighet og reproduksjonsevne ble studert. For sammenligning ble cellene også grodd på glass-disker og SiPt-brikker uten KNN-filmer. Resultatene fra celle-forsøkene viste at ingen av typene KNN-filmer var giftige for cellene, og at cellene ved flere anledninger foretrakk KNN-filmene fremfor glass-diskene. Resultatene kvalifiserer KNN-filmer til videre biologiske forsøk mot implanterbar anvendelse.

Kort oppsummert har denne doktorgraden videreutviklet materialet KNN som en potensiell arvtager for det piezoelektriske materialet PZT, spesielt med tanke på bio-medisinske applikasjoner/helse og medisin. En helt ny framstillingsplattform for piezoelektriske KNN-filmer er utviklet i denne doktorgraden, og arbeidet viser at KNN-filmer har potensialet for å kunne brukes i implanterbar elektronikk.

Contents

1

Introduction

1.1 Background and motivation

Electronic devices have become commonplace in today's society. We live side-by-side with electronics and utilize their benefits in all parts of our daily lives. The health sector is no exception, and in some cases these devices have found their way into our bodies as implantable electronic aids. The most common example is probably the artificial cardiac pacemaker, first successfully applied in 1958.[1] However, the interplay and communication between our body and such medical electronic devices is not trivial. The human body is an incredibly complex system, functioning with mechanical motions, fueled by chemical energy and controlled by electrochemical nerve signals. Having transducing components that can convert signals and translate between these processes and medical devices is therefore extremely valuable in modern medicine.[2] Examples include instruments that can monitor blood pressure (mechanical signal ↔ electric signal), blood sugar content (chemical signal ↔ electric signal) or cognitive activity (electrochemical signal ↔ electric signal).

Conversion between mechanical and electric signals can be performed passively with materials exhibiting the *piezoelectric effect*,[3,4] illustrated in Figure 1.1. Piezoelectricity was first demonstrated in 1880 by Pierre and Jacques Curie and later successfully theorized by Woldemar Voigt in the 1890s, although scientists like Marie Curie, Pierre Duhem, Wilhelm Röntgen and William Thomson (alias Kelvin) also contributed to the understanding of piezoelectricity.[5] The piezoelectric effect is a phenomenon arising from crystallographic asymmetry and is characterized by the creation of an electrical polarization across a material during deformation (*direct* effect). The effect is also reversible – an applied electrical field across the material will cause structural strain (*indirect/converse* effect), see Figure 1.1.

Piezoelectricity is caused by asymmetric displacement of the anions and cations in the piezoelectric material during deformation (Figure 1.2), resulting in a change in polarization across the material. Because of this, piezoelectricity is only observed in materials with non-centrosymmetric crystal structures. The simple interplay between mechanical and electrical signals makes the piezoelec-

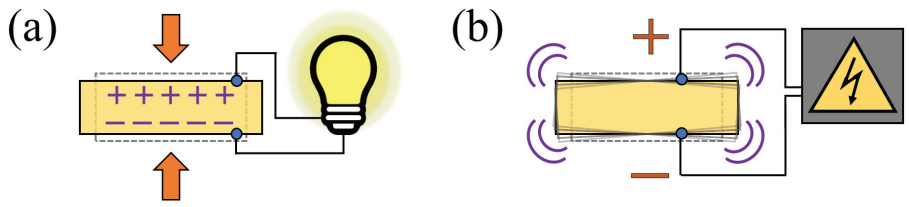

Figure 1.1: Illustration of the (a) direct and (b) indirect/converse piezoelectric effects.

tric materials incredibly useful, for example as sensors, actuators or energy harvesters.[6,7] Due to this versatility, piezoelectric components have found their way into almost all electronic devices today, from loud-speakers and pressure sensors to ultrasound devices and micro electromechanical systems (MEMS).[8]

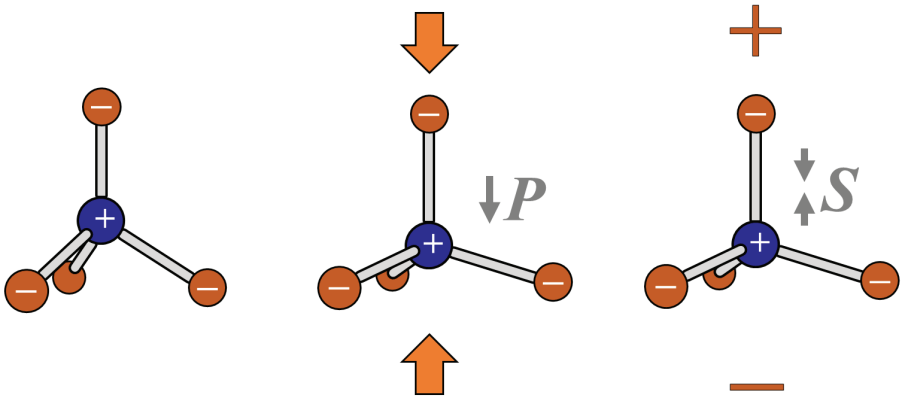

Figure 1.2: Crystal structure of a piezoelectric material at rest (left), during mechanical deformation (middle) and as subjected to an electric field (right).

The materials with the highest piezoelectric performance to date are the *ferroelectric* ceramics.[9–12] Ferroelectric materials form a subset of the piezoelectric materials, as presented in Figure 1.3 (a). The ferroelectric materials are characterized by having a remanent polarization at zero electric field that can be switched by application of an external electric field. Inherently the ferroelectric materials consist of *domains* wherein the polarization is oriented in the same

direction. These domains can be aligned by applying a strong unidirectional electric field across a ferroelectric material in a process termed *poling* (Figure 1.3 (b)). Following this, ferroelectric materials can have a macroscopic polarization and exhibit a homogeneous piezoelectric performance due to the additive polarization of the domains, despite having a polycrystalline microstructure. This flexibility in polarization orientation gives rise to the characteristic ferroelectric polarization-electric field hysteresis loop illustrated in Figure 1.3 (c).

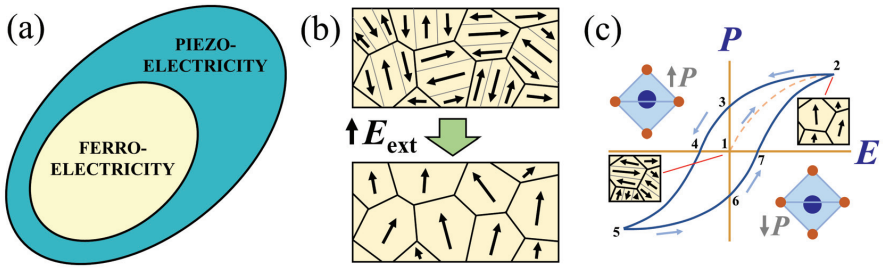

Figure 1.3: (a) The relationship between piezo- and ferroelectricity. (b) Ceramic grains containing ferroelectric domains with random orientation (top) and the same grains after poling (bottom). (c) Ferroelectric hysteresis loop of polarization as a function of electric field.

Although ferroelectricity was discovered in Rochelle Salt in the 1920s, the "ferroelectric era" in the history of piezoelectricity did not kick off until the 1940s when the phenomena was found in the ceramic perovskite barium titanate ($BaTiO_3$, BT).[13] The following decade, around 20 new perovskite structured ferroelectric ceramics were found, including lead zirconate titanate ($PbZr_xTi_{1-x}O_3$, PZT)[14] and potassium sodium niobate ($K_xNa_{1-x}NbO_3$, KNN).[15] Early on, an exceptionally high piezoelectric response was observed in PZT, owing to a morphotropic phase boundary in the composition $PbZr_{0.55}Ti_{0.45}O_3$.[16,17] The following decades, ferroelectric perovskites based on PZT dominated the piezoelectric marked, and consequently they became a common component in consumer electronics.[18] The PTZs were first out-performed in the late 1990s by the relaxor-based single crystals of $Pb(Zn_{1/3}Nb_{2/3})O_3$–$PbTiO_3$ (PZN-PT) and $Pb(Mg_{1/3}Nb_{2/3})O_3$–$PbTiO_3$ (PMN-PT), which to date are the best performing piezoelectric perovskites.[10,19,20] For the last two decades the focus has been shifted towards developing lead-free piezo-

electric materials due to stricter regulations worldwide regarding the use of heavy metals like lead in civil applications.[21–29] Among these, KNN has received considerable attention due to decent piezoelectric properties and a high Curie temperature.[30–38] After the discovery of ferroelectricity in KNN in 1959,[15] a renaissance for the material came in 2004 when Saito et al.[39] reported on chemically and structurally modified KNN with piezoelectric properties comparable to PZT. By doping KNN with Li^+, Sb^{5+} and Ta^{5+}, and using reactive-templated grain growth (RTGG), Saito and coworkers obtained textured KNN ceramics with a piezoelectric coefficient of 416 $pC\,N^{-1}$. The research on KNN has since been comprehensive, as demonstrated by the fact that more than 35 different elements have been used as chemical additives in the effort to improve the ferroelectric and piezoelectric properties of KNN.[31,32,36] Currently, the highest piezoelectric performance for KNN-based ceramics measured by d_{33} is above 700 $pC\,N^{-1}$.[40]

It is not difficult to imagine applications of piezoelectric components in implantable electronic devices: Blood pressure sensors for implantable cardioverter defibrillators,[41,42] energy harvesters and activity sensors for artificial pacemakers,[42–48] actuators for microfluidic and drug-delivering systems.[49–56] Multiple other applications have been proposed.[57] However, there are several challenges to address when designing and developing such piezoelectric components.[58,59] The first constraint is the size limit to the dimensions of an implantable device, which obviously affects the upper size limit of the piezoelectric element. In most cases this means scaling down at least one geometrical dimension to the nano- or micro-region, ruling out conventional solid-state synthesis techniques. Secondly, there are the functional properties of such piezoelectric components. In addition to having a high efficiency in terms of piezoelectric performance, the chosen material system should be robust in terms of cycling fatigue and ageing as some electronic medical implants have an expected lifetime of several years.[58,59] And finally, the piezoelectric component must be designed so that it is interacting (at least) neutrally with the biological environment in which it is placed, i.e. exhibit *biocompatibility*.[60–63] This concept of biocompatibility is reciprocal: The biological environment should not be destructive for the device/component, and the device/component should not be destructive for the biological environment – at least not destructive to the point of device/component failure or persistent

degradation of the biological environment. This challenge is not trivial; even if the piezoelectric component is not harmful for the biology surrounding it, the biological surroundings can be fatal for the piezoelectric component. The component must withstand both the chemical aggressiveness of body fluid (water, ions, proteins) as well as the biological inhospitality of the host (cells, bacteria). The shortcut around this, hermetically encapsulation within a bioinert material, can swiftly choke the functionality of the piezoelectric component.

1.2 Aim of the work

The overall aim of this work was to develop lead-free piezoelectric oxide films for biomedical applications based on the ferroelectric material potassium sodium niobate (KNN). More specifically, the work aimed at developing an aqueous synthesis platform for KNN thin films and to evaluate if these films can be viable as medically implantable (*in vivo*) piezoelectric materials, for example as implantable sensors or energy harvesters. Such applications span a wide range of material property requirements, such as overall piezoelectric performance, resistance to loading cycle fatigue and ageing (both piezoelectric and mechanical), and biocompatibility. For this reason, the project targeted a bottom-up approach so that these end specifications for the KNN films could be tailored in the synthesis. Moreover, all aspects of the work were performed to minimize the use of hazardous chemicals and complex processing steps in the materials synthesis. Not only would this keep the environmental footprint and possible health risk associated with the processing at a minimum, but it would also maximize the accessibility of the synthesis for industry due to low manufacturing costs.

To form a synthesis platform for the project, a processing route to phase pure KNN films was developed based on previous work in our group.[64] The processing route was based on aqueous chemical solution deposition (CSD), as this technique offers a large process parameter space, excellent stoichiometry control and low temperature processing, which is important when working with alkali metals. The synthesis platform also has the potential of low-cost/high-volume manufacturing of thin films. The nucleation kinetics of ternary oxide phases in the precursor system proved to be of detrimental importance for the final phase composition of the KNN thin films, and this work includes a comprehensive study of how the precursor chemistry can be engineered/manipulated to control the nucleation kinetics. The role of the type of precursor solution on the final microstructure of the films was also thoroughly investigated using several characterization techniques, such as X-ray diffraction (XRD) and transition electron microscopy (TEM).

In order to improve the functional properties of the KNN thin films, composi-

tional engineering was investigated. Compositional engineering of KNN has previously been extensively studied in terms of enhancing the piezoelectric properties,[31,32,36] but the most prominent dopants, Li^{+}, Sb^{5+} and Ta^{5+}, are not suitable for implantable devices due to health concerns. Therefore, the dopants evaluated were chosen based on their non-toxicity, piezoelectric enhancement properties and on preliminary results on their effect on reducing ion release from KNN. The two different heterovalent dopants Ca^{2+} and $CaTiO_3$ were examined, Ca^{2+} being a A-site donor dopant and $CaTiO_3$ being a charge-neutral co-dopant (Ca^{2+} and Ti^{4+} on A- and B-site, respectively). The dopants' effect on phase morphology, dielectric behavior and microstructure in KNN was thoroughly studied and put in context to piezoelectric performance of the KNN films.

The final synthesis part of the work explored a new processing route to KNN films on flexible substrates. Fabrication of KNN films on flexible supports allow for high-performing MEMS devices with minimal loss of functionality to mechanical clamping. The processing was based on the aqueous synthesis platform developed earlier in the thesis and utilized a ZnO release layer to detach the KNN film from the initial rigid substrate, a method first described by Liu and coworkers.[65] Precursor solutions and processing parameters for the ZnO release layer and a $BaTiO_3$ buffer layer were developed and curing conditions and deposition parameters for the flexible polymer were optimized. Characterization of phase morphology and microstructure were performed consecutively for each processing step. Suggestions for further optimization and expansion of this synthesis route was also discussed.

In vitro cytotoxicity studies were performed to form a first approximation of the biocompatibility of KNN films. The potential challenge with deconvolving which biological responses were triggered by the film and which by the substrate was solved by running parallel tests on substrates with no deposited films. Cell proliferation and cell morphology assays using rat Schwann cells, human 161BR fibroblast cells and human SH-SY5Y neuroblastoma cells were conducted in collaboration with Dr. Holsinger's group at the Laboratory of Molecular Neuroscience and Dementia, Brain and Mind Centre, The University of Sydney. The biological responses to the KNN films were examined using immunocytochemistry, confocal microscopy, scanning electron microscopy (SEM) and spectrophotometry.

2

Literature review

2.1 Piezoelectric materials

2.1.1 Phenomena and characteristics

The history of piezoelectricity

The discovery of piezoelectricity

"We have found a new method for developing polar electricity in (...) crystals, which consists of subjecting them to variations in pressure along their hemihedral axes"[66]

With these words, the French brothers Pierre and Jacques Curie announced their discovery of *piezoelectricity* in 1880.[5] In their work, P. and J. Curie measured electric tension upon compression of the ten non-symmetrical crystals cane sugar, boracite, calamine, quartz, Rochelle salt, sodium chlorate, tartaric acid, topaz, tourmaline and zinc blende, and the brothers related the observed effect to the known pyroelectric property of some of these crystals.[5,67] Pyroelectric materials, which actually form a subset of the piezoelectric materials, had been known since the mid-1700s and are characterized by the change in electric polarization of a material upon heating and cooling.[68] P. and J. Curie demonstrated that piezoelectricity was related to crystal symmetry, but they had only demonstrated the *direct* piezoelectric effect, i.e. formation of electric polarization by mechanical strain. The *converse* piezoelectric effect, i.e. the formation of mechanical strain by electric polarization, was predicted by Gabriel Lippmann in 1881 and experimentally confirmed by various researchers short time after, including the Curie brothers.[5,67] The phenomenon got its name in 1881 by Wilhelm Hankel, who named the property after the Greek word for "to press" – *piezein*.[5] A full theoretical model of piezoelectricity describing the thermodynamics and molecular/atomistic theory behind the phenomenon was not achieved until the end of the 1890s after years of opposing theories and models by scientists like Woldemar Voigt, Ernest Mallard, Paul Czermak, Eduard Riecke, Friedrich Pockels, Pierre Duhem, Wilhelm Röntgen and William Thomson (alias Kelvin). The slow process of forming a theoretical model for piezoelectricity was in large because piezo-

electricity essentially involves several complex subdisciplines, including electromagnetism, crystal mechanics/elasticity, crystal physics and crystallography, and due to limited theoretical models for crystals in general at the time.[3,5] For example, pyroelectricity, which was discovered a century earlier, gained its theoretical model from the work on the model for piezoelectricity.

Ferroelectricity, perovskites and PZT

In the early years of the 1900s an electrical analogy to ferromagnetism was hypothesized among scientists, i.e. the possibility of a material to have a remanent electrical polarization that can be switched by an electric field.[13,18,69] In 1920, the effect was observed in Rochelle salt crystals by Joseph Valasek.[70] Rochelle salt (potassium sodium tartrate) was a known pyroelectric (1824) and piezoelectric (1880) double salt with a complex crystal structure, and the salt remained the only known ferroelectric material until the phenomenon was observed in potassium dihydrogen phosphate (KH_2PO_4, KDP) in 1935.[13,18,69] During the 1930s the first thermodynamic and atomistic models of ferroelectricity were drafted based on experiments with Rochelle salt and KDP, but the complex crystal structure of these salts was a challenge for this work.[13] The brittle and water-soluble nature of Rochelle salt and KDP also limited the interest in ferroelectricity at this point in history.[13,71]

Attempting to develop capacitors with high dielectric constants during World War II, researchers found an astonishingly high permittivity ($\epsilon_r > 1100$) in $BaTiO_3$ (BT), a mixed oxide ceramic with a perovskite crystal structure.[13,18,69,71] The high permittivity in $BaTiO_3$ was related to ferroelectricity in 1944, and this chemically and mechanically stable ceramic was acknowledged as a useful piezoelectric transducer already the year after.[18,71] An incredibly important discovery regarding the ferroelectric ceramics was the ability to align the ferroelectric domains in these materials (i.e. *poling*) so that the materials could exhibit a uniform piezoelectric performance despite being polycrystalline.[18] By the end of the 1940s, two new ferroelectric compounds were discovered ($LiNbO_3$, $LiTaO_3$), and during the 1950s 25 new families of ferroelectrics were found.[13,18] Among these new materials were the perovskites $PbZr_xTi_{1-x}O_3$ (PZT)[14] and $K_xNa_{1-x}NbO_3$ (KNN).[15] Already during the 1950s PZT stood out as an excellent piezoelectric material, and scientists found a peak in performance for the composition

$PbZr_{0.52}Ti0.48O_3$.[16,17] In addition to superb piezoelectric properties, the PZT material system exhibited good thermal stability, it was easy to pole, relatively simple and inexpensive to fabricate, and it allowed for compositional engineering to tune the dielectric properties, for example with Nb^{5+} on the Zr^{4+}/Ti^{4+} site or La^{3+} on the Pb^{2+} site.[13,18] From the 1950s and 60s, solid solutions based on ferroelectric PZT have dominated the piezoelectric transducer marked up until today,[8,11,12,18,72] but in the last two decades there has been a shift in focus from the lead-based piezoelectric materials to lead-free piezoelectric materials.[21–29]

Towards lead-free piezoelectric materials

Lead is a toxic heavy metal,[73,74] and the World Health Organization identifies lead as 1 of 10 chemicals globally of major health concern as of 2019.[75] The environmental and health risks associated with lead are present throughout the lifecycle of the metal, starting during mining and refining of the lead ore and persisting during production, use and disposal of lead-containing products.[76] Because of this, restrictions and regulations to the use (*Restriction of the use of certain hazardous substances in electrical and electronic equipment*, RoHS) and disposal (*Waste electrical and electronic equipment*, WEEE) of lead and other dangerous substances in electronic devices were adopted by the European Parliament in 2003[77,78] and revised in 2011/2012.[79,80] Several legislative bodies worldwide have since adopted similar restrictions.[81–85] However, exceptions to these legislations exist for components with no suitable alternatives available, and piezoelectric ceramics are subjected to this in Exemption 7(c)-I in RoHS.[86] Because of this PZT can still be used in consumer electronics, and it is estimated that the world production of PZT was 2500 tons as of 2018.[76] After the first RoHS legislation was adopted by the European Union in 2003, the pursuit to find lead-free alternatives to PZT ceramics has been comprehensive, as illustrated in Figure 2.1.[21–29] The most studied lead-free piezoelectric ceramic are alkali niobates (KNN), the bismuth-alkali titanates ($Bi_{0.5}(Na_K)_{0.5}TiO_3$, BNKT) and the barium titanates (BT), but no lead-free ceramic class has been found to replace PZT in all of its applications as of today.[23,26–29]

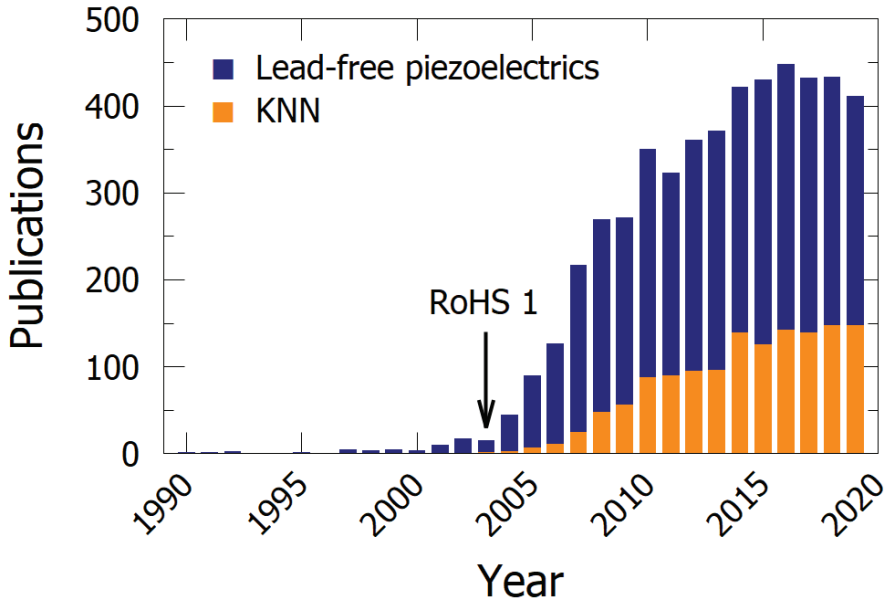

Figure 2.1: The number of publications on lead-free piezoelectric materials and KNN from 1990 to 2019. The arrow indicates the year the European Parliament adapted the first RoHS legislation. Data collected from Scopus.

Mechanisms and characteristics

Hierarchy of properties and crystal symmetries

To understand and successfully describe the piezoelectric properties of KNN, it is important to address the characteristics of some related material classes, especially the dielectric and ferroelectric materials. All piezoelectric materials are inherently dielectric, and some piezoelectric materials are pyroelectric and ferroelectric.[4,87–90] The relationship between di-, piezo-, pyro- and ferroelectricity is presented in Figure 2.2 (a) and demonstrates a hierarchy of increasingly exclusive properties. The new properties that emerge at each step down the hierarchy in Figure 2.2 (a) can be characterized and quantified by new measuring techniques. However, the addition of new properties in each step might affect the

properties in the parent classes, and it is sometimes valuable to characterize the materials in a more exclusive class by probing properties in a parent class. Ferroelectric phase transitions can for example be measured through dielectric permittivity studies.

Piezoelectricity, pyroelectricity and ferroelectricity are all properties related to structural geometry, and the three properties can only be observed in materials with certain crystal symmetries, as illustrated in Figure 2.2 (b).[4,88,90,91] Piezoelectric materials must have non-centrosymmetric crystal structures, and 20 of the 32 crystal classes allow for piezoelectricity. Pyro- and ferroelectric materials have crystal structures with unique polar axes, and only 10 out of the 32 crystal classes have this property. Although the crystal symmetry can predict if a material is piezo- or pyroelectric, experimental investigations must be conducted to quantify these properties.[90]

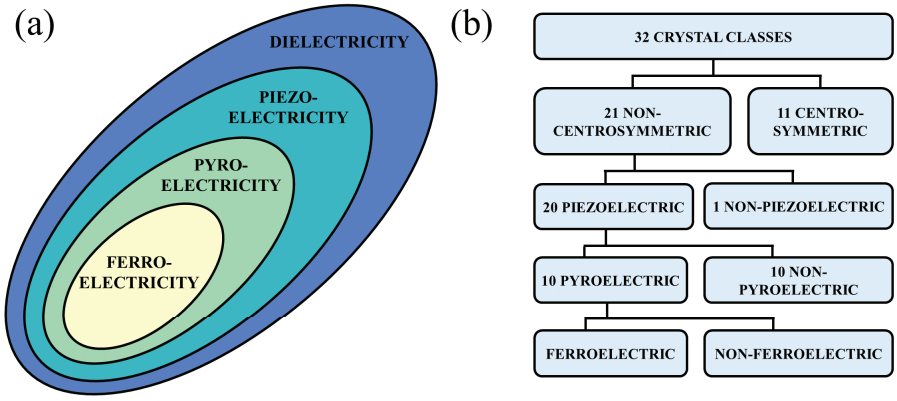

Figure 2.2: (a) Hierarchy of properties in dielectric materials. (b) Hierarchy of crystal classes relating to piezo-, pyro- and ferroelectricity.

Dielectricity: characteristics and figures of merit

Ideal dielectric materials have zero conductivity under DC current, and when a voltage is applied across a dielectric material the charged species (e.g. electrons, ions, dipolar molecules, space charges etc.) in the material will *polarize*.[89,91–93] *Polarization* (P, [$\mathrm{C\,m^{-2}}$]) is the displacement of charge in an electric field, and

how easily polarization can be induced in a material is given by the material's *polarizability* (α, [$\mathrm{C\,m^2\,V^{-1}}$]). A material's *capacitance* (C, [F or $\mathrm{C\,V^{-1}}$]) is the amount of polarized (stored) charge in a material per volt applied. The capacitance of a material (C_m) relative to the capacitance of free space (C_0) is defined as the material's *dielectric constant* or the *relative permittivity* (ϵ_r, [-]) of the material:

$$\epsilon_r = \frac{C_m}{C_0} \tag{2.1}$$

Due to the difference in mobility of the species that contribute to polarization (electrons, ions etc.), the value of the permittivity of a material is highly temperature and frequency dependent. The permittivity of a material will also have a phase shift when subjected to an electric field, and permittivity is therefore often treated as a complex function with a real and an imaginary part:[89,91–93]

$$\epsilon_r = \epsilon' + i\epsilon'' \tag{2.2}$$

The energy dissipation associated with this phase shift (e.g. through heat) is termed *dielectric loss* and is parameterized with the loss tangent ($\tan\delta$, [-]). If neglecting loss through conductivity, the loss tangent is defined as the ratio of the imaginary and the real part of the permittivity:[87,89,91–93]

$$\tan\delta = \frac{\epsilon''}{\epsilon'} \tag{2.3}$$

The *electrical quality factor* (Q_e, [-]) is simply the inverse of the dielectric loss, as presented in Equation 2.4.[87]

$$Q_e = \frac{1}{\tan\delta} \tag{2.4}$$

Equivalent to the dielectric loss factor ($\tan\delta$) and the electric quality factor (Q_e), the *mechanical loss factor* ($\tan\phi$) and *mechanical quality factor* (Q_m) describe the energy dissipation due to phase shift when a material is strained in response to applied stress.[87]

The *dielectric susceptibility* (χ, [-]) of a material is the permittivity of the material after the contribution from the permittivity of free space is subtracted ($\chi = \epsilon_r - 1$).[89,91–93]

Piezoelectricity: a story of crystal asymmetry

Piezoelectricity is a material property where external mechanical stress (σ) induces electric polarization (P) in a material.[4,87,88,90] This property is also reversible: an external electric field (E) across said material will induce a mechanical strain (S). These electromechanical phenomena are termed the *direct* and *indirect*/*converse* piezoelectric effect, respectively. The piezoelectric effect is a consequence of crystallographic asymmetry, where the crystal structure of the material lack centrosymmetric symmetry. Upon mechanical deformation along certain directions of these non-centrosymmetric structures, oppositely charged species are displaced disproportionally, resulting in a local polarization. This is illustrated for a structure with tetragonal coordination in Figure 2.3 (a). Conversely, in an external electric field aligned in the same direction as the deformation in Figure 2.3 (a), the charged species will polarize according to the direction of the electric field and the structure will deform (Figure 2.3 (b)).

The electromechanical coupling in piezoelectricity is linear, and the proportionality between polarization, electric field, strain and stress is quantified by four *piezoelectric coefficients*, defined by the following four partial derivatives:[3,87,94]

$$d = \left(\frac{\partial S}{\partial E}\right)_\sigma = \left(\frac{\partial P}{\partial \sigma}\right)_E \tag{2.5}$$

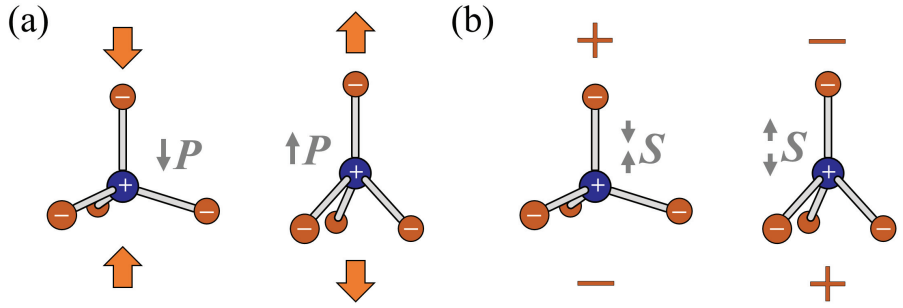

Figure 2.3: (a) The direct piezoelectric effect of a tetragonally coordinated structure. Applied stress (arrows) disproportionally displace anions and cations, resulting in polarization. (b) The converse piezoelectric effect on a tetragonally coordinated structure. Applied electric fields (+, −) polarize the structure, resulting in structural deformation.

$$g = \left(-\frac{\partial E}{\partial \sigma}\right)_P = \left(\frac{\partial S}{\partial P}\right)_\sigma \tag{2.6}$$

$$e = \left(-\frac{\partial \sigma}{\partial E}\right)_S = \left(\frac{\partial P}{\partial S}\right)_E \tag{2.7}$$

$$h = \left(-\frac{\partial \sigma}{\partial P}\right)_S = \left(-\frac{\partial E}{\partial S}\right)_P \tag{2.8}$$

The piezoelectric coefficients d ([$\mathrm{CN^{-1}}$ or $\mathrm{mV^{-1}}$], "charge coefficient") and g ([$\mathrm{NV^{-1}m^{-1}}$ or $\mathrm{m^2C^{-1}}$], "voltage coefficient") are the most common, as these are indicators of how efficient a piezoelectric material is at developing vibration from electricity or voltages from mechanical stress, respectively.[17,87,94] However, the direct and converse piezoelectric effect are most often described by using d according to Equations 2.9 and 2.10, respectively:[3,4,90,91,94]

$$P_k = d_{kij}\sigma_{ij} \tag{2.9}$$

$$S_{ij} = d_{kij}E_k \tag{2.10}$$

The Einstein summation convention is applied for repeated indices in Equations 2.9 and 2.10. Since polarization and electric field are first-rank tensors/vectors and stress and strain are second-rank tensors, the piezoelectric coefficients are third-rank tensors.[3,4,91,94] Notation for the direction of the applied stimulus (stress, electric field) and induced effect (polarization, strain) is added in subscript when reporting the piezoelectric coefficients. The three components describing these tensor directions can be reduced to two numbers ($i, j = 1, 2, \ldots, 6$) using Voigt notation and exploiting symmetry characteristics. For the longitudinal piezoelectric coefficients (d_{33}, g_{33} etc.), the direction of the stimulus and induced effect are both along the "c-direction" of a unit cell.

How efficient a piezoelectric material converts between electrical and mechanical energy is described by the electromechanical coupling factor (k, [-]) according to Equations 2.11 and 2.12.[3,87]

$$k^2 = \frac{\text{electrical energy converted to mechanical energy}}{\text{input electrical energy}} \tag{2.11}$$

$$k^2 = \frac{\text{mechanical energy converted to electrical energy}}{\text{input mechanical energy}} \tag{2.12}$$

Since the transformation of energy never is ideal, the electromechanical coupling factor will always have a value $k < 1$.[87]

Reporting on piezoelectric performance of materials is done in several ways de-

pending on the intended field of application.[26,87] For non-resonant applications (e.g. sensors, microphones, energy harvesters), the product of d and g ($d \cdot g$, [$pm^3\,J^{-1}$]) is usually reported. For resonant applications (e.g. oscillators, sonars, ultrasonic devices), the product of k^2 and Q_m ($k^2 \cdot Q_m$, [-]) is usually reported. For actuation applications (e.g. loud-speakers, injectors), the ratio of S_{max} and E_{max} (S_{max}/E_{max}, [$pm\,V^{-1}$]) is usually reported. For high-output applications (e.g. spark-ignitors, buzzers), the piezoelectric coefficient d is usually reported.

Surprisingly, piezoelectricity is not an uncommon material property. 21 of the 32 crystal classes are non-centrosymmetric, and 20 of these allow for piezoelectricity.[4,87,90,91] An estimated 30 % of all known materials today are non-centrosymmetric, and thousands of these have measurable piezoelectric activity.[4] Piezoelectricity is found in natural polymers and composites like wood, silk, bone, tendon,[95] and in natural occurring minerals like quartz (SiO_2), zincite (ZnO), zincblende (ZnS), tourmaline, sillenite ($Bi_{12}SiO_{20}$) and greenockite (CdS).[91] When it comes to piezoelectric materials for technological applications, however, only a couple of hundreds have sufficiently high piezoelectric response.[4] This group of piezoelectric materials are dominated by the *polar* piezoelectric materials.[4,18,87,88,90,96]

Pyro- and ferroelectricity: polar crystal structures

Pyroelectric materials are characterized by having a spontaneous polarization (P_s), illustrated in Figure 2.4 (a).[87,91,93,94] The spontaneous polarization is a result of the polar crystal structure of these materials, and pyroelectricity is only possible in crystal systems with a unique polar axis.[91,94] The spontaneous polarization in pyroelectric materials is temperature dependent:[93,94]

$$\Delta P_s = p \Delta T \tag{2.13}$$

In Equation 2.13, p is the *pyroelectric coefficient* ([$C\,m^{-2}\,K^{-1}$]) and quantifies the temperature dependency of the spontaneous polarization. p is defined by the partial derivative form of Equation 2.13:[94]

$$p = \frac{\partial P_s}{\partial T} \tag{2.14}$$

Ferroelectric materials are a subset of the pyroelectric materials, and they are characterized by having a spontaneous polarization that can be switched by an external electric field (Figure 2.4 (b)).[87,91,93,94] A consequence of this is the existence of ferroelectric *domains* in these materials, i.e. regions of homogeneously oriented polarization.[4,90,94,97] Since the spontaneous polarization in ferroelectric materials can be switched, the ferroelectric domains can be manipulated to have the same polarization direction by applying a strong enough electric field. The boundaries between the domains, called *domain walls*, are mobile. When a ferroelectric material is subjected to an electric field, favorably oriented domains can grow on the expense of less favorably oriented domains by domain wall migration. This process, illustrated in Figure 2.4 (c), is called *poling* and allows polycrystalline ferroelectric samples to have a macroscopic polarization and to exhibit a macroscopic piezoelectric effect.[18,88,94,96]

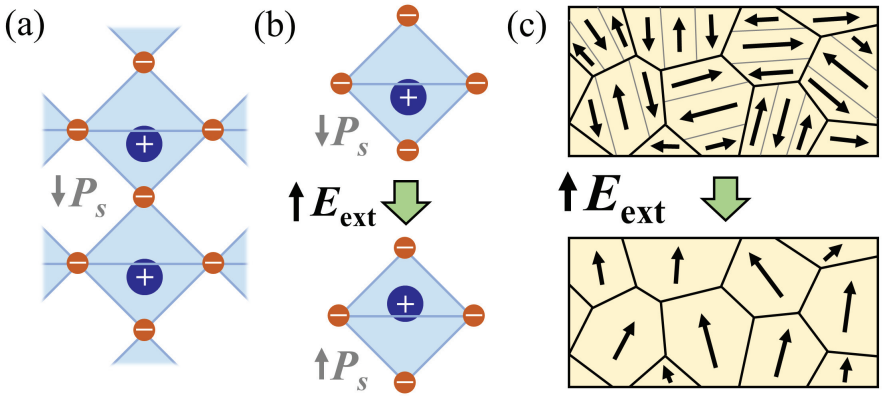

Figure 2.4: (a) Spontaneous polarization (P_s) in the crystal structure of a pyroelectric material. (b) Switching of the spontaneous polarization in a ferroelectric crystal by application of an external electric field (E_{ext}). (c) Poling of domains in a polycrystalline ferroelectric sample by application of an external electric field.

Due to the polarization switching in ferroelectric materials, the materials' polarization and strain form hysteresis loops when measured in a switching electric field (P-E loops and S-E loops, respectively), as illustrated in Figure 2.5.[94,96,98,99] By analyzing these curves, the remanent polarization (P_r), saturation polarization (P_{sat}), maximum achievable strain (S_{max}) and coercive electric field (E_c) of a ferroelectric material can be determined. However, many more characteristics can be inferred from these measurements, as P-E and S-E loops are affected by several factors, including material properties (e.g. grain morphology, phases and phase boundaries, compositional impurities, sample geometry, sample conductivity), aging and measuring conditions (e.g. electric field amplitude, frequency, temperature, stress, fatigue).[98]

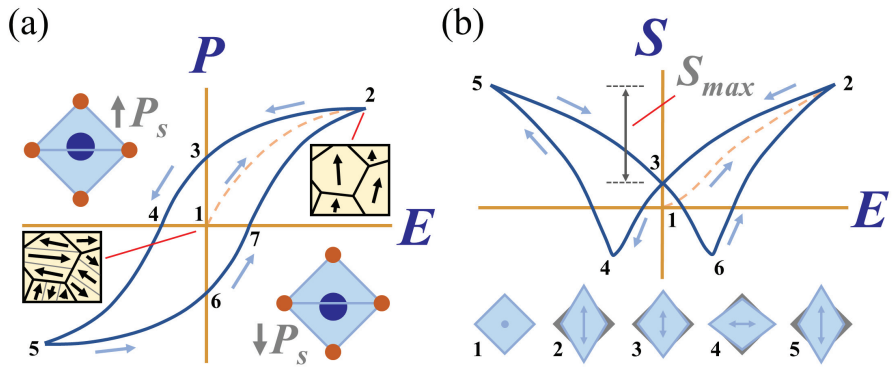

Figure 2.5: (a) Polarization-electric field hysteresis loop (P-E loop) of a polycrystalline ferroelectric material. Point 1: random domain orientation and no net polarization. Points 2 and 5: polarization saturation (P_{sat}). Points 3 and 6: remanent polarization (P_r). Points 4 and 7: coercive electric field (E_c). The direction of the spontaneous polarization is illustrated with MO_6 octahedra. (b) Strain-electric field hysteresis loop (S-E loop) of a polycrystalline ferroelectric material. Point 1: no net strain. Points 2 and 5: Peak strain (S_{pol}). Point 3: remanent strain (S_{rem}). Points 4 and 6: coercive electric field (E_c). Maximum (achievable) strain (S_{max} = S_{pol} - S_{rem}) is marked in the figure. The strain directions at each point is illustrated with MO_6 octahedra.

Ferroelectric materials have an upper boundary temperature where they lose their spontaneous polarization, called the Curie temperature (T_C, [K]).[87,88,94,96] This temperature is associated with a phase transition where the crystal struc-

ture of the material changes from a polar symmetry to a non-polar symmetry.[91,94] A ferroelectric material cooled through the Curie temperature will obtain a randomly oriented domain structure and no net macroscopic polarization, as this minimizes large-area surface charges and therefore minimizes the energy of the system. Around the Curie temperature, the relative permittivity of ferroelectric materials spikes due to enhanced fluctuation at the phase transition. Above the Curie temperature, the relative permittivity follows the Curie-Weiss law, presented in Equation 2.15.[87,93,96]

$$\epsilon_r = \frac{C}{T - T_0} \tag{2.15}$$

where C is the material specific Curie constant ([K]) and T_0 (also θ) is the Curie-Weiss temperature ([K]).

The commercially most important ferroelectric materials are the perovskites due to their thermodynamic stability, rich chemistry and malleable phase symmetry.[90,96,100] The perovskite crystal structure consists of a large and a small cation (A and B, respectively) and an anion (X, usually O^{2-}), with stoichiometry corresponding to ABX_3.[91,100] The structure is composed by corner-sharing BX_6 octahedra and A cations in 12-fold cuboctahedral coordination between the octahedra, as illustrated in Figure 2.6. The ferroelectric polarization in these structures arise from displacement of the B cation in the oxygen octahedra.

The ideal perovskite structure is centrosymmetric with the point group symmetry $m3m$, however most perovskites have structures slightly distorted from the ideal structure.[90,91,93,100] The degree of distortion from ideality can be estimated using the Goldschmidt's tolerance factor t,[102]

$$t = \frac{(r_A + r_O)}{\sqrt{2}(r_B + r_O)} \tag{2.16}$$

where r_A, r_B and r_O correspond to the ionic radii of the A cation, B cation

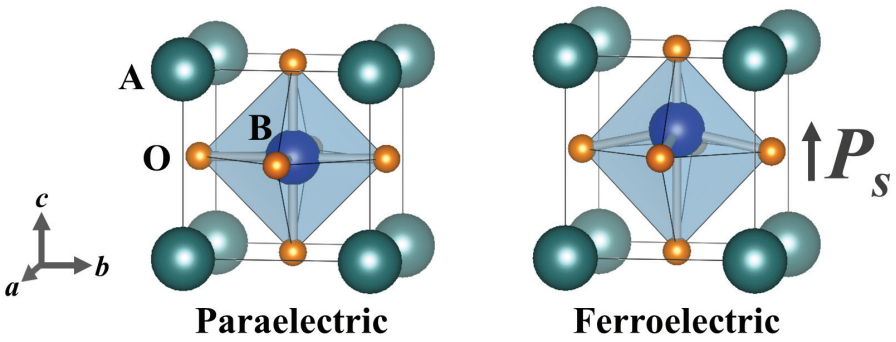

Figure 2.6: The perovskite (ABO_3) unit cell with cubic (left) and tetragonal (right) symmetry. The off-centered B cation in the tetragonal unit cell allows for ferroelectric polarization. The tetragonality and polarization displacement are exaggerated to illustrate the effects. The figure was made using the software VESTA.[101]

and O anion, respectively. In general, tolerance factors below 1 favor rhombohedral distortions, tolerance factors above 1 favor tetragonal distortions, and tolerance factors around 1 (0.97-1.02) are associated with morphotropic phase boundaries.[23,90,100] These distortions are incredibly important for ferroelectric perovskites as they not only allow for ferroelectric polarization, but also determine the crystal phases of the materials and thereby dictate the possible polarization directions of the off-centered B cation.[91,103] Six symmetries are available for the perovskite structures depending on the B cation displacement: Cubic (space group (s.g.) $Pm-3m$, no polarization), tetragonal (s.g. $P4mm$, polarization along $[100]_{pc}$), orthorhombic (s.g. $Amm2$, polarization along $[110]_{pc}$), rhombohedral (s.g. $R3m$, polarization along $[111]_{pc}$), monoclinic (s.g. Cm, polarization along $[hk0]_{pc}$) and triclinic (s.g. $P1$, polarization along $[hkl]_{pc}$).[23,100,104] These symmetries with their respective polarization directions are illustrated in Figure 2.7. The monoclinic symmetries are associated with higher ferroelectric performance due to unrestricted polarization rotation mechanisms.[9,11]

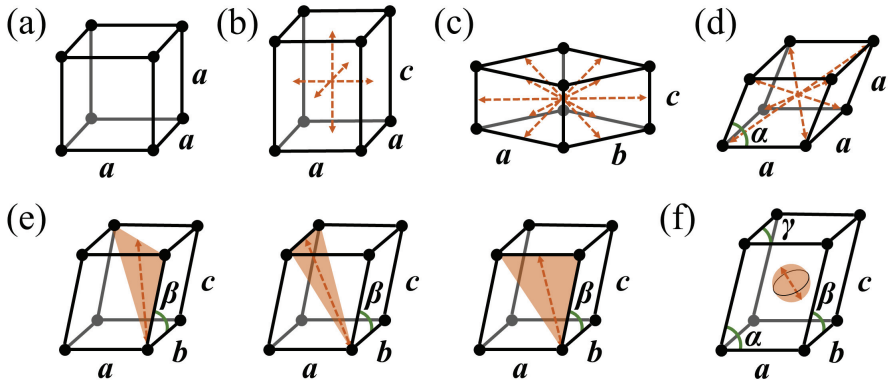

Figure 2.7: Illustrations of the crystal systems (a) cubic, (b) tetragonal, (c) orthorhombic, (d) rhombohedral, (e) monoclinic and (f) triclinic. Polarization directions are included. Adapted from [103].

Applications of piezoelectric materials

In the immediate decades after its discovery, piezoelectricity was regarded as a laboratory curiosity rather than an applicable phenomenon.[67,69] The first applications of piezoelectric materials were the use of quartz and Rochelle salt crystals as underwater sonars for detection of submarines in the period between World War 1 and 2.[8,67,69] During World War 2 piezoelectric oscillators were applied for ground-to-ground and ground-to-air communication on the battlefield.[67] The first use of the ferroelectric ceramics in the 1940s and 50s were as capacitors due to their high dielectric permittivity, but these materials were soon also utilized for their piezoelectric properties in vibration transducers, explosive-to-electrical transducers and electro-optics.[18,67] The boom of the consumer electronics age in the 1970s and 80s saw a massive demand for piezoelectric materials as tweeters/buzzers, cheap speakers, simple actuators, frequency resonators (quartz clocks) and even ignition sources for lighters.[8,18] Piezoelectric materials have since been employed as various types of sensors, including accelerometers, gyroscopes, surface acoustic wave sensors, acoustic emission sensors, gas sensors and pressure sensors.[8,105] Piezoelectric materials are especially suitable for high-temperature sensor applications, for example as knock sensors in com-

bustion engines and as engine fluid sensors.[8,105,106] Piezoelectric actuators are utilized in a wide range of technologies due to their microscopic precision, low energy consumption and fast response time.[7,8] These include injectors in ink jet printers, diesel injection engines and 3D printing machines, adjusting motors for camera lenses and intersatellite communication devices, micro-actuators in minimally invasive surgery tools, and nanoactuators in photoetching machines for semiconductor chip manufacturing.[7] On top of this comes medical applications, including ultrasound devices and implantable piezoelectric materials (described in *Piezoelectric materials in medical implants* on page 72).[8] The market value of piezoelectric components was estimated to be $21.6 billion USD in 2015 and the market is expected to grow to over $30.0 billion USD by 2022.[8]

2.1.2 Materials

Lead-free piezoelectric materials

General requirements

To successfully replace lead-based piezoceramics on the global market, alternative materials must be developed that perform equally good or better than the established lead-containing counterpart.[23,26] It is generally believed that no single composition can replace lead-based ceramics in all fields of application, and great progress has been made towards specially tailored lead-free materials capable of replacing lead-based ceramics in certain areas.[23,26–29] In general, lead-free materials have higher mechanical strength, lower permittivity and good electromechanical coupling factors compared to lead-based materials,[25] and their lower density often make them comparable to the lead-based materials in terms of piezoelectric performance per weight.[22] Further, several lead-free materials have been developed that are on par with or even better than the lead-based ones in terms piezoelectric coefficient, temperature stability and electromechanical coupling factors.[29] Yet, competing with the lead-based materials on performance is just one piece of the puzzle, and several other factors need to be fulfilled before lead-free materials can fully compete with the lead-based ones.[23,26] The lead-free materials of the future must not only perform better than the lead-free materials of today, but they must also be reliable over millions of cycles, they must be non-

toxic to produce, use and dispose, they must be inexpensive to manufacture, and they must have a sufficiently wide temperature window of processing.[23,26]

Lead-free materials

Although the research on lead-free materials has been comprehensive and include a wide range of materials, three material families stand out as especially promising candidates to replace lead-based ceramics.[21–29] These families are the alkali niobate-based family (KNN), the barium titanate-based family (BT) and the bismuth-alkali titanate-based family (BNT). A schematic of piezoelectric performance of these three lead-free materials versus PZT is presented in Figure 2.8.

KNN-based: Due to good piezoelectric properties, high Curie temperatures, compositional flexibility and a rich phase morphology, the KNN family is the lead-free material that has received most attention the last two decades.[22–29] A thorough review of KNN ceramics is given in $K_xNa_{1-x}NbO_3$ on page 30.

BT-based: BT-based ceramics have received much attention due to relatively high coupling factors (k_p ~50 %) and good piezoelectric properties (d_{33} = 190-750 $\mathrm{pC\,N^{-1}}$).[25,27–29,107] The solid solutions with $CaZrO_3$ ($Ba_{1-x}Ca_xZr_{1-y}Ti_yO_3$, BCZT) have been of special focus the last decade due to excellent piezoelectric properties ($d_{33} > 700\,\mathrm{pC\,N^{-1}}$).[25,27–29,107] The BT systems doped with Ca^{2+} and Sn^{4+} ($Ba_{1-x}Ca_xSn_{1-y}Ti_yO_3$, BCSnT) and Ca^{2+} and Hf^{4+} ($Ba_{1-x}Ca_xHf_{1-y}Ti_yO_3$, BCHT) have also received considerable attention.[107] However, the BT-based family has issues with low Curie temperatures (T_C = 110-130 °C), severely limiting the application possibilities of these materials.[25,27–29,107]

BNT-based: BNT-based ceramics have moderately high depolarization temperatures (T_d > 300 °C) and high remanent polarizations (P_r ~ 40 $\mu\mathrm{C\,cm^{-2}}$), but their piezoelectric coefficients are on the low-end of the lead-free materials (d_{33} < 200 $\mathrm{pC\,N^{-1}}$).[24,25,27–29] BNT-based materials also have high conductivity and large coercive fields, making them difficult to polarize.[22,24,25,29] Binary solid solutions of BNT with $Bi_{0.5}K_{0.5}TiO_3$ (BKT) and BT have been targeted.[23,27–29] BNT-BKT materials have high depolarization temperatures, but these materials have issues with low piezoelectric properties and difficult sintering conditions.[23,28,29] BNT-BT materials have decent piezoelectric properties, but these materials have issues with leakage currents, high dielectric loss and low depolar-

ization temperatures.[23,27,29] The BNT-BT system has, however, significant field induced strain properties, making these materials suitable for actuator applications.[108] Ternary systems (e.g. BNT-BKT-BT, BNT-BT-KNN) have also been studied.[23,25,29,108]

Other: A wide range of other lead-free piezoelectric materials have been investigated. The tungsten bronze-structured ceramics ($(A1)_2(A2)_4C_4(B1)_2(B2)_8O_{30}$, TB, e.g. $Sr_xBa_{1-x}Nb_2O_6$) are the largest group of ferroelectric materials after the perovskites.[22,23,27] The high Curie temperatures and thermal stability of these materials make them suitable for high-temperature sensor applications.[106] The piezoelectric properties of the TBs are inferior to the perovskites, however, and their anisotropic crystal structure only allow for piezoelectric responses in certain crystallographic directions.[22,23,27] The bismuth layered structured ferroelectrics ($Bi_2A_{n-1}B_nO_{3n+3}$, BLSF, e.g. $Bi_4Ti_3O_{12}$, Bi_3TiTaO_9, $CaBi_4Ti_4O_{15}$), composed by pseudo-perovskite layers $(A_{n-1}B_nO_{3n+1})^{2-}$ stacked between sheets of $(Bi_2O_2)^{2+}$, have low dielectric constants, low dielectric loss and high Curie temperatures.[22,25,27] The piezoelectric properties of the BLSFs are however modest, and their high coercive fields and anisotropic structures make them difficult to polarize.[22,25,27] Other lead-free piezoelectric materials include $LiNbO_3$,[23] $ZnSnO_3$,[27] $BiFeO_3$,[29,109] $BiAlO_3$,[25] langasites ($A_3BC_3D_2O_{14}$ LGS, e.g. $La_3Ga_5SiO_{14}$, $Ca_3Ga_2Ge_4O_{14}$),[25,105] hexagonal manganites (h–$R$$MnO_3$, e.g. $YMnO_3$)[110] and polymer-based materials.[51]

$K_xNa_{1-x}NbO_3$

Crystal structure and phase morphology

The potassium sodium niobates are a family of inorganic materials with the general formula $K_xNa_{1-x}NbO_3$.[111] The $K_xNa_{1-x}NbO_3$ family is composed by solid solutions of the two perovskites $KNbO_3$ and $NaNbO_3$, and all compositions x in the $K_xNa_{1-x}NbO_3$ family takes the perovskite crystal structure (A = K^+, Na^+, B = Nb^{5+} in ABO_3).[30] The end components, $KNbO_3$ and $NaNbO_3$, have different properties and influence the solid solution in different ways: $KNbO_3$ is ferroelectric at room temperature, and has a relatively simple polymorphism, going from rhombohedral (R) to orthorhombic (O) at $T_{R\text{-}O} = -10\,°C$, from orthorhombic to tetragonal (T) at $T_{O\text{-}T} = 225\,°C$, and from tetragonal to cubic (C)

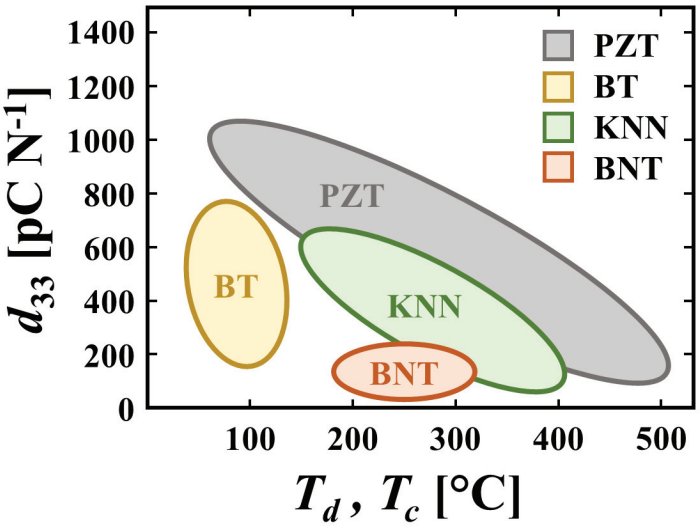

Figure 2.8: Piezoelectric coefficient (d_{33}) as a function of depolarization temperature (T_d) or Curie temperature (T_C) for the material families PZT, BT, KNN and BNT. The figure is based on data from[29,37,109]

at $T_{\text{T-C}} = T_C = 435\,°\text{C}$.[112,113] The potassium ions in $KNbO_3$ are slightly oversized relative to the ideal perovskite structure ($t = 1.05$), causing the structure to have a tetragonal distortion.[113] $NaNbO_3$ is antiferroelectric at room temperature, and goes from rhombohedral to orthorhombic at $T_{\text{R-O}} = -100\,°\text{C}$, through four different orthorhombic phases ($T_{\text{O1-O2}} = 373\,°\text{C}$, $T_{\text{O2-O3}} = 480\,°\text{C}$, $T_{\text{O3-O4}} = 520\,°\text{C}$), then from orthorhombic to tetragonal at $T_{\text{O-T}} = 575\,°\text{C}$, and from tetragonal to cubic at $T_{\text{T-C}} = T_C = 640\,°\text{C}$.[114] The sodium ions in $NaNbO_3$ are undersized relative to the ideal perovskite structure ($t = 0.795$), causing the structure to have strong octahedral tilting distortion.[113] Combined, $K_xNa_{1-x}NbO_3$ takes the phase morphology of $KNbO_3$ for most compositions ($0.02 < x < 1$), as illustrated in the pseudo-binary phase diagram in Figure 2.9.[87,115] For compositions $x < 0.4$, $K_xNa_{1-x}NbO_3$ adopts the octahedral tilting of $NaNbO_3$,[115,116] which is associated with a stronger polarization.[113] Optimal ferroelectric performance is found in compositions around $x = 0.5$, and this is the composition usually associated

with the abbreviated term "KNN".[30–38] At this composition, KNN has phase transitions at $T_{R\text{-}O} = -123\,°C$, $T_{O\text{-}T} = 210\,°C$ and $T_{T\text{-}C} = T_C = 410\,°C$, and solidus and liquidus points at 1140 and 1280 °C, respectively.[31,117] KNN is usually described as orthorhombic (s.g. $Amm2$) at room temperature,[31,87] but the structure has a slight monoclinic distortion ($\beta = 90.33°$) and is most accurately described with a monoclinic symmetry with s.g. Pm, see Table 2.1.[118,119] The relationship between the orthorhombic and monoclinic unit cell parameters is presented in Figure 2.10. The $x = 0.5$ composition of KNN has a tolerance factor $t = 1.01$, calculated using Equation 2.16 and ionic radii of the elements.[120] The elements forming KNN (K, Na, Nb) are all abundant[121] and non-toxic to humans[†],[23,122] but the environmental footprint of niobium mining and extraction has been questioned.[123]

Table 2.1: Unit cell parameters of $K_{0.5}Na_{0.5}NbO_3$ ceramics at room temperature for the monoclinic (s.g. Pm) and orthorhombic (s.g. $Amm2$) symmetries.

Symmetry	a [Å]	b [Å]	c [Å]	β [°]	**Ref.**
Monoclinic	4.00468(4)	3.94464(3)	4.00200(5)	90.3327(5)	118
Orthorhombic	3.9576(2)	5.6388(4)	5.6662(6)	-	124

Properties

Selected properties of KNN ceramics are presented in Tables 2.2 and 2.3. Pure KNN has a density of $\rho = 4.51\,g\,cm^{-3}$, an E-modulus of $E = 104\,GPa$ and a relatively low thermal expansion coefficient of $\alpha = 4.72 \cdot 10 - 6$.[15,117,125] Stoichiometric KNN has a high Curie temperature (> 400 °C) and a good electromechanical coupling factor ($k \sim 0.5$),[15,23,31] but the piezoelectric properties of the material are modest ($d33$ = 80-160 $pC\,N^{-1}$, $S_{max}/E_{max} = 150\,pm\,V^{-1}$, $Q_m = 130$).[15,30,108] However, the low crystallographic density of KNN cause the piezoelectric performance per weight of the material to be competitive with other piezoelectric materials.[28] The piezoelectric properties of KNN can also be improved 5- to 10-fold by compositional engineering (see *Compositional engineering and additives*, page 34).[31,32,36]

[†]Potassium is an essential element, but it is toxic in high concentrations.

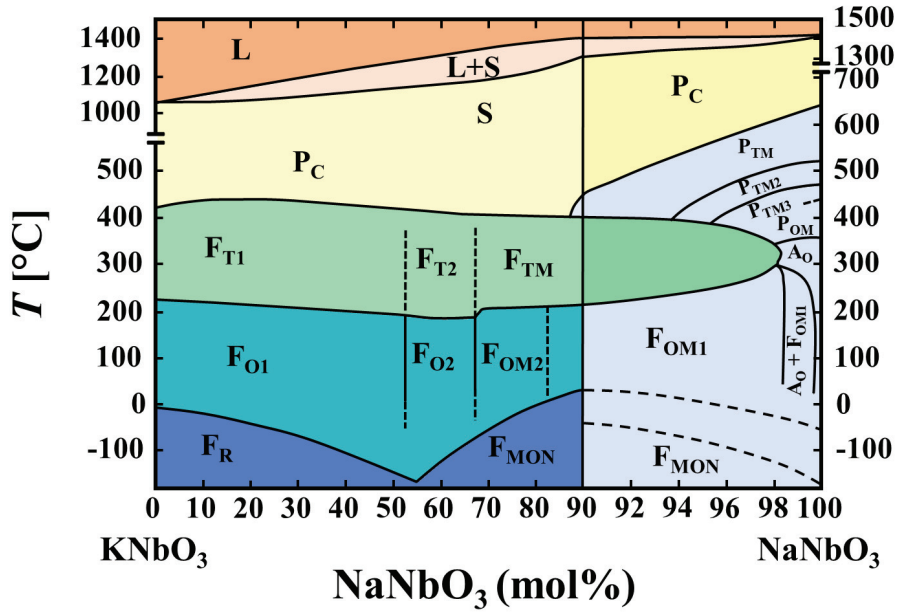

Figure 2.9: The pseudo-binary phase diagram of the $KNbO_3$-$NaNbO_3$ system. Adapted from [87], with permission from Elsevier, © 1971.

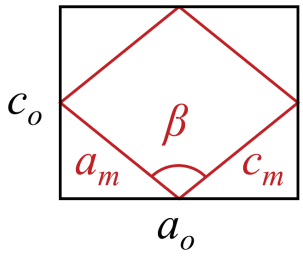

$$a_o = a_m \sin(\beta/2) + c_m \sin(\beta/2)$$
$$b_o = 2\, b_m$$
$$c_o = c_m \cos(\beta/2) + a_m \cos(\beta/2)$$

Figure 2.10: The relationship between orthorhombic unit cell parameters (a_o, b_o, c_o) and monoclinic unit cell parameters (a_m, b_m, c_m, β).

Table 2.2: Mechanical properties of KNN ceramics.

Property	Value	Ref.
Thermal expansion coefficient, α	$2.96 \cdot 10^{-6}$ (30-195 °C) $4.35 \cdot 10^{-6}$ (208-364 °C) $7.52 \cdot 10^{-6}$ (434-790 °C) $4.72 \cdot 10^{-6}$ (ave. 30-790 °C)	125
Young's modulus, E	104 GPa	15
Poisson ratio, ν	0.27	15

Compositional engineering and additives

The use of chemical additives in KNN ceramics is almost always aiming at improving the functional properties of the material, but the mechanisms by which this is achieved differ.[30,31,36,127] The earliest work on chemical modification of KNN was concerned with improving the poor sintering of the material during solid-state synthesis, and considerable improvements in the functional properties have been achieved using sintering aids.[36,117,127] More recently the engineering of phase boundaries has been the main focus for improving the piezoelectric properties of KNN ceramics.[31,32,36,37] Work has also been put into improving the fatigue behavior and dielectric properties.[34,36] A list of selected doping compounds is presented in Table 2.4.

Sintering aids: Solid-state processing of pure KNN ceramics is challenging due to a narrow sintering window close to the solidus temperature and alkali volatilization at elevated temperatures.[127] The use of sintering aids can induce cation mobility at lower temperatures, usually through the formation of liquid phases or vacancies.[36,117,127] Liquid-phase sintering can be induced by different copper- or zinc-based compounds like CuO, $K_4CuNb_8O_{23}$ (KCN), $K_{5.4}Cu_{1.3}Ta_{10}O_{29}$ (KCT), ZnO and $K_{1.94}Zn_{1.06}Ta_{5.19}O_{15}$, but various other additives have also been used.[31,32,36,117,127] Promotion of vacancies is typically induced by aliovalent doping with binary oxides on either A- or B-site in KNN, which include compounds like MgO, Mn_xO_y, La_2O_3, Fe_2O_3 and ZnO.[31,32,36,117,127] Ternary compounds with Li^+ like $LiNbO_3$, $LiTaO_3$, $LiSbO_3$ have also been shown to decrease the sinter-

Table 2.3: Properties of KNN, BT and PZT at room temperature. Tolerance factors calculated using Equation 2.16 and ionic radii from [120]. Values of tolerance factors for PZT are given for $PbZr_{0.52}Ti_{0.48}O_3$.

Property	**KNN**	**$BaTiO_3$**	**Soft PZT**	**Hard PZT**
Symmetry	Orthorhombic/ monoclinic (s.g. $Amm2/Pm$) [118]	Tetragonal (s.g. $P4mm$) [107]	Zr-rich: rhombohedral (s.g. $3m$), Ti-rich: tetragonal (s.g. $4mm$) [91]	Zr-rich: rhombohedral (s.g. $3m$), Ti-rich: tetragonal (s.g. $4mm$) [91]
Tolerance factor, t	1.01	1.06	0.99	0.99
Crystallographic density, ρ	4.51 $g cm^{-3}$ [117]	6.02 $g cm^{-3}$ [126]	7.55-7.64 $g cm^{-3}$ [17]	7.55-7.64 $g cm^{-3}$ [17]
Dielectric permittivity, ϵ_r	290-586 [30]	1700 [107]	1700-3400 [21]	1000-1300 [21]
Curie temperature, T_C	410 °C [31]	130 °C [107]	190-365 °C [21]	300-328 °C [21]
Coupling factor, k_{33}	0.51 [15]	0.49 [107]	0.71 [26]	0.54 [26]
Piezoelectric coefficient, d_{33}	80-160 $pC N^{-1}$ [30]	191 $pC N^{-1}$ [107]	375-590 $pC N^{-1}$ [21]	225-290 $pC N^{-1}$ [21]
Normalized strain, S_{max}/E_{max}	150 $pm V^{-1}$ [108]	594 $pm V^{-1}$ [108]	600 $pm V^{-1}$ [26]	-
Mechanical quality factor, Q_m	130 [15]	300 [21]	65-75 [21]	> 1000 [21]

ing temperature.[127] In addition to improved densification, some sintering aids improve functional properties by diffusing into the KNN lattice or segregating on the grain boundaries.[30,36,127] For example, Cu-based compounds have been shown to have a hardening effect on KNN, ZnO has been shown to increase the Curie temperature and manganese oxides have been demonstrated to reduce leakage and dielectric loss.[36,127]

Phase boundary engineering: Improving piezoelectric properties through engineering of phase boundaries in KNN involves shifting $T_{\text{O-T}}$ or $T_{\text{R-O}}$ (or both) towards the operation temperature to stabilize more polarization directions, as illustrated in Figure 2.11.[31,32,36,37] Reduction of the onset temperature for the O-T phase boundary using ion substitution with Li^+, Ta^{5+} and Sb^{5+} is arguably the most common doping strategy, but a range of other compounds can influence the O-T phase transition.[31,32,37] The R-O phase transition is more difficult to engineer but can be shifted by for example using Ta^{5+}, Sb^{5+} and various zirconates as additives.[31,37] The highest d_{33} value measured for KNN ceramics ($\sim 700\,\text{pC}\,\text{N}^{-1}$) is reported for a textured sample with R-O phase boundary at room temperature.[10] Superb piezoelectric properties (d_{33} = 400-600 $\text{pC}\,\text{N}^{-1}$) can also be obtained by shifting both the R-O and the O-T phase boundary, creating an R-O-T phase boundary (also known as R-T or "new" phase boundary).[31,32,37] Some dopants are able to both reduce $T_{\text{O-T}}$ and increase $T_{\text{R-O}}$ (e.g. Sb^{5+}, Ta^{5+}, $Bi_{0.5}(Na,K)_{0.5}FO_3$ (F = Hf^{4+}, Zr^{4+}, Ti^{4+})), but generally a multi-component composition is required to create the R-O-T phase boundary. The thermal stability of the piezoelectric properties of KNN can be improved by Li^+, Zn^{2+}, $CaZrO_3$, $AgNbO_3$, $Bi_{0.5}Na_{0.5}ZrO_3$, BNT.[32,36]

Other dopants: Some dopants can improve the resistance to cycling fatigue by preventing domain wall pinning, including samarium oxide, BKT and some titanates and zirconates.[36] Reduction of dielectric loss and leakage current can be promoted using multivalent dopants (e.g. manganese, cobalt), and such dopants are often used to improve the piezoelectric response in KNN thin films.[33,34,36]

Table 2.4: Examples of dopants and additives in KNN ceramics.[31,32,36,37,117,127]

Doping mechanism		**Dopants**
Sintering aids	Liquid-phase	CuO, KCN, KCT, $CuNb_2O_6$, ZnO, $K_{1.94}Zn_{1.06}Ta_{5.19}O_{15}$, $Na_2B_4O_7 \cdot {}_{10}H_2O$ (borax), K,Na-germanate, LiF, Li_2O, Na_2O
	Vacancies	MgO, CaO, SrO, BaO, Eu_2O_3, La_2O_3, SnO_2, MnO, MnO_2, Mn_3O_4, ZnO, MoO_3, La_2O_3, Bi_2O_3, Fe_2O_3, V_2O_5, ZrO_2, Co_2O_3
	Other	$LiNbO_3$, $LiTaO_3$, $LiSbO_3$
Phase boundaries	O-T	$ATiO_3$ (A = Ca^{2+}, Ba^{2+}, Sr^{2+}, $(Ba_{0.95}Sr_{0.05})^{2+}$, $[(Bi_{0.5}Na_{0.5})_{0.94}Ba_{0.06}]^{2+}$), $LiBO_3$ (B = Nb^{5+}, Sb^{5+}, Ta^{5+}), $Bi_{0.5}C_{0.5}TiO_3$ (C = Na^+, K^+, Li^+), $BiMO_3$ (M = Sc^{3+}, Al^{3+}, Fe^{3+}, Co^{3+})
	R-T	Sb^{5+}, Ta^{5+}, $DZrO_3$ (D = Ca^{2+}, Ba^{2+}, Sr^{2+}), $BiMO_3$ (M = Sc^{3+}, Al^{3+}, Fe^{3+}, Co^{3+})
	R-O-T	Sb^{5+}, Ta^{5+}, $BiMO_3$ (M = Sc^{3+}, Al^{3+}, Fe^{3+}, Co^{3+}), $EZrO_3$ (E = Ca^{2+}, Ba^{2+}, Sr^{2+}, $(Bi_{0.5}K_{0.5})^{2+}$, $(Bi_{0.5}Ag_{0.5})^{2+}$, $[Bi_{0.5}(Na_{0.7}K_{0.2}Li_{0.1})_{0.5}]^{2+}$, $[Bi_{0.5}(Na_{0.82}K_{0.18})_{0.5}]^{2+}$), $Bi_{0.5}(Na,K)_{0.5}FO_3$ (F = Hf^{4+}, Zr^{4+}, Ti^{4+}), BNT, BKT + combinations of O-T dopants and R-T dopants
	Thermal stability	Li^+, Zn^{2+}, $CaZrO_3$, $AgNbO_3$, $Bi_{0.5}Na_{0.5}ZrO_3$, BNT
Other	Fatigue resistance	Sm_2O_3, $CaTiO_3$, $MgTiO_3$, $CaZrO_3$, $SrZrO_3$, BKT
	Dielectric properties	Mn_xO_y, Co_2O_3

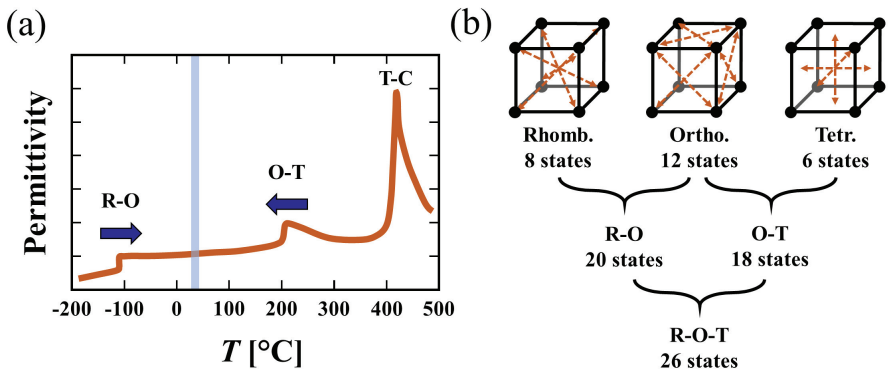

Figure 2.11: (a) Temperature dependence of the permittivity in KNN illustrating the three phase transitions rhombohedral-orthorhombic (R-O), orthorhombic-tetragonal (O-T) and tetragonal-cubic (T-C). Phase boundary engineering involves moving the R-O and/or O-T phase transition towards room temperature (blue line). (b) Polarization directions in rhombohedral, orthorhombic and tetragonal symmetries. Combinations of directions are available at the phase transitions between the symmetries.

2.2 Ceramic thin films

2.2.1 General characteristics

Size matters

Electronic technology is in a constant pursuit for functional components with smaller sizes, higher performances and lower energy consumption. *Passive* and *active* electronic components (e.g. resistors, capacitors, inductors, transistors, tunnel diodes) are currently pushing the boundaries of nanotechnology and are on the verge of leaping into quantum technology.[128] The *electromechanical* components are following some orders of magnitude behind and are currently transitioning from the micrometer-range to the nanometer-range.[129,130] For the electromechanical components, the *thin film* design represents a practical compromise between the micro- and macro-world, as they have a macro-sized areal extension which makes them easy to integrate with other electronic technology, and a micro-sized thickness (typically $< 2\,\mu m$), which gives the thin films many of the characteristics and advantages of nanomaterials.[131]

In contrast to electromagnetic systems, piezoelectric components exhibit excellent scaling with size and retain much functionality down to the nanometer region.[132] Because of this, piezoelectric thin films represent a promising technology for electromechanical components.[94,132,133] Both piezoelectric effects can be utilized in such components, and piezoelectric thin films offer the opportunity for broad-range, high-sensitivity sensors (direct effect) and large motion, low-voltage actuators (indirect effect).[132,133] Although piezoelectric thin films retain much of the properties observed for bulk ceramics of the same materials, boundary conditions at the nanoscale will influence the thin film properties.[94] For example, interfacial phenomena (space charges, strain gradients, compositional variations) and substrate clamping effects start to influence the functional properties when sample thickness is pushed into the nanometer range.[133] The small volume also affects the accumulative randomness of overall grain orientation, causing polycrystalline piezoelectric ceramics that exhibit no net piezoelectric effect in bulk due to cancellation of polarization directions (e.g. ZnO) to obtain net piezoelectric

performance as thin film.[94]

The effect of the substrate

The substrate can influence many of the thin film's properties and in that effect the overall thin film performance, and the type of substrate should therefore be selected with care.[131] Because of the wide use of silicon in semiconductor technology, substrates based on single-crystal Si wafers are the most used support for thin film technology.[129,133,134] However, substrates based on single-crystal ceramics (e.g. $SrTiO_3$, MgO, Al_2O_3), various metals (e.g. Ti, Ni, steel), glasses and polymers (e.g. polyimide, silicones) are also used as these can introduce different mechanical properties to the device or induce specific structural or phase growth in the thin films.

Mechanical clamping
In most cases, thin films are supported by a thicker substrate, making thin films in practice a composite system.[131] The substrate is typically several hundred microns thick, causing the mechanical properties of the film-substrate composite system to be completely dominated by the mechanical properties of the substrate.[132] This causes a clamping effect on the in-plane elastic properties in the thin film, which leads to a reduction in the effective piezoelectric effect ($d_{33,f}$, $e_{31,f}$) in accordance to Equations 2.17 and 2.18.[132,133,135]

$$d_{33,f} = d_{33} - \frac{2s_{13}^E}{s_{11}^E + s_{12}^E} d_{31} = d_{33} - 2s_{13}^E e_{31,f} \quad , \quad d_{33,f} < d_{33} \tag{2.17}$$

$$e_{31,f} = e_{31} - \frac{c_{13}^E}{c_{33}^E} e_{33} = e_{31} - c_{13}^E d_{33,f} \quad , \quad |e_{31,f}| > |e_{31}| \tag{2.18}$$

Here, d_{33} and e_{31} are the unconstrained out-of-plane piezoelectric coefficients, d_{31} and e_{33} are the unconstrained in-plane piezoelectric coefficients, and s_{1j} and c_{i3} are the elastic stiffness coefficients of the film. A reduced clamping effect can

be obtained by using substrates with low stiffness, i.e. flexible substrates.

Mechanical stress and strain
Stresses can be induced in the film during synthesis if the thermal expansion coefficients of the substrate and the film are different.[136] The bilateral misfit stress (σ) in a film formed at temperature T_0 and cooled down to temperature T can be calculated by Equation 2.19,

$$\sigma = \frac{(\alpha_f - \alpha_s)(T_0 - T)E_f}{1 - \nu_f} \tag{2.19}$$

where α_f and α_s are the thermal expansion coefficients of the film and the substrate, respectively, E_f is the Young's modulus and ν_f is the Poisson ratio of the film. Such stresses can induce defects in the film's crystal structure or even macroscopic cracks and fractures.[136] However, the stress-induced strain in films from the substrate can be tailored and utilized to improve the piezoelectric properties of thin films.[132] Misfit strain can for instance dictate the stability of the phases in the thin film, and by tuning the thermal misfit strain the phase of the film can be engineered.[137] Such strain-engineering has lately received much attention, including for KNN thin films.[138–141] Figure 2.12 shows a calculated strain-temperature phase diagram for KNN thin films.[141]

Mechanical stresses can also arise in thin epitaxial films due to different lattice parameters between the film and the substrate.[131] Epitaxial growth of thin films requires a lattice mismatch less than ~9 %, and an increasing degree of polycrystallinity is usually observed up to this value.[131,142] As the thickness of an epitaxial film increases, so does the elastic strain energy (E_c) in the film. At a critical film thickness, d_c, the accumulated elastic strain energy exceeds the energy for a relaxed film, and lattice defects form in the film to accommodate the stress.[131] The defects introduced are usually lattice dislocations[142] but point defects like oxygen vacancies accommodating misfit stress has also been reported.[143] The critical film thickness (d_c) can be calculated from

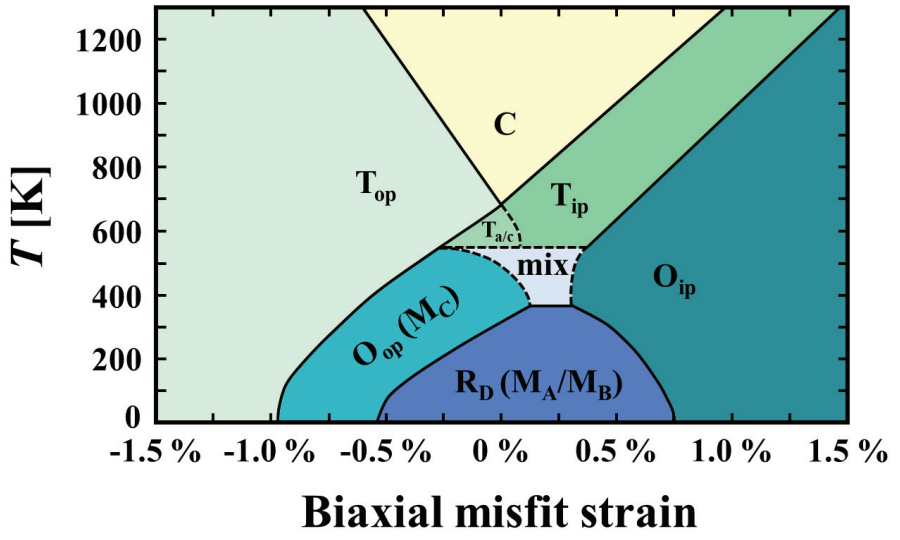

Figure 2.12: Temperature-misfit strain phase diagram for (001)-oriented epitaxial $K_{0.5}Na_{0.5}NbO_3$ thin films, obtained from 3D phase-field modeling. The phases are paraelectric cubic (C), ferroelectric tetragonal with out-of-plane (T_{op}), in-plane (T_{ip}) and mixed polarization ($T_{a/c}$), ferroelectric orthorhombic with out-of-plane (O_{op}) and in-plane polarization (O_{ip}), ferroelectric rhombohedral with distorted polarization (R_D) and a region of several stable phases (mix). Figure is modified from [141].

$$d_c = \frac{b}{8\pi(1+\nu_f)f}\ln\left(\frac{\beta d_c}{b}\right) \tag{2.20}$$

where b is the Burgers vector, f is the misfit value describing the misfit ratio of the film and substrate lattice, and β is a constant. [131]

Substrate induced orientation

The substrate surface (crystallographic orientation, microstructure) can influence thin film characteristics during synthesis. [94,131–133] By matching the crystallographic structure of the substrate to the thin film, preferential orientation of the film can be achieved, which in turn can maximize the anisotropic piezo-

electric properties of the film.[94,132,133] For thin film synthesis through chemical solutions, this is obtained through heterogeneous nucleation and growth on the substrate.[144] Various degrees of preferential orientation can be achieved.[131] Epitaxial growth implies a single crystal thin film almost perfectly matching the crystallographic orientation of the substrate. Texturing implies growth of grains with a set out-of-plane crystallographic orientation and a random in-plane orientation. Because of their crystallographic similarities to many piezoelectric thin films, single crystal ceramics (e.g. $SrTiO_3$, MgO, Al_2O_3) are usually used as orientation inducing substrates.

Substrate induced phase nucleation

Heterogeneous nucleation might alter the energy landscape for nucleation of different phases in a thin film system.[133] Choosing substrates that favor nucleation of the main piezoelectric phase can promote phase purity in material systems with parasitic secondary phases close in energy to the main phase (e.g. $Na_2Nb_8O_{21}$/KNN).[145]

Designs of thin film devices

A wide range of device designs based on piezoelectric thin films has been developed based on the area of application, but the most common designs are cantilever structures, membrane/diaphragm structures, bridge-structures and stack type configurations (Figure 2.13 (a)).[7,50,132,146–148] The designs are developed to optimize the performance of the piezoelectric film when used in different situations, e.g. actuation/motors,[7] MEMS/bioMEMS,[50,132] energy harvesting[148] or sensors.[146] The electrode configuration can also be tailored based on application and measuring mode, although traditionally a top-bottom (TB) or interdigitated design (IDE) is used, as illustrated in Figure 2.13 (b).[132] TB electrodes capture out-of-plane piezoelectric properties while IDE electrodes capture in-plane properties.

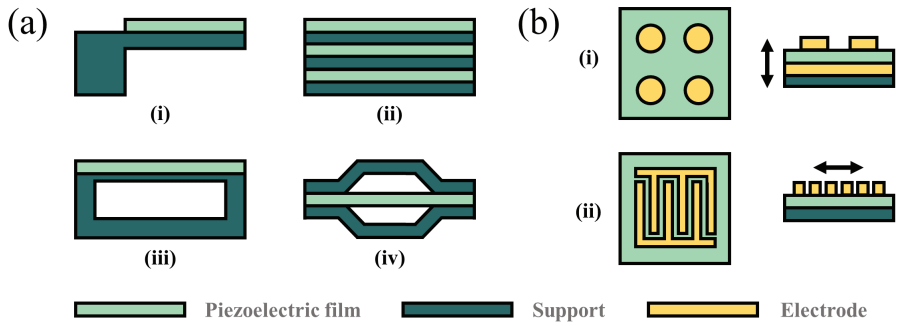

Figure 2.13: (a) Side view of thin film device designs, including (i) cantilever, (ii) stack, (iii) membrane and (iv) bride-type structures. (b) Electrode configurations, including (i) top-bottom electrode capturing out-of-plane properties and (ii) interdigitated electrodes capturing in-plane properties.

2.2.2 Synthesis of ceramic thin films

Top-down and bottom-up approaches

Processing techniques of nanomaterials can be divided into top-down and bottom-up methods as illustrated in Figure 2.14.[149] In the top-down methods, the nanomaterial is processed out of a larger piece of the material, for example by mechanical grinding, mechanical chemical polishing, laser machining and various forms of lithography (e.g. optical, e-beam, nanoimprint, scanning probe).[149–151] In the bottom-up methods, the nanomaterial is grown from atomic or molecular precursors, for example through a vapor phase or a chemical solution.[149,152,153] For ceramic thin films, the bottom-up methods are usually preferred as they can deliver films of complex compositions with nano-size resolution at a relatively high output rate.[149] The following sections will focus on the bottom-up synthesis methods.

Vapor phase processing

Vapor phase synthesis is based on transport of the nanomaterial components through a vapor phase and the deposition of these components, or the reac-

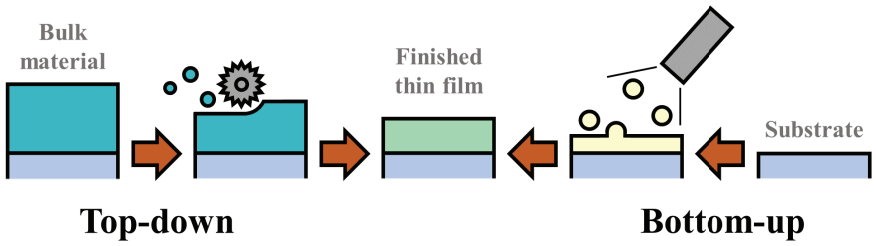

Figure 2.14: Illustration of the two categories of nanomaterial synthesis; top-down and bottom-up synthesis.

tion product of these components, on a substrate.[153–157] The components can be atoms, molecules or small clusters of the material to be deposited. Vapor phase processing is divided onto two categories: (i) physical vapor deposition and (ii) chemical vapor deposition.[153]

(i) Physical vapor deposition

Physical vapor deposition (PVD) is characterized by a process where the material to be deposited goes from a condensed state in the precursor target to a vapor state and then back to a condensed state on the substrate.[154,155] This process is usually conducted under vacuum or controlled atmosphere. There are several types of PVD techniques, including *pulsed laser deposition* (PLD),[158,159] *sputter deposition*,[160,161] *arc vapor deposition*[162,163] and *ion plating*.[164] PLD has been used to deposit $K_xN_{1-x}NbO_3$ thin films on various substrates, including $Pt_{80}Ir_{20}$, SiPt, SiO_2/Si, Pt/MgO, $SrTiO_3$, $La_{0.7}Sr_{0.3}MnO_3$ (LSMO)/$SrTiO_3$ and LSMO/$LaAlO_3$.[165–171] Radio frequency magnetron sputtering has been used to deposit $K_xN_{1-x}NbO_3$ thin films on $Pt_{80}Ir_{20}$, SiPt, Pt/MgO, $LaNiO_3$/Si, $LaNiO_3$/Si, $LaAlO_3$, $SrRuO_3$/$SrTiO_3$ and $SrRuO_3$/Pt/MgO.[172–178]

(ii) Chemical vapor deposition

Chemical vapor deposition (CVD) is characterized by formation of the desired material through chemical reaction of volatile precursor species on or in vicinity to the substrate, and the process is usually conducted at elevated temperatures.[156,157] Different types of CVD techniques have been developed, includ-

ing *metalorganic chemical vapor deposition* (MOCVD),[179,180] *atomic layer deposition* (ALD)[181] and *molecular beam epitaxy* (MBE) which is essentially a mixed PVD/CVD technique.[154,182] MOCVD has been used to deposit $K_xN_{1-x}NbO_3$ thin films on SiO_2/Si, SiN_x/Si, $SrTiO_3$, Al_2O_3, $NdGaO_3$, $DyScO_3$, $TbScO_3$ and $GdScO_3$.[183–186] ALD has been used to deposit KNN thin films on Si and Pt/Si.[187,188]

Chemical solution processing

Chemical solution deposition (CSD) is a versatile processing technique used to fabricate high quality ceramic films in a wide range of compositions.[134,144,189–191] The technique is based on depositing a chemical solution containing the components of the targeted material on a substrate, and then thermally process the deposited film to form the final material. The CSD process can be divided into four steps, as illustrated in Figure 2.15. These are the preparation of the chemical solution, deposition of the chemical solution to a substrate, drying and pyrolysis of the deposited solution, and finally crystallization of the deposited layer.

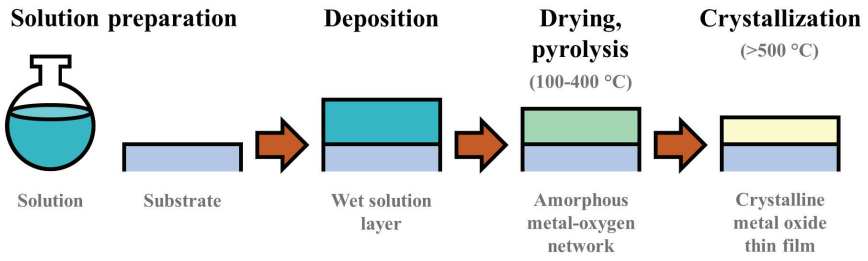

Figure 2.15: Schematic of the main steps of chemical solution deposition; solution preparation, deposition, condensation/pyrolysis and crystallization.

Solution preparation

The chemical solution preparation is the most crucial step in CSD synthesis as the solution chemistry in large dictates the processing parameters in the subsequent steps of the synthesis and the final quality of the thin film.[134,144,189,190] The chemical solution must meet several requirements in order to form a high-

quality ceramic film:[144] (i) The metal cations or metal cation complexes must be sufficiently soluble in the solvent so that the chemical solution is stable. (ii) The solution must sufficiently wet the substrate to obtain a homogeneous deposition with nano-sized thickness. (iii) The rheology of the chemical solution must be tailored to the deposition technique to form a wet layer of appropriate thickness. (iv) No phase separation/recrystallization of precursor components should occur during drying or pyrolysis to retain the atomistic homogeneity of the cations. (v) All constituents of the chemical solution but the metal cations must decompose during the thermal treatment to avoid undesired residues. (vi) The solution must form a phase pure, dense and crack-free thin film during thermal processing.

Different CSD methods are often categorized based on the characteristics of the chemical solution system used, and these include sol-gel synthesis, chelate routes, metal organic decomposition (MOD), Pechini and modified Pechini methods, the citrate route, the nitrate route, aqueous solution-gel processes, molecular precursors, polymer assisted deposition (PAD), microemulsions and liquid exfoliation.[144,190,191] Sol-gel synthesis with alkoxide based precursors is the most frequently reported CSD method as it offers excellent control over solution purity, stability, reactivity and rheology, in addition to being susceptible to a wide range of chemical modifications.[191,192] The disadvantage with this method is the cost and toxicity associated with the metal alkoxide precursors and the solvents (e.g. 2-methoxyethanol) and the need for an inert atmosphere during synthesis.[134,144,192] A cost-effective and environmentally friendly alternative is to use aqueous precursor systems.[191,193] The rich chemistry of aqueous solutions allows for synthesis compatibility with many material systems, and synthesis can be conducted under ambient conditions.[191,193] However, aqueous CSD has its own challenges, especially issues with the stability of higher-valency cations in water and poor wetting properties of the solutions.[144,193]

Deposition

Deposition of the chemical solution to the substrate must be performed in a way that ensures a homogeneous liquid layer with thickness in the nano-range.[144,190] There are several techniques available depending on the substrate geometry and the thickness and conformality requirements for the final thin film. The most common techniques are spin-coating, dip-coating and spray-coating, but

other techniques have been developed, including Langmuir-Blodgett deposition, chemical bath deposition, inkjet-printing, electrochemical deposition and liquid atomic layer deposition.[144,189–191] For one-sided deposition on flat substrates, spin-coating is the preferred deposition technique since the method offers highly uniform films at a high production rate and using simple equipment.[144,194] Deposition of the solution onto the substrate is typically performed using a filtered syringe, and solvent layer thinning is performed through liquid flow upon spinning of the substrate at rates of ~ 1000-8000 rpm.[144] The thinning rate of the solution during spinning is described by Equation 2.21:[194]

$$\frac{dh}{dt} = -\frac{2\rho\omega^2 h^3}{3\eta} \tag{2.21}$$

where t is the spin time, h is the thickness of the deposited solution layer, ρ is the solution density, ω is the rotation rate (spin velocity) and η is the solvents viscosity. As evident from Equation 2.21 the final thickness of the deposited solvent layer is independent on distance from the substrate center, meaning that flow physics inherently favor film uniformity.[194] Equation 2.21 also shows that the thickness of the solvent layer can be engineered by altering solution viscosity, spin rate and spin time.

Thermal processing: drying and pyrolysis

Following deposition, the deposited wet film in thermally processed to first form an amorphous metal-oxygen network through drying and pyrolysis.[134,144,189,190] Drying of the wet film typically takes place at temperatures of 100-200 °C, and is performed to immobilize/entrap cations (e.g. through complexation, gel formation etc.) and to remove most of the solvent through evaporation. Performing these processes at low temperatues (< 200 °C) prevent formation of large defects like pores, cracks and blisters in the final film. Pyrolysis is usually performed at 200-400 °C, and involves combustion and/or decomposition of additives, non-metal components and remaining solvent.

Thermal processing: crystallization

The final part of CSD is crystallization of the targeted phase in the film, and this

process usually requires temperatures > 500 °C.[134,144,189,190] While cation immobilization and pyrolysis is solution dependent, the crystallization is mostly material system and substrate dependent.[195] Although the crystallization is thermodynamically favored at all temperatures below the melting point of the system (illustrated in Figure 2.16 (a)), the energy required to overcome the nucleation energy barrier is only achieved at a certain temperature (illustrated with region II and III in Figure 2.16 (b)).[195] As shown in Figure 2.16 (b), only heterogeneous nucleation (nucleation on substrate interface) is favored at low temperatures (region II), while both homogeneous and heterogeneous nucleation is possible at higher temperatures (region III). If the substrate has a specific crystallographic orientation, epitaxy or texturing of the thin film can be promoted by heterogeneous nucleation.[134,195] This is then simply induced by choosing a crystallization temperature within region II in Figure 2.16 (b). The energy barriers for homogeneous and heterogeneous nucleation (ΔG^*) are dependent on the driving force for crystallization (ΔG_v), the interfacial energy (γ) and the contact angle (θ, only for heterogeneous nucleation), according to Equations 2.22 and 2.23, respectively:[144,189,195]

$$\Delta G^*_{\text{homo}} = \frac{16\pi\gamma^3}{3(\Delta G_v)^2} \tag{2.22}$$

$$\Delta G^*_{\text{hetero}} = \frac{16\pi\gamma^3}{3(\Delta G_v)^2} f(\theta) \quad , \quad f(\theta) = \frac{2 - 3\cos\theta + (\cos\theta)^3}{4} \tag{2.23}$$

Processing considerations for flexible thin films

Using substrates with low elastic stiffness (metal foils, polymers) can drastically reduce the clamping effect and thereby increase the performance of piezoelectric thin films.[196–198] There are two methods to synthesize ceramic thin films on flexible substrates: (i) direct deposition and (ii) transfer synthesis.[199]

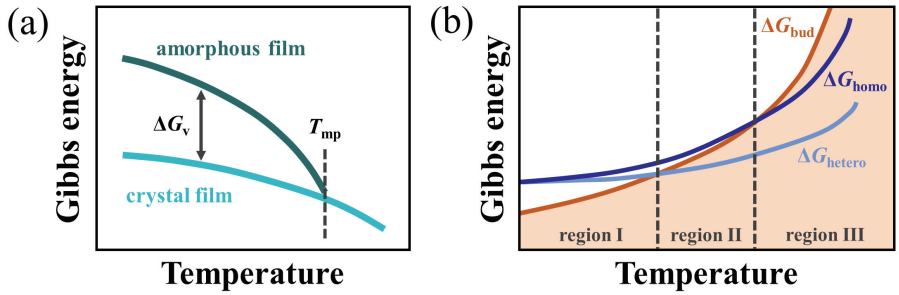

Figure 2.16: (a) Gibbs energy versus temperature for an amorphous film and the corresponding crystalline film. The Gibbs energy difference between the two phases (ΔG_v) is the driving force for nucleation, and this becomes zero at the melting point of the system (T_{mp}). (b) Gibbs energy versus temperature for the activation energy of homogenous nucleation (ΔG_{homo}) and heterogeneous nucleation (ΔG_{hetero}), and the overall available energy budget for the system (ΔG_{bud}). Spontaneous heterogeneous nucleation occurs in region II and III, while homogeneous nucleation occurs spontaneous only in region III. Adapted from [134], with permission from Royal Society of Chemistry, © 2014.

(i) Direct deposition

Direct deposition is fabrication of the ceramic thin film directly on the flexible substrate, as illustrated in Figure 2.17 (a).[199] Metal foil substrates are mechanically and thermally robust and thin film synthesis can often proceed at normal conditions on these substrates.[200,201] For polymeric substrates, however, direct synthesis must be performed below the decomposition point of the polymer.[199] This involves low temperature crystallization and can be induced by using seeding layers/crystallization seeds, UV or laser irradiation, microwaves, hydrothermal processing and photochemical activation methods.[191,199,202] Today, PVD is capable of room temperature synthesis,[202] and advanced CSD (a-CSD) techniques have brought processing temperatures from 400-750 °C down to 200-550 °C.[191] Examples of ceramic thin films synthesized by the direct deposition method include PZT,[200,201] BCZT,[203] AlN[204] and KNN.[205]

(ii) Transfer synthesis

Transfer synthesis involves synthesis of the ceramic thin film on a thermally robust substrate, and then using a lift-off technique to transfer the prepared

film over to the flexible substrate (Figure 2.17 (b)).[199] The lift-off procedure can be performed by melting/dissociation the film-substrate interface or by using a release/sacrificial layer. The former requires that either the substrate or the thin film can be melted or thermally dissociated, exemplified with KNN on sapphire[206] and PZT on sapphire.[207] A sacrificial release layer can for example be composed of Si,[198] SiO_2,[208] ZnO[65] or NaCl.[209] ZnO is especially interesting as it can be etched away with weak and harmless acids (e.g. acetic acid) compared to Si and SiO_2 that require hydrofluoric acid, and at the same time ZnO can withstand CSD of solutions with pH around 7 (NaCl would dissolve).

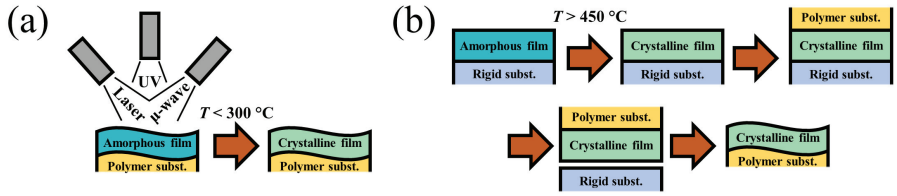

Figure 2.17: (a) Direct deposition synthesis of ceramic thin film on polymeric substrates. The technique requires low temperature ($T < 300\,°C$) crystallization of the amorphous film, e.g. aided by laser, UV irradiation or microwaves. (b) Transfer synthesis of ceramic thin films on polymeric substrates. The technique includes high temperature crystallization ($T > 450\,°C$) on a rigid substrate and then a transfer of the crystal film onto the flexible substrate, e.g. using of a sacrificial release layer.

2.2.3 KNN thin films

Properties of KNN thin films

Selected properties of KNN-based thin films fabricated through various synthesis techniques (PLD, RF-magnetron sputtering, MOCVD, ALD and CSD) are presented in Table 2.5. The piezoelectric properties of the thin films are in many of the cases recorded with local measurement techniques like piezoresponse force microscopy (PFM), and these values can be problematic to directly compare due to their correlation with the stiffness of the measurement tip-sample contact.[210] Most of the d_{33} values reported are in the range of 14.5-90 $pm\,V^{-1}$,[171,172,176,177,185,211–224] but some studies have reported on values

above 100 pm V^{-1}.[188,225–227]

KNN-based ceramics are vulnerable to the development of off-stoichiometry and the creation of niobium rich parasitic secondary phases during thermal processing due to the volatile nature of alkali species at elevated temperatures.[127] This is also a prominent issue in the fabrication of KNN thin films and is often prevented by using an excess of alkali metals in the synthesis.[33,34] KNN thin films are also prone to exhibit low dielectric resistivity due to leakage currents caused by point defects like oxygen vacancies and electron holes, and multivalent dopants like manganese and cobalt have been proved to effectively reduce these leakage currents.[33,34]

Table 2.5: Properties of KNN-based thin films synthesized through PLD, RF-magnetron sputtering (RF-M.S.), MOCVD, ALD and CSD.

Composition	Substrate	Synthesis technique	Thickness [nm]	Piezoelectric coefficient	Diel. perm. [-]	Rem. pol. [$\mu C\,cm^{-1}$]	Ref.
$(K_{0.5}Na_{0.5})NbO_3$	$Pt_{80}Ir_{20}$	PLD	270		520	12	165
$(K_{0.5}Na_{0.5})NbO_3$	$(La,Sr)MnO_3$/ $LaAlO_3$	PLD	220			21.3	167
$0.92(Na_{0.5}K_{0.5})NbO_3$ – $0.06BaZrO_3$ – $0.02(Bi_{0.5}Li_{0.5})TiO_3$	Pt/MgO	PLD	2000		682	24.5	169
$0.95(Na_{0.49}K_{0.49}Li_{0.02})$ $(Nb_{0.8}Ta_{0.2})O_3$–$0.05\,CaZrO_3$	$(La,Sr)MnO_3$/ $SrTiO_3$	PLD	280		1185	14	170
$(K_{0.5}Na_{0.5})NbO_3$	SiPt	PLD	750	d_{33}: $58\,pm\,V^{-1}$ e_{31}: $-5.6\,C\,m^{-1}$		12.6	171
$(K_{0.5}Na_{0.5})NbO_3$	$Pt_{80}Ir_{20}$	RF-M.S.	3500	d_{33}: $14.5\,pm\,V^{-1}$	489	6.14	172
$(K_{0.5}Na_{0.5})NbO_3$	$LaAlO_3$	RF-M.S.	730		470	1.9	173
$(K_{0.62}Na_{0.38})NbO_3$	Pt/MgO	RF-M.S.	3000	e_{31}: $-3.6\,C\,m^{-1}$	185		175
$(K_{0.56}Na_{0.44})NbO_3$	SiPt	RF-M.S.	3000	e_{31}: $-5.5\,C\,m^{-1}$	598		175
$(K_{0.54}Na_{0.46})NbO_3$	$LaNiO_3$/Si	RF-M.S.	600	d_{33}: $58\,pm\,V^{-1}$	899	12	176
$(K_{0.5}Na_{0.5})NbO_3$	$SrRuO_3$/$SrTiO_3$	RF-M.S.	1000	d_{33}: $36\,pm\,V^{-1}$	677	8	177

$(K_{0.16}Na_{0.84})NbO_3$	$SrRuO_3$/Pt/MgO	RF-M.S.	500-2500	e_{31}: $-2.4\,C\,m^{-1}$	320	20-25	178
$(K_{0.5}Na_{0.5})NbO_3$	SiO_2/Si, SiN_x/Si	MOCVD	300		142		183
$(K_{0.5}Na_{0.5})NbO_3$	$SrTiO_3$, Al_2O_3, SiO_2/Si, SiN_x/Si	MOCVD	300		142		184
$(K_{0.9}Na_{0.1})NbO_3$	$NdGaO_3$, $SrTiO_3$, $DyScO_3$, $TbScO_3$, $GdScO_3$	MOCVD	28	d_{33}: $29\,pm\,V^{-1}$			185
$(K_{0.7}Na_{0.3})NbO_3$	$TbScO_3$	MOCVD	25-35		5160		186
$(K_{0.5}Na_{0.5})NbO_3$	SiPt	ALD					187
$(K_{0.52}Na_{0.48})NbO_3$	SiPt	ALD	120	d_{33}: $105\,pm\,V^{-1}$			188
$(K_{0.5}Na_{0.5})NbO_3$	SiPt	CSD	600	d_{33}: $46\,pm\,V^{-1}$		7	211
$0.94(K_{0.52}Na_{0.58})NbO_3$-$0.06LiNbO_3$	SiPt	CSD	400	d_{33}: $192\,pm\,V^{-1}$	625	9.7	225
$(K_{0.5}Na_{0.5})NbO_3$	SiPt	CSD	250	d_{33}: $40\,pm\,V^{-1}$		10	212
$(K_{0.5}Na_{0.5})NbO_3$	SiPt	CSD	1290	d_{33}: $74\,pm\,V^{-1}$ g_{33}: $28.3\,mm\,VN^{-1}$	295		213
$(K_{0.5}Na_{0.5})(Nb_{0.8}Ta_{0.2})O_3$ + 0.5 % Mn^{2+}	SiPt	CSD	500	d_{33}: $58\,pm\,V^{-1}$		14	214
$(K_{0.5}Na_{0.5})(Nb_{0.7}Ta_{0.3})O_3$	SiPt	CSD	500	d_{33}: $62\,pm\,V^{-1}$		10.5	216
$(K_{0.5}Na_{0.5})(Nb_{0.7}Ta_{0.3})O_3$	SiPt	CSD	500	d_{33}: $61\,pm\,V^{-1}$	863	10.5	215

$(K_{0.4925}Na_{0.4925}Li_{0.015})NbO_3$	SiPt	CSD	1290	d_{33}: 83.1 pm V^{-1} g_{33}: 36.2 mm V N^{-1}	259		217
$(K_{0.48}Na_{0.48}Li_{0.04})$ $(Nb_{0.9}Ta_{0.1})O_3$ + 0.5 % Mn^{2+}	SiPt	CSD	750	d_{33}: 61 pm V^{-1}	2650	16.1	218
$0.95(K_{0.5}Na_{0.5})NbO_3$- $0.05CaZrO_3$ + 1 % Mn^{2+}	SiPt	CSD	1000	d_{33}: 32 pm V^{-1}		7.5	219
$(K_{0.5}Na_{0.5})NbO_3$ + 2 % Mn^{2+}	Nb:$SrTiO_3$	CSD	270	d_{33}: 50.5 pm V^{-1}		17.3	220
$(K_{0.5}Na_{0.5})NbO_3$ + 2 % Co^{2+}	SiPt	CSD	1600	d_{33}: 49.9 pm V^{-1}	628	7.5	221
$(K_{0.5}Na_{0.5})NbO_3$ + 2 % Co^{2+}	SiPt	CSD	1600	d_{33}: 49 pm V^{-1}	600-650	7.54	222
$(K_{0.5}Na_{0.5})NbO_3$	SiPt	CSD	1440	d_{33}: 83.3 pm V^{-1}	529		223
$(K_{0.5}Na_{0.5})NbO_3$ + 0.5 % Mn^{2+}	SiPt	CSD	1000	d_{33}: 90 pm V^{-1} e_{31}: −8.5 C m^{-1}		10	224
$(1-x)$ $(K_{0.48}Na_{0.52})(Nb_{0.95}Sb_{0.05})O_3$ -$xBi_{0.5}(Na_{0.82}K_{0.18})_{0.5}ZrO_3$, x =0.01-0.07	SiPt	CSD	500- 2000	d_{33}: 184 pm V^{-1} g_{33}: 39.4 mm V N^{-1}	528		227
$(K_{0.5}Na_{0.5})NbO_3$	Pt/Al_2O_3	CSD	350	d_{33}: 124 pm V^{-1}	103		226

CSD of KNN thin films

CSD is one of the most frequently reported synthesis routes to KNN thin films,[33,34] and the literature on the topic is comprehensive.[64,139,205,211–264] The most common CSD method for fabrication of KNN thin films is sol-gel synthesis using niobium ethoxide and alkali ethoxides or acetates as precursors and 2-methoxyethanol (2-MOE) as solvent.[139,211–223,225–242,244,245,249–251,253,255–260,262–264] A significant advantage of the 2-MOE based sol-gel method compared to other methods is the superb precursor solution stability, enabling high-concentration solutions that have long shelf lives and that can produce ceramic layers of several hundred nanometers per deposition. However, these solutions are composed by harmful and expensive chemicals, and the solutions are extremely sensitive to moisture, meaning they have to be prepared in inert atmospheres. Several chemical additives are used in 2-MOE based method, including acetylacetone as chelating agent, acetic acid and ethylenediaminetetraacetic acid (EDTA)/diethanolamine (DEA)/monoethanolamine (MEA) as stabilizing agents, polyvinylpyrrolidone (PVP) to improve densification and N-N dimethylformamide as drying control additive. Solutions based on other solvents have also been reported, including propionic acid (PPA),[205] ethanol,[243] mixtures of *n*-propanol (*n*-PrOH) and 1,2-propanol (1,2-PrOH)[246,252] and water.[64,247,248,254,261] The water-based solutions are based on the modified Pechini route with citric acid and ethylene glycol,[247,261] the citrate route with just citric acid[248,254] or other aqueous solution-gel processes.[64] These precursor solutions use less harmful chemicals than the 2-MOE sol-gel method, but controlling the chemistry in these precursor systems is often challenging.

SiPt is the most common substrate for CSD synthesis of KNN thin films,[139,211–219,221–225,227,230–242,244,245,247,248,250,251,255,256,258–262,264] but substrates like SiO_2/Si,[228,246,252] ZrO_2/Si,[229,230] $LaNiO_3$/Si,[261] MgO,[238] metals,[205,243,254] Al_2O_3[226,246] and $SrTiO_3$[64,139,220,249,253,257,263] have also been reported. The thermal treatment is usually conducted in three stages; drying at 150-450 °C, pyrolysis at 300-650 °C and crystallization at 450-800 °C. Several studies have proved that the final microstructure of CSD derived KNN thin films can be engineered by controlling the thermal processing[249,254,260] or solution

chemistry.[64,226,242,247] Selected properties of KNN-based thin films fabricated through CSD are presented in Table 2.6.

Table 2.6: Properties of KNN-based thin films synthesized through CSD. *Piezoelectric coefficient from hydrostatic pressure.

Composition	Substrate	Solvent	Thick-ness [nm]	d_{33} [$pm\,V^{-1}$]	Diel. perm. [-]	Rem. pol. [$\mu C\,cm^{-1}$]	Ref.
$(K_{0.5}Na_{0.5})NbO_3$	SiO_2/Si	2-MOE	250				228
$(K_{0.5}Na_{0.5})NbO_3$	ZrO_2/Si	2-MOE	500			38.7	229
$(K_{0.5}Na_{0.5})NbO_3$	SiPt, ZrO_2/Si	2-MOE	500			16.2	230
$(K_{0.5}Na_{0.5})NbO_3$	SiPt	2-MOE	600	46	540	7.0	211
$(K_{0.5}Na_{0.5})NbO_3$	SiPt	2-MOE	600			7.0	231
$(K_{0.5}Na_{0.5})NbO_3$	SiPt	2-MOE	200		218	1.6-1.9	232
$(K_{0.475}Na_{0.475}Li_{0.05})NbO_3$	SiPt	2-MOE	250-350			9.75	233
$(K_{0.5}Na_{0.5})NbO_3$	SiPt	2-MOE	250	40		10	212
$(K_{0.47}Na_{0.47}Li_{0.06})NbO_3$	SiPt	2-MOE	400	192	625	9.7	225
$(K_{0.5}Na_{0.5})NbO_3$	SiPt	2-MOE	1290	74	295	~ 2-6	213
$(K_{0.5}Na_{0.5})NbO_3$	SiPt	2-MOE	120		258	3.54	234
$(K_{0.5}Na_{0.5})NbO_3$	SiPt	2-MOE	250		100-300	6.4	235
$(K_{0.5}Na_{0.5})NbO_3$	SiPt	2-MOE	200			3-4	236
$(K_{0.5}Na_{0.5})NbO_3$ + 2 % Mn^{2+}	SiPt	2-MOE	1300		521	7.2	237
$(K_{0.5}Na_{0.5})(Nb_{0.8}Ta_{0.2})O_3$ + 0.5-1 % Mn^{2+}	SiPt	2-MOE	500	58		14	214

$(K_{0.5}Na_{0.5})NbO_3$	Pt/MgO, SiPt	2-MOE	600-650			20.5	[238]
$(K_{0.5}Na_{0.5})NbO_3$	SiPt	2-MOE	320			~ 1-5	[239]
$(K_{0.4925}Na_{0.4925}Li_{0.015})NbO_3$	SiPt	2-MOE	1290	83.1	259		[217]
$(K_{0.5}Na_{0.5})(Nb_{0.7}Ta_{0.3})O_3$	SiPt	2-MOE	500	62		10.5	[216]
$(K_{0.5}Na_{0.5})(Nb_{0.7}Ta_{0.3})O_3$	SiPt	2-MOE	400-650	61	863	10.5	[215]
$(K_{0.5}Na_{0.5})NbO_3$ + 0.5 % Mn^{2+}	SiPt	2-MOE	530-610		500-2000	19.2	[240]
$0.9625(K_{0.5}Na_{0.5})(Nb_{0.92}Sb_{0.08})O_3$-$0.0375\,LiTaO_3$	SiPt	2-MOE	300		250-350	9.5	[241]
$(K_{0.5}Na_{0.5})NbO_3$	SiPt	2-MOE	220-250		610	8	[242]
$(K_{0.5}Na_{0.5})NbO_3$	Pt tubular	EtOH	1000	19.1*	2000		[243]
$(K_{0.5}Na_{0.5})NbO_3$ + 0.5 % Mn^{2+}	SiPt	2-MOE	200		400-1200	16	[244]
$(K_{0.48}Na_{0.48}Li_{0.04})(Nb_{0.9}Ta_{0.1})O_3$ + 0.5 % Mn^{2+}	SiPt	2-MOE	700-800	61	2650	16.1	[218]
$0.95(K_{0.5}Na_{0.5})NbO_3$-$0.05\,CaZrO_3$ + 0.5-1 % Mn^{2+}	SiPt	2-MOE	1000	32		7.5	[219]
$(K_{0.5}Na_{0.5})NbO_3$ + 0.5 % Mn^{2+}	SiPt	2-MOE	830			9	[245]
$(K_{0.5}Na_{0.5})NbO_3$ + 2 % Mn^{2+}	Nb:$SrTiO_3$	2-MOE	270	50.5		17.3	[220]
$(K_{0.5}Na_{0.5})NbO_3$ + 1-3 % Mn^{2+} or Co^{2+}	SiPt	2-MOE	1600	49.9	628	7.5	[221]
$(K_{0.65}Na_{0.35})NbO_3$	Pt/Al_2O_3 $Pt/SiO_2/Si$	n-PrOH + 1,2-PrOH	200				[246]

$(K_{0.5}Na_{0.5})NbO_3$	SiPt	H_2O	300			~ 5	[247]
$(K_{0.5}Na_{0.5})NbO_3$	SiPt	H_2O			280	22.1	[248]
$(K_{0.5}Na_{0.5})NbO_3$ + 1-3 % Co^{2+}	SiPt	2-MOE	1600	49	600-650	7.54	[222]
$(K_{0.5}Na_{0.5})NbO_3$ + 2 % Mn^{2+}	Nb:$SrTiO_3$	2-MOE	400			~ 8-10	[249]
$(1-x)(K_{0.5}Na_{0.5})NbO_3$-$xSrTiO_3$, x = 0-0.25	SiPt	2-MOE	220		150-500	~ 2-4	[250]
$(K_{0.5}Na_{0.5})NbO_3$	SiPt	2-MOE	250				[251]
$(K_{0.65}Na_{0.35})NbO_3$	Pt/SiO_2/Si	n-PrOH + 1,2-PrOH	100				[252]
$(K_{0.4925}Na_{0.4925}La_{0.005})NbO_3$	$SrTiO_3$	2-MOE	500		200-600	8 (6)	[253]
$(K_{0.5}Na_{0.5})NbO_3$	Ti	H_2O			350-500	< 1	[254]
$(K_{0.5}Na_{0.5})NbO_3$	SiPt	2-MOE	1400	83.3	529		[223]
$(K_{0.41}Na_{0.41}Ag_{0.18})NbO_3$	SiPt	2-MOE	2160			3.59	[255]
$(K_{0.5}Na_{0.5})NbO_3$ + 0.5 % Mn^{2+}	SiPt		1000	90		10	[224]
$(K_{0.5}Na_{0.5})NbO_3$ + 0.5 % Mn^{2+}	SiPt	2-MOE	500		600-700	~ 5-7.5	[256]
$(K_{0.47}Na_{0.47}Li_{0.06})NbO_3$	Nb:$SrTiO_3$	2-MOE	200		600-750		[257]
$(K_{0.4925}Na_{0.4925}Li_{0.015})NbO_3$ + 2 % Mn^{2+}	SiPt	2-MOE	500		500-900	11.75	[258]
$(1-x)(K_{0.48}Na_{0.52})(Nb_{0.95}Sb_{0.05})O_3$-$xBi_{0.5}(Na_{0.82}K_{0.18})_{0.5}ZrO_3$, x =0.01-0.07	SiPt	2-MOE	500-2000	184	528		[227]
$(K_{0.5}Na_{0.5})NbO_3$	Ni-W	PPA	120				[205]

$(K_{0.5}Na_{0.5})NbO_3$	SiPt, $Pt/SrTiO_3$	2-MOE	335		146-170	2.65-4.56	139
$(K_{0.5}Na_{0.5})NbO_3$	$Nb:SrTiO_3$	H_2O	180-345		870-2250		64
$(K_{0.5}Na_{0.5})NbO_3$	SiPt	2-MOE					259
$(K_{0.5}Na_{0.5})NbO_3$	SiPt, $LaNiO_3/Si$	H_2O			150-900	~ 0.5-1.5	261
$0.96(K_{0.49}Na_{0.49}Li_{0.02})(Nb_{0.8}Ta_{0.2})O_3$-$0.04CaZrO_3$ + 2 % Mn^{2+}	SiPt	2-MOE	200	24.3	150-550	6	260
$(K_{0.5}Na_{0.5})(Nb_{1-x}(Ti,Ta)_x)O_3$ + 4 % Mn^{2+}, x =0.02-0.08	SiPt	2-MOE	230-300			< 15	262
$(1-x)(K_{0.5}Na_{0.5})NbO_3$-$xBaZrO_3$ + 1.5 % Mn^{2+}, x =0-0.08	$Nb:SrTiO_3$	2-MOE	200		300-750	8	263
$(K_{0.5}Na_{0.5})NbO_3$	Pt/Al_2O_3	2-MOE	330-350	124	103		226
$(K_{0.5}Na_{0.5})NbO_3$ + 0.5 % Mn^{2+}	SiPt	2-MOE	1000		700-1000	6.6	264

2.3 Implantable medical devices and biocompatibility

2.3.1 Implantable medical devices

Medical implants and biomaterials

Definitions

Medical implants are commonplace in modern medicine, and they consist of a wide range of devices, including total hip joint prosthetics, artificial pacemakers, contraceptive devices and vascular stents, to mention some. The purpose of most medical implants is to replace (e.g. hip joint prosthetics), support (e.g. vascular stents) or enhance (e.g. cochlear implants) biological structures/systems in the host, but new technologies are broadening the scopes of these devices (e.g. spinal cord stimulators for pain relief). The vast variety of medical implants available makes it challenging to put an exact definition on the term.[265] The current consensus for the term in the field is "a medical device made from one or more biomaterials that is intentionally placed, either totally or partially, within the body".[265]

In contrast to transplants, medical implants are man-made devices constructed by, traditionally non-living, biomaterials.[266] The definition of the term *biomaterial* has changed with the development of the field.[265,267] The current consensus for the term from the Chengdu Definitions in Biomaterials Conference Consensus Conference 2019 reads:[265] "A material designed to take a form that can direct, through interactions with living systems, the course of any therapeutic or diagnostic procedure". The term is synonymous with the term *biomedical material*.

History of medical implants and biomaterials

There exist several examples of materials being fixed partially of fully enclosed inside the human body from as far back as 32.000 years ago, but these procedures were rarely successful due to severe infections after surgery.[266,268] The modern concept of medical implants came after the development of the aseptic surgery techniques by Lister in the 1860s.[269,270] The use of sterile equipment greatly

reduced the risk of fatal post-operative infections, and experiments with various medical implants took off.[266,270] Until the 1950s, medical implant technology was largely centered around the application of more chemical resistant steels and alloys, as well as making increasingly complex implants for bones and joints.[61,266] In the years after World War II, high-performing metal alloys, ceramics and synthetic polymers developed and used by the militaries during the war were suddenly available for medical engineers and surgeons, and the development of new types of implants exceeded.[266,268] In the 60s and 70s, the first materials specially designed for use inside the body were developed, laying the foundation for the field of *biomaterials*.[266,268,271–273] These materials, referred to as *first-generation* biomaterials, were designed to be as chemically and biologically inert as possible to minimize device degradation and immune- and inflammatory responses from the host. Examples of early hard- and soft-tissue implants developed in the 60s and 70s are presented in Figure 2.18.

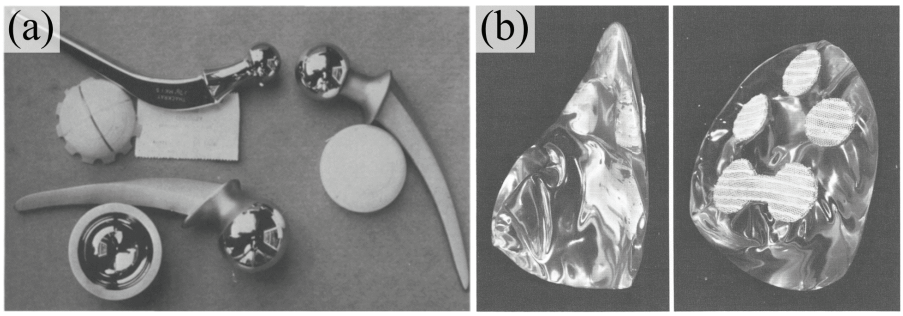

Figure 2.18: (a) Prosthesis models for total hip replacement. Top left: Charnley prosthesis (stainless steel femoral component, high density polyethylene cup). Right: Chernley-Muller prosthesis (cast Vitallium® femoral component, high density polyethylene cup). Bottom left: McKee-Farrar prosthesis (cast Vitallium® femoral component and cup). Reprinted from[274], with permission from Elsevier, © 1973. (b) The Cronin–Gerow silicone breast implant developed in the 1960s. The white patches on the implant is Dacron mesh to help prothesis orientation after implantation. Reprinted from[275], with permission from Elsevier, © 1971.

By 1980, around 40 different materials and 50 different devices had been developed and put to clinical use, and millions of devices were implanted annu-

ally.[271,272] During the 80s and 90s, a new generation of biomaterials was developed and put to clinical use. These *second-generation* biomaterials were, in contrast to the prior *bioinert* materials, designed to either actively elicit biological responses and reactions from the host (*bioactive*) or to gradually degrade and decompose into non-harmful components over time (*bioresorbable*).[273] Bioactive materials saw clinical use from the mid-80s, and already by the start of the 90s bioactive materials was being utilized in multiple medical areas.[276] The bioresorbable materials were designed to be chemically broken down into non-harmful components and resorbed by the host over time, i.e. being replaced by the local biological tissue after playing out its role. By 1984, resorbable sutures made of a copolymer of poly(lactic) and poly(glycolic) acids (PGLA) were standard in clinical practice, and resorbable fracture fixation plates and screws and drug releasing systems were becoming increasingly used.[271,272,276] During the early 1990s, *third-generation* biomaterials were tested in clinical trials. These materials combine the properties from the two classes of second-generation biomaterials, in that they are both bioactive and bioresorbable.[272,273,277] By the mid-00s, several third-generation bioactive glasses were approved by the FDA and on the marked for medical use.[277] Examples of first-, second- and third-generation biomaterials are presented in Table 2.7.

Today, the global medical implant market is a multi-billion dollar industry in strong growth.[284] The European Commission estimates that the market provides 110 billion Euros in sales and employs 675,000 people in Europe.[285] There is no commonly accepted figure on how many medical devices that have been put on the global market, but the International Medical Devices Database (IMDD) have recorded over 7200 different types of medical implants by November 2019.[286] In Norway alone, the number of primary hip arthroplasties was 9553 in 2018.[287] New users of artificial cardiac pacemakers and implantable cardioverter-defibrillators (IDC) counted 4313.[288,289] Both numbers are all-time highs for the 12th year in a row.

Current research on medical implants

Since 2000, especially two technologies have dominated the research area of medical implants. These technologies are *tissue engineering* and *microelectronics*, both of which are a direct result of the exponentially growing ad-

Table 2.7: Some examples of biomaterials.[61,266,271,273,276–283] m = metal/alloy, m* = metalloid, p = polymer, g = glass, gc = glass-ceramic, c = ceramic.

Generation	Property	Materials
First-generation	Bioinert	316L stainless steel (m), Ti-alloys (m), Nitinol (m), Co-Cr alloys (Vitallium®, Stellite®) (m), Zr-alloys (Oxinium®) (m), Ni-Co alloys (MP35N®) (m), platinum (m), gold (m), tantalum (m), zirconium (m), niobium (m), silicon (m*), PTFE (Teflon®) (p), PA (Nylon®) (p), PP (p), PET (Dacron®) (p), PVC (p), PU (p), PMMA (p), poly-siloxane (p), UHMWPE (p), PEEK (p), alumina (Biolox®) (c), zirconia (c), silicon nitride (c), titanium nitride (c), lithium disilicate (gs), fused silica/quartz (g), borosilicate glass (Kimble N-51A®) (g), 8625 BG (SCHOTT 8625®) (g)
Second-generation	Bioactive	Hydroxyapatite (c), heat-treated 45S5 BG (Ceravital®) (gc), apatite-wollastonite (A/W) (gc), 45S5 BG (Bioglass® MEP®, Bioglass®-EPI, Bioglass® ERMI®, Bioglass® Douek-MED™) (g), S53P4 BG (BoneAlive®) (g), Sr-doped BG (StronBone®) (g)
	Bioresorbable	Magnesium (m), magnesium-calcium alloys (m), PLA (p), PGA (p), PCL (p), PGLA (p), PSU (p), polydioxanone (p), silk (p), calcium sulfate/plaster of Paris (c), tricalcium phosphate (c), Na-Ca-P BG (Corglaes®) (g)
Third-generation	Bioactive and bioresorbable	45S5 BG (Bioglass® NovaMin®, Bioglass® NovaBone®, Biomet 3i Biogran®) (g), 70S30C BG (MedCell Theraglass®) (g), 13-93B3 BG (DermaFuse™/Mirragen™) (g), 58S BG (g), 77S BG (g)

vances the contemporary fields of biotechnology/biomaterials science and nanotechnology/computer science, respectively. A brief overview of current research within tissue engineering is given in the next paragraph. Advances in electronic implants is described in *Implantable electronic medical devices* on page 66.

With the development of tissue engineering, there has been a shift in focus in the implant society from *replacing* biological structures/systems to *regeneration* of biological structures/systems.[283,290,291] Tissue engineering is the use of cells, biomaterials and growth factors to engineer new biological tissue either *ex vivo* or *in vivo*.[282,292] The main principle is to seed living reprogrammed cells or stem cells on a biomaterial scaffold and to induce growth of a targeted biological tissue using a specialized environment (e.g. bioreactors, chemicals, enzymes etc.). Tissue engineering has proven to be technically challenging and expensive, but the technology has the potential of offering the world inexpensive and tailored organs and biological tissue on demand and without the need of donors. Although tissue engineering still is on the research stage, large steps towards clinical use has been achieved recently within neural,[293] bone,[294] vascular,[295] skin[296] and cartilage[297] tissue engineering. Recent advances in additive manufacturing has also given tissue engineering researchers a new tool for synthesizing scaffolds.[298]

Implantable electronic medical devices

History of electronic implants

The development of electronic implants started with solving the following problem: how to communicate with a device that is inside the human body. The invention and commercialization of the transistor in the 1940s and 50s enabled engineers to produce small and energy-efficient radio-frequency transmitters, resulting in *biotelemetry*.[59] By 1959, devices for gastrointestinal tract and other cavities were invented,[299] and by the 1960s deep-body implantation of simple radio-transmitting sensors were developed. These *telemetric systems*, developed for monitoring and diagnosis, were the first class of implantable electronic developed.

In the 1950s, the advances in biomaterials and micro-electronics enabled researchers to stimulate the peripheral and central nervous system (i.e. neu-

rostimulation) remotely using implantable electrodes.[300] In 1958, Elmqvist and Senning used a implantable myocardial electrode to control the heart rate of a Swedish patient suffering from intermittent complete heart block (Adam-Stokes syndrome).[1] This was the first artificial cardiac pacemaker to be implanted in a human, and the first to come of many implantable "open-loop" *stimulation systems* developed for local therapy and treatment; In 1961 the first cochlear implant (CI) was applied.[301] In 1967 the first spinal cord stimulator, an implantable pain relief electrode, was tested.[302] In 1976 the first sacral anterior root stimulators for bladder control was implanted.[303] In 1980, the first ICD was implanted.[304] In 1987, the first middle ear implantable hearing device was implanted.[305] In 1989 the first invasive brain-computer interfaces (BCIs) were implanted.[306]

The last category of electronic implants to be developed was the closed-loop control systems.[59] These implants are stimulation systems with sensors that can give correcting feedback to the stimulation control, enabling automated health care. Examples include paralyzed limb control, drug infusion systems, and sensor-regulated artificial cardiac pacemakers. For example, a modern artificial pacemaker regulates the pacing based on activity of the host body, acceleration and respiration rate.[42]

Today, dozens of electronic implants have been developed and commercialized.[307] Modern examples of telemetric systems include implantable pressure sensors,[41,308] myoelectric sensors,[309,310] temperature transponders,[311,312] loop recorders (ILR)/cardiac monitors[313] and sensors for continuous glucose monitoring (CGM).[314] Examples of stimulators include sacral nerve stimulators for bladder control,[315] spinal cord stimulators for pain relief[316] and drug pumps.[317] Examples of closed-loop systems are the artificial cardiac pacemaker[318] and ICDs.[319] A list of various types of implantable electronic medical devises are given in Table 2.8. Four generations of artificial cardiac pacemakers are depicted in Figure 2.19.

Challenges

Remarkably, the current challenges for implantable electronic medical devices are more or less identical to the challenges 60 years ago: (i) The need for chronic power supply, (ii) finding appropriate device packaging and (iii) size restric-

Table 2.8: Examples of implantable and ingestible electronic medical devices.[42,52,306,307,315–322]

Doping mechanism	Medical devices
Sensors, telemetry	Pressure sensors (CardioMEMS™HF System), activity/movement sensors, myoelectric sensors, temperature sensors, accelerometers (STMicroelectronics' MIS2DH), oxygen sensors (Medtronic's Oxytrax), loop recorders/cardiac monitoring systems (Medtronic's Reveal™XT, SJM's Confirm Rx™), BCIs, digital pills/ingestible sensors (Otsuka/Proteus Abilify MyCite®), endoscopy capsules (Medtronic PillCam™)
Stimulators (open-loop systems)	Sacral nerve (bladder, bowel) stimulator (Medtronic's Interstim™), gastric electrical stimulators (Medtronic's Enterra™), spinal cord (pain) stimulators (Medtronic's Intellis™, Boston Scientific's Spectra WaveWriter™), deep brain stimulators (Medtronic's Activa™, Boston Scientific's Vercise™), bone conductive hearing aid devices (Medtronic's Alpha 2 MPO ePlus™, Cochlear's Baha®), cochlear implants (Cochlear's Nucleus®, Advanced Bionics' HiRes™Ultra), retinal implants (Second Sight's Argus®), implantable drug pumps (Medtronic's SynchroMed™), diaphragmatic nerve stimulators (Synapse Biomedical's NeuRx®, Avery Biomedical Devices' Mark IV™)
Sensors and stimulators (closed-loop systems)	Artificial cardiac pacemakers (Medtronic's Adapta™, Medtronic's Kappa 400™, Boston Scientific's Vitalio™), ICDs (Medtronic's Visia AF™, Boston Scientific's Vigilant™), cardiac resynchronization therapy systems (Medtronic's Claria MRI™, Boston Scientific's Intua™)
Other	Microship implants (VivoKey Technologies' Spark)

tions of the hardware compromising functionality and power-efficiency.[58,59] The twenty-first century addition to the list is (iv) cybersecurity and privacy issues with implantable medical devices.[323] The difference solving these issues now compared to 1960 is that a lot of the technology required to overcome these challenges already exists in micro-electronics and nanotechnology, and it just needs to be implemented in medical implant technology.[58]

Figure 2.19: Four generations of artificial cardiac pacemakers. From left to right: Cordis' Omni-Stanicor®, Cordis' Sequicor®, Medtronic's Thera® and Medtronic's Adapta™.

(i) Chronic power supply: Implantable electronic devices require electricity to function, and the power requirement varies from the micro-watt range (pacemakers, IDCs, neuro-stimulators) to the milli-watt range (cochlear implant, retinal stimulator) dependent on the type of device.[44,324] At the same time as electronic circuitry has become more power efficient, medical implants have become more sophisticated (e.g. closed-loop systems, wireless communication) and therefore more energy demanding.[44] Today most electronic implants use lithium-based batteries as their source of power.[44] Despite major advances in battery technology the last six decades, batteries have quite limited energy storage capacities.[324] For pacemakers and ICDs, which usually have a battery lifetime of 10 years, this means replacement of device through surgery. In addition to be inconvenient to patients and expensive to the healthcare system, recent studies have shown that such revision and replacement surgeries of electronic implants is a large risk factor for infection.[325,326] Several strategies are being researched in order to solve the challenges with power supply for medical implants.[44,58,324,327] In addition to optimize the circuitry and device software to reduce leakages and losses during operation,[324] *energy harvesting* from natural or artificial sources has been proposed as a possible solution for endless power-supply.[44,58,324,327–329] Wireless energy harvesting by implants using induction and radio-frequency (RF)

transmission is already in clinical use.[58] Other energy harvesting systems are being developed, including optical/infrared and ultrasonic power transmission, vibrational energy harvesting from the natural surroundings using piezoelectric-, electromagnetic- and electrostatic systems, thermoelectric harvesting and the use of biofuel cells.[44,58,324,327–329]

(ii) Device packaging: Choosing appropriate packaging materials for the implantable electronic device is important for shielding the electronics from the body and the body from the electronics.[59,279] The human body is a demanding environment for materials, and implantable medical devices must be durable in terms of mechanical strength, wear and corrosion/degradation resistance, have low permeability rates, have a surface temperature difference to the body of maximum 2 °C, and be non-harmful to the surrounding tissue and the biological host. To counter this, the preferred packaging technology has been to make a hermetical seal around the electronic device using bioinert materials.[330] Metals are the most common materials used for device packaging (e.g. Ti-alloys, Ni-Co alloys, noble metals, Pt/Ir alloys), but bioinert polymers (e.g. silicone rubber, epoxies, PU, PI), glasses (e.g. quartz, fused silica and borosilicate) and ceramics (e.g. alumina, sapphire and ruby) are also used.[59,279,330] Hermetic packaging of implantable medical devices has some drawbacks, as the protective cover increases the size of the device and attenuates signals to and from the device. Non-hermetic micro-packaging, using thin layers of polymer coatings, is currently researched as a possible alternative to hermetical packaging.[331,332] Researchers are also developing bioresorbable electronic implants intended for short-term applications.[333,334]

(iii) Size-restriction: Implantable electronic devices have always been subjected to strict size-restrictions due to the limited space inside the human body.[59] It is generally accepted that the total weight of the implant should not exceed 2 % of the hosts body weight to minimize discomfort and to make it compatible with normal human activity, and the device should also have a specific gravity (density) similar to the surrounding tissue.[59] Having a small size is also beneficial for the power consumption of the device, as smaller electrical components use less power.[44,59,324] A reduction in implant size will also decrease foreign body responses, inflammatory responses and overall wound healing time.[335,336] Im-

plantable device sizes have gone down orders of magnitude since they entered clinical use 60 years ago, but current implant sizes are still too large for many application areas.[58,59,279] Historically, engineers have avoided size limitations by dividing implants into locally situated sensors and/or stimulators that are connected to a central battery and circuitry hub via wiring (e.g. cochlear implants, ICDs and pacemakers).[279] The shrinking of electronic circuits and the use of application-specific integrated circuits (ASIC) has reduced the electronic implant sizes.[59] However, the power source (battery) and device packaging have always been, and still are, the major contributors to implant size and weight.[58] While device packaging can be further reduced using micro-packaging,[331,332] battery technology is seemingly reaching a finite size with today's technology.[279] One of the prominent solutions to reduce the size of the power sources is energy harvesting/scavenging as described above.[44,58,324,327–329]

(iv) Cybersecurity and privacy issues: Many implantable electronic medical devices today have telemetric systems that allow medical personnel to track power/battery level, read stored patient records captured by the device and/or change implant settings.[321,323,337–339] Moreover, there is a trend for new devices to have networking-functions for 24/7 monitoring and direct communication with the user/host.[321,323] These advances in wireless communication are improving the lives of millions of patients with electronic implants, but the cybersecurity measures for the software in these medical devices have been shown to be highly vulnerable towards cyber threats from third parties.[321,323,337–339] Today cybersecurity weaknesses have been found in over a hundred electronic medical devices.[321] Although there is an urgent need for better security measures for electronic medical devices, experts are debating how strong the possible countermeasures (e.g. encryption) should be, especially regarding authentication to access in case of medical emergency.[338]

Current research on implantable electronic medical devices

Research and new technology in the field of implantable electronics have in the last two decades been dominated by development of micro- and nanoelectronics.[322] For biosensor technology, nano-sensors have gained a lot of attention due to their small size, low power consumption and accuracy.[197,322,340,341] Developing micro-sized chemical sensors has been a challenge for the last 30

years in the development of total chemical analysis systems (TAS), but such devices are now expected to enter clinical use in the near future.[53,54,56] The development of micro-electromechanical systems for biological applications, bioMEMS, has also gained considerable attention the last two decades.[49,50,342,343] BioMEMS are being used to develop micro-devices for drug delivery and possibly closed-loop micro-systems that can both diagnose and treat the user automatically in real time.[49,343,344]

Piezoelectric materials in medical implants

Piezoelectricity for tissue regeneration

Piezoelectric behavior is observed in many biological tissues and notably in bones,[95,345] and the generation of local potential gradients on bone is linked to osteogenesis.[346] In general, electrical stimulation has been shown to affect cellular behavior, including cell adhesion, migration, orientation, proliferation and differentiation.[347–351] Because of this, piezoelectric materials have been clinically tested as bioactive implants for orthopedic applications since the 1970s with varying results.[352–356] However, recent studies have found piezoelectric ceramics to enhance cellular responses both *in vitro* and *in vivo*, and they remain highly relevant for future bone implant coatings.[357–359] The recent interest in tissue engineering has called for the development of bioactive scaffolds,[282,290,292] and piezoelectric materials have been proposed as potential "smart" scaffold materials due to their electrical stimulation properties.[51,360–367] Especially piezoelectric polymers have received much attention due to their light weight, low price, high chemical resistance, thermal and mechanical stability, biocompatibility with both hard and soft tissue, and their compatibility with other organic and inorganic materials to form hybrid systems/composites.[51,362,366]

Piezoelectricity for implantable electronics

Hearing implants: Piezoelectric materials are used in middle-ear hearing implants (e.g. Envoy Medical's Esteem®)[305,368] and bone-conduction hearing implants (e.g. Cochlear's Osia®)[369,370]. For the middle-ear implants, a processor behind the ear picks up sound and transfer it to a subcutaneous receiver using radio-frequency signals, and the receiver translates these signals into electrical signals and sends them to a piezoelectric or electromagnetic transducer.[305,368]

The transducer, which is anchored to one of the bones in the middle-ear, transfers the electrical signal to the cochlea and the hearing nerve by vibration. For the bone-conduction hearing implants, the transducer is either percutaneously or subcutaneously fixed to the outer skull.[369,370] The bone-conduction hearing implants are thus less invasive than the middle-ear implants, but the percutaneous devices can be susceptible to infections and site complications since they penetrate the skin.[305,369]

Sensors: Piezoelectric materials are currently used as activity sensors in artificial cardiac pacemakers (e.g. Medtronic's Kappa 400™).[42,48,49] A piezoelectric crystal in the activity sensor detects physical movement, and the sensor can then help regulate the pacing-rate of the artificial pacemaker. Some artificial pacemakers are also supplied with piezoelectric sensors on the pacing lead for right ventricular pressure monitoring.[42] Current research on implantable piezoelectric sensors is dominated by nanotechnology, and researchers are developing piezoelectric thin films, nano-wires and nano-cantilevers for sensing of vibrations, force/pressure, flow, acceleration, mass and humidity.[47,55,196,341,364,365]

Microfluidic systems: Researchers are currently developing piezoelectric actuators for implantable microfluidic systems such as biomedical microelectromechanical systems (bioMEMS), lab-on-a-chip (LOC) and micro total analysis systems (μTAS).[49–56] Piezo-actuated microvalves, -pumps and -mixers have been developed since the 1980s,[50,53,54] but recent advances in piezoelectric surface acoustic wave (SAW) technology have enabled researchers to size modulate, split, trap, tweeze, pump, mix, jet and nebulize droplets down to picolitre sizes.[55] For "classical" piezoelectric actuation, the micropumps are usually designed with an out-of-plane fluctuating piezoelectric membrane on top of a thin liquid reservoir.[50,52] Debiotech™has developed an implantable drug injection device called MIP that utilizes such piezoelectric actuation.[52,307]

Energy harvesters: The chronic need of power is one of the main challenges with implantable electronics,[44,58,59,324] and a lot of research is conducted on using piezoelectric materials for energy harvesting/scavenging.[44,46,47,196,327,329,364,365,371] Most research is focused on piezoelectric nano-wires/-fibers of ZnO, $BaTiO_3$ and PVDF-based polymers[46,47,364,365,371]

or PZT- and PMN-PT-based flexible thin films.[46,47,196,364] Although many prototypes have been made, the small size required for implantable energy harvesters limits the power output of the devices.[44,372] A minimum requirement for application of an energy harvester disc with the size of a quarter size dollar coin is set to 100 µW (0.124 $\mu W mm^{-3}$) of continuous power from low frequency (<100 Hz) ambient vibrations, and research is currently closing in on this benchmark.[372]

2.3.2 Biocompatibility

The concept of biocompatibility

Definition

In materials science biocompatibility is concerned with the performance of a material in a specific biological context,[61] but the use of the term is controversial.[373] In its broadest context, *biocompatibility* is defined by IUPAC as the "ability to be in contact with a living system without producing an adverse effect".[62] In context of using materials for biomedical therapy, the biocompatibility is usually defined as "the ability of a material to perform with an appropriate host response in a specific application".[60–63,265] Although being short, the definition is underpinned by three principles:[61,63] (i) The material itself must perform with a desired function in the medical therapy situation (i.e. the material must tolerate the specific biologic environment). (ii) The material must induce an appropriate response from the biological host (i.e. the material must not cause harm to the biologic environment). (iii) The response from the material-biological host system is application specific and may vary from one situation to another (i.e. biocompatibility is not a universal material property). As such, biocompatibility should be regarded as a characteristic of a specific material-biological host system, not a descriptor for a material.[61,373] A material can never be "biocompatible", but it can have excellent biocompatibility in one or more situations.[373]

For medical implants a practical measure of the biocompatibility associated with the implant-biological host system is to look at to which degree the homeostatic mechanisms of the biological host are perturbed upon implantation.[335,374] This can be achieved by quantifying the extent of pathophysiologic processes activated, and how fast these are resolved, after the implant is placed in the

host. The characteristic pathophysiologic process associated with implants is the *foreign-body reaction*.[335,374–377]

Host response to implants: Wound healing and the foreign-body reaction
The generic host reaction to a medical implant is rooted in the fact that (almost) all implants are composed by materials that are foreign to the biological host, and the initial interaction between implant and biological host is directly influencing the characteristics of the long-term implant-host system.[374,376,377] The placement of a medical implant in a biological environment requires injection, insertion or surgical implantation. In all cases the surrounding biological tissue is injured, which onsets a series of mechanisms by the host to maintain homeostasis (sometimes referred to as wound healing). This continuum of mechanisms can be divided into individual stages based on the molecular, cellular and/or systemic processes involved:[335,374–378] (1) Implantation/injury, (2) blood-biomaterial interactions, (3) provisional matrix formation, (4) acute inflammation, (5) chronic inflammation, (6) granulation tissue formation, (7) foreign-body reaction, (8) fibrosis/fibrous capsule development. While the first stages (stage (1) to (6)) are similar for all wound healing processes following tissue injury, the last stages of the healing process ((7) and (8)) are exclusive to implants. The duration for each stage varies greatly, from a few minutes to days or weeks.[374] It is important to note that the list of individual stages is a simplified model of a continuum of complex processes.[374,376–378] The stages are also closely linked to each other, and they often occur simultaneously or with overlapping onsets. A schematic of the stages and processes is presented in Figure 2.20. A summary of the effect of implant material on local tissue is presented in Table 2.9.

Table 2.9: Implant materials and the response of surrounding tissue.

Implant material	**Tissue response**
Toxic	Surrounding tissue dies
Bioinert (non-porous)	Fibrous encapsulation
Bioinert (porous)	Implant-tissue bond formation, tissue ingrowth
Bioactive	Implant-tissue bond formation
Bioresorbable	Surrounding tissue replaces material

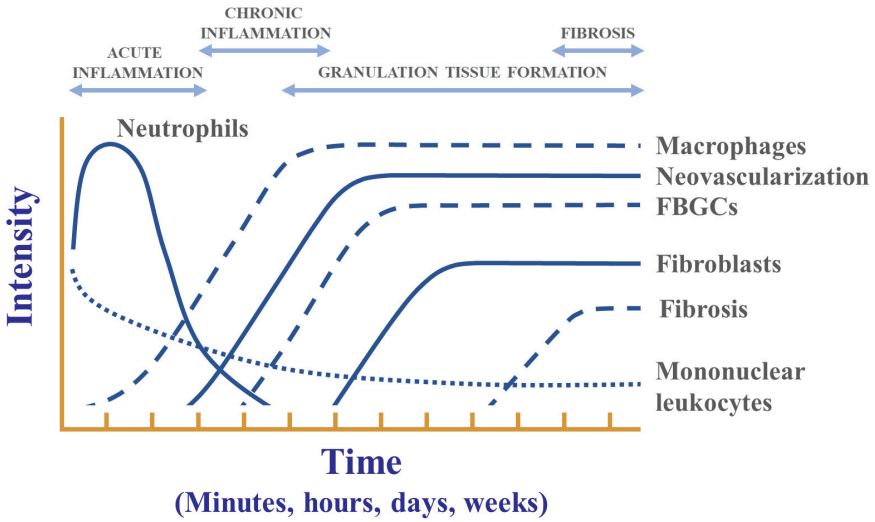

Figure 2.20: Overview of cell activities and processes after implantation of a medical device. Adapted from[379], with permission from Springer Nature, © 2017.

(1) Implantation/injury: The medical implant is placed at site of function through injection, insertion or surgical implantation. Vascularized tissue around the implant is injured in the process.[376,377]

(2) Blood-biomaterial interactions: Following implantation, blood stream from the vascular system into the injured tissue (exudation).[374] The blood leak from the injured tissue and encounter the implant/biomaterial. As blood encounter the implant, fibrin (blood clotting protein) and other proteins in the blood immediately adsorbs to the surface of the implant, forming binding sites for protein-specific receptors on cells.[335,377]

(3) Provisional matrix formation: Cells and platelets start binding to the protein layer, releasing signaling molecules and inflammatory mediators.[335,377] A blood-based transient provisional matrix (thrombus), consisting of fibrin, activated blood platelets, inflammatory products, inflammatory cells and endothelial cells, forms within minutes or hours of implantation.[374,376,377]

(4) Acute inflammation: Acute inflammation proceed by the immune response from leukocytes (white blood cells).[335,374–377] Neutrophils, the predominant leukocyte in the blood, and mononuclear cells (i.e. monocytes and lymphocytes) arrive in large numbers, releasing granules filled with cytotoxic enzymes (degranulation) and start adsorbing to the surface of the implant in effort ingest/engulf it (phagocytosis).[374,376,377,380] Macrophages, another leukocyte, start accumulating and adsorbing on the surface. Acute inflammation resolves within minutes, hours or a few days.[374]

(5) Chronic inflammation: Persistent inflammatory stimuli, such as the continuous presence of an implant, lead to chronic inflammation.[335,374–377] Chronic inflammation is mainly perpetuated by macrophages, but monocytes and lymphocytes are also present.[335,375–377] Chronic inflammation is usually resolved within days due to granulation tissue formation around the implant, and persistent chronic inflammation (> 3 weeks) is usually an indication of infection.[376,377]

(6) Granulation tissue formation: The wound healing process, primarily involving formation of granulation tissue (scar tissue), is initiated within a day after implantation.[374,376,377] Microphages, initially present as inflammation response, mediate the healing process by releasing enzymes, cytokines and growth factors that are important for tissue reorganization and fibroblast/vascular endothelial cell migration and proliferation.[377,380] The fibroblasts and endothelial cells start developing granulation tissue by forming connective tissue and microscopic blood vessels (neovascularization), respectively, 3-5 days after implantation.[374,376] The total healing process involving granulation tissue formation is dependent on the extent of injury inflicted during implantation.[374,376,377]

(7) Foreign-body reaction: The foreign-body reaction (FBR) is unique to implants and other large foreign bodies in wound healing. Microphages can only phagocytose foreign bodies smaller than 10 µm.[380] When the microphages are unable to phagocytose the implant, they coalesce into foreign-body giant cells (FBGC, Langhans cells).[335,374,376,377,380] These cells continue attempting to phagocytose the implant by adhering to the surface (frustrated phagocytosis), sometimes for the entire lifetime of the implant.[374,380] Together with granulation tissue, macrophages, fibroblast and endothelial cells, the FBGCs form a layer around

the implant. The composition and thickness of this layer are directly dependent on the implant, e.g. its size, shape, porosity, surface roughness and composition.[335,374] Formation of FBGCs is usually observed after 7-14 days.[376] For implants composed by bioactive materials or porous bioinert materials, formation of the FBR layer and possibly ingrowth of local tissue is the end-stage in the healing process.[374] For implants made of bioresorbable materials, enzymes and reactive oxygen species (ROS) released by the FBGCs will gradually degrade the implant, eventually causing adsorption of the implant.[377]

(8) Fibrous encapsulation: In the case of implants with smooth, bioinert surfaces, fibrous encapsulation (fibrosis) is initiated by the FBGCs.[335,374,376,377] Like the macrophages, the FBGC may start releasing cytokines and growth factors that stimulate surrounding fibroblasts and endothelial cells.[377] This triggers fibroblasts to overproduce extracellular matrix proteins, forming a collagen-rich connective tissue that encapsulates the implant.[374,376,377] This capsule forms an isolating seal between the FBR layer/implant and the surrounding tissue that regulates and sometimes contain inflammatory mediators and signaling molecules from the macrophages and FBGCs at the implant interface.[374,376,377] Fibrosis usually occurs over months.[335]

Minimizing the foreign-body reaction

Minimizing the foreign-body reaction will not only speed up the healing time for the host, but also relieve the implant of long-term chemical hostility that can degrade its components and limit the degree of fibrosis around the implant which can compromise its functionality.[335,377] The duration and intensity of the foreign-body reaction is mainly dependent on the host's physiological condition, the implantation procedure, the type of tissue at the implant site, and the implant design.[61,335,374,377] For the implant design, a range of variables can influence the foreign-body reaction: Size, shape, mechanical properties, bulk material composition, macro-/micro-/nano-porosity, surface material composition, surface topography, surface energy, surface electrical properties, corrosion parameters and metal ion toxicity (for metal implants), degradation profile and degradation product/leaching chemical toxicity (for polymeric implants) and dissolution/degradation profile and degradation product toxicity (for ceramic implants).

The implant surface has a central role in the inflammation response and healing process during the first two to four weeks after implantation.[376] Most techniques for modulating the foreign-body reaction are based on surface modification of the implant to reduce the inflammatory response.[335,376,377] These techniques can be divided into passive and active modulation.[377] Passive modulation can be achieved through chemical or topographic modifications of the implant.[376,377] Active modulation involves direct stimulation of the cells involved in the inflammatory processes and the foreign-body reaction using bioactive molecules and coatings.[335,377]

Testing biocompatibility

From the laboratory to the patient

To truly know the biocompatibility of an implant or an implant material, its performance and effect on the biological host must be evaluated in the specific situation in which it is designed to perform, i.e. in clinical trials with human hosts. However, testing new biomaterials and medical implants directly in human subjects is both impractical and unethical. Therefore, new devices/materials usually go through a series of tests before entering clinical trials. The testing starts with basic chemical and physical assessments and gradually go through various *in vitro* cell tests before being assessed *in vivo* through animal trials and clinical trials, as illustrated in Figure 2.21.[320,381,382]

Figure 2.21: Testing hierarchy for medical devices/materials.

There exist no universal set of tests and assays to evaluate biocompatibility.[378] Different governments and agencies worldwide operate with different sets of regulations and standards.[320,383–385] However, the International Organization for Standardization (ISO) has developed a set of recommended standards in the process of evaluating the safety of medical devices.[63] These include standards for

quality management (ISO 13485),[386] risk management (ISO 14971),[387] biological evaluation (ISO 10933)[388] and clinical trials (ISO 14155).[389]

For a first approximation to biocompatibility through biological tests, the biological evaluation standards (ISO 10933 part 1-20) are usually used. The 10993 standard series includes a list of assays to be considered to use when testing medical devices.[388] Of the medical devices listed in the standard, the long-term implantable medical devices (>30 days) have the most assays suggested to be considered. These include: Cytotoxicity, sensitization, irritation or intracutaneous reactivity, material mediated pyrogenicity, acute systemic toxicity, subacute toxicity, subchronic toxicity, chronic toxicity, implantation effects, hemocompatibility, genotoxicity, carcinogenicity, reproductive/developmental toxicity and degradation assay. The evaluation suggests not only to test the medical device itself, but also to assess degradation products and leachables (ISO 10933 part 13-17).[390–394] There is also a guidance of how to use the other parts of the 10993 standard series in the case of medical devices composed by or containing nanomaterials (ISO 10993-22).[395]

Chemical and physical assays for testing biocompatibility
Knowing the chemical and physical properties of the medical device/material is an important first step in assessing its biological safety.[382] The components making up the device should not be toxic, nor react or degrade to form toxic products. Depending on the application, the device/material surface should be engineered to interact appropriately with the surroundings. The device/material must also have a chemical and mechanical stability appropriate for the application. An overview of chemical, physio-chemical, morphological and topological characterization standards is described in ISO 10993-18[396] and 10993-19.[397] Selected assays for device/material characteristics associated with affecting biocompatibility are described below.

Release of degradation products/leachables: Release of degradation products/leachables test the device/material in solutions to quantify release products like ions, molecules or particles. The device/material is typically placed in a medium over long periods (e.g. distilled water, phosphate-buffered saline (PBS), simulated body fluid), while the solution is regularly screened for released ion,

molecules, debris/particles etc.[398]

Wettability: For inflammatory cells to attach to a device/material, proteins need to adsorb to the surface to make binding sites for the cells.[377] The initial non-specific protein adsorption is dependent on the wettability of the surface, and proteins like fibrin, albumin and immuglobin G bind to the implant surface through hydrophobic interactions.[399,400] Hydrophobic surfaces are therefore associated with more intense foreign-body responses upon implantation. Hydrophobicity can be assessed by measuring contact angle of a liquid.

Protein adsorption: Affinity for protein adsorption on device/material is linked to biocompatibility (see *Wettability*).[399,400] Protein adsorption on the device/material can be measured directly using several different techniques, including solution depletion assays, optical analysis and spectroscopy.[401]

Topography: Surface topography can affect biocompatibility, as the topography of the surface of a device/material can dictate protein adsorption and -unfolding[400] in addition to facilitating cell orientation/adhesion, morphology, differentiation and proliferation as nanosized roughness can mimic extracellular matrices.[377,400,402,403] Surface topography can be measured using scanning electron microscopy (SEM) or atomic force microscopy (AFM).

In vitro assays for testing biocompatibility

In vitro biological evaluations can give a prediction of biocompatibility by identifying if there are any potential hazards for specific cells growing in the presence of the device/material.[381,382,404] *In vitro* assays are popular due to the relative low complexity and expense of these tests but results from *in vitro* assays need to be validated through *in vivo* assays and clinical trials before a device or material can be regarded as safe for medical implantation.

In vitro cytotoxicity: *In vitro* cytotoxicity testing is described in ISO 10933-5:2009[405] and is the most common assessment of biocompatibility in literature.[335,382,404,406] *In vitro* cytotoxicity testing assesses cell viability (e.g. activity (adherence, differentiation, metabolism, proliferation, secretion of trophic factors), damage, death, growth, morphology) during direct or indirect contact with the device/material or device/material extract.

Cell death, metabolic activity and reproductive activity/proliferation can be assessed through four different assays:[404,406] dye exclusion assays, colorimetric assays, fluorometric assays and luminometric assays. (i) Dye exclusion assays probe the resistance of cells to exclude a dye (Figure 2.23 (a)). Whereas viable cells will exclude dyes, dead or dying cells have lost their membrane integrity and will be stained by the dye. Examples of common staining dyes include trypan blue, eosin, Congo red and erythrosine. (ii) Colorimetric assays probe the metabolic/mitochondrial activity of cells. Most of these assays are based on spectrophotometric detection of colored metabolic products of various tetrazolium salts, including 3-(4,5-dimethylthiazol -2-yl)-2,5-diphenyltetrazolium bromide (MTT), 2-(2-methoxy-4-nitrophenyl)-3-(4-nitrophenyl)-5-(2,4-disulfophenyl)-2H-tetrazolium (WST-8/CCK-8) and lactate dehydrogenase (LDH), see Figure 2.22. Assays not based on tetrazolium salts include alkaline phosphatase assay (ALP/pNPP), sulforhodamine B assay (SRB), neutral red uptake (NRU) and crystal violet assay (CVS). (iii) Fluorometric assays probe the capacity of enzymes in viable cells to convert nonfluorescent markers to fluorescent dyes. The conversion is quantified by fluorescent microscopy. Examples include alamarBlue, CFDA-AM and GF-AFC. (iv) Luminometric assays probe the presence of the cell energy carrier molecule adenosine triphosphate (ATP) through a luminescent reaction with luciferin. Since ATP concentration is cells is directly related to cell viability, luminescent microscopy of the luciferin/ATP reaction give a quantitative measure of the number of viable cells present.[406]

Cell morphology, growth, adherence and differentiation can be assessed visually using optical microscopy, SEM and immunofluorescence microscopy. For transparent samples or device/material extracts, optical confocal microscopy can be used non-invasively and directly to visually inspect cell appearance. For SEM characterization (Figure 2.23 (b)), the cells need to be fixated and dehydrated before imaging. Immunofluorescence microscopy uses antibodies to anchor fluorescent dyes to specific cell structures (Figure 2.23 (c)). Common fluorescent stains include DAPI which binds to adenine-thymine rich regions in DNA and thereby stain cell nuclei, β-tubulin which binds to microtubules and thereby stain cell cytoskeletons, and various cell-specific markers (e.g. GFAP which binds to glial cells). Figure 2.23 illustrates the three different imaging techniques immunoflu-

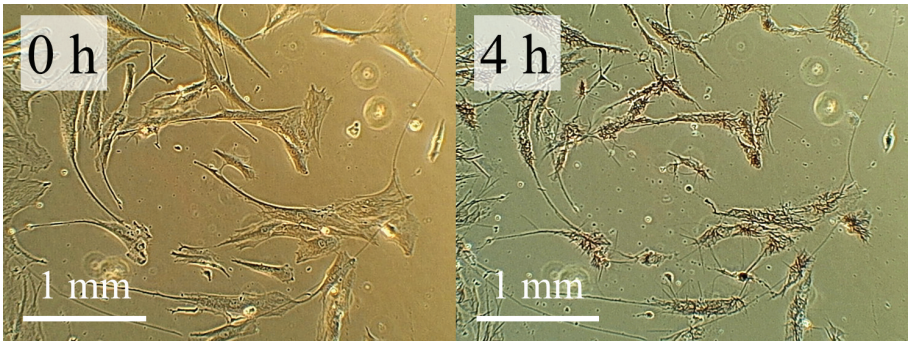

Figure 2.22: Confocal microscope image of 161BR fibroblast cells 0 h (left) and 4 h (right) after the addition of MTT solution. Dark purple formazan crystals can be observed inside and around the cells after 4 h.

orescence microscopy, SEM and regular optical microscopy.

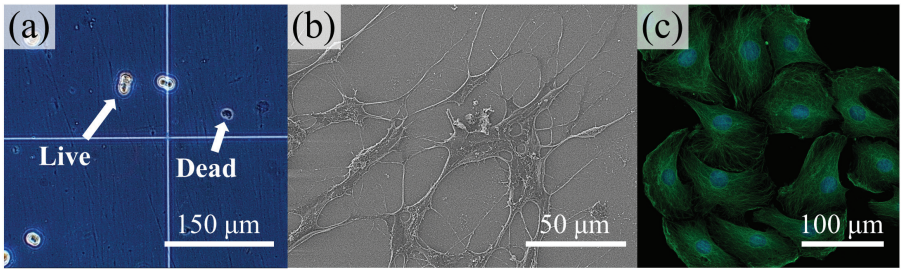

Figure 2.23: (a) Optical microscopy of PC12 cells stained with trypan blue (dye exclusion assay). (b) SEM image of SH-SY5Y neuronal cells. (c) Immunofluorescence microscopy of rat Schwann cells stained with β-tubulin (green) and DAPI (blue).

In vitro genotoxicity: *In vitro* genotoxicity testing is described in ISO 10933-3:2014[407] and is targeted if there are components in the device/material that can potentially interact with genetic material.[382] The tests applied should probe three critical measures of mutagenicity: Gene mutations, structural chromosome aberrations and numerical chromosome aberrations. Testing for *in vivo* genotoxicity and carcinogenic potential should be targeted in the event of a positive *in vitro* genotoxicity test.

In vitro hemocompatibility: *In vitro* hemocompatibility evaluation is described in ISO 10993-4:2017[408] and is necessary for devices/materials that potentially will be in contact with blood.[382] Depending on the application of the medical device/material, five different assays should be considered: hemolysis, thrombosis, coagulation, platelets, hematology and the complement system. For implants, both *in vitro* and *in vivo* hemocompatibility studies should conducted.

In vitro irritation: *In vitro* irritation evaluation is described in ISO 10933-23 (under development at time of writing) and is a complimentary assessment to *in vivo* irritation evaluation.[382] *In vitro* irritation evaluation assesses the viability of reconstructed tissue in contact with the device/material. Tissue viability is determined using colorimetric assays (e.g. MTT, WST-8 etc.) and the test is run with both positive and negative controls. The tissue used is a reconstructed model using live cells on a supporting matrix. Although reconstructed skin models are the most commonly used for *in vitro* irritation analysis, eye and mucosal models are available. Negative *in vitro* irritation test results must be confirmed with *in vivo* assays.

In vivo assays for testing biocompatibility

Chemical/physical characterization and *in vitro* biological evaluations using cell-based assays can give predictions for the biocompatibility of a medical device/material, but such tests can never capture the full systemic response from a biological host.[381,382] The *in vivo* assays are designed to either confirm/refute corresponding *in vitro* assays, e.g. *in vivo* genotoxicity assays (ISO 10933-3:2014),[407] *in vivo* hemocompatibility assays (ISO 10993-4:2017)[408] and *in vivo* irritation assays (ISO 10993-10:2010[409] and ISO 10993-23 (under development at time of writing)), or to complement the *in vitro* assays, e.g. *in vivo* carcinogenicity assays (ISO 10933-3:2014[407] and ISO/TR 10993-33:2015),[410] *in vivo* implantation assays (ISO 10993-6:2016),[411] *in vivo* sensitization assays (ISO 10993-10:2010)[409] and *in vivo* systematic toxicity assays (ISO 10993-11:2017).[412]

Biocompatibility of piezoelectric ceramics and KNN

The effect of piezoelectricity and ferroelectricity on biocompatibility

Electrical gradients and potentials formed by ion concentration differences across

cell membranes play a central role in cell behavior.[347–349] As mentioned in *Piezoelectricity for tissue regeneration* on page 72, external electrical stimulation of tissue has been shown to be able to promote cell migration, orientation, proliferation and differentiation.[347–351] Because of this, electrical potentials formed by piezoelectric and ferroelectric ceramics can strongly influence the biocompatibility of the material-cell system.[57,413–422] Piezoelectric stimulation using ceramic nanoparticles and films has been demonstrated to influence cell growth and expression of neuronal cells[413–415] and osteogenic cells[416–418] *in vitro*. To promote the polarization in these ceramics, the system was mechanically stimulated using vibrations or ultrasound in the range of 100-1 000 000 Hz. For ferroelectric ceramics, a mechanical stimulus is not necessary to promote electrical polarization, and researchers have demonstrated enhanced proliferation and expression of cells grown on poled ferroelectric ceramics.[420] The direction of the ferroelectric polarization has been shown to influence cell behavior as different cell types are attracted to different polarities.[421,422] For example, macrophage and fibroblast cells are attracted to positive and negative potentials, respectively.[348] Researchers have also shown that cells are affected by strong polarization gradients between ferroelectric domains with opposite direction, as illustrated in Figure 2.24.[419] For cell stimulation using either piezoelectric and ferroelectric polarization, screening charges must be considered, as these will reverse the potential of the surface polarity.[423,424]

Biocompatibility studies on piezoelectric ceramics

Ceramics in general usually exhibit excellent biocompatibility with biological systems due to their chemical inertness.[266,273,276,280] This entails many piezoelectric ceramics, and a wide range of these materials have been tested for biocompatibility both *in vitro* and *in vivo*, including KNN, PZT, PMN-PT, $BaTiO_3$, $Ba_{1-x}Ca_xZr_{1-y}Ti_yO_3$ (BCZT), $KNbO_3$, $LiNbO_3$, $LiTaO_3$, $KTiOPO_4$, $0.94Na_{0.5}Bi_{0.5}TiO_3-0.06BaTiO_3$, $Bi_{5-x}La_xTi_3FeO_{15}$, ZnO, AlN and BN.[203,204,206,208,352–356,359,413–422,425–445]

Lead-based ceramics: Lead-based piezoelectric ceramics like PZT and PMN-PT have both been studied *in vivo*[208,355] and *in vitro*.[206,425,426] Neither PZT or PMN-PT induce acute cytotoxic responses in biological tissue, but these materials release lead ions when subjected to aqueous environments and are therefore potent

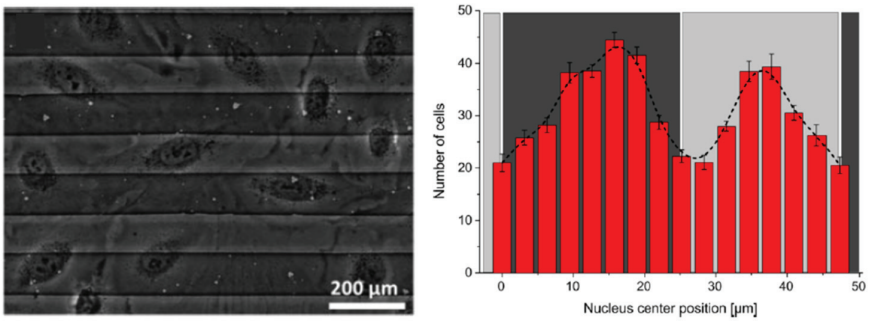

Figure 2.24: Phase contrast image of REF52 fibroblast cells on periodically poled ferroelectric $LiTaO_3$ (left). The cells avoid positioning their nuclei on the ferroelectric domain walls/boarders (right). Reprinted from [419], with permission from American Vacuum Society, © 2013.

of causing chronic cytotoxic damage. [206,426,446]

$BaTiO_3$-based ceramics: The biocompatibility of $BaTiO_3$-based ceramics like $BaTiO_3$ and BCZT has been readily tested both *in vivo* [352–354] and *in vitro*. [203,359,414,426,430–432,439] $BaTiO_3$ composites with other ceramics like TiO_2 and hydroxyapatite [356,427–429] or polymers [415,417,418,433,434] have also been studied. Overall, $BaTiO_3$-based ceramics mostly perform on par or better than controls.

Other piezoelectric ceramics: The ferroelectric ceramics $LiNbO_3$ and $LiTaO_3$ are often used as model systems for testing the effect surface polarization on cells due to their high remanent polarizations, and the materials perform well in *in vitro* cytotoxicity tests. [419–422,430] The studies on $KNbO_3$ nanoparticles and films, [430,435] $Bi_{5-x}La_xTi_3FeO_{15}$ (x = 0, 1) nanofibers, [436] $0.94\,Na_{0.5}Bi_{0.5}TiO_3 - 0.06\,BaTiO_3$ pellets [426] and AlN films [204] are limited but show promising results. Dispersions of BN nanotubes exhibit cytocompatibility in *in vitro* studies with PC12 cells. [413] $KTiOPO_4$ and ZnO nanoparticles are found to be somewhat and highly cytotoxic, respectively. [430]

Biocompatibility studies on KNN-based ceramics

Biocompatibility studies have been performed on various forms of KNN ceramics, including bulk samples/pellets,[437,440,441,443,445,447] powders and powder extracts,[438,439,444] and films.[206,442] The studies cover both chemical/physical characterization (chemical stability,[206,438,439,444] protein adsorption[443]), *in vitro* biological evaluation (cell adhesion and morphology,[206,437,440,445] cytotoxicity,[206,438,439,443] cell proliferation)[206,437,440–443,445] and *in vivo* biological evaluation.[206] Antibacterial properties of KNN samples have also been studied.[441,445]

Chemical stability/ion release: The chemical stability of KNN ceramics has been studied by ion release tests in aqueous solutions for 4-28 days.[206,438,439,444] KNN ceramics are prone to lose ions to solutions, and K^+/Na^+ release from KNN powders is reported to be as high as 20-80 ppm in distilled water[444] and up to 10 000 ppm in saline solutions at 37 °C.[438,439] K^+ and Na^+ more readily leach from KNN than Nb^{5+} due to their lower cation field strength, and Nb^{5+} release from KNN is in the range of 0.1-10 ppm.[206,438,439,444] Nb^{5+} release from KNN ceramics is 2 to 3 orders of magnitude lower than Pb^{2+} release from PZT ceramics.[206] The ion release from KNN is pH dependent, and K^+/Na^+ release is increased in acidic environments while Nb^{5+} release is increased in basic solutions.[444]

Protein adsorption: The adsorption of bovine serum albumin (BSA) proteins on poled and unpoled KNN ceramics has been studied using the bicinchoninic acid assay.[443] Due to the isoelectric point of BSA protein being around pH 4.7 and testing was conducted around pH 7.4, protein adsorption was higher for the poled KNN samples compared to the unpoled sample. The increased protein adsorption was linked to increased MC3T3-E1 osteoblast cell proliferation on the poled samples.

Cytotoxicity: Acute cytotoxicity for KNN ceramics after 24 h has been evaluated using powder extracts and MTT assays[438,439] and pellet/film surfaces and fluorometric assays.[206,443] The former assays are quantitative and found a cell viability of ~80 % for KNN compared to the control.[438,439] The latter assays are qualitative and found low toxicity after 24 h.[206,443] Subacute cytotoxicity for KNN films after 7 days using a fluorometric assay found a 99 % viability of neuronal cells.[442]

Cell proliferation: Cell proliferation on KNN ceramics up to 7 days has been stud-

ied for several cell lines.[206,437,440,441,443,445] KNN thin films have been reported to induce similar proliferation rates of MG-63 cells to PZT films and controls after 1, 3 and 5 days.[206] Studies comparing KNN and hydroxyapatite pellets have found cell proliferation to be higher on KNN samples for human osteoblast-like cells (Saos-2 cells),[440] and higher on hydroxyapatite samples for rat mesenchymal stem cells.[441] The effect of surface polarization on proliferation rates has also been targeted for KNN ceramics, and poled KNN pellets have been reported to induce higher proliferation rates compared to unpoled KNN.[437,441,443,445] The strength of the surface polarization is also reported to be positively correlated with cell proliferation.[445] The polarization direction (positive/negative) also influence cell proliferation, and studies have found that KNN samples with a positive polarization yields higher proliferation of MC3T3-E1 osteoblast cells[443] while KNN samples with a negative polarization yields higher proliferation of rat mesenchymal stem cells.[441]

Cell adhesion and morphology: Cell adhesion and morphology of various cell lines have been studied on both dense KNN samples,[440,445] porous KNN samples[437] and KNN thin films.[206] Human osteoblast-like cells (Saos-2) have been reported to adhere and spread out equally well on KNN and hydroxyapatite samples,[440] and MG-63 cells have been reported to adhere well to KNN thin films.[206] Surface polarization is reported to affect cell morphology for both porous and dense KNN samples.[437,445] In one study, SEM images of rat osteoblast cells on poled and unpoled porous KNN samples showed more well-defined three-dimensional cell structures on the poled samples.[437] In another study, rat mesenchymal stem cells stained with fluorescent dyes had a more spread out morphology and longer pseudopodia on the poled KNN samples compared to the cells on the unpoled KNN sample.[445] The cell spreading was also dependent on the strength of the surface polarization, and the largest spreading area was observed on the sample with the strongest polarization.

In vivo assays: One study has investigated *in vivo* implantation of KNN.[206] The work studied the histological effect of implantation of KNN in rat thighs for 7 days and the performance of a KNN energy harvester prototype on a porcine heart. The study found no inflammation after 7 days of implantation in the muscular tissue around the implant in the rat models, and demonstration of energy

harvesting from the porcine heart using the KNN prototype was successful.

Antibacterial studies: Antibacterial assays have been reported for dense KNN samples.[441,445,447] In these studies, poled KNN samples with positive polarization showed significant antibacterial properties towards *Staphylococcus aureus* and *Escherichia coli*. A positive correlation between surface polarization strength and antibacterial properties was demonstrated in two of the studies.[445,447] The antibacterial properties were linked with formation of reactive oxygen species (ROS) on the surfaces of the samples.[441,445,447]

3

Materials and methods

3.1 Synthesis

3.1.1 Preparation of solutions

A complete list of the chemicals used to prepare the precursor solutions is presented in Table 3.1.

Table 3.1: List of chemicals used in the preparation of the precursor solutions.

Chemical name	**Chemical formula**	**Purity [%]**	**Supplier**
Ammonium niobate (V) oxalate hydrate (NAmOx)	$NH_4NbO(C_2O_4)_2{\cdot}xH_2O$	99.99	Sigma-Aldrich, St. Louis, MO, USA
Aq. ammonia solution	NH_4OH (aq)	25	VWR Chemicals, Radnor, PA, USA
Aq. ammonia solution	NH_4OH (aq)	30	Sigma-Aldrich
Barium nitrate	$Ba(NO_3)_2$	99.9	Sigma-Aldrich
Calsium nitrate hydrate	$Ca(NO_3)_2{\cdot}4H_2O$	99	Sigma-Aldrich
Citric acid (CA)	$C_6H_8O_7$	99.5	Sigma-Aldrich
DL-malic acid (MA)	$C_4H_6O_5$	99	Sigma-Aldrich
Ethylenediaminetetra-acetic acid (EDTA)	$C_{10}H_{16}N_2O_8$	98	Sigma-Aldrich
Potassium nitrate	KNO_3	99	Alfa Aesar, Haverhill, MA, USA
Sodium nitrate	$NaNO_3$	99	Sigma-Aldrich
Ti-isopropoxide	$Ti[OCH(CH_3)_2]_4$	97	Sigma-Aldrich
Zinc oxide	ZnO	99	Sigma-Aldrich

KNN precursor solutions

Oxalic acid-complexed solution (KNN-Ox)

The oxalic acid-complexed solutions, hereafter referred to as KNN-Ox, were prepared based on the synthesis reported by Pham and coworkers.[64] A flow diagram of the route is given in Figure 3.1. $NH_4NbO(C_2O_4)_2{\cdot}xH_2O$ was dissolved in deionized water for 16 h at 80 °C. The niobium concentration of the solutions was determined by thermogravimetric standardization at 1100 °C. Pre-dried $NaNO_3$ and KNO_3 were added to the niobium solutions with a 5 mol% excess of alkali metals, and the solutions were stirred for 2 h at 70 °C. The niobium concentrations of the final solutions were typically ~0.25 M.

Malic acid-complexed solution (KNN-MA)

The malic acid-complexed solutions, hereafter referred to as KNN-MA, were prepared based on the synthesis reported by Madaro.[124] A flow diagram of the route is given in Figure 3.1. $NH_4NbO(C_2O_4)_2{\cdot}xH_2O$ was dissolved in deionized water for 4 h at 70 °C, followed by precipitation of niobic acid by adjusting the pH to ~11 by addition of ammonia (25 %). The solutions was stirred for 2 h at 80 °C and then aged at room temperature for 12 h. The precipitated niobic acid was washed three times with ammonia (1 %), and then dissolved in an aqueous solution of DL-malic acid with a molar ratio corresponding to 1:2 (Nb:malic acid). The pH was adjusted to ~7-8 by addition of ammonia (25 %), and the solutions were stirred for 2-12 h at 70 °C. The niobium concentration of the solutions was determined by thermogravimetric standardization at 1100 °C. Finally, pre-dried $NaNO_3$ and KNO_3 were added to the solutions with a 5 mol% excess of Na^+ and K^+, and the solutions were stirred for 1 h at 50 °C. The niobium concentrations of the final solutions were typically ~0.1 M.

Doping with Ca^{2+} and $CaTiO_3$

KNN solutions with 0.5 mol% Ca^{2+} doping and 0.5 mol% $CaTiO_3$ doping, hereafter referred to as KNN-Ca^{2+} and KNN-$CaTiO_3$ respectively, were prepared by adding aqueous solutions of calcium and titanium to KNN-MA solutions. To prepare the calcium solution, $Ca(NO_3)_2{\cdot}4H_2O$ was dissolved in an aqueous solution of ethylenediaminetetraacetic acid (EDTA) with a molar ratio corresponding to 1:2 (Ca:EDTA). The solution was stirred for 1 h at 60 °C and the pH was adjusted

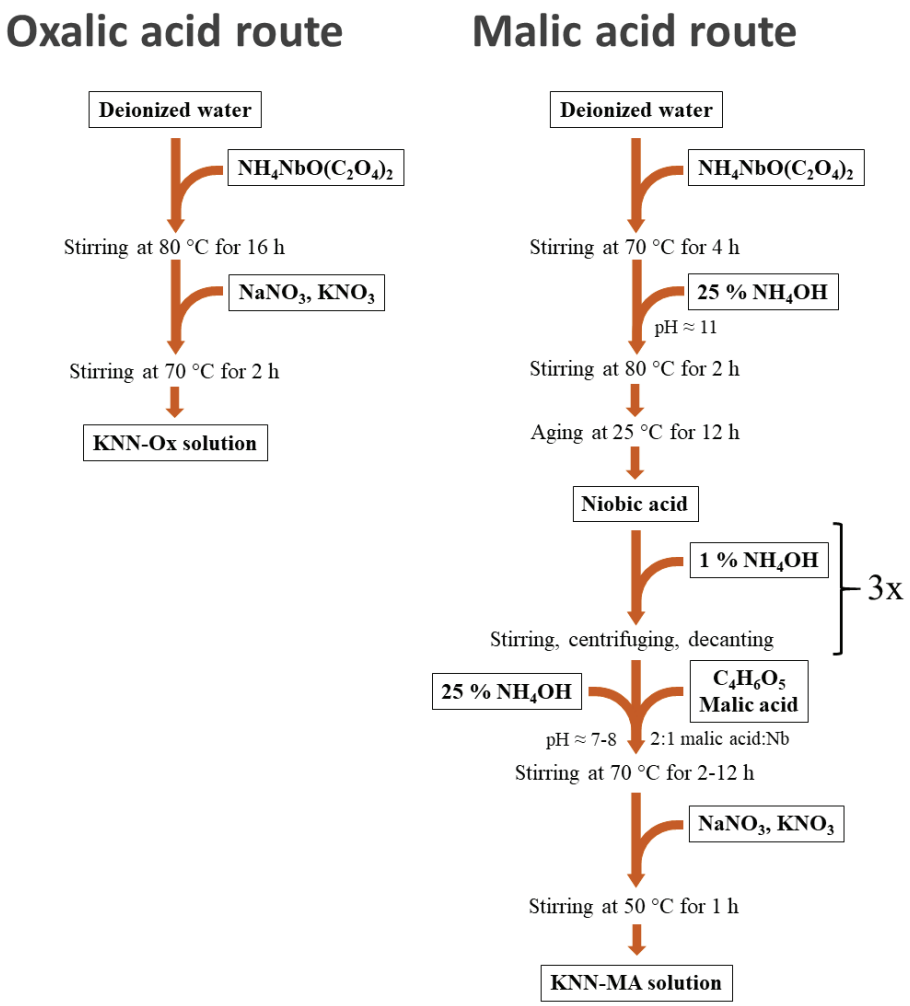

Figure 3.1: Float diagram of the oxalic acid route (left) and malic acid route (right) to aqueous KNN solutions.

to ~8 by addition of ammonia (25 %). The concentration of the calcium solution was $3.23 \cdot 10^{-2}$ M, determined by thermogravimetric analysis by measuring re-

maining weigh after heat treatment at 800 °C. To prepare the titanium solution, Ti-isopropoxide was added to an aqueous solution of citric acid (CA) with a molar ratio corresponding to 1:3 (Ti:CA). The solution was stirred for 12 h at 80 °C and the pH was adjusted to ~7 by addition of ammonia (30 %). The concentration of the titanium solution was $7.52 \cdot 10^{-1}$ M, determined by thermogravimetric analysis at 1000 °C.

ZnO precursor solutions

ZnO solutions were prepared by dissolving ZnO in an aqueous solution of citric acid (CA) with a molar ratio corresponding to 1:1 (Zn:CA). The pH was adjusted until the solutions became transparent (~9) by addition of ammonia (25 %) at 70 °C. The concentration of the ZnO solutions were typically ~0.28 M, determined by the final volume of the solution.

$BaTiO_3$ (BT) precursor solution

The BT precursors solution was prepared based on the synthesis reported by Ræder and coworkers,[448] where aqueous solutions of barium and titanium were mixed in stoichiometric amount corresponding to $BaTiO_3$. The titanium solution was prepared by the method described previously in the section on doping of KNN solutions (page 94). To prepare the barium solution, EDTA was dissolved in deionized water at 60 °C and the pH of the solution was adjusted to ~7 by addition of ammonia (30 %). Pre-dried $Ba(NO_3)_2$ was dissolved in the EDTA solution, and CA was added to the solution as a secondary complexing agent. The pH was then readjusted to ~7 by addition of ammonia (30 %). The molar ratio of Ba^{2+} to complexing agents was 1:1:2 (Ba:EDTA:CA). The concentration of the BT solution was 0.13 M.

3.1.2 Preparation of films

Fabrication of thin films was achieved by spin coating of the aqueous precursor solutions, as illustrated in Figure 2.15 on page 46. The thicknesses of the films were engineered by repeating the deposition and heat treatment steps from 2 to 30 times. An overview of all the films prepared is presented in Table 3.2.

Table 3.2: List of films prepared in this thesis.

Work	**Film(s)**	**Precursor solution(s)**	**Dopants**	**Substrate(s)**	**Furnace**
Paper I	KNN	KNN-Ox, KNN-MA	*Undoped*	(100) $SrTiO_3$	RTP-1, RTP-2
Paper II	KNN, KNN-Ca^{2+}, KNN-$CaTiO_3$	KNN-MA	*Undoped*, 0.5 mol% Ca^{2+}, 0.5 mol% $CaTiO_3$	SiPt	RTP-2
Manuscript I	ZnO, KNN/ZnO, BT/ZnO, KNN/BT/ZnO, KNN (flex)	ZnO, BT, KNN-MA	*Undoped*	SiPt, PDMS	RTP-3
Manuscript II	KNN, KNN-$CaTiO_3$	KNN-MA	*Undoped*, 0.5 mol% $CaTiO_3$	SiPt	RTP-3

Substrates and supports

The different types of substrates used for thin film fabrication is presented in Table 3.3. The elastomer for the flexible polydimethylsiloxane (PDMS) support is included in the table. Prior to deposition the SiPt substrates were sonicated in isopropanol and rinsed with acetone, and both the SiPt and $SrTiO_3$-based substrates were cleaned with oxygen plasma (Femto, Diener Electronic, Ebhausen, Germany).

Table 3.3: List of substrates and supports used in the thin film preparation.

Substrate	Dimensions	Supplier
(100) $SrTiO_3$, STO	10x10x0.5 mm^3	Crystal-GmbH, Berlin, Germany
100 nmPt(111)/30 nmTiO_x/ 500 nmSiO_2/Si(100), SiPt	10x10x0.7 mm^3	SINTEF MiNaLab, Oslo, Norway
Sylgard 184 silicone elastomer, PDMS	N/A	Dow Europe GmbH, Horgen, Switzerland

Deposition of solutions

Droplets of the solutions were transferred to the substrates using a filtered syringe (0.2 µm cellulose acetate membrane) and a thin layer of the solution was deposited on the substrates by using a spin coater (WS-400A-6NPP/C-1 or WS-400B-6NPP-LITE/AS, Laurell Technologies, Montgomery, PA, USA) operating at 3500 rpm for 40 s. Prior to heat treatment the deposited films were dried on a hotplate at 200 °C for 3 min.

Heat treatment

The deposited films were subjected to pyrolysis and annealing in rapid thermal processing (RTP) furnaces. Three different furnaces (RTP-1, RTP-2, RTP-3) were used, see Table 3.4. RTP-1 and RTP-2 were used in Paper I, RTP-2 was used in Paper II, and RTP-3 was used in Manuscript I and Manuscript II.

Table 3.4: List of RTP furnaces used for thin film preparation.

RTP furnace	Model name	Atmosphere	Supplier
RTP-1	Jetfirst 200 mm (radiation furnace)	Flowing O_2	Jipelec, Semco Technologies, Montpellier, France
RTP-2	Rapid heating plate	Ambient (air)	Custom made, described in [449]
RTP-3	AccuThermo AW610 (desktop radiation furnace)	Flowing synthetic air (80 %/20 % of N_2/O_2)	Allwin21, Morgan Hill, CA, USA

The heating programs for the different films are displayed in Figure 3.2. For the KNN films in Paper I and II and Manuscript I and II and ZnO films in Manuscript I a two-step heating program was used, involving pyrolysis for each deposited layer (550 °C, 5 min) and a final annealing after all the depositions were completed (700 °C, 10 min), using a heating and cooling rate of 100 °C min^{-1} (Figure 3.2 (a)). For the BT films in Manuscript I a one-step heating program with both pyrolysis and annealing was used for each deposited layer (Figure 3.2 (b)). The BT heating program involved heating to 455 °C using a heating rate of 90 °C min^{-1}, then heating to 588 °C using a heating rate of 40 °C min^{-1}, and then to 710 °C using a heating rate of 300 °C min^{-1}. 710 °C was held for 5 min, before cooling back to room temperature using a cooling rate of 100 °C min^{-1}.

Lift-off technique for flexible films

The lift-off technique was performed by depositing a ZnO release layer and a KNN film on a SiPt substrate by conventional CSD, based on the method reported by Liu and coworkers.[65] A schematic of the synthesis process to flexible KNN films is presented in Figure 3.3. The deposition of the ZnO release layer, the BT buffer layer and the KNN films (step I and II in Figure 3.3) was performed using aqueous CSD.

Before deposition of the flexible polymer support (step III in Figure 3.3), the KNN

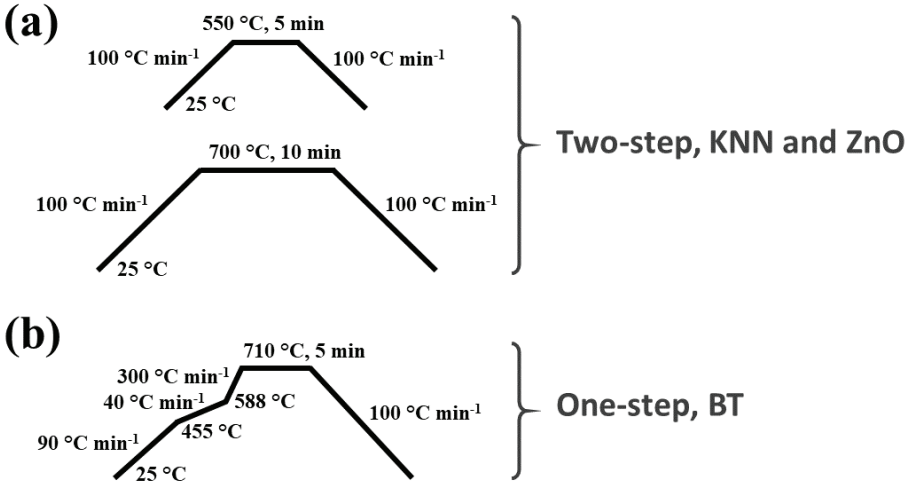

Figure 3.2: (a) Two-step heating program (pyrolysis and annealing in separate steps) for KNN and ZnO films. (b) One-step heating program (pyrolysis and annealing in same step) for BT films.

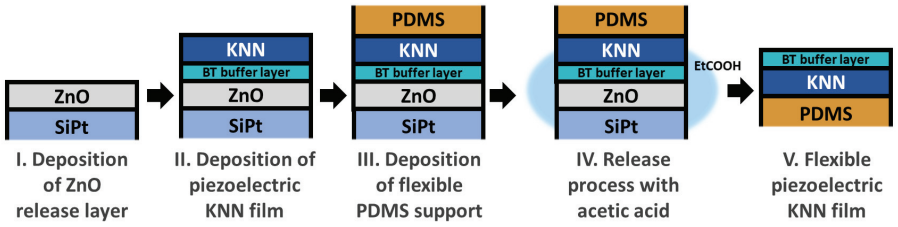

Figure 3.3: Synthesis process of flexible KNN films. Step I and II: High-temperature CSD processing of ZnO release layer, BT buffer layer and KNN film. Step III: Deopisition of flexible PDMS support. Step IV: Release of KNN-PDMS composite by dissolving the ZnO layer in acetic acid.

film was cleaned with oxygen plasma for 2 min. A PDMS elastomer solution was made by mixing 1 part curing agent and 5 parts base. The elastomer solution was degassed for 40 min in a vacuum desiccator prior to deposition. ~0.5 mL of degassed elastomer solution was added to the KNN-ZnO sample and deposited

onto the KNN film using a spin coater operating at 500 rpm for 30 s. The elastomer solution was then cured for 7 d at room temperature. After curing, excess PDMS along the edges of the sample was removed using a scalpel. The sample was immersed in an aqueous solution of 33 vol% acetic acid (100 %, Merck KGaA, Darmstadt, Germany) preheated to 60 °C (step IV in Figure 3.3), and kept in the acidic solution until the ZnO layer was dissolved (1-3 h). After release, the free-standing KNN film was rinsed in deionized water.

3.1.3 Preparation of powders

Powders were prepared from the solutions by first drying the precursor solutions in a sol-gel furnace (Carbolite Gero, Nabertherm, Lilienthal, Germany) for 8-24 h at 100-200 °C. The dried powders where then crushed in a mortar and calcined in a muffle furnace (T 15/12/P330, Nabertherm, Lilienthal, Germany), using a heating rate of 200 °C h^{-1}. The temperature and hold time of the calcinations were varied depending on the type of the subsequent characterization.

3.2 Characterization

3.2.1 Thin film characterization

X-ray diffraction

X-ray diffraction (XRD) patters of thin films were recorded using two different setups. Gracing incidence X-ray diffraction (GIXRD) patterns were recorded using a 2° incidence angle and Cu Kα radiation (D8 Advance, Bruker, Billerica, MA, USA). Conventional Bragg-Brentano X-ray diffraction (θ-2θ XRD) patterns were recorded parallel to the (100) direction of the substrates using monochromatic Cu Kα radiation (D5005, Siemens, Karlsruhe, Germany).

Scanning electron microscopy

Scanning electron microscopy (SEM) of thin films was performed using an acceleration voltage of 10 kV and an in-lens detector (Ultra 55, Carl Zeiss AG, Oberkochen, Germany). For cross sectional images the films were cleaved using a combined diamond tip scriber and impulse breaker apparatus (DXIII, Dynatex, Santa Rosa, CA, USA).

Transmission electron microscopy

Transmission electron microscopy (TEM) of thin films was performed in both bright field imaging (BFI) and high resolution (HR) mode, using an acceleration voltage of 200 kV (JEM-2100 and JEM-2100F, Jeol, Tokyo, Japan). Fast Fourier transform (FFT) algorithms were applied to selected areas in the HR-TEM micrographs to analyze the local crystal structure close to the interface of the films and substrates. Scanning precession electron diffraction (SPED) was used to obtain crystal orientation maps of the samples, and structural misorientation of the films relative to the substrates was calculated from the recorded precession electron diffraction (PED) data. Acquisition and template matching of the PED patterns were performed using TEM orientation imaging hardware and software (ASTAR, NanoMEGAS, Brussels, Belgium). A pseudo-cubic crystal structure for KNN was used as template for the PED pattern matching, see Table 3.5. Prepa-

ration of TEM samples was performed by using a focused ion beam (FIB) system and a standard lift-out technique (Helios Nanolab DualBeam, FEI Company, Hillsboro, OR, USA).

Table 3.5: Atomic positions and unit cell parameters of the pseudo-cubic crystal structure of KNN used as template in the PED pattern matching.

Element	***x***	***y***	***z***	**Occ.**
K	0.0	0.0	0.0	0.5
Na	0.0	0.0	0.0	0.5
Nb	0.5	0.5	0.5	1.0
O	0.0	0.5	0.5	1.0
Unit cell lengths:	$a = b = c = 3.983\,\text{Å}$			
Unit cell angles:	$\alpha = \beta = \gamma = 90°$			

Infrared spectroscopy

Infrared (IR) spectroscopy of thin films was performed using a diffuse reflection cell (Praying Mantis, Harrick Scientific, Ossining, NY, USA) and a Fourier transform infrared (FTIR) spectrometer (VERTEX 80v, Bruker). An aperture of 8 mm and a resolution of $4\,\text{cm}^{-1}$ was used. Substrates with no deposited films were used as backgrounds.

Atomic force microscopy

Atomic force microscopy (AFM) was used to study surface topography of thin films (Multimode V, Veeco Metrology, Plainview, NY, USA). Surface roughness of the films was calculated based on measurements of areas of 5x5 μm^2 at the center and edges of the films.

Contact angle measurements

The contact angle of droplets of deionized water on thin films were measured at 37 °C to assess surface hydrofobocity (DSA100, KRÜSS, Hamburg, Germany).

Electrical characterization

Deposition of electrodes
Deposition of interdigitated electrodes (IDE) was performed through a lift-off process using a negative UV-photoresist (ma-N 400 series, Micro Resist Technology, Berlin, Germany) and a maskless aligner (MLA 150, Heidelberg Instruments, Heidelberg, Germany). E-beam evaporation was used to deposit a 5 nm titanium bonding layer and 20 nm platinum electrodes (Custom ATC-2200V, AJA International Inc., Scituate, MA, USA). 100 electrode fingers with length of 900 µm, width of 3.311 µm and distance of 6.689 µm were deposited.

Deposition of regular 100 nm thick platinum top and bottom electrodes was performed using a shadow mask and e-beam evaporation (Custom ATC-2200V, AJA International Inc.). Prior to deposition the films were cleaned with oxygen plasma for 2 min (Femto, Diener Electronic). The diameters of the circular top electrodes were 0.5 and 1.0 mm. After deposition the films with the electrodes were annealed in flowing O_2 at 400 °C for 2.5 h (AccuThermo AW610, Allwin21).

Polarization and capacitance versus electric field
A piezoelectric evaluation system was used to measure polarization and capacitance as a function of electric field at room temperature (aixPES, aixACCT, Aachen, Germany). Polarization versus electric field (P-E) was measured using frequencies from 0.1 to 5000 Hz. Capacitance versus electric field (C-E) was measured at 500 Hz using AC amplitudes of 50 mV.

Permittivity versus temperature and frequency
Impedance spectroscopy was performed on the films using a rapid heating plate (RTP-2) to measure dielectric permittivity in the temperature range 150 to 420 °C and the frequency range of 1 to 10^6 Hz (Alpha-A High Performance Frequency Analyzer, Novocontrol Technologies, Montabaur, Germany). Measurements were performed using AC amplitudes of 50 mV.

3.2.2 Powder characterization

X-ray powder diffraction

X-ray powder diffraction patterns were recorded Cu Kα radiation (D8 Advance, Bruker). Curve fitting using the Pawley method was performed on the diffraction patterns. The patterns were fitted to a monoclinic space group (Pm) with starting lattice parameters $a = c = 4.000\,\text{Å}$, $b = 3.950\,\text{Å}$ and $\beta = 90.33°$.

Infrared spectroscopy

IR spectroscopy was performed using a diamond attenuated total reflection cell (Platinum ATR, Bruker) and a FTIR spectrometer (VERTEX 80v, Bruker). An aperture of 5 mm and a resolution of $4\,\text{cm}^{-1}$ was used.

Thermogravimetric analysis and mass spectroscopy

Thermogravimetric analysis (TGA) was used to analyze the thermal decomposition of the dried precursor solutions (STA 449C, Netzsch, Selb, Germany). A mass spectrometer was used in combination with the TGA measurements (QMS 403C, Netzsch). The measurements were performed with flowing O_2 and synthetic air in the temperature range 100 to 725 °C using a heating rate of $10\,°\text{C}\,\text{min}^{-1}$.

3.3 *In vitro* studies

3.3.1 Cell culturing

Human 161BR fibroblast cells, rat Schwann cells and human SH-SY5Y neuroblastoma cells were cultured in 3 mL media in T25 flasks at 37 °C and 5 % CO_2 until confluent. The media used for the different cell lines were as following:

- **161BR fibroblast cells**: Eagle's MEM with 15 % fetal bovine serum (FBS), 2 mM L-Glutamine, 1 % non-essential amino acids (NEAA) and 1 % Penicillin Streptomycin (Pen-Strep).
- **Rat Schwann cells**: Ham's F12 with 10 % FBS, 2 mM L-Glutamine and 1 % Pen-Strep.
- **SH-SY5Y neuroblastoma cells**: Ham's F12/Dulbecco's MEM (1:1) with 10 % FBS, 1 % sodium pyruvate, 1 % 1 M HEPES, 1 % NEAA, 1 % sodium bicarbonate, 1 % Pen-Strep.

All media and components were purchased from Sigma-Aldrich (Seven Hills, NSW, Australia). The media was changed every 3 days. When confluent, the cells were lifted from the T25 flask using 0.025 % trypsin (in 1xPBS no calcium, no magnesium) and seeded onto 13 mm diameter glass coverslips (control; Hurst Scientific, WA, Australia), SiPt, KNN/SiPt and KNN-$CaTiO_3$/SiPt in a 24-well plate along with 500 µL media. Three samples were used for each material and control.

3.3.2 Sample sterilization

Three types of samples were used in the in vitro studies; undoped KNN films (~50 nm) on SiPt substrates (KNN/SiPt), KNN films co-doped with 0.5 mol% Ca^{2+} and Ti^{4+} (~50 nm) on SiPt substrates (KNN-$CaTiO_3$/SiPt), and SiPt substrates without deposited films. The samples were sterilized using 25 kGy of gamma irradiation from a cobalt-60 source. The glass control samples were sterilized by dipping in ethanol and flaming over a Bunsen burner. All the samples and

control samples were rinsed once with 1X phosphate buffered saline (PBS, Sigma-Aldrich) before cell seeding.

3.3.3 *In vitro* assays

MTT proliferation assays

Cell proliferation of 161BR fibroblast and Schwann cells was assessed using MTT colorimetric assays. The cells were grown for up to 7 days in media at 37 celsius and 5 % CO_2, and the media was changed every 2 days after seeding. MTT colorimetric assays were performed on the cells after 1, 3, 5 and 7 days of culturing. The colorimetric assays were performed by first removing the culture media and then adding 50 µL of an MTT solution (5 gL^{-1} MTT (VWR/Amresco) in 1X PBS) and 450 µL of serum-free Eagle's MEM (161BR fibroblast cells) or serum-free Ham's F12 medium (Schwann cells) to the wells. After incubating the cells for 4 h at 37 °C and 5 % CO_2, the MTT solution was carefully removed and the formed formazan crystals were dissolved in isopropanol with 4 mM HCl and 0.1 % Nonidet P-40 (VWR/Amresco) using a mixer for 10 min. The isopropanol with the dissolved formazan was then transferred to a 96-well plate for spectrophotometric analysis at λ = 560 nm (Chameleon Multilabel, Hidex, Turku, Finland). The one-way ANOVA analysis method was used to determine the statistical significance of the data.

Morphology assays

Cell morphology of 161BR fibroblast cells, Schwann cells and SH-SY5Y cells was studied using SEM. The cells were grown for 3-5 days in media at 37 °C and 5 % CO_2, after which the cells were washed twice with 500 µL 1X PBS and fixed with 300 µL glutaraldehyde (3 % in 1X PBS, Sigma-Aldrich), both preheated to 37 °C. The well plate was then placed in zip lock bag to prevent loss of glutaraldehyde through evaporation and stored at 4 °C for 20 h. The glutaraldehyde was then removed, and the cells were washed twice with 300 µL 1X PBS at 4 °C for 10 min. The cells were hydrated twice with deionized water for 10 min prior to the dehydration procedure. To gradually dehydrate the cells, ethanol-water washes with an increasing concentration of ethanol were used. The concentrations used were

30, 50, 70, 80, 90 and 100 vol% ethanol. Each washed was performed for 12 min, and the 100 vol% ethanol wash was performed twice. The cells were then left for the ethanol to evaporate over a period of 24 h. SEM of the dehydrated cells was performed using an acceleration voltage of 5 kV and mixed detection of backscatter and secondary electrons (TM3030Plus, Hitachi, Tokyo, Japan).

Immunofluorescence microscopy

Cell viability of 161BR fibroblast and Schwann cells was studied using immunofluorescent microscopy. The cells were grown in media at 37 °C and 5 % CO_2 until ~90 % confluency (3-5 days), after which the cells were washed twice with 600 µL 1X PBS and fixed with 300 µL paraformaldehyde (4 % in 1X PBS, Sigma-Aldrich), both preheated to 37 °C. The well plate was then placed in a zip lock bag to prevent loss of paraformaldehyde through evaporation and incubated at 37 °C for 10 min. The paraformaldehyde was then removed, and the cells were washed three times with 300 µL 1X PBS. To allow for antibody penetration into the cells, the cells were permeabilized with 300 µL Triton X-100 in 1X PBS (0.1 %) for 15 min at room temperature. After, the cells were washed three times with 300 µL 1X PBS. To prevent non-specific antibody-protein interaction, the cells were blocked using 300 µL bovine serum albumin (BSA) in 1X PBS (1 %) for 60 min at room temperature. The cell cytoskeletons were immunostained with 300 µL monoclonal β-Tubulin primary antibody (1:5000 dilution in PBS, Sigma-Aldrich) for 16 h at 4 °C. The primary antibody was removed, and the cells were washed three times with 300 µL 1X PBS. To detect the β-Tubulin primary antibodies 300 µL of Alexa Fluor® 488-conjugated rabbit anti-mouse IgG (H+L) secondary antibody (1:5000 dilution in PBS, Life Technologies) was added and left in for 45 min in room temperature and away from light. After, the cells were washed once with 300 µL 1X PBS. The cell nuclei were immunostained with 50 µL 4',6-diamidino-2-phenylindole (DAPI, 0.1 g L^{-1} PBS, Sigma-Aldrich) for 3 min at room temperature. The cells were then washed twice with 300 µL 1X PBS, and the samples were mounted on glass coverslips using dibutyl phthalate in xylene (DPX). The immunostained cells were imaged using confocal microscopy (LSM800, Zeiss).

4

Summary of results

This chapter gives a summary of the main results from the PhD work. The chapter is divided into five sections. Sections 4.1-4.4 are each dedicated to the main findings of one of the four papers and manuscripts included in the dissertation. In the last section (Section 4.5) the thesis is summarized combined with a brief outlook.

4.1 Aqueous processing of KNN films (Paper I)

4.1.1 Precursor chemistry, decomposition and phase purity

The first objective of the project was to develop a synthesis platform to KNN thin films based on aqueous CSD. Two water-based chemical solutions, an oxalic acid-complexed solution (KNN-Ox) and a malic acid-complexed solution (KNN-MA), were chosen based on previous work on these precursor solutions.[64,124,450] The preparation of these solutions is described in Section 3.1.1 on page 94.

XRD patterns of dried powders from the KNN-Ox and KNN-MA precursor solutions calcined at various temperatures are presented in Figure 4.1, The data demonstrate that phase pure KNN powder can be synthesized from both precursor solutions by thermal treatment at 700 °C. This is in accordance with previous reports on these solutions.[124,450] The XRD patterns also show that dried powders from the KNN-Ox solution start crystallizing at a lower temperature (~450 °C) than powders from the KNN-MA solution (~500 °C). Furthermore, a parasitic alkali metal deficient phase, $K_4Nb_6O_{17}$, crystallized together with the perovskite phase in the KNN-Ox powder at 450 °C. This phase was not present in KNN-Ox powders calcined at 500 °C or above, and it was not observed in any of the KNN-MA powders.

The two solutions were further used to prepare films described by the procedure given in Section 3.1.2 on page 96. GIXRD patterns of pyrolyzed (500 °C) and annealed (700 °C) KNN thin films deposited on (100) single crystal STO substrates from the two precursor solutions are presented in Figure 4.2. The diffraction patterns of the films demonstrate the presence of KNN, but the diffraction pat-

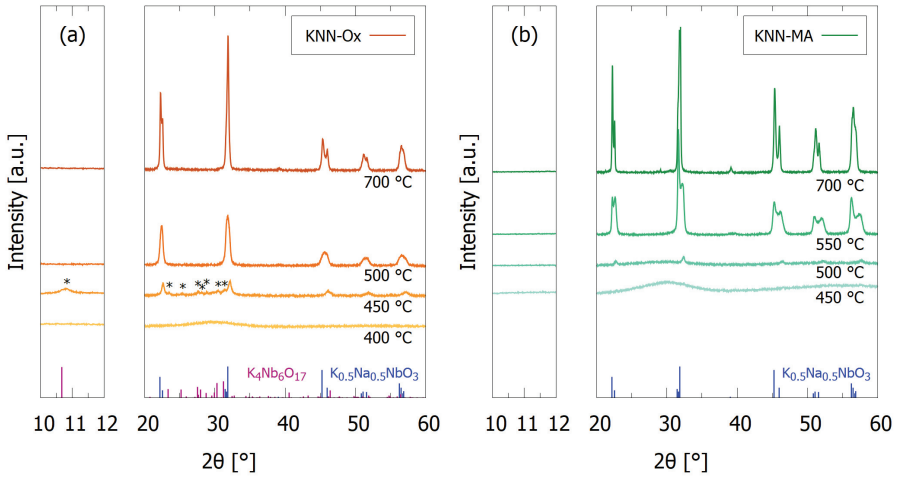

Figure 4.1: XRD patterns of powders from the (a) KNN-Ox and (b) KNN-MA solutions calcined at various temperatures. Reflections from the $K_4Nb_6O_{17}$ phase are indicated with *. Reference patterns for $K_{0.5}Na_{0.5}NbO_3$ (blue, PDF card 00-061-0315)[118] and $K_4Nb_6O_{17}$ (purple, PDF card 04-009-6408)[451] are included.

terns of the films prepared by the KNN-Ox precursor solution contained also reflections due to the presence of the alkali metal deficient phases ($K_4Nb_6O_{17}$, $K_2Nb_4O_{11}$). The presence of secondary phases in films derived from the KNN-Ox solutions is in line with previous work.[64] The films made from the KNN-MA precursor solution were phase pure when processed in air (Figure 4.2 (d)), while they contained secondary phases when processed in O_2 (Figure 4.2 (b)). The GIXRD results suggest that it is impossible to remove alkali metal deficient phases from the films once they are formed, opposite of what was observed for calcined powders from the KNN-Ox solution. This is probably due to a higher loss of alkali metals through evaporation during thermal processing of the films compared to powders, leading to an irreversible change in the overall cation stoichiometry in the film.

The phase compositions of calcined powders and thin films from the KNN-Ox and KNN-MA precursor solutions were demonstrated to be governed by the ther-

mal decomposition of the carbon and nitrogen containing amorphous network in the precursors upon calcination/pyrolysis. Thermal analysis of the dried powder from the KNN-MA solution revealed a delayed decomposition compared to powders from the KNN-Ox solution, as shown by the TGA-MS data in Figure 4.3. Combined with the XRD patterns in Figures 4.1 and 4.2, the presence of carbon containing residues around 450-550 °C in the KNN-MA precursor was shown to suppress the nucleation of $K_4Nb_6O_{17}$ and to shift the nucleation temperature of the perovskite phase upwards compared to the KNN-Ox precursor. It was demonstrated that an increase in the partial pressure of oxygen promotes an earlier decomposition of the residues in the KNN-MA precursor around 500 °C, leading to the formation of parasitic phases also in the films made from that precursor solution in O_2 (Figure 4.2 (b)). These combined results demonstrate that the nucleation kinetics and thereby the phase composition can be controlled by thermal processing of the KNN films including both temperature-time profile and atmosphere.

4.1.2 Microstructure and texturing

Dense KNN films were prepared by spin coating using both the KNN-Ox and KNN-MA precursor solutions. The thickness of the films on the (100) STO substrates were uniform as shown in Figure 4.4. The film thickness per deposition for the KNN-MA solution was ~17 nm, inferred from the SEM micrographs in Figures 4.4.

A columnar microstructure was observed in the KNN films prepared from the KNN-MA precursor solution on the (100) STO substrate. This is shown in the TEM micrographs in Figure 4.5. The columnar grains grew throughout the thickness of the film, except for a 1-3 nm thick epitaxial layer towards the film-substrate interface. The local in-plane orientation of the columnar grains were demonstrated to have a polycrystalline symmetry based on pole figures and PED misorientation mappings (Figures 5 and A.3 in Paper I), but the average out-of-plane orientation was determined to have substantial (100) texturing, as observed by the XRD patterns in Figure 4.6. A proposed nucleation mechanism for the observed microstructure of the films is a mixed heteroepitaxial and homo-

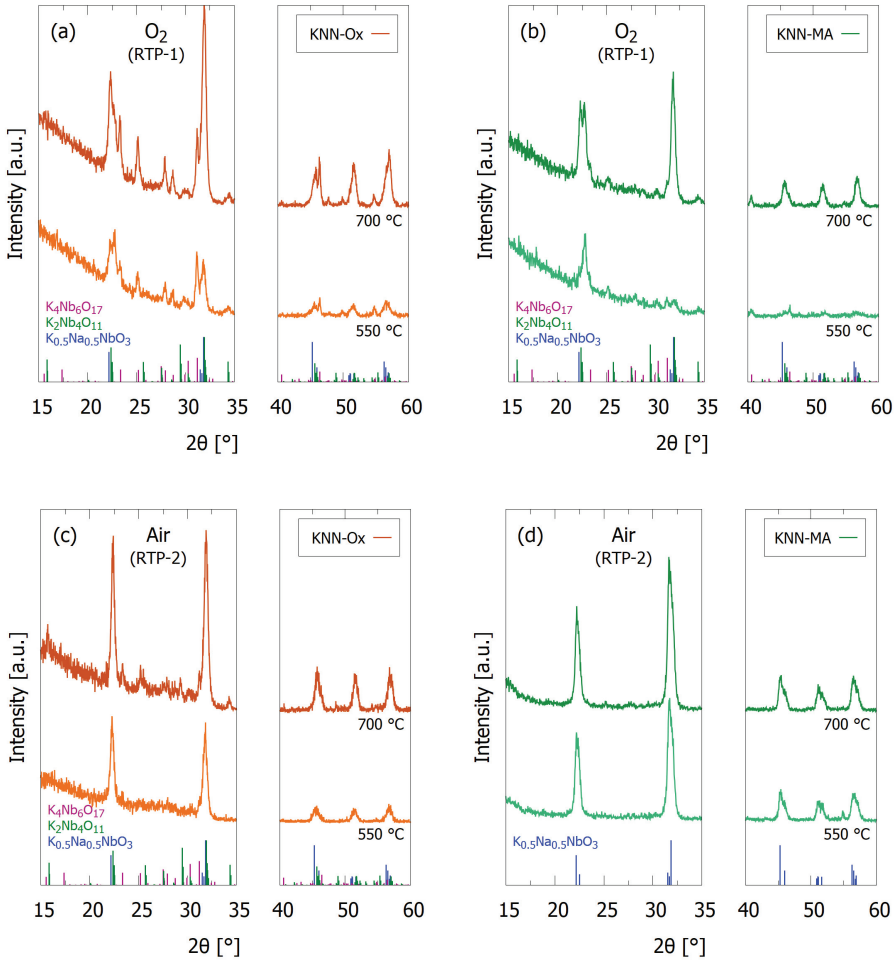

Figure 4.2: GIXRD patterns of thin films from the (a), (c) KNN-Ox and (b), (d) KNN-MA precursor solutions thermally processed in (a), (b) O_2 and (c), (d) air. Reference patterns for $K_{0.5}Na_{0.5}NbO_3$ (blue, PDF card 00-061-0315),[118] $K_2Nb_4O_{11}$ (green, pattern from)[452] and $K_4Nb_6O_{17}$ (purple, PDF card 04-009-6408)[451] are included.

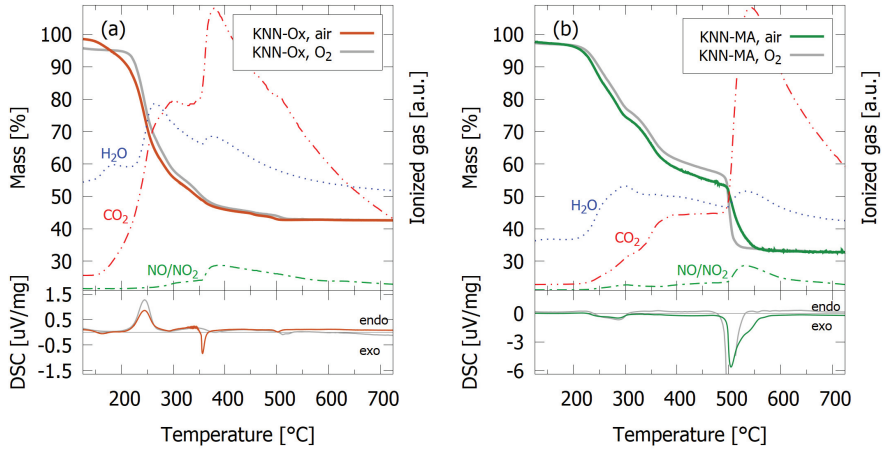

Figure 4.3: Thermogravimetric analyses with mass spectroscopy (TGA-MS) of dried powders from the (a) KNN-Ox and (b) KNN-MA solutions. Differential scanning calorimetry (DSC) curves from the measurements are included.

geneous nucleation and growth in the first deposited layer, and heterogeneous nucleation and growth in the subsequent layers.

Epitaxial growth of KNN films from CSD on STO substrates has previously been demonstrated by avoiding crystallization during pyrolysis and by the use of a high heating rate (40-50 °C s^{-1}) up to the final annealing stage.[64,249] Application of such a thermal processing program could be an interesting topic for further optimization of the fabrication of the KNN films.

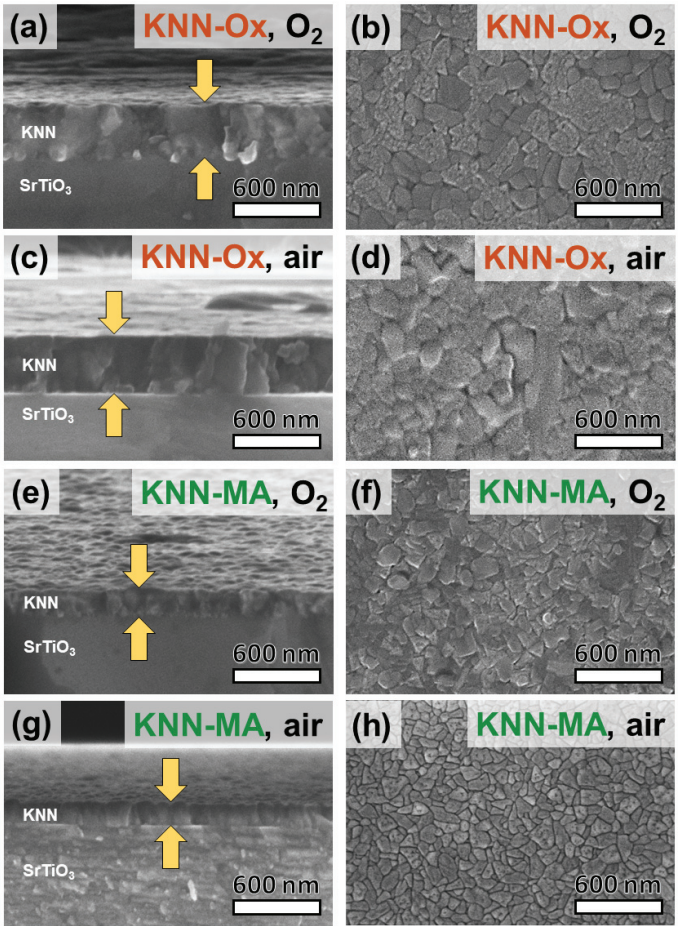

Figure 4.4: SEM micrographs of KNN films prepared from the (a)-(d) KNN-Ox and (e)-(h) KNN-MA precursor solutions.

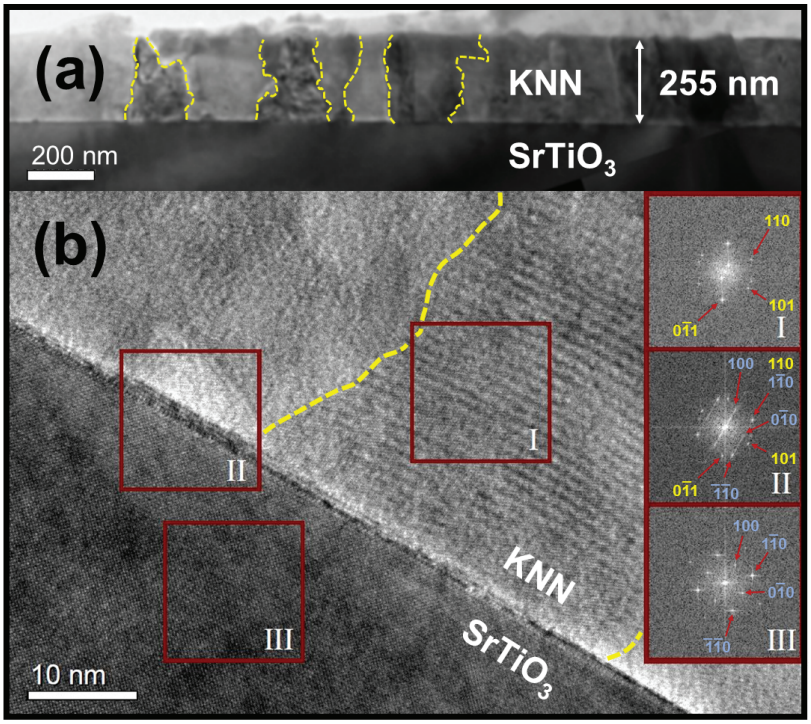

Figure 4.5: (a) Bright field imaging and (b) high-resolution TEM micrographs of a KNN film prepared from the KNN-MA solution in air on (100) STO illustrating the columnar microstructure of the films. Electron diffraction patterns from the film (I), the STO substrate (III) and the interface (II) is included. Reprinted from [453].

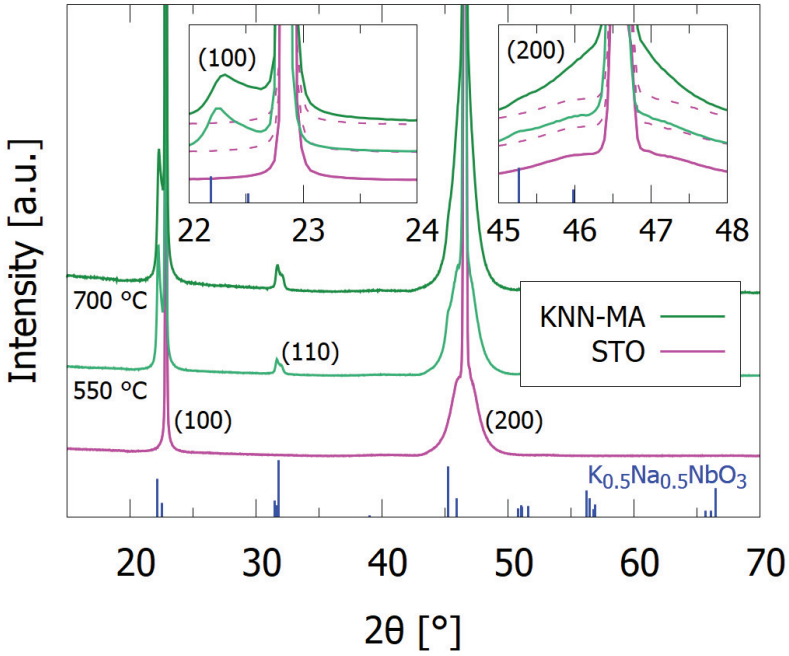

Figure 4.6: θ-2θ XRD of pyrolyzed and annealed KNN films prepared from the KNN-MA solution in air on (100) STO. Reference pattern for $K_{0.5}Na_{0.5}NbO_3$ (blue, PDF card 00-061-0315)[118] is included.

4.2 Compositional engineering and ferroelectric characterization (Paper II)

4.2.1 Introduction of dopants and silicon substrates

Based on the synthesis platform developed in Paper I, compositional engineering of KNN films was targeted with the aim of improving the stability and ferroelectric properties of the films. Two different heterovalent substitutions were investigated, namely Ca^{2+} doping and Ca^{2+}-Ti^{4+} co-doping ($CaTiO_3$ doping). The malic acid-complexed solution (KNN-MA) described in Paper I was chosen as the fundament for this work to avoid secondary phases. Platinized silicon (SiPt) was also introduced since silicon is the standard substrate in electronics industry.

Aqueous solutions corresponding to KNN with 0.5 mol% Ca^{2+} doping and 0.5 mol% $CaTiO_3$ doping were prepared by adding appropriate amounts of Ca^{2+}- and Ti^{4+}-solutions to the KNN-MA precursor solution, as described in Section 3.1.1 on page 94. XRD analysis of calcined powders from the doped precursor solutions showed no additional reflections, but minor changes in the unit cell parameters were observed, indicating that the dopants were incorporated into the KNN crystal lattice (Figures 1 and S.1 in Paper II). Only reflections from the perovskite phase were observed in the GIXRD patterns, as seen in Figure 4.7. SEM micrographs of the films, presented in Figure 4.8, demonstrate dense and uniform microstructures in all compositions. A reduction in grain size with doping can be inferred from the top-view SEM images in Figure 4.8 and the powder XRD patterns, suggesting that Ca^{2+} and Ti^{4+} reduce the cation mobility and grain growth during thermal processing. In contrast to KNN films deposited on (100) STO, which had significant (100) texturing, the KNN films deposited on SiPt were polycrystalline without crystallographic texture (Figure S.3 in Paper II). The XRD and SEM results demonstrate that both undoped and doped high-quality KNN films can be fabricated on SiPt substrates by aqueous CSD.

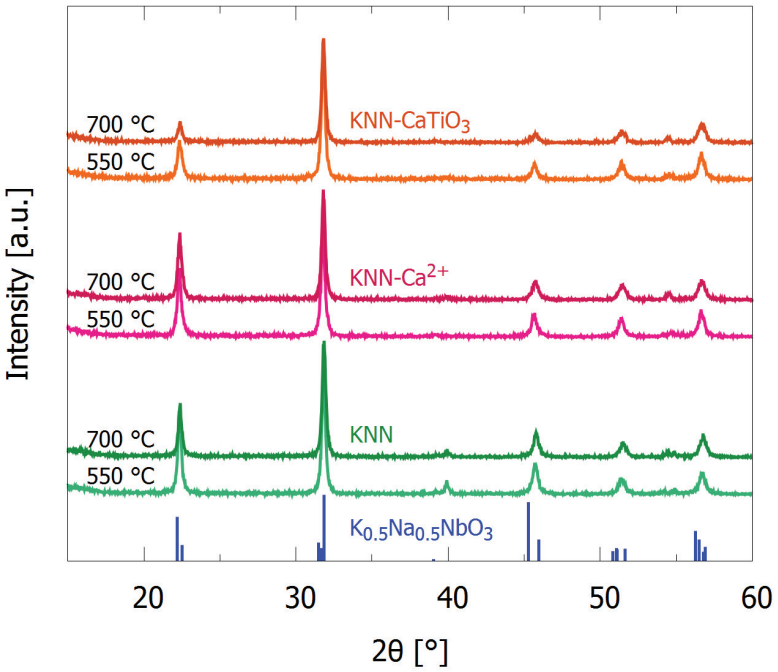

Figure 4.7: GIXRD patterns of undoped, Ca^{2+} doped and $CaTiO_3$ doped KNN thin films deposited on SiPt substrates. Reference pattern for $K_{0.5}Na_{0.5}NbO_3$ (blue, PDF card 00-061-0315)[118] is included. Figure reprinted from[454] with permission from The Royal Society of Chemistry.

4.2.2 Ferroelectric characterization

Ferroelectric characterization of the KNN films on SiPt substrates was carried out by depositing circular Pt electrodes on top of the films, as described in Section 3.2.1 on page 104. The polarization as a function of electric field for the three KNN films measured at 10 Hz and using 100 $kV\,cm^{-1}$ bias (Figure 4.9), demonstrates ferroelectric polarization switching in the doped films. This was not observed for the undoped KNN films regardless of applied frequency and field bias. The frequency dependency of P-E loops from the doped KNN films is presented

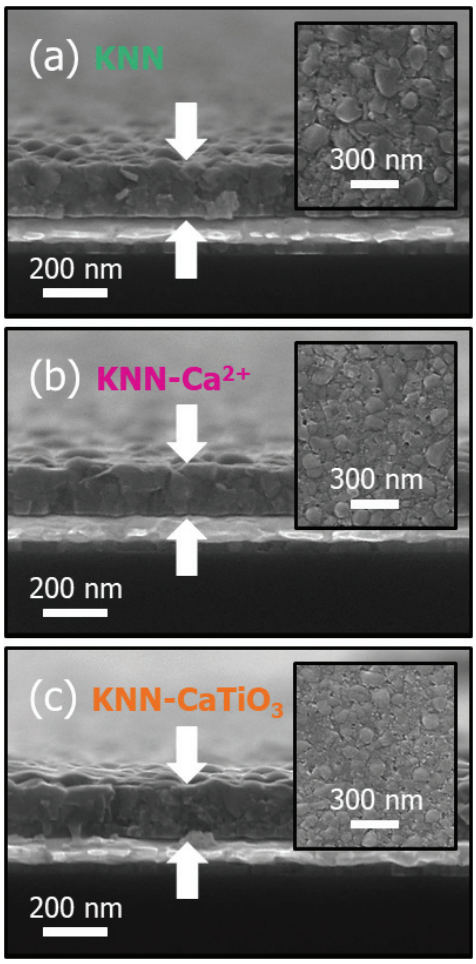

Figure 4.8: Cross-section SEM micrographs of (a) undoped, (b) Ca^{2+} doped and (c) $CaTiO_3$ doped KNN thin films deposited on SiPt substrates. The films were prepared by deposition of 15 layers. The insets show top-view images of the microstructure. Figure reprinted from [454] with permission from The Royal Society of Chemistry.

in Figure 4.10 and shows a decrease in polarization with increasing frequency. The remanent polarization measured for the KNN-$CaTiO_3$ film is comparable to

previous reports on KNN films from CSD.[211,214,219,221,235,237,242,249]

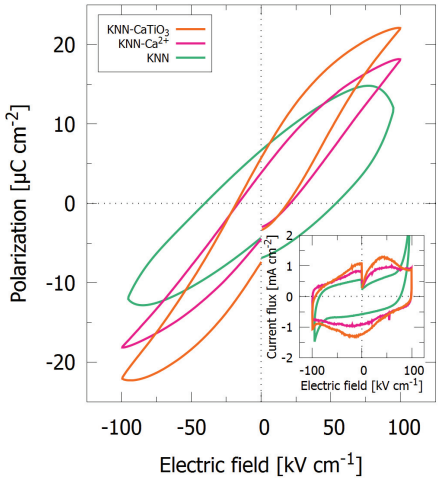

Figure 4.9: Polarization as a function of electric field for the films with the three KNN compositions, measured at 10 Hz and using 100 $kV cm^{-1}$ bias. The current fluxes during measurement is included. Figure reprinted from[454] with permission from The Royal Society of Chemistry.

Doping with Ca^{2+} and $CaTiO_3$ was also shown to influence the dielectric permittivity of the films. The permittivity of the films as a function of temperature is displayed in Figure 4.11. An increase of ~15 and ~30 °C was observed for the Ca^{2+} and $CaTiO_3$ doped films compared to undoped KNN, respectively, at 150 °C. The same increase was observed in capacitance versus electric field measurements at room temperature (Figure 6 in Paper II). The values for the dielectric permittivity presented in Figure 4.11 are among the highest reported for KNN films from CSD.[215,217,218,221,235,240,241,243,244,248,250,253,254,257,258,260] The dopants were not found to have a significant influence on the phase transitions induced from the permittivity measurements, as previously reported for KNN ceramics doped with $CaTiO_3$.[455–459]

The improved ferroelectric properties of the doped KNN films compared to the undoped films is argued to be caused by the dopants' influence on the point de-

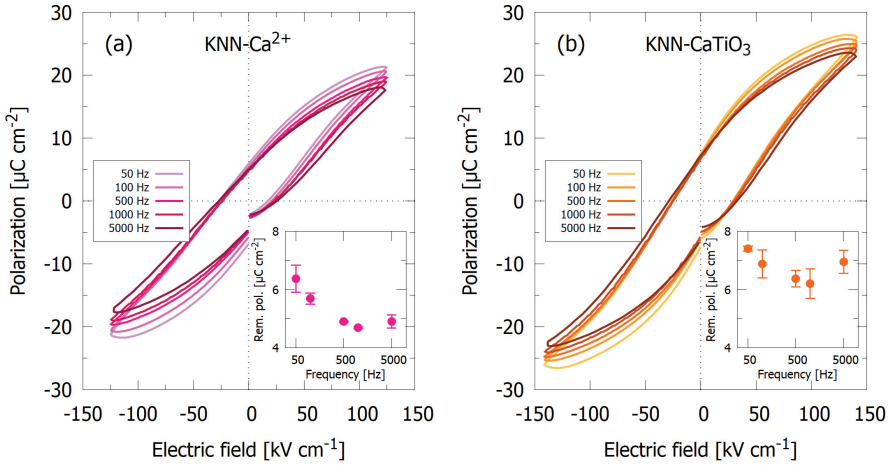

Figure 4.10: Polarization as a function of electric field for (a) Ca^{2+} doped and (b) $CaTiO_3$ doped KNN films, measured at frequencies between 50 and 5000 Hz. Measured remanent polarizations are included in the figures. Figure reprinted from[454] with permission from The Royal Society of Chemistry.

fect concentration in the films. Charged defects like oxygen vacancies have been reported to pin the ferroelectric domain walls and thereby reduce the ferroelectric response.[460,461] Co-doping with Ca^{2+} and Ti^{4+} should increase the energy of formation for lattice defects, as the formation energy of oxygen vacancies is higher in $CaTiO_3$ than in $KNbO_3$.[462,463] Based on ionic radius and charge, Ca^{2+} is expected to enter the A-site in KNN, in which case some mechanism for charge compensation must take place. Three mechanisms for incorporation of Ca^{2+} on the A-site in KNN were suggested, leading to A-site deficiency (A < B), stoichiometric A : B ratio (A = B) and A-site excess (A > B), respectively:

$$CaO(s) + 2A_A^x \rightarrow A_2O(s) + Ca_A^\bullet + V_A' \tag{4.1}$$

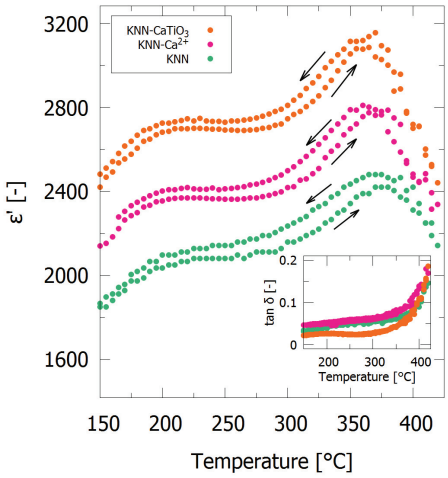

Figure 4.11: Dielectric permittivity as a function of temperature for the three KNN compositions, measured at 1 kHz between 150 and 420 °C, using a 50 mV AC amplitude. The loss tangent ($\tan\delta$) of the measurement is provided in the inset. Arrows indicate heating/cooling. Figure reprinted from [454] with permission from The Royal Society of Chemistry.

$$2\,CaO(s) + Nb_2O_5(s) + V_O^{\bullet\bullet} \rightarrow 2\,Ca_A^{\bullet} + 2\,Nb_{Nb}^{x} + 7\,O_O^{x} \tag{4.2}$$

$$CaO(s) + V_A' + V_O^{\bullet\bullet} \rightarrow Ca_A^{\bullet} + O_O^{x} \tag{4.3}$$

For low-temperature processing of KNN and when using an excess of alkali metals, both of which were the case in this work, Equations 4.2 and 4.3 are the likely mechanisms for Ca^{2+} incorporation. These mechanisms reduce the amount of oxygen vacancies and could therefore explain the improved ferroelectric properties in the Ca^{2+} doped KNN films compared to the undoped films.

4.3 Processing of flexible KNN films (Manuscript I)

4.3.1 Development of processing route

The aqueous synthesis platform of KNN films established in the first part of the work was further developed with the aim to fabricate KNN films on flexible substrates. The processing was based on a lift-off technique reported by Liu and coworkers[65] and the aqueous CSD synthesis platform developed in Paper I and II. In the process, KNN films were deposited and thermally processed on rigid substrates followed by transferring of the ceramic films to a polymeric support by etching of a ZnO release layer between the substrate and the film. A description of the processing route is presented in Section 3.1.2 on page 99.

SiPt substrates were used as supports during thermal processing of the films. PDMS was chosen as flexible support based on the chemical stability, tunable mechanical properties and biocompatibility of silicones.[464] The ZnO release layers[465] and BT buffer layers[448] were deposited from aqueous solutions described previously, and the KNN films were made from the KNN-MA precursor solution described in Paper I and II.

Successful release of KNN films on PDMS supports was demonstrated by selective etching of the ZnO release layer using acetic acid. The KNN films without Pt bottom electrodes were semi-transparent, as shown in Figure 4.12. GIXRD patterns, presented in Figure 4.13, identify the flexible films to be KNN as they only contain Bragg reflections from the (100) and (110) planes of orthorhombic KNN in addition to the reflections from Pt. A SEM micrograph of a flexible KNN film is presented in Figure 4.14, showing a homogenous and dense KNN layer on top of a Pt bottom electrode and PDMS.

Top and bottom Pt electrodes were deposited on the flexible films for ferroelectric characterization (Figure S.3 in Manuscript I), but the measurements were dominated by leakage currents (S.6 in Manuscript I).

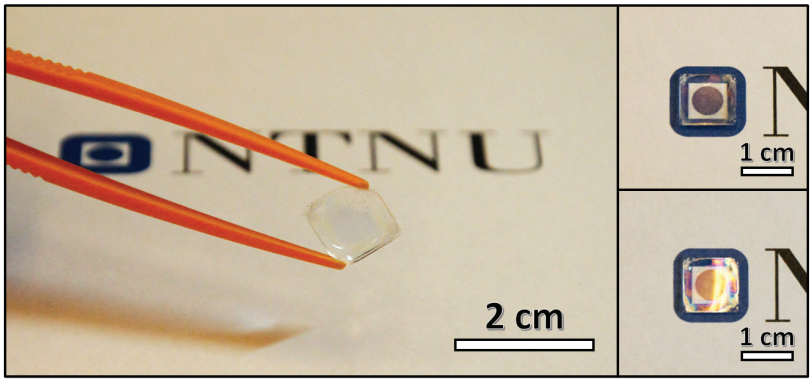

Figure 4.12: Images of a semi-transparent flexible KNN film on PDMS.

4.3.2 Phase composition

The ZnO release layer crystallized in the wurtzite structure as evident from the GIXRD pattern in Figure 4.15. Some (103) orientation is observed in the ZnO layer, as evident from the reflection at $2\theta = 62.7°$. Successful deposition of BT was also demonstrated using GIXRD (Figure 4.15) and IR (Figure S.2 in Manuscript I). Introduction of a BT buffer layer was shown to be detrimental to obtain phase pure KNN films on the ZnO release layer. Deposition of KNN films directly onto ZnO resulted in formation of the alkali metal deficient secondary phase $K_4Nb_6O_{17}$, as demonstrated by the GIXRD patterns and SEM images in Figure 4.15. Several explanations for the formation of the $K_4Nb_6O_{17}$ phase were discussed. The ZnO layer was demonstrated to have (103) preferential orientation (Figure 4.15), and $K_4Nb_6O_{17}$ was suggested to be induced by templated nucleation on the ZnO surface. Another suggestion was a reduction of the decomposition temperature of the KNN precursor solution on ZnO, resulting in less suppressed nucleation as discussed in Paper I. Reactions between the ZnO and the alkali metals in the KNN precursor was disregarded as mechanism for $K_4Nb_6O_{17}$ formation due to the absent of stable compounds in the K_2O-ZnO and Na_2O-ZnO binary systems.[466,467]

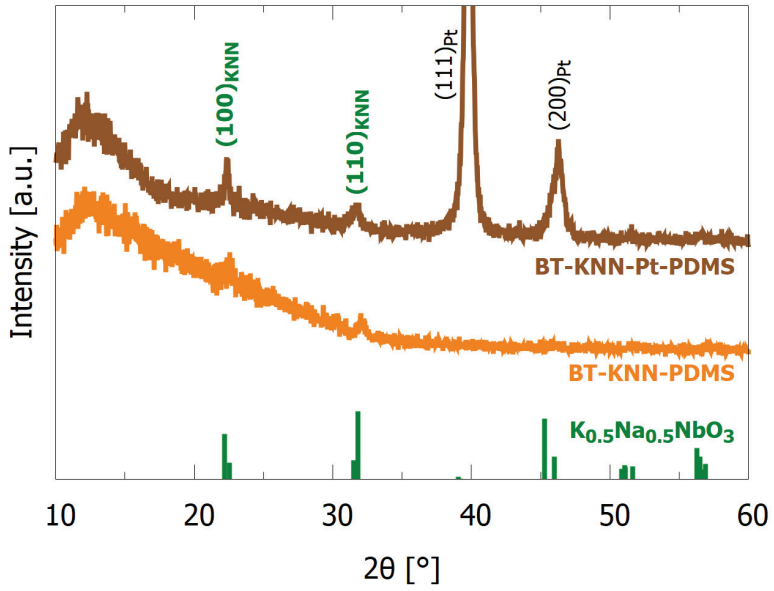

Figure 4.13: GIXRD patterns of flexible KNN films on PDMS. Reflections from the KNN film and Pt electrode are marked. Reference pattern for $K_{0.5}Na_{0.5}NbO_3$ (green, PDF card 00-061-0315)[118] is included.

4.3.3 Microstructure and further optimization

The microstructure of the flexible KNN films revealed that several defects and cracks were introduced in the films during the process (Figure S.4 in Manuscript I). Introduction of a Pt bottom electrode greatly decreased the number of defects. However, there was still induced cracks in the KNN films with Pt electrodes, as evident from the SEM micrographs in Figure 4.16. The origin of these flaws was argued to be strain in the film introduced during handling after the release from the rigid substrate. Such stresses could be avoided by more careful handling and by fixing the flexible film to a carrier substrate after release (e.g. as in Figure S.3 in Manuscript I). Another factor could be built-up strains from mismatch of the thermal expansion coefficients during thermal processing of the

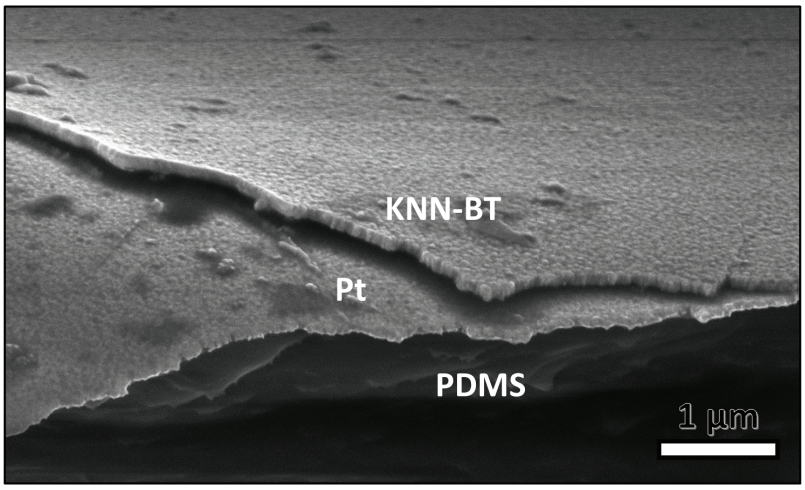

Figure 4.14: SEM micrograph of flexible KNN film on PDMS. The KNN film has a thin BT buffer layer deposited on top. A Pt bottom electrode was deposited between the PDMS support and the KNN film.

layers on the silicon-based substrate. The thermal expansion coefficient of Si ($2.59 \cdot 10^{-6}$ K^{-1})[468] is smaller than the coefficients for ZnO ($5.7 \cdot 10^{-6}$ K^{-1}),[469] BT ($11.34 \cdot 10^{-6}$ K^{-1})[470] and KNN ($4.72 \cdot 10^{-6}$ K^{-1}),[125] causing these layers to be under tensile strain after cooling.

The leaky behavior of the films during ferroelectric characterization (Figure S.6 in Manuscript I) is likely due to short circuiting between top and bottom electrodes due to the micro-cracking of the films. Further optimization of the synthesis could avoid defect formation in the films and result in crack free films with good piezoelectric properties. As such, the lift-off technique described in Manuscript I holds the potential for environmentally friendly and cost-effective piezoelectric KNN micro-components with high output performance. The synthesis route is also possible to apply to other ceramic material systems, e.g. other ferroelectric material,[448,471] transparent conductive materials[472,473] and optical active materials.[474]

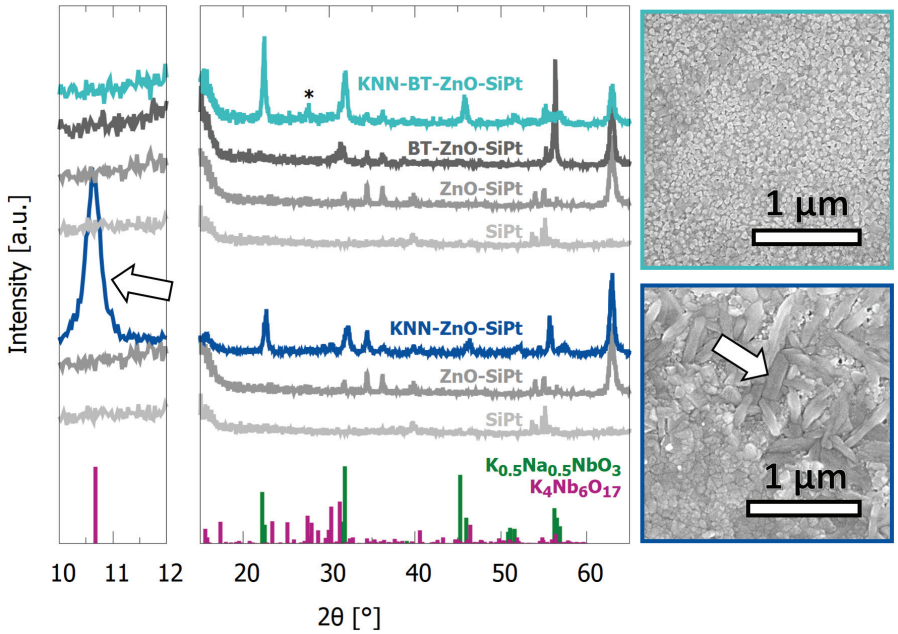

Figure 4.15: GIXRD patterns and top-view SEM micrographs of KNN films deposited on SiPt substrates. The arrows mark a reflection at ~10° and elongated grains in the diffraction pattern and microstructure, respectively, of KNN films without a buffer layer (blue), both of which are assigned to the $K_4Nb_6O_{17}$ phase. The KNN films with the BT buffer layer (cyan) did not contain the secondary phase. * indicates an unidentified reflection. Diffraction patterns from the substrate, the ZnO release layer and the BT buffer layer are also shown (grey). Reference patterns for $K_{0.5}Na_{0.5}NbO_3$ (green, PDF card 00-061-0315)[118] and $K_4Nb_6O_{17}$ (purple, 04-009-6408)[451] are included.

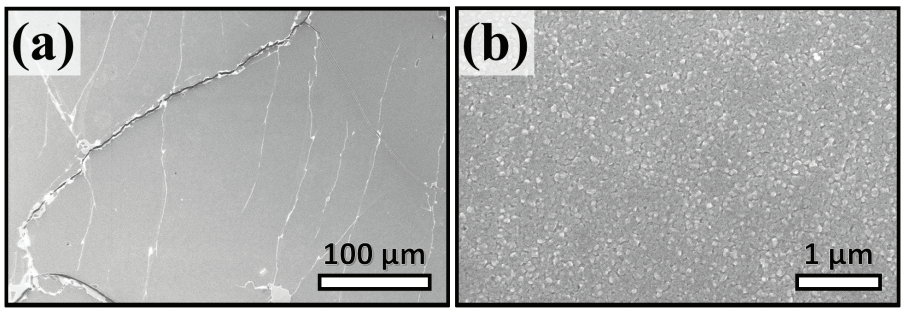

Figure 4.16: SEM micrographs of the surface of the flexible KNN films on PDMS with Pt bottom electrode. (a) Macroscopic defects are present in the film. (b) Areas with no defects are observed in the local microstructure.

4.4 *In vitro* biocompatibility testing of KNN films (Manuscript II)

In the final part of this thesis, *in vitro* cytotoxicity testing was performed on KNN films in order to assess the biocompatibility of the films with three different cell lines. The biological testing was performed with undoped and 0.5 mol% $CaTiO_3$ doped KNN films on SiPt substrates, of which the synthesis and ferroelectric characterization were described in Paper II. SiPt substrates with no film were also tested in order to deconvolute the effect from the films and the substrates. Phase composition, surface roughness and surface hydrophobicity of the samples were analyzed prior to the *in vitro* testing. The three cell lines used in the biological studies were human 161BR fibroblast cells, rat (glial) Schwann cells and human SH-SY5Y neuroblastoma cells. Glass coverslips were used as negative controls as they have been reported to support cell attachment and proliferation for both fibroblast [421,475] and glial cells. [476,477] The *in vitro* assays performed are described in Section 3.3.3 on page 107.

4.4.1 Characterization of the films prior to *in vitro* testing

The undoped and 0.5 mol% $CaTiO_3$ doped KNN films on SiPt substrates were phase pure (Figure S.1 in Manuscript II) and had uniform and dense microstructures with an average thickness of ~50 nm (Figure 1 in Manuscript II). The surface roughness of the KNN films was substantially higher than the roughness of the SiPt substrates and glass controls (Figure 4.17 (a)), owing to the grain structure of the films (Figure 2 in Manuscript II). The surface hydrophobicity is more uniform between the samples (Figure 4.17 (b)), and all the samples have surfaces that are moderately hydrophilic with contact angles between 50 and 60°.

4.4.2 Assessment of biocompatibility

The results from the colorimetric assays on fibroblast and glial cells, presented in Figure 4.18 (a) and (b) respectively, demonstrated that both KNN film compositions support cell proliferation equally well or better than the glass control

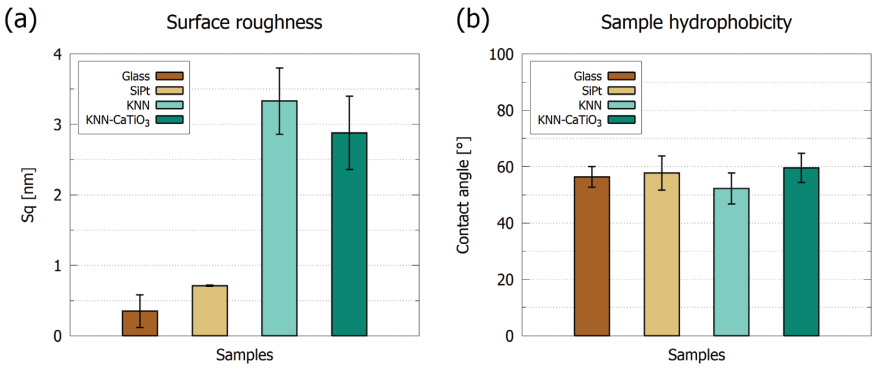

Figure 4.17: (a) RMS surface roughness (Sq) calculated from AFM measurements scanning areas of 5x5 µm on the samples. (b) Contact angle measurements of distilled water droplets on the sample surfaces at 37 °C.

samples. The Schwan cell proliferation rates on undoped KNN films after 3 and 5 days were significantly better than on the control samples. Moreover, the SiPt substrates accommodated consistently the highest proliferation rates for both cell lines.

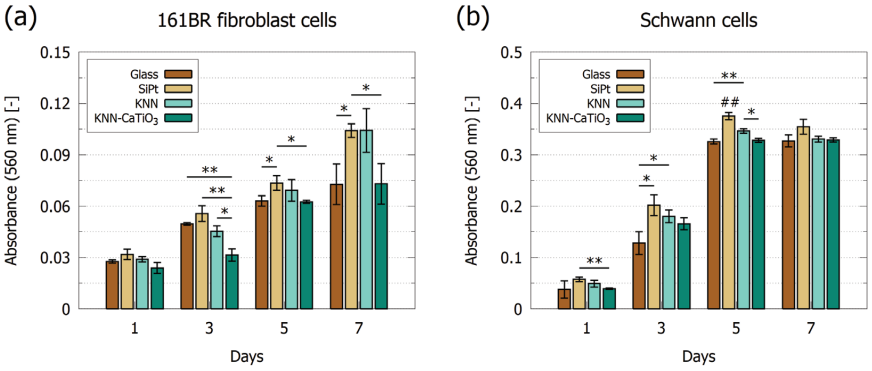

Figure 4.18: Proliferation rates after 1, 3, 5 and 7 days for (a) human 161BR fibroblast cells and (b) rat Schwann cells grown on glass coverslips (control), SiPt substrates, KNN films and KNN-CaTiO3 films. Statistical significance is indicated ($* = p < 0.05$, $** = p < 0.01$). ## refers to a difference of $p < 0.01$ between SiPt and each of the other samples.

Cell viability and morphology after being cultured on the KNN films and SiPt substrates were assessed using immunofluorescence microscopy and SEM (Figure 4.19). The 161BR fibroblast cells were observed to spread out more on the SiPt substrates and undoped KNN films compared to the KNN-$CaTiO_3$ films and the glass controls. The cell density of Schwann cells was observed to be higher on the SiPt substrates and undoped KNN films compared to the KNN-$CaTiO_3$ films and the glass controls. Preliminary morphology results of neuronal cells show excellent adhesion and neurite outgrowth on all samples (Figure S.2 in Manuscript II).

The results from the *in vitro* experiments demonstrate that KNN is a non-cytotoxic ceramic that exhibits biocompatibility with a wide range of cell lines. This is in agreement with previous *in vitro* studies on KNN ceramics.[206,437,439,439–443,445,447] To the best of our knowledge our results are also the first to establish platinized silicon substrates as non-cytotoxic. Combined with the AFM and hydrophobicity measurements (Figure 4.17) the results further suggest that fibroblast and glial cells are indifferent to differences in surface roughness between 0.3 and 3.3 nm, and that these cell types respond well to moderately hydrophilic surfaces ($\theta \sim 50$-$60°$).

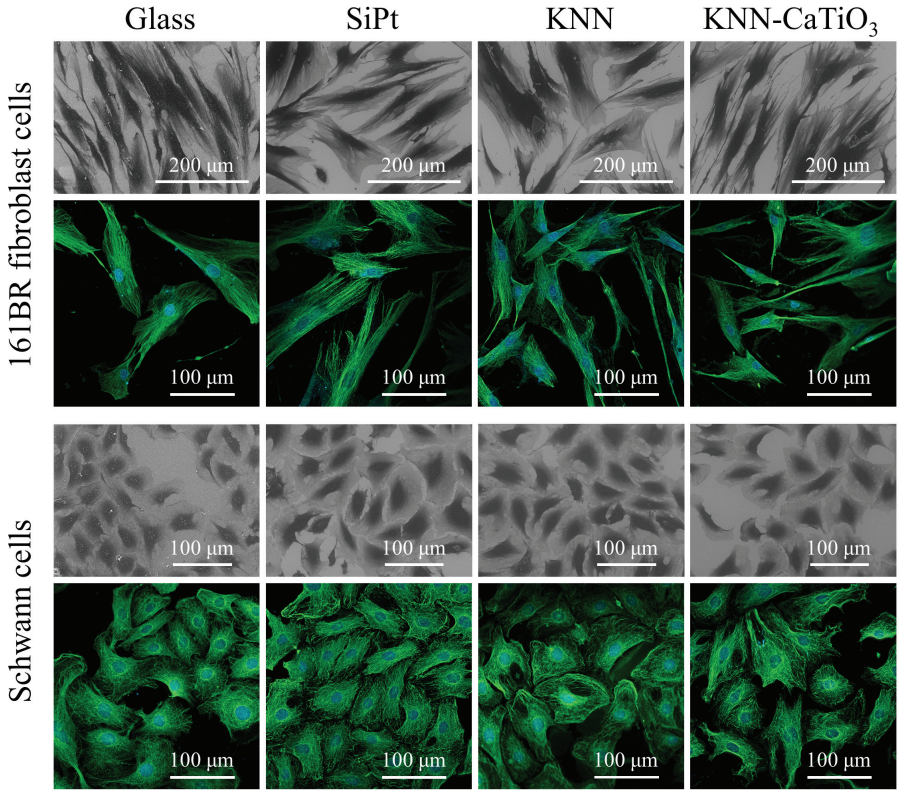

Figure 4.19: SEM micrographs and confocal immunofluorescence images of 161BR fibroblast and Schwann cells after being grown on glass coverslips, SiPt substrates, KNN thin films and KNN-$CaTiO_3$ thin films for 5 (161BR fibroblast cells) and 3 days (Schwann cells). Cell cytoskeletons and nuclei are stained with β-tublin (green) and DAPI (blue), respectively.

4.5 Overview and outlook

The aim of this project was to develop an aqueous synthesis platform to lead-free ferroelectric KNN thin films for biomedical applications. A major part of the thesis was devoted to the development of the environmentally friendly and cost-effective synthesis route to KNN films. The project included the exploration of film fabrication on single crystal (100) oriented STO substrates, industry-compatible Si-based substrates and flexible polymeric supports for high-output applications. Advanced structural and functional characterization of the films were also carried out. A correlation between the precursor chemistry and the phase composition of the films was established, and a link between thermal processing parameters and the resulting film texture. The ferroelectric performance of the films was improved with the introduction of dopants. Finally, comprehensive *in vitro* biocompatibility studies were performed to demonstrate the cytocompatibility of the films. Are the KNN films developed in this project ready to enter service *in vivo*? There is still a way to go, but this study has definitely nudged the world some nanometers closer to practical use of piezoelectric KNN films in biomedical applications. The aim to develop an aqueous synthesis platform to lead-free ferroelectric KNN thin films was successful. The thesis work has also demonstrated excellent biocompatibility of KNN films on SiPt with cells *in vitro*.

Several aspects of the work would be interesting to investigate further. Firstly, the link between film texture and thermal processing would be interesting to explore in depth. Pham and coworkers reported on epitaxial growth in KNN films from a KNN-Ox precursor solution by avoiding nucleation during pyrolysis and using a rapid temperature ramp during annealing and crystallization of the films.[64] It would be interesting to see if this could be replicated for the KNN-MA precursor solution developed in Paper I, which could result in epitaxial and phase pure KNN films. Secondly, the water-based synthesis platform developed in this project holds room for expansion into more complex compositions to further improve the functional properties of the KNN films. There are also possibilities to use other material systems in parts of the work, as demonstrated with $BaTiO_3$ on the flexible supports. Thirdly, piezoelectric characterization measuring d_{33} of the KNN films on SiPt and flexible supports could further demonstrate the

promising qualities of these materials for future applications. Lastly, the interplay between cells and films could be further explored by studying the effect of ferroelectric poling and mechanical loading on cell behavior.

At the time of writing this thesis it has been more than 60 years since ferroelectricity was first observed in solid solutions of $KNbO_3$ and $NaNbO_3$,[15] and 16 years since Saito and coworkers measured an astonishingly high piezoelectric coefficient of 416 $pC\,N^{-1}$ in chemically and structurally modified KNN.[39] The first Restriction of Hazardous Substances Directive (RoHS 1) banning the use of lead in consumer electronics was adapted by the European Union 17 years ago,[77] and a tremendous amount of research has been focused on developing lead-free piezoelectric materials over the last two decades.[21–29] So, where do we stand today in terms of lead-free piezoelectric materials? And what are the prospects for the future of this technology?

The PZTs are still the dominant class of materials on the piezoelectric market,[478] and the amended exception to the RoHS 2 directive from 2018 (Exemption 7(c)-I)[86] is expected to be prolonged when it is up for evaluation in 2021.[35] However, significant advances in the development of lead-free materials have been made, including inorganic (e.g. KNN, BNT, BT) and organic (e.g. PVDF) alternatives.[27,478] Prototypes of some of these materials have been reported to have piezoelectric properties better than commercial PZT. Despite this, the overall properties of these materials (electromechanical coupling factor, thermal stability, mechanical properties) still need improvement in order to compete with the PZTs.[478]

For KNN specifically, the upcoming years look promising. KNN ceramics have been applied in shear mode inkjet printer heads and multilayer actuators for some years now.[479] From 2013 to 2018 around 200 patent applications were filed for KNN,[35] and around 40 new applications have been filed since then.[†] Around 40 % of these patents are for KNN films, and companies like Intel, TDK Electronics and Hitachi metal are among the KNN film patent owners.[34] Judging by the number of new patent applications, the use of KNN films is expected to increase

[†]"Google patents" search engine,[480] keywords: "lead-free", "piezoelectric", "potassium sodium niobate", and "ceramic".

over the next years. Yet, the research on KNN film synthesis is deemed underdeveloped compared to bulk synthesis,[35] suggesting that more research on film fabrication is still necessary to bring KNN films to the market.

Bibliography

[1] Rune Elmqvist and Åke Senning. An implantable pacemaker for the heart. *Medical Electronics. Proceedings of the Second International Conference on Medical Electronics, Paris*, 24:27, 1959.

[2] Tatsuo Tagawa, Toshiyo Tamura, and P. Ake Oberg. *Biomedical Sensors and Instruments*. CRC Press, 2 edition, 2011. doi: 10.1201/b10775.

[3] Jiashi Yang. *An Introduction to the Theory of Piezoelectricity*, volume 9. Springer, New York, 2005. doi: 10.4057/jsr.11.2_51.

[4] Andrei L. Kholkin, Nikolay A. Pertsev, and Alexander V. Goltsev. Piezoelectricity and Crystal Symmetry. In Ahmad Safari and E. Koray Akdogan, editors, *Piezoelectric and Acoustic Materials for Transducer Applications*, chapter 2, pages 17–38. Springer Science and Business Media, 2008. doi: 10.1007/978-0-387-76540-2_2.

[5] Shaul Katzir. *The Beginnings of Piezoelectricity: a study in mundane physics*. Springer Science and Business Media, 2007. ISBN 978-1-4020-4670-4.

[6] Walter Heywang, Karl Lubitz, and Wolfram Wersing, editors. *Piezoelectricity: evolution and future of a technology*. Springer Science and Business Media, vol. 114 edition, 2008. ISBN 978-3-540-68680-4.

[7] Xiangyu Gao, Jikun Yang, Jingen Wu, Xudong Xin, Zhanmiao Li, and Xiaoting Yuan. Piezoelectric Actuators and Motors: Materials, Designs, and Applications. *Advanced Materials Technologies*, 5(1):1900716, 2020. doi: 10.1002/admt.201900716.

[8] Alicia María Manjón-Sanz and Michelle R Dolgos. Applications of Piezoelectrics: Old and New. *Chemistry of Materials*, 30(24):8718–8726, 2018. doi: 10.1021/acs.chemmater.8b03296.

[9] Huaxiang Fu and Ronald E. Cohen. Polarization rotation mechanism for ultrahigh electromechanical response in single-crystal piezoelectrics. *Nature*, 403(6767):281–283, 2000. doi: 10.1038/35002022.

[10] Fei Li, Dabin Lin, Zibin Chen, Zhenxiang Cheng, Jianli Wang, Chunchun Li, Zhuo Xu, Qianwei Huang, Xiaozhou Liao, Long-qing Chen, Thomas R Shrout, and Shujun Zhang. Ultrahigh piezoelectricity in ferroelectric ceramics by design. *Nature Materials*, 17(April):349–354, 2018. doi: 10.1038/s41563-018-0034-4.

[11] Dragan Damjanovic. Contributions to the piezoelectric effect in ferroelectric single crystals and ceramics. *Journal of the American Ceramic Society*, 88(10):2663–2676, 2005. doi: 10.1111/j.1551-2916.2005.00671.x.

[12] Dragan Damjanovic. Comments on origins of enhanced piezoelectric properties in ferroelectrics. *IEEE Transactions on Ultrasonics, Ferroelectrics, and Frequency Control*, 56(8):1574–1585, 2009. doi: 10.1109/TUFFC.2009.1222.

[13] Leslie Eric Cross and Robert E. Newnham. History of Ferroelectrics. *Ceramics and Civilization*, 3:289–305, 1987.

[14] Etsuro Sawaguchi. Ferroelectricity versus Antiferroelectricity in the Solid Solutions of $PbZrO_3$ and $PbTiO_3$. *Journal of the Physical Society of Japan*, 8(5):615–629, 1953. doi: 10.1143/JPSJ.8.615.

[15] L. Egerton and Dolores M. Dillon. Piezoelectric and Dielectric Properties of Ceramics in the System Potassium-Sodium Niobate. *Journal of the American Ceramic Society*, 42(9):438–442, 1959. doi: 10.1016/j.ceramint.2011.04.097.

[16] B. Jaffe, R. S. Roth, and S. Marzullo. Piezoelectric Properties of Lead Zirconate-Lead Titanate Solid-Solution Ceramics. *Journal of Applied Physics*, 25(6):809–810, 1954. doi: 10.1063/1.1721741.

[17] D. A. Berlincourt, C. Cmolik, and H. Jaffe. Piezoelectric Properties of Polycrystalline Lead Titanate Zirconate Compositions. *Proceedings of the IRE*, 48(2):220–229, 1960. doi: 10.1109/JRPROC.1960.287467.

[18] Gene H Haertling. Ferroelectric Ceramics: History and Technology. *Journal of the American Ceramic Society*, 82(4):797–818, 1999. doi: 10.1111/j.1151-2916.1999.tb01840.x.

[19] Seung-Eek Park and Thomas R. Shrout. Ultrahigh strain and piezoelectric behavior in relaxor based ferroelectric single crystals. *Journal of Applied Physics*, 82(4):1804–1811, 1997. doi: 10.1063/1.365983.

[20] L. Bellaiche and David Vanderbilt. Intrinsic Piezoelectric Response in Perovskite Alloys: PMN-PT versus PZT. *Physical Review Letters*, 83(7):1347–1350, 1999. doi: 10.1103/PhysRevLett.83.1347.

[21] Thomas R. Shrout and Shujun J. Zhang. Lead-free piezoelectric ceramics: Alternatives for PZT? *Journal of Electroceramics*, 19(1):111–124, 2007. doi: 10.1007/s10832-007-9047-0.

[22] P. K. Panda. Review: Environmental friendly lead-free piezoelectric materials. *Journal of Materials Science*, 44(19):5049–5062, 2009. doi: 10.1007/s10853-009-3643-0.

[23] J. Rödel, W. Jo, K. T. P. Seifert, E. M. Anton, T. Granzow, and D. Damjanovic. Perspective on the development of lead-free piezoceramics. *Journal of the American Ceramic Society*, 92(6):1153–1177, 2009. doi: 10.1111/j.1551-2916.2009.03061.x.

[24] A. Safari and M. Abazari. Lead-free piezoelectric ceramics and thin films. *IEEE Transactions on Ultrasonics, Ferroelectrics, and Frequency Control*, 57(10):2165–2176, 2010. doi: 10.1109/TUFFC.2010.1674.

[25] Indrani Coondoo, Neeraj Panwar, and Andrei Kholkin. Lead-free piezoelectrics: Current status and perspectives. *Journal of Advanced Dielectrics*, 03(02):1330002, 2013. doi: 10.1142/S2010135X13300028.

[26] Jürgen Rödel, Kyle G Webber, Robert Dittmer, Wook Jo, Masahiko Kimura, and Dragan Damjanovic. Transferring lead-free piezoelectric ceramics into application. *Journal of the European Ceramic Society*, 35(6):1659–1681, 2015. doi: 10.1016/j.jeurceramsoc.2014.12.013.

[27] Huige Wei, Hui Wang, Yijie Xia, Dapeng Cui, Yapeng Shi, Mengyao Dong, Chuntai Liu, Tao Ding, Jiaoxia Zhang, Yong Ma, Ning Wang, Zicheng Wang, Ye Sun, Renbo Wei, and Zhanhu Guo. An overview of lead-free piezoelectric materials and devices. *Journal of Materials Chemistry C*, 6(46):12446–12467, 2018. doi: 10.1039/c8tc04515a.

[28] P. K. Panda and B. Sahoo. PZT to lead free piezo ceramics: A review. *Ferroelectrics*, 474(1):128–143, 2015. doi: 10.1080/00150193.2015.997146.

[29] Ting Zheng, Jiagang Wu, Dingquan Xiao, and Jianguo Zhu. Recent development in lead-free perovskite piezoelectric bulk materials. *Progress in Materials Science*, 98(June):552–624, 2018. doi: 10.1016/j.pmatsci.2018.06.002.

[30] Jing Feng Li, Ke Wang, Fang Yuan Zhu, Li Qian Cheng, and Fang Zhou Yao. (K,Na)NbO_3-based lead-free piezoceramics: Fundamental aspects, processing technologies, and remaining challenges. *Journal of the American Ceramic Society*, 96(12):3677–3696, 2013. doi: 10.1111/jace.12715.

[31] Jiagang Wu, Dingquan Xiao, and Jianguo Zhu. Potassium-Sodium Niobate Lead-Free Piezoelectric Materials: Past, Present, and Future of Phase Boundaries. *Chemical Reviews*, 115:2559–2595, 2015. doi: 10.1021/cr5006809.

[32] Jie Xing, Ting Zheng, Jiagang Wu, Dingquan Xiao, and Jianguo Zhu. Progress on the doping and phase boundary design of potassium-sodium niobate lead-free ceramics. *Journal of Advanced Dielectrics*, 8(3):1830003, 2018. doi: 10.1142/S2010135X18300037.

[33] Hae Jin Seog, Aman Ullah, Chang Won Ahn, Ill Won Kim, Sun Young Lee, Jungmin Park, Hai Joon Lee, Sung Sik Won, and Seung-Hyun Kim. Recent Progress in Potassium Sodium Niobate Lead-free Thin Films. *Journal of Korean Physical Society*, 72(12):1467–1483, 2018. doi: 10.3938/jkps.72.1467.

[34] Su Wei Zhang, Zhen Zhou, Jin Luo, and Jing Feng Li. Potassium-Sodium-Niobate-Based Thin Films: Lead Free for Micro-Piezoelectrics. *Annalen der Physik*, 531(7):1800525, 2019. doi: 10.1002/andp.201800525.

[35] Hao Cheng Thong, Chunlin Zhao, Zhen Zhou, Chao Feng Wu, Yi Xuan Liu, Zong Zheng Du, Jing Feng Li, Wen Gong, and Ke Wang. Technology transfer of lead-free (K, Na)NbO_3-based piezoelectric ceramics. *Materials Today*, 29:37–48, 2019. doi: 10.1016/j.mattod.2019.04.016.

[36] Yichi Zhang and Jing Feng Li. Review of chemical modification on potassium sodium niobate lead-free piezoelectrics. *Journal of Materials Chemistry C*, 7(15):4284–4303, 2019. doi: 10.1039/c9tc00476a.

[37] Xiang Lv, Jianguo Zhu, Dingquan Xiao, Xi Xiang Zhang, and Jiagang Wu. Emerging new phase boundary in potassium sodium-niobate based ceramics. *Chemical Society reviews*, 49(3): 671–707, 2020. doi: 10.1039/c9cs00432g.

[38] Jurij Koruza, Hairui Liu, Marion Höfling, Mao Hua Zhang, and Philippe Veber. (K,Na)NbO_3-based piezoelectric single crystals: Growth methods, properties, and applications. *Journal of Materials Research*, 35(8):990–1016, 2020. doi: 10.1557/jmr.2019.391.

[39] Y. Saito, H. Takao, T. Tani, T. Nonoyama, K. Takatori, T. Homma, T. Nagaya, and M. Nakamura. Lead-free piezoceramics. *Nature*, 432:84–87, 2004. doi: 10.1038/nature03008.1.

[40] Peng Li, Jiwei Zhai, Bo Shen, Shujun Zhang, Xiaolong Li, Fangyuan Zhu, and Xingmin Zhang. Ultrahigh Piezoelectric Properties in Textured (K,Na)NbO_3-Based Lead-Free Ceramics. *Advanced Materials*, 30(8):1705171, 2018. doi: 10.1002/adma.201705171.

[41] Lawrence Yu, Brian J Kim, and Ellis Meng. Chronically Implanted Pressure Sensors: Challenges and State of the Field. *Sensors*, 14(11):20620–20644, 2014. doi: 10.3390/s141120620.

[42] Chu Pak Lau, Hung Fat Tse, A. John Camm, and Serge S. Barold. Evolution of pacing for bradycardias: Sensors. *European Heart Journal Supplements*, 9(I):11–22, 2007. doi: 10.1093/eurheartj/sum057.

[43] Bojing Shi, Zhou Li, and Yubo Fan. Implantable Energy-Harvesting Devices. *Advanced Materials*, 1801511:1–18, 2018. doi: 10.1002/adma.201801511.

[44] Achraf Ben Amar, Ammar B. Kouki, and Hung Cao. Power approaches for implantable medical devices. *Sensors*, 15(11):28889–28914, 2015. doi: 10.3390/s151128889.

[45] Leilei Li, Jie Xu, Junting Liu, and Feng Gao. Recent progress on piezoelectric energy harvesting: structures and materials. *Advanced Composites and Hybrid Materials*, 1(3):478–505, 2018. doi: 10.1007/s42114-018-0046-1.

[46] Canan Dagdeviren, Zhou Li, and Zhong Lin Wang. Energy Harvesting from the Animal/Human Body for Self-Powered Electronics. *Annual Review of Biomedical Engineering*, 19(1):85–108, 2017. doi: 10.1146/annurev-bioeng-071516-044517.

[47] Moinul Haq. Application of piezo transducers in biomedical science for health monitoring and energy harvesting problems. *Materials Research Express*, 6:022002, 2019. doi: 10.1088/2053-1591/aaefb8.

[48] Klaus Malinowski. Interindividual Comparison of Different Sensor Principles for Rate Adaptive Pacing. *Pacing and Clinical Electrophysiology*, 21(11):2209–2213, 1998. doi: 10.1111/j.1540-8159.1998.tb01154.x.

[49] Amy C.Richards Grayson, Rebecca S. Shawgo, Audrey M. Johnson, Nolan T. Flynn, Yawen Li, Michael J. Cima, and Robert Langer. A BioMEMS Review: MEMS Technology for Physiologically Integrated Devices. *Proceedings of the IEEE*, 92(1):6–21, 2004. doi: 10.1109/JPROC.2003.820534.

[50] Anthony K. Au, Hoyin Lai, Ben R. Utela, and Albert Folch. Microvalves and micropumps for BioMEMS. *Micromachines*, 2:179–220, 2011. doi: 10.3390/mi2020179.

[51] Vanessa F. Cardoso, Daniela M. Correia, Clarisse Ribeiro, Margarida M. Fernandes, and Senentxu Lanceros-Méndez. Fluorinated polymers as smart materials for advanced biomedical applications. *Polymers*, 10(2):161, 2018. doi: 10.3390/polym10020161.

[52] Mohammad Zaki Aj, Satish K. Patil, Dheeraj T. Baviskar, and Dinesh K. Jain. Implantable drug delivery system: A review. *International Journal of PharmTech Research*, 4(1):280–292, 2012. ISSN 09744304.

[53] A. Manz, N. Graber, and H. M. Widmer. Miniaturized Total Chemical Analysis Systems: a Novel Concept for Chemical Sensing. *Sensors and actuators B: Chemical*, 1(1-6):244–248, 1990. doi: 10.1016/0925-4005(90)80209-I.

[54] Arun Arora, Giuseppina Simone, Georgette B. Salieb-Beugelaar, Jung Tae Kim, and Andreas Manz. Latest Developments in Micro Total Analysis Systems. *Analytical Chemistry*, 82(12):4830–4847, 2010. doi: 10.1021/ac100969k.

[55] Y. Q. Fu, J. K. Luo, N. T. Nguyen, A. J. Walton, A. J. Flewitt, X. T. Zu, Y. Li, G. McHale, A. Matthews, E. Iborra, H. Du, and W. I. Milne. Advances in piezoelectric thin films for acoustic biosensors, acoustofluidics and lab-on-chip applications. *Progress in Materials Science*, 89:31–91, 2017. doi: 10.1016/j.pmatsci.2017.04.006.

[56] Yehezkiel Steven Kurniawan. Micro Total Analysis System Application for Biomedicals: A Mini-Review. *Biomedical Journal of Scientific and Technical Research*, 12(4):9442–9443, 2019. doi: 10.26717/bjstr.2019.12.002294.

[57] A. Blázquez-Castro, A. García-Cabañes, and M. Carrascosa. Biological applications of ferroelectric materials. *Applied Physics Reviews*, 5:041101, 2018. doi: 10.1063/1.5044472.

[58] Kateryna Bazaka and Mohan V. Jacob. Implantable Devices: Issues and Challenges. *Electronics*, 2(1):1–34, 2013. doi: 10.3390/electronics2010001.

[59] Wen H. Ko. Early History and Challenges of Implantable Electronics. *ACM Journal on Emerging Technologies in Computing Systems (JETC)*, 8(2):1–9, 2012. doi: 10.1145/2180878.2180880.

[60] David F. Williams. *The Williams dictionary of biomaterials*. Liverpool University Press, 1999. ISBN 0-85323-921-5.

[61] David F. Williams. On the mechanisms of biocompatibility. *Biomaterials*, 29(20):2941–2953, 2008. doi: 10.1016/j.biomaterials.2008.04.023.

[62] Michel Vert, Yoshiharu Doi, Karl Heinz Hellwich, Michael Hess, Philip Hodge, Przemyslaw Kubisa, Marguerite Rinaudo, and François Schué. Terminology for biorelated polymers and applications (IUPAC recommendations 2012). *Pure and Applied Chemistry*, 84(2):377–410, 2012. doi: 10.1351/pac-rec-10-12-04.

[63] Laleh Ghasemi-Mobarakeh, Davood Kolahreez, Seeram Ramakrishna, and David Williams. Key terminology in biomaterials and biocompatibility. *Current Opinion in Biomedical Engineering*, 10:45–50, 2019. doi: 10.1016/j.cobme.2019.02.004.

[64] Ky-nam Pham, Nikolai Helth Gaukås, Maxim Morozov, Thomas Tybell, Per Erik Vullum, Tor Grande, and Mari-Ann Einarsrud. Epitaxial $K_{0.5}Na_{0.5}NbO_3$ thin films by aqueous chemical solution deposition. *Royal Society Open Science*, 6:180989, 2019. doi: 10.1098/rsos.180989.

[65] Tianning Liu, Margeaux Wallace, Susan Trolier-McKinstry, and Thomas N. Jackson. High-temperature crystallized thin-film PZT on thin polyimide substrates. *Journal of Applied Physics*, 122(16):164103, 2017. doi: 10.1063/1.4990052.

[66] Jacques Curie and Pierre Curie. Développement par compression de l'électricité polaire dans les cristaux hémièdres à faces inclinées. *Bulletin de la Société minéralogique de France*, 3(4): 90–93, 1880. doi: 10.3406/bulmi.1880.1564.

[67] Warren P. Mason. Piezoelectricity, its history and applications. *Journal of the Acoustical Society of America*, 70(6):1561–1566, 1981. doi: 10.1121/1.387221.

[68] Sidney B. Lang. History of pyroelectricity. In *Sourcebook of Pyroelectricity*, chapter II, pages 85–153. CRC Press, 2 edition, 1974. doi: 10.1080/00150199908214903.

[69] Georg Busch. Early history of ferroelectricity. *Ferroelectrics*, 74(1):267–284, 1987. doi: 10.1080/00150198708201307.

[70] J. Valasek. Piezo-electric and allied phenomena in Rochelle salt. *Physical Review*, 17(4):475–481, 1921. doi: 10.1103/PhysRev.17.475.

[71] R. E. Newnham and L. Eric Cross. Ferroelectricity: The foundation of a field from form to function. *MRS Bulletin*, 30(11):845–848, 2005. doi: 10.1557/mrs2005.272.

[72] David I Woodward, Jesper Knudsen, and Ian M Reaney. Review of crystal and domain structures in the $PbZr_xTi_{1-x}O_3$ solid solution. *Physical Review B*, 72:104110, 2005. doi: 10.1103/PhysRevB.72.104110.

[73] Gagan Flora, Deepesh Gupta, and Archana Tiwari. Toxicity of lead: A review with recent updates. *Interdisciplinary Toxicology*, 5(2):47–58, 2012. doi: 10.2478/v10102-012-0009-2.

[74] Prasenjit Mitra, Shailja Sharma, Purvi Purohit, and Praveen Sharma. Clinical and molecular aspects of lead toxicity: An update. *Critical Reviews in Clinical Laboratory Sciences*, 54(7-8): 506–528, 2017. doi: 10.1080/10408363.2017.1408562.

[75] World Health Organization. Lead poisoning and health, accessed 03.03.2020. URL https://www.who.int/news-room/fact-sheets/detail/lead-poisoning-and-health.

[76] Andrew J. Bell and Otmar Deubzer. Lead-free piezoelectrics - The environmental and regulatory issues. *MRS Bulletin*, 43(8):581–587, 2018. doi: 10.1557/mrs.2018.154.

[77] European Parliament and the European Council. EU-Directive 2002/95/EC: Restriction of the use of certain hazardous substances in electrical and electronic equipment (RoHS). *Official Journal of the European Union*, 46:19–23, 2003.

[78] European Parliament and the European Council. EU-Directive 2002/96/EC: Waste electrical and electronic equipment (WEEE). *Official Journal of the European Union*, 46:24–38, 2003.

[79] European Parliament and the European Council. EU-Directive 2011/65/EU on the restriction of the use of certain hazardous substances in electrical and electronic equipment (RoHS). *Official Journal of the European Union*, 174:88–110, 2011.

[80] European Parliament and the European Council. EU-Directive 2012/19/EC: Waste electrical and electronic equipment (WEEE). *Official Journal of the European Union*, 197:38–71, 2012.

[81] Japan Electronics and Information Technology Industries Association. JIS C 0950:2008 The marking for presence of the specific chemical substances for electrical and electronic equipment, 2008.

[82] National Consumer Product Safety Standardisation Technical Commission. China GB/T xxxxx Safety requirements for hazardous chemicals in consumer products (draft), 2017.

[83] Environment and Labor Committee of the National Assembly of Korea. Act for Resource Recycling of Electrical and Electronic Equipment and Vehicles (No. 6319), 2007.

[84] Norwegian Ministry of the Environment. Regulations Relating to Restrictions on the Manufacture, Import, Export, Sale and Use of Chemicals and Other Products Hazardous to Health and the Environment (Produktforskriften), 2004.

[85] The Swiss Federal Council. Ordinance on the Reduction of Risks relating to the Use of Certain Particularly Dangerous Substances, Preparations and Articles (No. 814.81), 2005.

[86] European Parliament and the Council of the European Union. Directive (EU) 2017/2102 of the european parliament and of the council of 15 November 2017 amending Directive 2011/65/EU on the restriction of the use of certain hazardous substances in electrical and electronic equipment. *Official Journal of the European Union*, L 305(October):8–11, 2017.

[87] Bernhard Jaffe, William R. Cook, and Hans Jaffe. *Piezoelectric ceramics*. Academic Press, 3 edition, 1971. ISBN 0-12-379550-8.

[88] M. Lines and A. Glass. *Principles and Applications of Ferroelectrics and Related Materials*. Oxford University Press, 1977. doi: 10.1093/acprof:oso/9780198507789.001.0001.

[89] Wei Gao and Nigel M. Sammes. *An introduction to electronic and ionic materials*. World Scientific, 1999. ISBN 9-810-23473-2.

[90] Susan Trolier-Mckinstry. Crystal Chemistry of Piezoelectric Materials. In A. Safari and E. K. Akdogan, editors, *Piezoelectric and Acoustic Materials for Transducer Applications*, chapter 3, pages 39–56. Springer Science and Business Media, 2008. doi: 10.1007/978-0-387-76540-2_3.

[91] R. E. Newnham. *Properties of materials anisotropy, symmetry, structure*. Oxford University Press, 2005. doi: 10.5860/choice.42-6504.

[92] J. M. Herbert. *Ceramic dielectrics and capacitors*. CRC Press, 1985. ISBN 978-2881240454.

[93] Anthony R. West. *Solid state chemistry and its applications*. John Wiley and Sons, Inc., 2 edition, 2014. ISBN 9781119942948.

[94] Dragan Damjanovic. Ferroelectric, dielectric and piezoelectric properties of ferroelectric thin films and ceramics. *Reports on Progress in Physics*, 61:1267, 1998. doi: 10.1088/0034-4885/61/9/002.

[95] Ryszard Wojnar. Piezoelectric phenomena in biological tissues. In *Piezoelectric nanomaterials for biomedical applications*, pages 173–185. Springer, Berlin, 2012. doi: 10.1007/978-3-642-28044-3_6.

[96] W. Wersing, W. Heywang, H. Beige, and H. Thomann. The Role of Ferroelectricity for Piezoelectric Materials. In W. Heywang, K. Lubitz, and W. Wersing, editors, *Piezoelectricity: evolution and future of a technology*, chapter 3. Springer, 2008. doi: 10.1007/978-3-540-68683-5_3.

[97] Abhijit Pramanick, Anderson D. Prewitt, Jennifer S. Forrester, and Jacob L. Jones. Domains, domain walls and defects in perovskite ferroelectric oxides: A review of present understanding and recent contributions. *Critical Reviews in Solid State and Materials Sciences*, 37(4):243–275, 2012. doi: 10.1080/10408436.2012.686891.

[98] Li Jin, Fei Li, and Shujun Zhang. Decoding the fingerprint of ferroelectric loops: Comprehension of the material properties and structures. *Journal of the American Ceramic Society*, 97(1): 1–27, 2014. doi: 10.1111/jace.12773.

[99] V. Mehling, Ch Tsakmakis, and D. Gross. Phenomenological model for the macroscopical material behavior of ferroelectric ceramics. *Journal of the Mechanics and Physics of Solids*, 55(10): 2106–2141, 2007. doi: 10.1016/j.jmps.2007.03.008.

[100] Mats Johnsson and Peter Lemmens. Crystallography and Chemistry of Perovskites. In H. Kronmüller and S. Parkin, editors, *Handbook of magnetism and advanced magnetic materials*. Wiley, vol. 4 edition, 2007. doi: 10.1002/9780470022184.hmm411.

[101] K. Momma and F. Izumi. VESTA: a three-dimensional visualization system for electronic and structural analysis. *Journal of Applied Crystallography*, 41, 2008. doi: 10.1107/S0021889811038970.

[102] V. M. Goldschmidt. Die Gesetze der Krystallochemie. *Die Naturwissenschaften*, 14:477–485, 1926. doi: 10.1007/BF01507527.

[103] Prashant R. Potnis, Nien Ti Tsou, and John E. Huber. A review of domain modelling and domain imaging techniques in ferroelectric crystals. *Materials*, 4(2):417–447, 2011. doi: 10.3390/ma4020417.

[104] David Vanderbilt and Morrel H. Cohen. Monoclinic and triclinic phases in higher-order Devonshire theory. *Physical Review B*, 63(9):094108, 2001. doi: 10.1103/PhysRevB.63.094108.

[105] Xiaoning Jiang, Kyungrim Kim, Shujun Zhang, Joseph Johnson, and Giovanni Salazar. High-temperature piezoelectric sensing. *Sensors (Switzerland)*, 14(1):144–169, 2014. doi: 10.3390/s140100144.

[106] Shujun Zhang and Fapeng Yu. Piezoelectric materials for high temperature sensors. *Journal of the American Ceramic Society*, 94(10):3153–3170, 2011. doi: 10.1111/j.1551-2916.2011.04792.x.

[107] M. Acosta, N. Novak, V. Rojas, S. Patel, R. Vaish, J. Koruza, G. A. Rossetti, and J. Rödel. $BaTiO_3$-based piezoelectrics: Fundamentals, current status, and perspectives. *Applied Physics Reviews*, 4(4), 2017. doi: 10.1063/1.4990046.

[108] Wook Jo, Robert Dittmer, Matias Acosta, Jiadong Zang, Claudia Groh, Eva Sapper, Ke Wang, and Jürgen Rödel. Giant electric-field-induced strains in lead-free ceramics for actuator applications - status and perspective. *Journal of Electroceramics*, 29(1):71–93, 2012. doi: 10.1007/s10832-012-9742-3.

[109] Dawei Wang, Ge Wang, Shunsuke Murakami, Zhongming Fan, Antonio Feteira, Di Zhou, Shikuan Sun, Quanliang Zhao, and Ian M. Reaney. $BiFeO_3$-$BaTiO_3$: A new generation of lead-free electroceramics. *Journal of Advanced Dielectrics*, 8(6):1–35, 2018. doi: 10.1142/S2010135X18300049.

[110] B. B. Van Aken, T. T.M. Palstra, A. Filippetti, and N. a. Spaldin. The origin of ferroelectricity in magnetoelectric $YMnO_3$. *Nature Materials*, 3:164–170, 2004. doi: 10.1038/nmat1080.

[111] G. Shirane, R. Newnham, and R. Pepinsky. Dielectric properties and phase transitions of $NaNbO_3$ and (Na,K)NbO_3. *Physical Review*, 96(3):581–588, 1954. doi: 10.1103/PhysRev.96.581.

[112] M D Fontana, A Ridah, Y Luspin, J L Servoin, F Gervais, F Brehat, and B Wyncke. Infrared spectroscopy in $KNbO_3$ through the successive ferroelectric phase transitions. *Journal of Physics C: Solid State Physics*, 17(3):483–514, 1984.

[113] K. Singh, S. Acharya, and D. V. Atkare. Qualitative analysis of tolerance factor, electronegativity and chemical bonding of some ferroelectric perovskites through MOT. *Ferroelectrics*, 315:91–110, 2005. doi: 10.1080/00150190590933050.

[114] X. B. Wang, Z. X. Shen, Z. P. Hu, L. Qin, S. H. Tang, and M. H. Kuok. High temperature Raman study of phase transitions in antiferroelectric $NaNbO_3$. *Journal of Molecular Structure*, 385(1):1–6, 1996. doi: 10.1016/S0022-2860(96)09397-0.

[115] D. W. Baker, P. A. Thomas, N. Zhang, and A. M. Glazer. A comprehensive study of the phase diagram of $K_xNa_{1-x}NbO_3$. *Applied Physics Letters*, 95(9):091903, 2009. doi: 10.1063/1.3212861.

[116] M. Ahtee and A. W. Hewat. Structural phase transitions in sodium-potassium niobate solid solutions by neutron powder diffraction. *Acta Crystallographica Section A*, 34(2):309–317, 1978. doi: 10.1107/S056773947800056X.

[117] Marija Kosec, Barbara Malič, Andreja Benčan, and Tadej Rojac. KNN-based piezoelectric ceramics. In A. Safari and E. K. Akdogan, editors, *Piezoelectric and Acoustic Materials for Transducer Applications*, chapter 5, pages 81–102. Springer Science and Business Media, 2008. doi: 10.1007/978-0-387-76540-2_5.

[118] J. Tellier, B. Malic, B. Dkhil, D. Jenko, J. Cilensek, and M. Kosec. Crystal structure and phase transitions of sodium potassium niobate perovskites. *Solid State Sciences*, 11(2):320–324, 2009. doi: 10.1016/j.solidstatesciences.2008.07.011.

[119] Ke Wang and Jing Feng Li. Analysis of crystallographic evolution in (Na,K)NbO_3-based lead-free piezoceramics by x-ray diffraction. *Applied Physics Letters*, 91(26):262902, 2007. doi: 10.1063/1.2825280.

[120] R.D. Shannon. Revised Effective Ionic Radii and Systematic Studies of Interatomie Distances in Halides and Chaleogenides. *Acta crystallographica section A: crystal physics, diffraction, theoretical and general crystallography*, 32(5):751–767, 1976. doi: 10.1107/S0567739476001551.

[121] U.S. Geological Survey. Mineral Commodity Summaries 2020: U.S. Geological Survey. Technical report, 2020.

[122] Cesar G. Fraga. Relevance, essentiality and toxicity of trace elements in human health. *Molecular Aspects of Medicine*, 26(4-5):235–244, 2005. doi: 10.1016/j.mam.2005.07.013.

[123] T. Ibn-Mohammed, S. C.L. Koh, I. M. Reaney, D. C. Sinclair, K. B. Mustapha, A. Acquaye, and D. Wang. Are lead-free piezoelectrics more environmentally friendly? *MRS Communications*, 7(1):1–7, 2017. doi: 10.1557/mrc.2017.10.

[124] Francesco Madaro. *Synthesis of textured $K_xNa_{1-x}NbO_3$ materials*. PhD thesis, Norwegian University of Science and Technology, 2010.

[125] Barbara Malič, Helena Razpotnik, Jurij Koruza, Samo Kokalj, Jena Cilenšek, and Marija Kosec. Linear thermal expansion of lead-free piezoelectric $K_{0.5}Na_{0.5}NbO_3$ ceramics in a wide temperature range. *Journal of the American Ceramic Society*, 94(8):2273–2275, 2011. doi: 10.1111/j.1551-2916.2011.04628.x.

[126] R. G. Rhodes. Barium titanate twinning at low temperatures. *Acta Crystallographica*, 4(2): 105–110, 1951. doi: 10.1107/s0365110x51000374.

[127] Barbara Malič, Jurij Koruza, Jitka Hreščak, Janez Bernard, Ke Wang, John G. Fisher, and Andreja Benčan. Sintering of lead-free piezoelectric sodium potassium niobate ceramics. *Materials*, 8(12):8117–8146, 2015. doi: 10.3390/ma8125449.

[128] Edward L. Wolf. *Quantum nanoelectronics: An introduction to electronic nanotechnology and quantum computing*. John Wiley and Sons, 2015. ISBN 978-3-527-40749-1.

[129] Manish Kumar Mishra, Vikas Dubey, P. M. Mishra, and Isharat Khan. MEMS Technology: A Review. *Journal of Engineering Research and Reports*, 4(1):1–24, 2019. doi: 10.9734/jerr/2019/v4i116891.

[130] Teodor Gotszalk. From MEMS to NEMS. In Paolo Di Barba and Wiak Slawomir, editors, *MEMS: Field Models and Optimal Design*, pages 115–141. Springer, 2020. doi: 10.1007/978-3-030-21496-8_12.

[131] Milton Ohring. *Materials science of thin films*. Elsevier, 2 edition, 2001. ISBN 0-12-524975-6.

[132] S. Trolier-Mckinstry and P. Muralt. Thin film piezoelectrics for MEMS. *Journal of Electroceramics*, 12(1-2):7–17, 2004. doi: 10.1023/B:JECR.0000033998.72845.51.

[133] Paul Muralt, Ronald G. Polcawich, and Susan Trolier-Mckinstry. Piezoelectric Thin Films for Sensors, Actuators, and Energy Harvesting. *MRS Bulletin*, 34(9):658–664, 2009.

[134] Nazanin Bassiri-Gharb, Yaser Bastani, and Ashley Bernal. Chemical solution growth of ferroelectric oxide thin films and nanostructures. *Chemical Society Review*, 43:2125–2140, 2014. doi: 10.1039/c3cs60250h.

[135] Paul Muralt. Piezoelectric thin films for MEMS. *Integrated Ferroelectrics*, 17(1-4):297–307, 1997. doi: 10.1080/10584589708013004.

[136] A. G. Evans and J. W. Hutchinson. The thermomechanical integrity of thin films and multilayers. *Acta Metallurgica Et Materialia*, 43(7):2507–2530, 1995. doi: 10.1016/0956-7151(94)00444-M.

[137] Lei Zhang, Yakun Yuan, Jason Lapano, Matthew Brahlek, Shiming Lei, Bernd Kabius, Venkatraman Gopalan, and Roman Engel-Herbert. Continuously Tuning Epitaxial Strains by Thermal Mismatch. *ACS Nano*, 12(2):1306–1312, 2018. doi: 10.1021/acsnano.7b07539.

[138] Meng Jun Zhou, Jian Jun Wang, Long Qing Chen, and Ce Wen Nan. Strain, temperature, and electric-field effects on the phase transition and piezoelectric responses of $K_{0.5}Na_{0.5}NbO_3$ thin films. *Journal of Applied Physics*, 123(15):154106, 2018. doi: 10.1063/1.5027505.

[139] Alexander Tkach, Andr Santos, Sebastian Zlotnik, Ricardo Serrazina, Olena Okhay, Igor Bdikin, Maria Elisabete Costa, and Paula M Vilarinho. Strain-Mediated Substrate Effect on the Dielectric and Ferroelectric Response of Potassium Sodium Niobate Thin Films. *Coatings*, 8:449, 2018. doi: 10.3390/coatings8120449.

[140] Liqiang Xu, Feng Chen, Feng Jin, Da Lan, Lili Qu, Kexuan Zhang, Zixun Zhang, Guanyin Gao, Haoliang Huang, Tian Li, Fapei Zhang, Ke Wang, Zhen Zhou, and Wenbin Wu. Tuning electrical properties and phase transitions through strain engineering in lead-free ferroelectric $K_{0.5}Na_{0.5}NbO_3$-$LiTaO_3$-$CaZrO_3$ thin films. *Applied Physics Letters*, 115(20):202901, 2019. doi: 10.1063/1.5125734.

[141] Bo Wang, Hao Nan Chen, Jian Jun Wang, and Long Qing Chen. Ferroelectric domain structures and temperature-misfit strain phase diagrams of $K_{1-x}Na_xNbO_3$ thin films: A phase-field study. *Applied Physics Letters*, 115(9):092902, 2019. doi: 10.1063/1.5116910.

[142] P. A. Langjahr, F. F. Lange, T. Wagner, and M. Rühle. Lattice mismatch accommodation in perovskite films on perovskite substrates. *Acta Materialia*, 46(3):773–785, 1998. doi: 10.1016/S1359-6454(97)00259-0.

[143] J. Gazquez, Shameek Bose, M. Sharma, M. A. Torija, S. J. Pennycook, C. Leighton, and M. Varela. Lattice mismatch accommodation via oxygen vacancy ordering in epitaxial $La_{0.5}Sr_{0.5}CoO_{3-delta}$ thin films. *APL Materials*, 1(1):012105, 2013. doi: 10.1063/1.4809547.

[144] Robert W. Schwartz, Theodor Schneller, and Rainer Waser. Chemical solution deposition of electronic oxide films. *Comptes Rendus Chimie*, 7:433–461, 2004. doi: 10.1016/j.crci.2004.01.007.

[145] Helena Bruncková, L'Ubomír Medvecký, and Pavol Hvizdoš. Effect of substrate on phase formation and surface morphology of sol-gel lead-free $KNbO_3$, $NaNbO_3$, and $K_{0.5}Na_{0.5}NbO_3$ thin films. *Chemical Papers*, 66(8):748–756, 2012. doi: 10.2478/s11696-012-0190-y.

[146] Mare Lethieeq, Franck Levassort, Dominique Certon, and Pascal Tran-Huu-Hue. Piezoelectric Transducer Design for Medical Diagnosis and NDE. In Ahmad Safari and E. K. Akdogan, editors, *Piezoelectric and Acoustic Materials for Transducer Applications*, pages 191–216. Springer Science and Business Media, 2008. doi: 10.1007/978-0-387-76540-2_10.

[147] Asif Khan, Zafar Abas, Heung Soo Kim, and Il Kwon Oh. Piezoelectric thin films: An integrated review of transducers and energy harvesting. *Smart Materials and Structures*, 25(5):053002, 2016. doi: 10.1088/0964-1726/25/5/053002.

[148] Suvrajyoti Mishra, Lakshmi Unnikrishnan, Sanjay Kumar Nayak, and Smita Mohanty. Advances in Piezoelectric Polymer Composites for Energy Harvesting Applications: A Systematic Review. *Macromolecular Materials and Engineering*, 304(1):1800463, 2019. doi: 10.1002/mame.201800463.

[149] Abhijit Biswas, Ilker S. Bayer, Alexandru S. Biris, Tao Wang, Enkeleda Dervishi, and Franz Faupel. Advances in top-down and bottom-up surface nanofabrication: Techniques, applications and future prospects. *Advances in Colloid and Interface Science*, 170(1-2):2–27, 2012. doi: 10.1016/j.cis.2011.11.001.

[150] Kenneth C. Cadien. Chemical Mechanical Polishing. In Krishna Seshan, editor, *Handbook of thin film deposition processes and techniques*, pages 501–512. William Andrew, 2 edition, 2001.

[151] Anoop N. Samant and Narendra B. Dahotre. Laser machining of structural ceramics-A review. *Journal of the European Ceramic Society*, 29(6):969–993, 2009. doi: 10.1016/j.jeurceramsoc.2008.11.010.

[152] Geoffrey A. Ozin and André Arsenault. *Nanochemistry: a chemical approach to nanomaterials*. Royal Society of Chemistry, 2 edition, 2015. ISBN 978-1-84755-895-4.

[153] K.-H. Habig. Chemical vapor deposition and physical vapor deposition coatings: Properties, tribological behavior, and applications. *Journal of Vacuum Science and Technology A*, 4(6):2832–2843, 1986. doi: 10.1116/1.573687.

[154] Donald M. Mattox. *Handbook of physical vapor deposition (PVD) processing*. William Andrew, 2 edition, 2010. ISBN 978-0-8155-2037-5.

[155] Donald M. Mattox. Physical vapor deposition (PVD) processes. *Metal Finishing*, 100:394–408, 2002. doi: 10.1016/S0026-0576(00)80350-5.

[156] Hugh O. Pierson. *Handbook of chemical vapor deposition: principles, technology and applications*. William Andrew, 1999. ISBN 0-8155-1432-8.

[157] Jan Otto Carlsson and Peter M. Martin. Chemical Vapor Deposition. In *Handbook of Deposition Technologies for Films and Coatings*, pages 314–363. Elsevier Ltd., third edit edition, 2010. doi: 10.1016/B978-0-8155-2031-3.00007-7.

[158] P. R. Willmott and J. R. Huber. Pulsed laser vaporization and deposition. *Reviews of Modern Physics*, 72(1):315–328, 2000. doi: 10.1103/revmodphys.72.315.

[159] H. M. Christen and G. Eres. Recent advances in pulsed-laser deposition of complex oxides. *Journal of Physics Condensed Matter*, 20(26):264005, 2008. doi: 10.1088/0953-8984/20/26/264005.

[160] P. J. Kelly and R. D. Arnell. Magnetron sputtering: A review of recent developments and applications. *Vacuum*, 56(3):159–172, 2000. doi: 10.1016/S0042-207X(99)00189-X.

[161] D. Depla, S. Mahieu, and J. E. Greene. Sputter Deposition Processes. In *Handbook of Deposition Technologies for Films and Coatings*, pages 253–296. Elsevier Ltd., third edit edition, 2010. doi: 10.1016/B978-0-8155-2031-3.00005-3.

[162] W. F. van Dorp and C. W. Hagen. A critical literature review of focused electron beam induced deposition. *Journal of Applied Physics*, 104(8), 2008. doi: 10.1063/1.2977587.

[163] Ian G. Brown. Cathodic arc deposition of films. *Annual Review of Materials Science*, 28(1):243–269, 1998. doi: 10.1146/annurev.matsci.28.1.243.

[164] S. Aisenberg and R. W. Chabot. Physics of Ion Plating and Ion Beam Deposition. *Journal of Vacuum Science and Technology*, 10(1):104–107, 1973. doi: 10.1116/1.1317915.

[165] Choong-Rae Cho, Alex Grishin, and Byung-Moo Moon. Ferroelectric $Na_{0.5}K_{0.5}NbO_3$ thin films by pulsed laser deposition. *Integrated Ferroelectrics*, 31(1-4):35–45, 2000. doi: 10.1080/10584580008215638.

[166] Takehisa Saito, Takahiro Wada, Hideaki Adachi, and Isaku Kanno. Pulsed laser deposition of high-quality $(K,Na)NbO_3$ thin films on $SrTiO_3$ substrate using high-density ceramic targets. *Japanese Journal of Applied Physics, Part 1: Regular Papers and Short Notes and Review Papers*, 43:6627–6631, 2004. doi: 10.1143/JJAP.43.6627.

[167] J. Miao, X. G. Xu, Y. Jiang, L. X. Cao, and B. R. Zhao. Ionized-oxygen vacancies related dielectric relaxation in heteroepitaxial $K_{0.5}Na_{0.5}NbO_3/La_{0.67}Sr_{0.33}MnO_3$ structure at elevated temperature. *Applied Physics Letters*, 95(13):132905, 2009. doi: 10.1063/1.3242009.

[168] Seiji Yamazoe, Yuzo Miyoshi, Kazuki Komaki, Hideaki Adachi, and Takahiro Wada. Ferroelectric properties of $(Na_{0.5}K_{0.5})NbO_3$-based thin films deposited on Pt/(001)MgO substrate by pulsed laser deposition with $NaNbO_3$ buffer layer. *Japanese Journal of Applied Physics*, 48:09KA13, 2009. doi: 10.1143/JJAP.48.09KA13.

[169] Aifen Tian, Wei Ren, Peng Shi, Xiaofeng Chen, Xiaoqing Wu, and Xi Yao. Ferroelectric $(K_{0.44}Na_{0.52}Li_{0.04})(Nb_{0.86}Ta_{0.10}Sb_{0.04})O_3$ thin films prepared by pulsed laser deposition. *Ferroelectrics*, 406(1):62–67, 2010. doi: 10.1080/00150193.2010.484337.

[170] Yuan Hang Li, Feng Chen, Guan Yin Gao, Hao Ran Xu, and Wenbin Wu. Ferroelectric, dielectric and leakage current properties of epitaxial (K,Na)NbO_3-$LiTaO_3$-$CaZrO_3$ thin films. *Journal of Electroceramics*, 34(4):249–254, 2015. doi: 10.1007/s10832-014-9981-6.

[171] Minh D. Nguyen, Matthijn Dekkers, Evert P. Houwman, Hien T. Vu, Hung N. Vu, and Guus Rijnders. Lead-free $(K_{0.5}Na_{0.5})NbO_3$ thin films by pulsed laser deposition driving MEMS-based piezoelectric cantilevers. *Materials Letters*, 164:413–416, 2016. doi: 10.1016/j.matlet.2015.11.044.

[172] Xin Wang, Sveinn Olafsson, and Lynnette D Madsen. Growth and characterization of $Na_{0.5}K_{0.5}NbO_3$ thin films on polycrystalline $Pt_{80}Ir_{20}$ substrates. *Journal of Materials Research*, 17(5):1183–1191, 2002. doi: 10.1557/JMR.2002.0175.

[173] Mats Blomqvist, Jung Hyuk Koh, Sergey Khartsev, Alex Grishin, and Johanna Andréasson. High-performance epitaxial $Na_{0.5}K_{0.5}NbO_3$ thin films by magnetron sputtering. *Applied Physics Letters*, 81(2):337–339, 2002. doi: 10.1063/1.1492854.

[174] Kenji Shibata, Fumihito Oka, Akira Nomoto, Tomoyoshi Mishima, and Isaku Kanno. Crystalline Structure of Highly Piezoelectric (K,Na)NbO_3 Films Deposited by RF Magnetron Sputtering. *Japanese Journal of Applied Physics*, 47(12):8909–8913, 2008. doi: 10.1143/JJAP.47.8909.

[175] Kenji Shibata, Fumihito Oka, Akio Ohishi, Tomoyoshi Mishima, and Isaku Kanno. Piezoelectric Properties of (K,Na)NbO_3 Films Deposited by RF Magnetron Sputtering. *Applied Physics Express*, 1(1):011501, 2008. doi: 10.1143/APEX.1.011501.

[176] Tao Li, Genshui Wang, Kui Li, Nossikpendou Sama, Denis Remiens, and Xianlin Dong. Influence of LNO top electrodes on electrical properties of KNN/LNO thin films prepared by RF magnetron sputtering. *Journal of the American Ceramic Society*, 96(3):787–790, 2013. doi: 10.1111/jace.12047.

[177] Tao Li, Genshui Wang, Kui Li, Gang Du, Ying Chen, Zhiyong Zhou, Denis Rémiens, and Xianlin Dong. Electrical properties of lead-free KNN films on SRO/STO by RF magnetron sputtering. *Ceramics International*, 40:1195–1198, 2014. doi: 10.1016/j.ceramint.2013.07.005.

[178] Isaku Kanno, Takuya Mino, Shuichiro Kuwajima, Takaaki Suzuki, Hidetoshi Kotera, and Kiyotaka Wasa. Piezoelectric Properties of (K,Na)NbO_3 Thin Films Deposited on (001) $SrRuO_3$/Pt/MgO. *IEEE Transactions on Ultrasonics, Ferroelectrics, and Frequency Control*, 54(12):2562–2566, 2007. doi: 10.1109/TUFFC.2007.577.

[179] Gerald B. Stringfellow. *Organometallic vapor-phase epitaxy: theory and practice*. Elsevier, 1999. ISBN 978-0-12-673842-1.

[180] John L. Zilko. Metal Organic Chemical Vapor Deposition: Technology and Equipment. In Krishna Seshan, editor, *Handbook of thin film deposition processes and techniques*, chapter 4, pages 151–204. William Andrew, 2 edition, 2001. doi: 10.1016/B978-081551442-8.50009-2.

[181] Richard W. Johnson, Adam Hultqvist, and Stacey F. Bent. A brief review of atomic layer deposition: From fundamentals to applications. *Materials Today*, 17:236–246, 2014. doi: 10.1016/j.mattod.2014.04.026.

[182] Marian A. Herman and Helmut Sitter. *Molecular beam epitaxy: fundamentals and current status*. Springer Science and Business Media, 2 edition, 2012. ISBN 978-3-642-80062-7.

[183] Choong-Rae Cho. c-Axis oriented (Na,K)NbO_3 thin films on Si substrates using metalorganic chemical vapor deposition. *Materials Letters*, 57:781–786, 2002. doi: 10.1016/S0167-577X(02)00872-8.

[184] Choong-Rae Cho and Byung Moo Moon. (Na,K)NbO_3 thin films using metalorganic chemical vapor deposition. *Integrated Ferroelectrics*, 45:39–48, 2002. doi: 10.1080/713718216.

[185] Jutta Schwarzkopf, Dorothee Braun, Michael Hanke, Reinhard Uecker, and Martin Schmidbauer. Strain engineering of ferroelectric domains in in $K_xNa_{1-x}NbO_3$ epitaxial layers. *Frontiers in Materials*, 4:26, 2017. doi: 10.3389/fmats.2017.00026.

[186] Sijia Liang, Yang Dai, L. Von Helden, J. Schwarzkopf, and R. Wördenweber. Surface acoustic waves in strain-engineered $K_{0.7}Na_{0.3}NbO_3$ thin films. *Applied Physics Letters*, 113(5):052901, 2018. doi: 10.1063/1.5035464.

[187] Henrik Hovde Sønsteby, Ola Nilsen, and Helmer Fjellvåg. Atomic layer deposition of (K,Na)(Nb,Ta)O_3 thin films. *Journal of Vaccuum Science and Technology A*, 34(4):041508, 2016. doi: 10.1116/1.4953406.

[188] Henrik H. Sønsteby, Ola Nilsen, and Helmer Fjellvåg. Chemical Uniformity in Ferroelectric $K_xNa_{1-x}NbO_3$ Thin Films. *Global Challenges*, 3(10):1800114, 2019. doi: 10.1002/gch2.201800114.

[189] Robert W. Schwartz. Chemical Solution Deposition of Perovskite Thin Films. *Chemistry of Materials*, 9(11):2325–2340, 1997. doi: 10.1021/cm970286f.

[190] Robert W. Schwartz and Manoj Narayanan. Chemical solution deposition - basic principles. In David B. Mitzi, editor, *Solution Processing of Inorganic Materials*, chapter 2, pages 33–76. Wiley, 2009. doi: 10.1002/9780470407790.ch2.

[191] Iñigo Bretos, Ricardo Jiménez, Jesús Ricote, and M. Lourdes Calzada. Low-temperature crystallization of solution-derived metal oxide thin films assisted by chemical processes. *Chemical Society Reviews*, 47(2):291–308, 2018. doi: 10.1039/c6cs00917d.

[192] Theodor Schneller, Rainer Waser, Marija Kosec, and David Payne, editors. *Chemical Solution Deposition of Functional Oxide Thin Films*. Springer, 2013. ISBN 9783211993101.

[193] Marlies K. Van Bael, An Hardy, and Jules Mullens. Aqueous Precursor Systems. In Theodor Schneller, Rainer Waser, Marija Kosec, and David Payne, editors, *Chemical Solution Deposition of Functional Oxide Thin Films*, chapter 5, pages 93–140. Springer, 2013. doi: 10.1007/978-3-211-99311-8_5.

[194] C. Jeffrey Birnie. Spin Coating: Art and Science. In Theodor Schneller, Rainer Waser, Marija Kosec, and David Payne, editors, *Chemical Solution Deposition of Functional Oxide Thin Films*, chapter 11, pages 263–274. Springer, 2013. doi: 10.1007/978-3-211-99311-8_11.

[195] Robert W. Schwartz and Manoj Narayanan. Thermodynamics and Heating Processes. In Theodor Schneller, Rainer Waser, Marija Kosec, and David Payne, editors, *Chemical Solution Deposition of Functional Oxide Thin Films*, chapter 15, pages 343–382. Springer, 2013. doi: 10.1007/978-3-211-99311-8_15.

[196] Geon Tae Hwang, Myunghwan Byun, Chang Kyu Jeong, and Keon Jae Lee. Flexible Piezoelectric Thin-Film Energy Harvesters and Nanosensors for Biomedical Applications. *Advanced Healthcare Materials*, 4(5):646–658, 2015. doi: 10.1002/adhm.201400642.

[197] Suji Choi, Hyunjae Lee, Roozbeh Ghaffari, Taeghwan Hyeon, and Dae Hyeong Kim. Recent Advances in Flexible and Stretchable Bio-Electronic Devices Integrated with Nanomaterials. *Advanced Materials*, 28(22):4203–4218, 2016. doi: 10.1002/adma.201504150.

[198] Jie Chen, Noor Nabulsi, Weijie Wang, Ja Yeon Kim, Min Ki Kwon, and Jae Hyun Ryou. Output characteristics of thin-film flexible piezoelectric generators: A numerical and experimental investigation. *Applied Energy*, 255(July):113856, 2019. doi: 10.1016/j.apenergy.2019.113856.

[199] Hiromitsu Kozuka. Wet processing for the fabrication of ceramic thin films on plastics. *Journal of Materials Research*, 28(5):673–688, 2013. doi: 10.1557/jmr.2013.13.

[200] Mark D. Losego, Leslie H. Jimison, Jon F. Ihlefeld, and Jon Paul Maria. Ferroelectric response from lead zirconate titanate thin films prepared directly on low-resistivity copper substrates. *Applied Physics Letters*, 86(17):172906, 2005. doi: 10.1063/1.1919388.

[201] Makiko Kobayashi, Cheng Kuei Jen, and Daniel Lévesque. Flexible ultrasonic transducers. *IEEE Transactions on Ultrasonics, Ferroelectrics, and Frequency Control*, 53(8):1478–1486, 2006. doi: 10.1109/TUFFC.2006.1665105.

[202] Sebastjan Glinsek, Barbara Malic, and Marija Kosec. Low-Temperature Processing. In Theodor Schneller, Rainer Waser, Marija Kosec, and David Payne, editors, *Chemical Solution Deposition of Functional Oxide Thin Films*, chapter 18, pages 431–444. Springer, 2013. doi: 10.1007/978-3-211-99311-8_18.

[203] N. D. Scarisoreanu, F. Craciun, V. Ion, R. Birjega, A. Bercea, V. Dinca, M. Dinescu, L. E. Sima, M. Icriverzi, A. Roseanu, L. Gruionu, and G. Gruionu. Lead-Free Piezoelectric (Ba,Ca)(Zr,Ti)O_3 Thin Films for Biocompatible and Flexible Devices. *ACS applied materials and interfaces*, 9 (1):266–278, 2017. doi: 10.1021/acsami.6b14774.

[204] Nathan Jackson, Lynette Keeney, and Alan Mathewson. Flexible-CMOS and biocompatible piezoelectric AlN material for MEMS applications. *Smart Materials and Structures*, 22(11): 115033, 2013. doi: 10.1088/0964-1726/22/11/115033.

[205] Jean-Claude Grivel, Karl Thydén, Jacob R Bowen, and Astri Bjørnetun Haugen. Deposition of highly oriented (K,Na)NbO_3 films on flexible metal substrates. *Thin Solid Films*, 650 (December 2017):7–10, 2018. doi: 10.1016/j.tsf.2018.02.008.

[206] Chang Kyu Jeong, Jae Hyun Han, Haribabu Palneedi, Hyewon Park, Geon-tae Hwang, Boyoung Joung, Seong-gon Kim, Hong Ju Shin, Il-suk Kang, Jungho Ryu, and Keon Jae Lee. Comprehensive biocompatibility of nontoxic and high-output flexible energy harvester using lead-free piezoceramic thin film. *Applied Materials*, 5:074102, 2017. doi: 10.1063/1.4976803.

[207] Myunghwan Byun. Poly(vinylpyrrolidone)-modification of sol-gel films for flexible piezoelectric energy harvesting systems. *Thin Solid Films*, 663:31–36, 2018. doi: 10.1016/j.tsf.2018.08.014.

[208] Bingwei Lu, Ying Chen, Dapeng Ou, Hang Chen, Liwei Diao, Wei Zhang, Jun Zheng, Weiguo Ma, Lizhong Sun, and Xue Feng. Ultra-flexible Piezoelectric Devices Integrated with Heart to Harvest the Biomechanical Energy. *Scientific Reports*, 5:16065, 2015. doi: 10.1038/srep16065.

[209] Dong Kyu Lee, Sungjoo Kim, Sein Oh, Jae Young Choi, Jong Lam Lee, and Hak Ki Yu. Water-Soluble Epitaxial NaCl Thin Film for Fabrication of Flexible Devices. *Scientific Reports*, 7(1): 1–7, 2017. doi: 10.1038/s41598-017-09603-5.

[210] Mao Hua Zhang, Hao Cheng Thong, Yi Xue Lu, Wei Sun, Jing Feng Li, and Ke Wang. (K,Na)NbO_3-based lead-free piezoelectric materials: An encounter with scanning probe microscopy. *Journal of the Korean Ceramic Society*, 54(4):261–271, 2017. doi: 10.4191/kcers.2017.54.4.10.

[211] Y. Nakashima, W. Sakamoto, H. Maiwa, T. Shimura, and T. Yogo. Lead-Free Piezoelectric (K,Na)NbO_3 Thin Films Derived from Metal Alkoxide Precursors. *The Japan Society of Applied Physics*, 46(14):L311–L313, 2007. doi: 10.1143/JJAP.46.L311.

[212] C. W. Ahn, S. Y. Lee, H. J. Lee, A. Ullah, J. S. Bae, E. D. Jeong, J. S. Choi, B. H. Park, and I. W. Kim. The effect of K and Na excess on the ferroelectric and piezoelectric properties of $K_{0.5}Na_{0.5}NbO_3$ thin films. *Journal of Physics D: Applied Physics*, 42(21):1–5, 2009. doi: 10.1088/0022-3727/42/21/215304.

[213] Phoi Chin Goh, Kui Yao, and Zhong Chen. Lead-free piezoelectric ($K_{0.5}Na_{0.5}$)NbO_3 thin films derived from chemical solution modified with stabilizing agents. *Applied Physics Letters*, 97 (10):102901, 2010. doi: 10.1063/1.3488808.

[214] Naoya Kondo, Wataru Sakamoto, Bong-yeon Lee, Takashi Iijima, Jun Kumagai, Makoto Moriya, and Toshinobu Yogo. Improvement in Ferroelectric Properties of Chemically Synthesized Lead-Free Piezoelectric (K,Na)(Nb,Ta)O_3 Thin Films by Mn Doping. *Japanese Journal of Applied Physics*, 49:09MA04, 2010. doi: 10.1143/JJAP.49.09MA04.

[215] Sun Young Lee, Chang Won Ahn, Jin Soo Kim, Aman Ullah, Hai Joon Lee, Hak-In Hwang, Jin Sik Choi, Bae Ho Park, and Ill Won Kim. Enhanced piezoelectric properties of Ta substituted-($K_{0.5}Na_{0.5}$)NbO_3 films: A candidate for lead-free piezoelectric thin films. *Journal of Alloys and Compounds*, 509(20):L194–L198, 2011. doi: 10.1016/j.jallcom.2011.03.031.

[216] Sun Young Lee, Jin Soo Kim, Chang Won Ahn, Aman Ullah, Hai Joon Lee, and Ill Won Kim. Influence of piezoelectric property on annealing temperature of Ta-substituted ($K_{0.5}Na_{0.5}$)NbO_3 thin films by chemical solution deposition. *Current Applied Physics*, 11:S157–S160, 2011. doi: 10.1016/j.cap.2011.01.032.

[217] Phoi Chin Goh, Kui Yao, and Zhong Chen. Lithium diffusion in (Li,K,Na)NbO_3 piezoeletric thin films and the resulting approach for enhanced performance properties. *Applied Physics Letters*, 99:092902, 2011. doi: 10.1063/1.3631761.

[218] C. W. Ahn, Hae Jin Seog, Aman Ullah, Sun Young Lee, Jin Won Kim, Sang Su Kim, Moonkyu Park, Kwangsoo No, and Ill Won Kim. Effect of Ta content on the phase transition and piezoelectric properties of lead-free ($K_{0.48}Na_{0.48}Li_{0.04}$) ($Nb_{0.995-x}Mn_{0.005}Ta_x$)$O_3$ thin film. *Journal of Applied Physics*, 111:024110, 2012. doi: 10.1063/1.3680882.

[219] Takumi Matsuda, Wataru Sakamoto, Bong-yeon Lee Takashi, Iijima Jun, Kumagai Makoto, and Moriya Toshinobu. Electrical Properties of Lead-Free Ferroelectric Mn-Doped $K_{0.5}Na_{0.5}NbO_3$-$CaZrO_3$ Thin Films Prepared by Chemical Solution Deposition. *Japanese Journal of Applied Physics*, 51:09LA03, 2012. doi: 10.1143/JJAP.51.09LA03.

[220] Qi Yu, Jing-Feng Li, Wei Sun, Zhen Zhou, Ying Xu, Zhen-Kun Xie, Feng-Ping Lai, and Qing-Ming Wang. Electrical properties of $K_{0.5}Na_{0.5}NbO_3$ thin films grown on Nb:$SrTiO_3$ single-crystalline substrates with different crystallographic orientations. *Journal of Applied Physics*, 113:024101, 2013. doi: 10.1063/1.4773542.

[221] Lingyan Wang, Wei Ren, Phoi Chin Goh, Kui Yao, Peng Shi, Xiaoqing Wu, and Xi Yao. Structures and electrical properties of Mn- and Co-doped lead-free ferroelectric $K_{0.5}Na_{0.5}NbO_3$ films prepared by a chemical solution deposition method. *Thin Solid Films*, 537:65–69, 2013. doi: 10.1016/j.tsf.2013.04.045.

[222] Lingyan Wang, Wei Ren, Peng Shi, and Xiaoqing Wu. Cobalt doping effects on structures and electrical properties of lead-free ferroelectric $K_{0.5}Na_{0.5}NbO_3$ films. *Journal of Alloys and Compounds*, 608:202–206, 2014. doi: 10.1016/j.jallcom.2014.04.118.

[223] Yumei Wang, Kui Yao, Meysam Sharifzadeh Mirshekarloo, Francis Eng, and Hock Tay. Effects and Mechanism of Combinational Chemical Agents on Solution-Derived $K_{0.5}Na_{0.5}NbO_3$

Piezoelectric Thin Films. *Journal of the American Ceramic Society*, 99(5):1631–1636, 2016. doi: 10.1111/jace.14139.

[224] Sung Sik Won, Joonhee Lee, Vineeth Venugopal, Dong-joo Kim, Jinkee Lee, Ill Won Kim, Angus I Kingon, and Seung-hyun Kim. Lead-free Mn-doped $(K_{0.5},Na_{0.5})NbO_3$ piezoelectric thin films for MEMS-based vibrational energy harvester applications. *Applied Physics Letters*, 108: 232908, 2016. doi: 10.1063/1.4953623.

[225] Fengping Lai, Jing-Feng Li, Zhi-Xiang Zhu, and Ying Xu. Influence of Li content on electrical properties of highly piezoelectric (Li,K,Na)NbO_3 thin films prepared by sol-gel processing. *Journal of Applied Physics*, 106(6):064101, 2009. doi: 10.1063/1.3223320.

[226] Alexander Tkach, André Santos, Sebastian Zlotnik, Ricardo Serrazina, Olena Okhay, Igor Bdikin, Maria Elisabete Costa, and Paula M. Vilarinho. Effect of solution conditions on the properties of sol-gel derived potassium sodium niobate thin films on platinized sapphire substrates. *Nanomaterials*, 9(11):1600, 2019. doi: 10.3390/nano9111600.

[227] Yumei Wang, Kui Yao, Xian Qin, Meysam Sharifzadeh Mirshekarloo, Xiaogang Liu, and Francis Eng Hock Tay. High Piezoelectric Performance and Phase Transition in Stressed Lead-Free (1–x)(K,Na)(Sb,Nb)O_3-x(Bi,Na,K)ZrO_3 Thin Films. *Advanced Electronic Materials*, 3(7): 1700033, 2017. doi: 10.1002/aelm.201700033.

[228] Kiyotaka Tanaka, Ken ichi Kakimoto, and Hitoshi Ohsato. Fabrication of highly oriented lead-free (Na, K)NbO_3 thin films at low temperature by Sol-Gel process. *Journal of Crystal Growth*, 294(2):209–213, 2006. doi: 10.1016/j.jcrysgro.2006.05.041.

[229] Fengping Lai and Jing Feng Li. Sol-gel processing of lead-free (Na,K)NbO_3 ferroelectric films. *Journal of Sol-Gel Science and Technology*, 42(3):287–292, 2007. doi: 10.1007/s10971-007-0741-9.

[230] Fengping Lai and Jing Feng Li. Sol-gel processing and characterization of (Na,K)NbO_3 lead-free ferroelectric films. *Ferroelectrics*, 358:181–187, 2007. doi: 10.1080/00150190701537257.

[231] Yoshifumi Nakashima, Wataru Sakamoto, Tetsuo Shimura, and Toshinobu Yogo. Chemical processing and characterization of ferroelectric (K,Na)NbO_3 thin films. *Japanese Journal of Applied Physics*, 46(10B):6971–6975, 2007. doi: 10.1143/JJAP.46.6971.

[232] X Q Wu, L Y Wang, W Ren, X Yan, P Shi, X F Chen, and X Yao. Preparation and Properties of (110) Oriented Lead-Free Sodium Potassium Niobate Thin Films by MOD Method. *Ferroelectrics*, 367(January 2015):61–66, 2008. doi: 10.1080/00150190802365947.

[233] Chang Won Ahn, E. D. Jeong, Sun Young Lee, Hai Joon Lee, Sun Hee Kang, and Ill Won Kim. Enhanced ferroelectric properties of $LiNbO_3$ substituted $Na_{0.5}K_{0.5}NbO_3$ thin films grown by chemical solution deposition. *Applied Physics Letters*, 93:212905, 2008. doi: 10.1063/1.3037214.

[234] X. Yan, W. Ren, X. Wu, P. Shi, and X. Yao. Lead-free (K,Na)NbO_3 ferroelectric thin films: Preparation, structure and electrical properties. *Journal of Alloys and Compounds*, 508:129–132, 2010. doi: 10.1016/j.jallcom.2010.08.025.

[235] Sun Young Lee, Jin Soo Kim, Chang Won Ahn, Hak In Hwang, and Won Kim. Impedance spectroscopy and relaxation phenomena of (Na,K) excess $Na_{0.5}K_{0.5}NbO_3$ thin films grown by chemical solution deposition. *Thin Solid Films*, 519(2):947–951, 2010. doi: 10.1016/j.tsf.2010.08.133.

[236] Anirban Chowdhury, Jonathan Bould, Michael G. S. Londesborough, and Steven J. Milne. Fundamental Issues in the Synthesis of Ferroelectric $Na_{0.5}K_{0.5}NbO_3$ Thin Films by Sol-Gel Processing. *Chemistry of Materials*, 22(10):3862–3874, 2010. doi: 10.1021/cm903697j.

[237] Lingyan Wang, Wei Ren, Peng Shi, Xiaofeng Chen, Xiaoqing Wu, and Xi Yao. Enhanced ferroelectric properties in Mn-doped $K_{0.5}Na_{0.5}NbO_3$ thin films derived from chemical solution deposition. *Applied Physics Letters*, 97(7):072902, 2010. doi: 10.1063/1.3479530.

[238] Yoshifumi Nakashima, Wataru Sakamoto, and Toshinobu Yogo. Processing of highly oriented (K,Na)NbO_3 thin films using a tailored metal-alkoxide precursor solution. *Journal of the European Ceramic Society*, 31(14):2497–2503, 2011. doi: 10.1016/j.jeurceramsoc.2011.04.031.

[239] Chiwon Kang, Jung-Hyun Park, Dongna Shen, Hosang Ahn, Minseo Park, and Dong-Joo Kim. Growth and characterization of $(K_{0.5}Na_{0.5})NbO_3$ thin films by a sol-gel method. *Journal of Sol-Gel Science and Technology*, 58:85–90, 2011. doi: 10.1007/s10971-010-2359-6.

[240] Sun Young Lee, Chang Won Ahn, Aman Ullah, Hae Jin Seog, Jin Soo Kim, Se Hwan Bae, and Ill Won Kim. Effect of Mn substitution on ferroelectric and leakage current characteristics of lead-free $(K_{0.5}Na_{0.5})(Mn_xNb_{1-x})O_3$ thin films. *Current Applied Physics*, 11(3):S266–S269, 2011. doi: 10.1016/j.cap.2011.03.050.

[241] Li Wang, Ruzhong Zuo, Longdong Liu, Hailin Su, Min Shi, Xiangcheng Chu, Xiaohui Wang, and Longtu Li. Preparation and characterization of sol-gel derived (Li,Ta,Sb) modified (K,Na)NbO_3 lead-free ferroelectric thin films. *Materials Chemistry and Physics*, 130(1-2):165–169, 2011. doi: 10.1016/j.matchemphys.2011.06.022.

[242] Alja Kupec, Barbara Malic, Jenny Tellier, Elena Tchernychova, Sebastjan Glinsek, and Marija Kosec. Lead-Free Ferroelectric Potassium Sodium Niobate Thin Films from Solution: Composition and Structure. *Journal of the American Ceramic Society*, 95(2):515–523, 2012. doi: 10.1111/j.1551-2916.2011.04892.x.

[243] J. Kwak, A. I. Kingon, and S. H. Kim. Lead-free $(Na_{0.5},K_{0.5})NbO_3$ thin films for the implantable piezoelectric medical sensor applications. *Materials Letters*, 82:130–132, 2012. doi: 10.1016/j.matlet.2012.05.079.

[244] Sun Young Lee, Hae Jin Seog, Chang Won Ahn, Aman Ullah, and Ill Won Kim. Interfacial Dead Layers on Lead Free Ferroelectric $(K_{0.5}Na_{0.5})(Mn_{0.005}Nb_{0.995})O_3$ Thin Films. *Japanese Journal of Applied Physics*, 51:09MD03, 2012. doi: 10.1143/JJAP.51.09MD03.

[245] Jungmin Park, Sung Sik Won, Chang Won Ahn, and Ill Won Kim. Ferroelectric photocurrent effect in polycrystalline lead-free $(K_{0.5}Na_{0.5})(Mn_{0.005}Nb_{0.995})O_3$ thin film. *Journal of the American Ceramic Society*, 96(1):146–150, 2013. doi: 10.1111/j.1551-2916.2012.05430.x.

[246] H. Brunckova, L. Medvecký, and P. Hvizdoš. Effect of substrate on microstructure and mechanical properties of sol-gel prepared (K, Na)NbO_3 thin films. *Materials Science and Engineering B: Solid-State Materials for Advanced Technology*, 178(4):254–262, 2013. doi: 10.1016/j.mseb.2012.12.003.

[247] Ting Lu, Kongjun Zhu, Jinsong Liu, Jing Wang, and Jinhao Qiu. Lead-free (K,Na)NbO_3 thin films derived from chemical solution deposition modified with EDTA. *Journal of Materials Science*, 25:1112–1116, 2014. doi: 10.1007/s10854-013-1696-y.

[248] Deqing Zhang, Fangyuan Zheng, Xiuying Yang, Hongmei Liu, and Maosheng Cao. Preparation and ferroelectric properties of $K_{0.5}Na_{0.5}NbO_3$ thin films derived from non-alcohol niobium salt sol-gel process. *Integrated Ferroelectrics*, 4587(September 2016):673–678, 2014. doi: 10.1080/10584587.2014.904166.

[249] Qi Yu, Jing-Feng Li, Yanna Chen, Li-Qian Cheng, Wei Sun, Zhen Zhou, and Zhanjie Wang. Effect of Pyrolysis Temperature on Sol-Gel Synthesis of Lead-free Piezoelectric (K,Na)NbO_3 Films on Nb:$SrTiO_3$ Substrates. *Journal of the American Ceramic Society*, 97:107–113, 2014. doi: 10.1111/jace.12675.

[250] Alja Kupec and Barbara Malič. Structural and dielectric properties of the lead-free (1-x)$K_{0.5}Na_{0.5}NbO_3$-x$SrTiO_3$ thin films from solutions. *Journal of Alloys and Compounds*, 596:32–38, 2014. doi: 10.1016/j.jallcom.2014.01.193.

[251] Alja Kupec, Hana Uršič, Raluca C. Frunză, Elena Tchernychova, and Barbara Malič. Microstructure-dependent leakage-current properties of solution-derived $(K_{0.5}Na_{0.5})NbO_3$ thin films. *Journal of the European Ceramic Society*, 35(13):3507–3511, 2015. doi: 10.1016/j.jeurceramsoc.2015.05.019.

[252] Helena Brunckova, L'ubomír Medvecký, Pavol Hvizdoš, and Juraj Durišin. Structural and nanomechanical properties of sol-gel prepared (K, Na)NbO_3 thin films. *Surface and Interface Analysis*, 47(11):1063–1071, 2015. doi: 10.1002/sia.5846.

[253] X. Vendrell, O. Raymond, D. A. Ochoa, J. E. García, and L. Mestres. Growth and physical properties of highly oriented La-doped (K,Na)NbO_3 ferroelectric thin films. *Thin Solid Films*, 577:35–41, 2015. doi: 10.1016/j.tsf.2015.01.038.

[254] L. Yao, K. Zhu, J. Wang, J. Liu, J. Qiu, M. Cheng, and Q. Gu. Annealing temperature effects on the electrical properties of (K,Na)NbO_3 thin film fabricated by a sol-gel process with a citrate precursor solution. *Ferroelectrics*, 493:47–53, 2016. doi: 10.1080/00150193.2016.1133213.

[255] Xiaomeng Li, Xiaoqing Wu, Peng Shi, and Zuo Guang Ye. Lead-Free piezoelectric diaphragm biosensors based on micro-machining technology and chemical solution deposition. *Sensors*, 16 (1):69, 2016. doi: 10.3390/s16010069.

[256] Byung Hoon Kim, Sun A. Yang, Sin Wook Kang, Gi Ppeum Choi, Sam Yeon Cho, Jin Kyu Han, Gyoung Ja Lee, Min Ku Lee, Hae Jin Seog, Ill Won Kim, and Sang Don Bu. Change of electrical properties of ($K_{0.5}Na_{0.5}$) ($Mn_{0.005}Nb_{0.995}$)O_3 thin films induced by gamma-ray irradiation. *Current Applied Physics*, 16(5):539–544, 2016. doi: 10.1016/j.cap.2016.01.009.

[257] Jin Luo, Wei Sun, Zhen Zhou, Yu Bai, Zhan Jie Wang, Guo Tian, Deyang Chen, Xingsen Gao, Fangyuan Zhu, and Jing-feng Li. Domain Evolution and Piezoelectric Response across Thermotropic Phase Boundary in (K,Na)NbO_3-Based Epitaxial Thin Films. *Applied Materials and Interfaces*, 9:13315–13322, 2017. doi: 10.1021/acsami.7b02263.

[258] Xinxiu Zhang, Jinsong Liu, Kongjun Zhu, Jing Wang, and Ziquan Li. Effects of Mn doping on dielectric and ferroelectric characteristics of lead-free (K,Na,Li)NbO_3 thin films grown by chemical solution deposition. *Journal of Materials Science: Materials in Electronics*, 28(1): 487–492, 2017. doi: 10.1007/s10854-016-5547-5.

[259] Shammi Kumar and Nagesh Thakur. Synthesis, structural and optical properties of $K_{0.5}Na_{0.5}NbO_3$ thin films prepared by spin coating route. *Bulletin of Materials Science*, 42 (4):135, 2019. doi: 10.1007/s12034-019-1790-8.

[260] Su Wei Zhang, Jin Luo, Zhen Zhou, and Jing Feng Li. Sol-gel processed highly (100)-textured (K, Na)NbO_3-based lead-free thin films: Effect of pyrolysis temperature. *Journal of the American Ceramic Society*, 102(5):2696–2705, 2019. doi: 10.1111/jace.16149.

[261] Wei Zhang, Haiyong Zhu, Xuehua Zhang, Hao Wu, Jianqiu Bao, and Fangren Hu. Structural and electrical study of highly (100)-oriented KNN films fabricated by a sol-gel non-alkoxide process. *Ceramics International*, 14(17):22156–22162, 2019. doi: 10.1016/j.ceramint.2019.07.234.

[262] Chao Zhao, Xianghe Meng, Wen Wang, and Yu Zhou. Energy storage performance of (K, Na)NbO_3 ferroelectric thin films with Mn-Ta and Mn-Ti co-doping. *Ceramics International*, 45(11):13772–13779, 2019. doi: 10.1016/j.ceramint.2019.04.073.

[263] Jin Luo, Suwei Zhang, Zhen Zhou, Yichi Zhang, Hyun Young Lee, Zhenxing Yue, and Jing Feng Li. Phase transition and piezoelectricity of $BaZrO_3$-modified (K,Na)NbO_3 lead-free piezoelectric thin films. *Journal of the American Ceramic Society*, 102(5):2770–2780, 2019. doi: 10.1111/jace.16172.

[264] Veronika Kovacova, Jung In Yang, Leonard Jacques, Song Won Ko, Wanlin Zhu, and Susan Trolier-Mckinstry. Comparative solution synthesis of Mn doped (Na,K)NbO_3 thin films. *Chemistry-A European Journal*, 26:1–10, 2020. doi: 10.1002/chem.202000537.

[265] Xingdong Zhang and David Williams, editors. *Definitions of biomaterials for the twenty-first century*. Elsevier, 2019. ISBN 978-0-12-818291-8.

[266] Joon Park and Roderic S. Lakes. *Biomaterials: an introduction*. Springer Science and Business Media, 2007. ISBN 978-0-387-37880-0.

[267] David F. Williams. On the nature of biomaterials. *Biomaterials*, 30(30):5897–5909, 2009. doi: 10.1016/j.biomaterials.2009.07.027.

[268] Buddy D. Ratner. A History of Biomaterials. In B. D. Ratner, A. S. Hoffman, F. J. Schoen, and J. E. Lemons, editors, *Biomaterials Science: An Introduction to Materials*, pages xli–liii. Academic Press, 3 edition, 2013. doi: 10.1016/B978-0-08-087780-8.00154-6.

[269] Joseph Lister. On the antiseptic principle in the practice of surgery. *British Medical Journal*, 2(351):246–248, 1867. doi: 10.1136/bmj.2.351.246.

[270] Ellis Harold and Sala Abdalla. *A History of Surgery*. CRC Press, 2018. ISBN 9780429867620.

[271] Larry L. Hench and Ian Thompson. Twenty-first century challenges for biomaterials. *Journal of the Royal Society Interface*, 7:S379–S391, 2010. doi: 10.1098/rsif.2010.0151.focus.

[272] Larry L. Hench and Julia M. Polak. Third-Generation Biomedical Materials. *Science*, 295 (5557):1014–1017, 2002. doi: 10.1126/science.1067404.

[273] J. Huang, X. Li, and Z. X. Guo. Biomechanical and biochemical compatibility in innovative biomaterials. In Jean-Pierre Boutrand, editor, *Biocompatibility and Performance of Medical Devices*, pages 23–46. Elsevier Ltd., 2 edition, 2020. doi: 10.1016/B978-0-85709-070-6.50004-3.

[274] Barry O. Weightman, Igor L. Paul, Robert M. Rose, Sheldon R. Simon, and Eric L. Radin. A comparative study of total hip replacement prostheses. *Journal of Biomechanics*, 6(3):299–311, 1973. doi: 10.1016/0021-9290(73)90052-3.

[275] T. D. Cronin and R. O. Brauer. Augmentation Mammaplasty. *The Surgical clinics of North America*, 51(2):441–452, 1971. doi: 10.1016/S0039-6109(16)39388-4.

[276] Larry L. Hench. Bioceramics: From Concept to Clinic. *Journal of the American Ceramic Society*, 74(7):1487–1510, 1991. doi: 10.1111/j.1151-2916.1991.tb07132.x.

[277] Larry L. Hench. The story of Bioglass®. *Journal of Materials Science: Materials in Medicine*, 17(11):967–978, 2006. doi: 10.1007/s10856-006-0432-z.

[278] Isabelle Denry and Julie A. Holloway. Ceramics for dental applications: A review. *Materials*, 3(1):351–368, 2010. doi: 10.3390/ma3010351.

[279] Yeun-Ho Joung. Development of Implantable Medical Devices: From an Engineering Perspective. *International neurourology journal*, 17:98–106, 2013. doi: 10.5213/inj.2013.17.3.98.

[280] Allan S. Hoffman. Section I.2: Classes of Materials Used in Medicine. In B. D. Ratner, A. S. Hoffman, F. J. Schoen, and J. E. Lemons, editors, *Biomaterials Science - An Introduction to Materials in Medicine*, chapter I.2.1-I.2., pages 63–392. Academic Press, 3 edition, 2013.

[281] Francesco Baino, Sepideh Hamzehlou, and Saeid Kargozar. Bioactive glasses: Where are we and where are we going? *Journal of Functional Biomaterials*, 9(1):25, 2018. doi: 10.3390/jfb9010025.

[282] Fergal J. O'Brien. Biomaterials and scaffolds for tissue engineering. *Materials Today*, 14(3): 88–95, 2011. doi: 10.1016/S1369-7021(11)70058-X.

[283] Larry L Hench. Biomaterials: a forecast for the future. *Biomaterials*, 19:1419–1423, 1998. doi: 10.1016/S0142-9612(98)00133-1.

[284] Market Research Future. Medical Implants Market Research Report - Global Forecast till 2023, 2019. URL https://www.marketresearchfuture.com/reports/medical-implant-market-2806.

[285] European Commission. Medical Devices, accessed 28.01.2020. URL https://ec.europa.eu/growth/sectors/medical-devices_nn.

[286] International Consortium of Investigative Journalists. International Medical Devices Database, , accessed 25.01.2020, 2019. URL https://www.icij.org/investigations/implant-files/.

[287] O. Furnes, J.-E. Gjertsen, G. Hallan, H. Visnes, T. Gundersen, A. M. Fenstad, I. A. Kvinnesland, E. Dybvik, and G. C. Kroken. Norwegian National Advisory Unit on Arthroplasty and Hip Fractures. Annual report. Technical report, 2019.

[288] Torkel Steen and S Platou Pacemaker. Norsk Pacemaker- og ICD-statistikk for 2017. *Hjerteforum*, 31(2):50–60, 2018.

[289] Eivind S. Platou. Norsk Pacemaker- og ICD-statistikk For 2018. *Hjerteforum*, 32(2), 2019.

[290] Meital Zilberman, editor. *Active Implants and Scaffolds for Tissue Regeneration*. Springer, Berlin, 2011. doi: 10.1007/978-3-642-18065-1.

[291] Amir A. Zadpoor and Jos Malda. Additive Manufacturing of Biomaterials, Tissues, and Organs. *Annals of Biomedical Engineering*, 45(1):1–11, 2017. doi: 10.1007/s10439-016-1719-y.

[292] Robert Lanza, Robert Langer, and Joseph P. Vacanti, editors. *Principles of tissue engineering*. Academic Press, 2011. ISBN 978-0-12-818422-6.

[293] Stephanie Knowlton, Shivesh Anand, Twisha Shah, and Savas Tasoglu. Bioprinting for Neural Tissue Engineering. *Trends in Neurosciences*, 41(1):31–46, 2018. doi: 10.1016/j.tins.2017.11.001.

[294] Livia Roseti, Valentina Parisi, Mauro Petretta, Carola Cavallo, Giovanna Desando, Isabella Bartolotti, and Brunella Grigolo. Scaffolds for Bone Tissue Engineering: State of the art and new perspectives. *Materials Science and Engineering C*, 78:1246–1262, 2017. doi: 10.1016/j.msec.2017.05.017.

[295] Dawit G. Seifu, Agung Purnama, Kibret Mequanint, and Diego Mantovani. Small-diameter vascular tissue engineering. *Nature Reviews Cardiology*, 10(7):410–421, 2013. doi: 10.1038/nrcardio.2013.77.

[296] Komal Vig, Atul Chaudhari, Shweta Tripathi, Saurabh Dixit, Rajnish Sahu, Shreekumar Pillai, Vida A. Dennis, and Shree R. Singh. Advances in Skin Regeneration Using Tissue Engineering. *International Journal of Molecular Sciences*, 18(4):789, 2017. doi: 10.3390/ijms18040789.

[297] Niamh Fahy, Mauro Alini, and Martin J. Stoddart. Mechanical stimulation of mesenchymal stem cells: Implications for cartilage tissue engineering. *Journal of Orthopaedic Research*, 36 (1):52–63, 2018. doi: 10.1002/jor.23670.

[298] Udayabhanu Jammalamadaka and Karthik Tappa. Recent Advances in Biomaterials for 3D Printing and Tissue Engineering. *Journal of Functional Biomaterials*, 9(1):22, 2018. doi: 10.3390/jfb9010022.

[299] R. Stuart Mackay. Radio Telemetering from Within the Human Body. *IRE Transactions on Medical Electronics*, ME-6(2):100–105, 1959. doi: 10.1109/IRET-ME.1959.5007926.

[300] Oscar Aquilina. A brief history of cardiac pacing. *Images in paediatric cardiology*, 8(2):17–81, 2006.

[301] William F House. Cochlear Implants. *Annals of Otology, Rhinology and Laryngology*, 85(3, pt 2):1–93, 1976. doi: 10.1177/00034894760850S303.

[302] C. N. Shealy, J. T. Mortimer, and J. B. Reswick. Electrical inhibition of pain by stimulation of the dorsal columns: preliminary clinical report. *Anesthesia and Analgesia*, 46(4):489–491, 1967. doi: 10.1213/00000539-196707000-00025.

[303] G. S. Brindley, C. E. Polkey, D. N. Rushton, and L. Cardozo. Sacral anterior root stimulators for bladder control in paraplegia: The first 50 cases. *Journal of Neurology, Neurosurgery and Psychiatry*, 49(10):1104–1114, 1986. doi: 10.1136/jnnp.49.10.1104.

[304] Melissa Matchett, Samuel F. Sears, Garrett Hazelton, Karian Kirian, Elynor Wilson, and Rajasekhar Nekkanti. The implantable cardioverter defibrillator: its history, current psychological impact and future. *Expert Review of Medical Devices*, 6(1):43–50, 2009. doi: 10.1586/17434440.6.1.43.

[305] David S. Haynes, Jadrien A. Young, George B. Wanna, and Michael E. Glasscock. Middle Ear Implantable Hearing Devices: An Overview. *Trends in Amplification*, 13(3):206–214, 2009. doi: 10.1177/1084713809346262.

[306] Ujwal Chaudhary, Niels Birbaumer, and Ander Ramos-Murguialday. Brain-computer interfaces for communication and rehabilitation. *Nature Reviews Neurology*, 12(9):513–525, 2016. doi: 10.1038/nrneurol.2016.113.

[307] Dennis Fitzpatrick. *Implantable electronic medical devices*. Elsevier, 2014. ISBN 978-0-12-416556-4.

[308] Ingelin Clausen and Thomas Glott. Development of Clinically Relevant Implantable Pressure Sensors: Perspectives and Challenges. *Sensors*, 14:17686–17702, 2014. doi: 10.3390/s140917686.

[309] Richard F. Weir, Phil R. Troyk, Glen A. DeMichele, Douglas A. Kerns, Jack F. Schorsch, and Huub Maas. Implantable myoelectric sensors (IMESs) for intramuscular electromyogram recording. *IEEE Transactions on Biomedical Engineering*, 56(1):159–171, 2008. doi: 10.1109/TBME.2008.2005942.

[310] Purushothaman Geethanjali. Myoelectric control of prosthetic hands: State-of-the-art review. *Medical Devices: Evidence and Research*, 9:247–255, 2016. doi: 10.2147/MDER.S91102.

[311] Susan D. Goodwin. Comparison of Body Temperatures of Goats, Horses, Sheep Measured with a Tympanic Infrared Thermometer, an Implantable Microchip Transponder, and a Rectal Thermometer. *Journal of the American Association for Laboratory Animal Science*, 37(3):51–55, 1998. ISSN 10600558.

[312] Jie Mei, Nico Riedel, Ulrike Grittner, Matthias Endres, Stefanie Banneke, and Julius Valentin Emmrich. Body temperature measurement in mice during acute illness: Implantable temperature transponder versus surface infrared thermometry. *Scientific Reports*, 8(1):1–10, 2018. doi: 10.1038/s41598-018-22020-6.

[313] Michele Brignole, Richard Sutton, Carlo Menozzi, Roberto Garcia-Civera, Angel Moya, Wouter Wieling, Dietrich Andresen, David G. Benditt, and Panos Vardas. Early application of an implantable loop recorder allows effective specific therapy in patients with recurrent suspected neurally mediated syncope. *European Heart Journal*, 27(9):1085–1092, 2006. doi: 10.1093/eurheartj/ehi842.

[314] U.S. Food and Drug Administration. FDA approves first continuous glucose monitoring system with a fully implantable glucose sensor and compatible mobile app for adults with diabetes, accessed 24.01.2020. URL https://tinyurl.com/ybtagrx3.

[315] Troy Sukhu, Michael J. Kennelly, and Raj Kurpad. Sacral neuromodulation in overactive bladder: A review and current perspectives. *Research and Reports in Urology*, 8:193–199, 2016. doi: 10.2147/RRU.S89544.

[316] Paul Verrills, Chantelle Sinclair, and Adele Barnard. A review of spinal cord stimulation systems for chronic pain. *Journal of Pain Research*, 9:481–492, 2016. doi: 10.2147/JPR.S108884.

[317] Lothar W. Kleiner, Jeremy C. Wright, and Yunbing Wang. Evolution of implantable and insertable drug delivery systems. *Journal of Controlled Release*, 181(1):1–10, 2014. doi: 10.1016/j.jconrel.2014.02.006.

[318] Malini Madhavan, Siva K. Mulpuru, Christopher J. McLeod, Yong Mei Cha, and Paul A. Friedman. Advances and Future Directions in Cardiac Pacemakers. *Journal of the American College of Cardiology*, 69(2):211–235, 2017. doi: 10.1016/j.jacc.2016.10.064.

[319] Christopher J. McLeod, Lucas Boersma, Hideo Okamura, and Paul A. Friedman. The subcutaneous implantable cardioverter defibrillator: State-of-the-art review. *European Heart Journal*, 38(4):247–257, 2017. doi: 10.1093/eurheartj/ehv507.

[320] Seeram Ramakrishna, Lingling TIan, Charlene Wang, Susan Liao, and Wee Eong Teo. *Medical Devices: Regulations, Standards and Practices*. Elsevier Ltd., 2015. ISBN 978-0-08-100291-9.

[321] Tahreem Yaqoob, Haider Abbas, and Mohammed Atiquzzaman. Security Vulnerabilities, Attacks, Countermeasures, and Regulations of Networked Medical Devices - A Review. *IEEE Communications Surveys and Tutorials*, 21(4):3723–3768, 2019. doi: 10.1109/COMST.2019.2914094.

[322] Ashraf Darwish, Gehad Ismail Sayed, and Aboul Ella Hassanien. The Impact of Implantable Sensors in Biomedical Technology on the Future of Healthcare Systems. *Intelligent Pervasive Computing Systems for Smarter Healthcare*, pages 67–89, 2019. doi: 10.1002/9781119439004.ch3.

[323] Carmen Camara, Pedro Peris-Lopez, and Juan E. Tapiador. Security and privacy issues in implantable medical devices: A comprehensive survey. *Journal of Biomedical Informatics*, 55:272–289, 2015. doi: 10.1016/j.jbi.2015.04.007.

[324] Anantha P. Chandrakasan, Naveen Verma, and Denis C. Daly. Ultralow-Power Electronics for Biomedical Applications. *Annual Review of Biomedical Engineering*, 10(1):247–274, 2008. doi: 10.1146/annurev.bioeng.10.061807.160547.

[325] Jens Cosedis Nielsen, Jens Christian Gerdes, and Niraj Varma. Infected cardiac-implantable electronic devices: Prevention, diagnosis, and treatment. *European Heart Journal*, 36(37):2484–2490, 2015. doi: 10.1093/eurheartj/ehv060.

[326] Larry M. Baddour, Yong Mei Cha, and Walter R. Wilson. Infections of Cardiovascular Implantable Electronic Devices. *New England Journal of Medicine*, 367(9):842–849, 2012. doi: 10.1056/NEJMcp1107675.

[327] Guangzu Zhang, Mingyu Li, Honglang Li, Qing Wang, and Shenglin Jiang. Harvesting Energy from Human Activity: Ferroelectric Energy Harvesters for Portable, Implantable, and Biomedical Electronics. *Energy Technology*, 6(5):791–812, 2018. doi: 10.1002/ente.201700622.

[328] Maria Teresa Todaro, Francesco Guido, Luciana Algieri, Vincenzo M. Mastronardi, Denis Desmaele, Gianmichele Epifani, and Massimo De Vittorio. Biocompatible, flexible, and compliant energy harvesters based on piezoelectric thin films. *IEEE Transactions on Nanotechnology*, 17 (2):220–230, 2018. doi: 10.1109/TNANO.2017.2789300.

[329] Faizan Ali, Waseem Raza, Xilin Li, Hajera Gul, and Ki Hyun Kim. Piezoelectric energy harvesters for biomedical applications. *Nano Energy*, 57(January):879–902, 2019. doi: 10.1016/j.nanoen.2019.01.012.

[330] Guangqiang Jiang and David D. Zhou. Technology advances and challenges in hermetic packaging for implantable medical devices. In *Implantable Neural Prostheses 2*, pages 27–61. Springer, New York, 2009. doi: 10.1007/978-0-387-98120-8_2.

[331] Leping Bu, Peng Cong, Hung I. Kuo, Xuesong Ye, and Wen Ko. Micro Package of Short Term Wireless Implantable Microfabricated Systems. *Proceedings of the 31st Annual International Conference of the IEEE Engineering in Medicine and Biology Society: Engineering the Future of Biomedicine, EMBC 2009*, pages 6395–6399, 2009. doi: 10.1109/IEMBS.2009.5333726.

[332] P. Wang, S. B. Lachhman, D. Sun, S. J.A. Majerus, M. S. Damaser, C. A. Zorman, P. X.L. Feng, and W. H. Ko. Non-Hermetic Micropackage for Chronic Implantable Systems. *International Symposium on Microelectronics*, 2013(1):166–170, 2013. doi: 10.4071/isom-2013-ta55.

[333] Xiaowei Yu, Wan Shou, Bikram K. Mahajan, Xian Huang, and Heng Pan. Materials, Processes, and Facile Manufacturing for Bioresorbable Electronics: A Review. *Advanced Materials*, 30 (28):1707624, 2018. doi: 10.1002/adma.201707624.

[334] Gi Doo Cha, Dayoung Kang, Jongha Lee, and Dae Hyeong Kim. Bioresorbable Electronic Implants: History, Materials, Fabrication, Devices, and Clinical Applications. *Advanced Healthcare Materials*, 8(11):1801660, 2019. doi: 10.1002/adhm.201801660.

[335] Yoshinori Onuki, Upkar Bhardwaj, Fotios Papadimitrakopoulos, and Diane J Burgess. A Review of the Biocompatibility of Implantable Devices: Current Challenges to Overcome Foreign Body Response. *Journal of Diabetes Science and Technology*, 2(6):1003–1015, 2008. doi: 10.1177/193229680800200610.

[336] Pierre Alexis Mouthuy, Sarah J.B. Snelling, Stephanie G. Dakin, Lidija Milković, Ana Čipak Gašparović, Andrew J. Carr, and Neven Žarković. Biocompatibility of implantable materials: An oxidative stress viewpoint. *Biomaterials*, 109:55–68, 2016. doi: 10.1016/j.biomaterials.2016.09.010.

[337] D. Halperin, T. S. Heydt-Benjamin, K. Fu, T. Kohno, and W. H Maisel. Security and privacy for implantable medical devices. *IEEE pervasive computing*, 7(1):30–39, 2008. doi: 10.1007/978-1-4614-1674-6.

[338] Riham Altawy and Amr M. Youssef. Security Tradeoffs in Cyber Physical Systems: A Case Study Survey on Implantable Medical Devices. *IEEE Access*, 4:959–979, 2016. doi: 10.1109/ACCESS.2016.2521727.

[339] Daniel Halperin, Shane S. Clark, Kevin Fu, Thomas S. Heydt-Benjamin, Benessa Defend, Tadayoshi Kohno, Benjamin Ransford, Will Morgan, and William H. Maisel. Pacemakers and Implantable Cardiac Defibrillators: Software Radio Attacks and Zero-Power Defenses. *IEEE Symposium on Security and Privacy (sp 2008)*, pages 129–142, 2008. doi: 10.1109/SP.2008.31.

[340] Roger Jagdish Narayan and Verma Nishant. Nanomaterials as Implantable Sensors. In *Materials for Chemical Sensing*, pages 123–139. Springer, Cham, 2017. doi: 10.1007/978-3-319-47835-7_6.

[341] Ashkan Shafiee, Elham Ghadiri, Jareer Kassis, and Anthony Atala. Nanosensors for therapeutic drug monitoring: implications for transplantation. *Nanomedicine*, 14(20):2735–2747, 2019. doi: 10.2217/nnm-2019-0150.

[342] Albert Folch. *Introduction to BioMEMS*. CRC Press, 2016. ISBN 9781466509382.

[343] Joel Coffel and Eric Nuxoll. BioMEMS for biosensors and closed-loop drug delivery. *International Journal of Pharmaceutics*, 544(2):335–349, 2018. doi: 10.1016/j.ijpharm.2018.01.030.

[344] Robert Farra, Norman F Sheppard Jr, Laura Mccabe, Robert M Neer, James M Anderson, John T Santini Jr., Michael J Cima, and Robert Langer. First-in-Human Testing of a Wirelessly Controlled Drug Delivery Microchip. *Science translational medicine*, 4(122):1–10, 2012. doi: 10.1126/scitranslmed.3003276.

[345] Eiichi Fukada and Iwao Yasuda. On the Piezoelectric Effect of Bone. *Journal of the Physical Society of Japan*, 12(10):1158–1162, 1957. doi: 10.1143/JPSJ.12.1158.

[346] Ryan C. Riddle and Henry J. Donahue. From streaming potentials to shear stress: 25 Years of bone cell mechanotransduction. *Journal of Orthopaedic Research*, 27(2):143–149, 2009. doi: 10.1002/jor.20723.

[347] S. Meng, M. Rouabhia, and Z. Zhang. Electrical stimulation in tissue regeneration. In *Applied biomedical engineering*, pages 37–62. InTech, 2011. ISBN 978-953-307-256-2.

[348] Luther C. Kloth. Electrical stimulation for wound healing: A review of evidence from in vitro studies, animal experiments, and clinical trials. *International Journal of Lower Extremity Wounds*, 4(1):23–44, 2005. doi: 10.1177/1534734605275733.

[349] Richard Balint, Nigel J. Cassidy, and Sarah H. Cartmell. Electrical Stimulation: A Novel Tool for Tissue Engineering. *Tissue Engineering - Part B: Reviews*, 19(1):48–57, 2013. doi: 10.1089/ten.teb.2012.0183.

[350] Yanhua Huang, Yee Li, Jian Chen, Hongxing Zhou, and Sheng Tan. Electrical stimulation elicits neural stem cells activation: New perspectives in CNS repair. *Frontiers in Human Neuroscience*, 9:586, 2015. doi: 10.3389/fnhum.2015.00586.

[351] Sheryl Ding, Peter Kingshott, Helmut Thissen, Martin Pera, and Peng Yuan Wang. Modulation of Human Mesenchymal and Pluripotent Stem Cell Behavior Using Biophysical and Biochemical Cues: A review. *Biotechnology and Bioengineering*, 114(2):260–280, 2017. doi: 10.1002/bit.26075.

[352] J. B. Park, G. H. Kenner, S. D. Brown, and J. K. Scott. Mechanical property changes of barium titanate (ceramic) after in vivo and in vitro aging. *Biomaterials, Medical Devices, and Artificial Organs*, 5(3):267–276, 1977. doi: 10.3109/10731197709118677.

[353] J. B. Park, A. F. von Recum, G. H. Kenner, B. J. Kelly, W. W. Coffeen, and M. F. Grether. Piezoelectric ceramic implants: A feasibility study. *Journal of Biomedical Materials Research*, 14(3):269–277, 1980. doi: 10.1002/jbm.820140308.

[354] J. B. Park, B. J. Kelly, G. H. Kenner, A. F. von Recum, M. F. Grether, and W. W. Coffeen. Piezoelectric ceramic implants: In vivo results. *Journal of Biomedical Materials Research*, 15 (1):103–110, 1981. doi: 10.1002/jbm.820150114.

[355] D. Schumacher, V. Strunz, and U. Gross. Does piezoceramic influence avian bone formation in the early postoperative phase? *Biomaterials*, 4(3):215–217, 1983. doi: 10.1016/0142-9612(83) 90014-5.

[356] Feng Jianqing, Yuan Huipin, and Zhang Xingdong. Promotion of osteogenesis by a piezoelectric biological ceramic. *Biomaterials*, 18(23):1531–1534, 1997. doi: 10.1016/S0142-9612(97) 80004-X.

[357] F. R. Baxter, C. R. Bowen, I. G. Turner, and A. C.E. Dent. Electrically active bioceramics: A review of interfacial responses. *Annals of Biomedical Engineering*, 38(6):2079–2092, 2010. doi: 10.1007/s10439-010-9977-6.

[358] Biranche Tandon, Jonny J. Blaker, and Sarah H. Cartmell. Piezoelectric materials as stimulatory biomedical materials and scaffolds for bone repair. *Acta Biomaterialia*, 73:1–20, 2018. doi: 10.1016/j.actbio.2018.04.026.

[359] Kara K. Poon, Matthias C. Wurm, Donald M. Evans, Mari Ann Einarsrud, Rainer Lutz, and Julia Glaum. Biocompatibility of (Ba,Ca)(Zr,Ti)O_3 piezoelectric ceramics for bone replacement materials. *Journal of Biomedical Materials Research - Part B Applied Biomaterials*, pages 1–9, 2019. doi: 10.1002/jbm.b.34477.

[360] Gianni Ciofani, Serena Danti, Leonardo Ricotti, Delfo D'Alessandro, Stefania Moscato, and Virgilio Mattoli. Applications of piezoelectricity in nanomedicine. In *Piezoelectric Nanomaterials for Biomedical Applications*, pages 213–238. Springer, Berlin, 2012. doi: 10.1007/978-3-642-28044-3_8.

[361] Amir Hossein Rajabi, Michael Jaffe, and Treena Livingston Arinzeh. Piezoelectric materials for tissue regeneration: A review. *Acta Biomaterialia*, 24:12–23, 2015. doi: 10.1016/j.actbio.2015.07.010.

[362] Clarisse Ribeiro, Vítor Sencadas, Daniela M. Correia, and Senentxu Lanceros-Méndez. Piezoelectric polymers as biomaterials for tissue engineering applications. *Colloids and Surfaces B: Biointerfaces*, 136:46–55, 2015. doi: 10.1016/j.colsurfb.2015.08.043.

[363] Attilio Marino, Giada Graziana Genchi, Edoardo Sinibaldi, and Gianni Ciofani. Piezoelectric Effects of Materials on Bio-Interfaces. *ACS Applied Materials and Interfaces*, 9(21):17663–17680, 2017. doi: 10.1021/acsami.7b04323.

[364] Mohammed Salim, Dhia Salim, Davannendran Chandran, Hakim S. Aljibori, and A. Sh Kherbeet. Review of nano piezoelectric devices in biomedicine applications. *Journal of Intelligent Material Systems and Structures*, 29(10):2105–2121, 2018. doi: 10.1177/1045389X17754272.

[365] Bahareh Azimi, Mario Milazzo, Andrea Lazzeri, Stefano Berrettini, Mohammed Jasim Uddin, Zhao Qin, Markus J. Buehler, and Serena Danti. Electrospinning Piezoelectric Fibers for Biocompatible Devices. *Advanced Healthcare Materials*, page 1901287, 2019. doi: 10.1002/adhm.201901287.

[366] Yuchao Li, Chengzhu Liao, and Sie Chin Tjong. Electrospun polyvinylidene fluoride-based fibrous scaffolds with piezoelectric characteristics for bone and neural tissue engineering. *Nanomaterials*, 9(7):952, 2019. doi: 10.3390/nano9070952.

[367] Kausik Kapat, Quazi T. H. Shubhra, Miao Zhou, and Sander Leeuwenburgh. Piezoelectric Nano-Biomaterials for Biomedicine and Tissue Regeneration. *Advanced Functional Materials*, page 1909045, 2020. doi: 10.1002/adfm.201909045.

[368] Guyan Andre Channer, Adrien A. Eshraghi, and Liu Xue–zhong. Middle Ear Implants: Historical and futuristic perspective. *Journal of Otology*, 6(2):10–18, 2011. doi: 10.1016/S1672-2930(11)50017-0.

[369] Sabine Reinfeldt, Bo Håkansson, Hamidreza Taghavi, and Måns Eeg-Olofsson. New developments in bone-conduction hearing implants: A review. *Medical Devices: Evidence and Research*, 8:79–93, 2015. doi: 10.2147/MDER.S39691.

[370] Ivo Dobrev, Jae Hoon Sim, Flurin Pfiffner, Alexander M. Huber, and Christof Röösli. Performance evaluation of a novel piezoelectric subcutaneous bone conduction device. *Hearing Research*, 370:94–104, 2018. doi: 10.1016/j.heares.2018.10.003.

[371] Xudong Wang and Jian Shi. Piezoelectric nanogenerators for self-powered nanodevices. In *Piezoelectric Nanomaterials for Biomedical Applications*, pages 135–172. Springer, Berlin, 2012. doi: 10.1007/978-3-642-28044-3_5.

[372] Shashank Priya, Hyun-Cheol Song, Yuan Zhou, Ronnie Varghese, Anuj Chopra, Sang-Gook Kim, Isaku Kanno, Liao Wu, Dong Sam Ha, Jungho Ryu, and Ronald G. Polcawich. A Review on Piezoelectric Energy Harvesting: Materials, Methods, and Circuits. *Energy Harvesting and Systems*, 4(1):3–39, 2017. doi: 10.1515/ehs-2016-0028.

[373] David F. Williams. There is no such thing as a biocompatible material. *Biomaterials*, 35(38): 10009–10014, 2014. doi: 10.1016/j.biomaterials.2014.08.035.

[374] James M. Anderson. Inflammation, wound healing, and the foreign-body response. In B. D. Ratner, A. S. Hoffman, F. J. Schoen, and J. E. Lemons, editors, *Biomaterials Science: An Introduction to Materials in Medicine*, chapter II.2.2, pages 503–512. Academic Press, 2013. doi: 10.1016/B978-0-08-087780-8.00044-9.

[375] A Remes and D F Williams. Immune response in biocompatibility. *The Biomaterials: Silver Jubilee Compendium*, 13(11):79–91, 1992. doi: 10.1016/B978-008045154-1.50012-5.

[376] James M. Anderson, Analiz Rodriguez, and David T. Chang. Foreign body reaction to biomaterials. *Seminars in Immunology*, 20(2):86–100, 2008. doi: 10.1016/j.smim.2007.11.004.

[377] Sandra Franz, Stefan Rammelt, Dieter Scharnweber, and Jan C Simon. Immune responses to implants - A review of the implications for the design of immunomodulatory biomaterials. *Biomaterials*, 32(28):6692–6709, 2011. doi: 10.1016/j.biomaterials.2011.05.078.

[378] James M. Anderson. Future challenges in the in vitro and in vivo evaluation of biomaterial biocompatibility. *Regenerative Biomaterials*, 3(2):73–77, 2016. doi: 10.1093/RB/RBW001.

[379] James M. Anderson and Sirui Jiang. Implications of the acute and chronic inflammatory response and the foreign body reaction to the immune response of implanted biomaterials. In Bruna Corradetti, editor, *The Immune Response to Implanted Materials and Devices*, pages 15–36. Springer, 2017. doi: 10.1007/978-3-319-45433-7.

[380] Zhidao Xia and James T. Triffitt. A review on macrophage responses to biomaterials. *Biomedical Materials*, 1(1):R1–R9, 2006. doi: 10.1088/1748-6041/1/1/R01.

[381] Daniel S. Kohane and Robert Langer. Biocompatibility and drug delivery systems. *Chemical Science*, 1(4):441–446, 2010. doi: 10.1039/c0sc00203h.

[382] W.H. De Jong, J.W. Carraway, and R.E. Geertsma. In vivo and in vitro testing for the biological safety evaluation of biomaterials and medical devices. In Jean-Pierre Boutrand, editor, *Biocompatibility and Performance of Medical Devices*, pages 123–166. Elsevier Ltd., 2 edition, 2020. doi: 10.1016/b978-0-08-102643-4.00007-0.

[383] A. T. Keene. Biological evaluation and regulation of medical devices in the European Union. In Jean-Pierre Boutrand, editor, *Biocompatibility and Performance of Medical Devices*, pages 413–440. Elsevier Ltd., 2 edition, 2020. doi: 10.1016/B978-0-08-102643-4.00017-3.

[384] K. Kojima and K. Sakaguchi. Biological evaluation and regulation of medical devices in Japan. In Jean-Pierre Boutrand, editor, *Biocompatibility and Performance of Medical Devices*, pages 441–474. Elsevier Ltd., 2 edition, 2020. doi: 10.1533/9780857096456.4.404.

[385] C. Shan and M. Liu. Biological evaluation and regulation of medical devices in China. In Jean-Pierre Boutrand, editor, *Biocompatibility and Performance of Medical Devices*, pages 475–488. Elsevier Ltd., 2 edition, 2020. doi: 10.1016/B978-0-08-102643-4.00019-7.

[386] ISO 13485:2016. *Medical devices — Quality management systems — Requirements for regulatory purposes*. ISO, Geneva, 2016.

[387] ISO 14971:2007. *Medical Devices—Application of Risk Management to Medical Devices*. ISO, Geneva, 2007.

[388] ISO 10993-1:2018. *Biological Evaluation of Medical Devices—Part 1: Evaluation and Testing Within a Risk Management Process*. ISO, Geneva, 2018.

[389] ISO 14155:2011. *Clinical investigation of medical devices for human subjects—Good clinical practice*. ISO, Geneva, 2011.

[390] ISO 10993-13:2010. *Biological evaluation of medical devices—Part 13: Identification and quantification of degradation products from polymeric medical devices*. ISO, Geneva, 2010.

[391] ISO 10993-14:2001. *Biological evaluation of medical devices—Part 14: Identification and quantification of degradation products from ceramics*. ISO, Geneva, 2001.

[392] ISO 10993-15:2019. *Biological evaluation of medical devices—Part 15: Identification and quantification of degradation products from metals and alloys*. ISO, Geneva, 2019.

[393] ISO 10993-16:2017. *Biological evaluation of medical devices – Part 16: Toxicokinetic study design for degradation products and leachables*. ISO, Geneva, 2017.

[394] ISO 10993-17:2002. *Biological evaluation of medical devices—Part 17: Establishment of allowable limits for leachable substances*. ISO, Geneva, 2002.

[395] ISO/TR 10993-22:2017. *Biological Evaluation of Medical Devices—Part 22: Guidance on Nanomaterials*. ISO, Geneva, 2017.

[396] ISO 10993-18:2020. *Biological Evaluation of Medical Devices-Part 18: Chemical Characterization of Materials*. ISO, Geneva, 2020.

[397] ISO/TS 10993-19:2006. *Biological evaluation of medical devices—Part 19: Physico-chemical, morphological and topographical characterization of materials*. ISO, Geneva, 2006.

[398] T. Hanawa. Metal ion release from metal implants. *Materials Science and Engineering C*, 24 (6-8):745–752, 2004. doi: 10.1016/j.msec.2004.08.018.

[399] Paul Thevenot, Wenjing Hu, and Liping Tang. Surface chemistry influences implant biocompatibility. *Current topics in medicinal chemistry*, 8(4):270–280, 2008. doi: 10.2174/156802608783790901.

[400] Alison G. Harvey, Ernie W. Hill, and Ardeshir Bayat. Designing implant surface topography for improved biocompatibility. *Expert Review of Medical Devices*, 10(2):257–267, 2013. doi: 10.1586/erd.12.82.

[401] Vladimir Hlady, Jos Bukis, and Herbert P. Jennissen. Methods for Studying Protein Adsorption. *Methods in Enzymology*, 309:402–429, 1999. doi: 10.1016/S0076-6879(99)09028-X.

[402] C. Simitzi, A. Ranella, and E. Stratakis. Controlling the morphology and outgrowth of nerve and neuroglial cells: The effect of surface topography. *Acta Biomaterialia*, 51:21–52, 2017. doi: 10.1016/j.actbio.2017.01.023.

[403] Anh Tuan Nguyen, Sharvari R. Sathe, and Evelyn K.F. Yim. From nano to micro: Topographical scale and its impact on cell adhesion, morphology and contact guidance. *Journal of Physics Condensed Matter*, 28(18):183001, 2016. doi: 10.1088/0953-8984/28/18/183001.

[404] Arie Bruinink and Reto Luginbuehl. Evaluation of Biocompatibility Using In Vitro Methods: Interpretation and Limitations. In *Tissue Engineering III: Cell - Surface Interactions for Tissue Culture*, pages 117–152. Springer, 2011. doi: 10.1007/978-3-642-28282-9.

[405] ISO 10993-5:2009. *Biological Evaluation of Medical Devices—Part 5: Tests for in vitro cytotoxicity*. ISO, Geneva, 2009. doi: 10.1097/00149078-199604150-00011.

[406] Özlem Sultan Aslantürk. In Vitro Cytotoxicity and Cell Viability Assays: Principles, Advantages, and Disadvantages. In Marcelo Larramendy and Sonia Soloneski, editors, *Genotoxicity: A Predictable Risk to Our Actual World*, pages 1–18. IntechOpen, 2018. doi: 10.5772/57353.

[407] ISO 10993-3:2014. *Biological Evaluation of Medical Devices—Part 3: Tests for Genotoxicity, Carcinogenicity and Reproductive Toxicity*. ISO, Geneva, 2014.

[408] ISO 10993-4:2017. *Biological Evaluation of Medical Devices—Part 4: Selection of Tests for Interactions With Blood*. ISO, Geneva, 2017.

[409] ISO 10993-10:2010. *Biological Evaluation of Medical Devices—Part 10: Tests for Irritation and Skin Sensitization*. ISO, Geneva, 2010.

[410] ISO/TR 10993-33:2015. *Biological Evaluation of Medical Devices—Part 33: Guidance on Tests to Evaluate Genotoxicity—Supplement to ISO 10993-3*. ISO, Geneva, 2015.

[411] ISO 10993-6:2016. *Biological Evaluation of Medical Devices—Part 6: Tests for Local Effects After Implantation*. ISO, Geneva, 2016.

[412] ISO 10993-11:2017. *Biological Evaluation of Medical Devices—Part 11: Tests for Systemic Toxicity*. ISO, Geneva, 2017.

[413] Gianni Ciofani, Serena Danti, Delfo D'Alessandro, Leonardo Ricotti, Stefania Moscato, Giovanni Bertoni, Andrea Falqui, Stefano Berrettini, Mario Petrini, Virgilio Mattoli, and Arianna Menciassi. Enhancement of neurite outgrowth in neuronal-like cells following boron nitride nanotube-mediated stimulation. *ACS Nano*, 4(10):6267–6277, 2010. doi: 10.1021/nn101985a.

[414] Attilio Marino, Satoshi Arai, Yanyan Hou, Edoardo Sinibaldi, Mario Pellegrino, Young Tae Chang, Barbara Mazzolai, Virgilio Mattoli, Madoka Suzuki, and Gianni Ciofani. Piezoelectric Nanoparticle-Assisted Wireless Neuronal Stimulation. *ACS Nano*, 9(7):7678–7689, 2015. doi: 10.1021/acsnano.5b03162.

[415] Carlos Mota, Massimiliano Labardi, Luisa Trombi, Laura Astolfi, Mario D'Acunto, Dario Puppi, Giuseppe Gallone, Federica Chiellini, Stefano Berrettini, Luca Bruschini, and Serena Danti. Design, fabrication and characterization of composite piezoelectric ultrafine fibers for cochlear stimulation. *Materials and Design*, 122:206–219, 2017. doi: 10.1016/j.matdes.2017.03.013.

[416] Giada Graziana Genchi, Edoardo Sinibaldi, Luca Ceseracciu, Massimiliano Labardi, Attilio Marino, Sergio Marras, Giorgio De Simoni, Virgilio Mattoli, and Gianni Ciofani. Ultrasound-activated piezoelectric P(VDF-TrFE)/boron nitride nanotube composite films promote differentiation of human SaOS-2 osteoblast-like cells. *Nanomedicine: Nanotechnology, Biology, and Medicine*, 14(7):2421–2432, 2018. doi: 10.1016/j.nano.2017.05.006.

[417] Cijun Shuai, Guofeng Liu, Youwen Yang, Wenjing Yang, Chongxian He, Guoyong Wang, Zheng Liu, Fangwei Qi, and Shuping Peng. Functionalized $BaTiO_3$ enhances piezoelectric effect towards cell response of bone scaffold. *Colloids and Surfaces B: Biointerfaces*, 185(October 2019):110587, 2020. doi: 10.1016/j.colsurfb.2019.110587.

[418] Attilio Marino, Jonathan Barsotti, Giuseppe De Vito, Carlo Filippeschi, Barbara Mazzolai, Vincenzo Piazza, Massimiliano Labardi, Virgilio Mattoli, and Gianni Ciofani. Two-Photon Lithography of 3D Nanocomposite Piezoelectric Scaffolds for Cell Stimulation. *ACS Applied Materials and Interfaces*, 7(46):25574–25579, 2015. doi: 10.1021/acsami.5b08764.

[419] Christof Christophis, Elisabetta Ada Cavalcanti-Adam, Maximilian Hanke, Kenji Kitamura, Alexei Gruverman, Michael Grunze, Peter A. Dowben, and Axel Rosenhahn. Adherent cells avoid polarization gradients on periodically poled $LiTaO_3$ ferroelectrics. *Biointerphases*, 8(1):1–9, 2013. doi: 10.1186/1559-4106-8-27.

[420] N. Craig Carville, Liam Collins, Michele Manzo, Katia Gallo, Bart I. Lukasz, Katey K. McKayed, Jeremy C. Simpson, and Brian J. Rodriguez. Biocompatibility of ferroelectric lithium niobate and the influence of polarization charge on osteoblast proliferation and function. *Journal of Biomedical Materials Research - Part A*, 103(8):2540–2548, 2015. doi: 10.1002/jbm.a.35390.

[421] Valentina Marchesano, Oriella Gennari, Laura Mecozzi, Simonetta Grilli, and Pietro Ferraro. Effects of Lithium Niobate Polarization on Cell Adhesion and Morphology. *ACS Applied Materials and Interfaces*, 7(32):18113–18119, 2015. doi: 10.1021/acsami.5b05340.

[422] P. Vaněk, Z. Kolská, T. Luxbacher, J. A.L. García, M. Lehocký, M. Vandrovcová, L. Bačáková, and J. Petzelt. Electrical activity of ferroelectric biomaterials and its effects on the adhesion, growth and enzymatic activity of human osteoblast-like cells. *Journal of Physics D: Applied Physics*, 49(17), 2016. doi: 10.1088/0022-3727/49/17/175403.

[423] Sergei V. Kalinin and Dawn A. Bonnell. Local potential and polarization screening on ferroelectric surfaces. *Physical Review B*, 63(12):125411, 2001. doi: 10.1103/PhysRevB.63.125411.

[424] Sergei V. Kalinin, C. Y. Johnson, and Dawn A. Bonnell. Domain polarity and temperature induced potential inversion on the $BaTiO_3$ (100) surface. *Journal of Applied Physics*, 91(6): 3816–3823, 2002. doi: 10.1063/1.1446230.

[425] Jianqiang Wen and Meili Liu. Piezoelectric ceramic (PZT) modulates axonal guidance growth of rat cortical neurons via RhoA, Rac1, and Cdc42 pathways. *Journal of Molecular Neuroscience*, 52(3):323–330, 2014. doi: 10.1007/s12031-013-0149-7.

[426] Matias Acosta, Rainer Detsch, Alina Grünewald, Virginia Rojas, Jan Schultheiß, Aleksandra Wajda, Robert W. Stark, Suman Narayan, Maciej Sitarz, Jurij Koruza, and Aldo R. Boccaccini. Cytotoxicity, chemical stability, and surface properties of ferroelectric ceramics for biomaterials. *Journal of the American Ceramic Society*, 101(1):440–449, 2018. doi: 10.1111/jace.15193.

[427] Zhensheng Li, Yang Qu, Xingdong Zhang, and Bangcheng Yang. Bioactive nano-titania ceramics with biomechanical compatibility prepared by doping with piezoelectric $BaTiO_3$. *Acta Biomaterialia*, 5(6):2189–2195, 2009. doi: 10.1016/j.actbio.2009.02.013.

[428] Frances R. Baxter, Irene G. Turner, Christopher R. Bowen, Jonathan P. Gittings, and Julian B. Chaudhuri. An in vitro study of electrically active hydroxyapatite-barium titanate ceramics using Saos-2 cells. *Journal of Materials Science: Materials in Medicine*, 20(8):1697–1708, 2009. doi: 10.1007/s10856-009-3734-0.

[429] A. K. Dubey, B. Basu, K. Balani, R. Guo, and A. S. Bhalla. Multifunctionality of perovskites $BaTiO_3$ and $CaTiO_3$ in a composite with hydroxyapatite as orthopedic implant materials. *Integrated Ferroelectrics*, 131(1):119–126, 2011. doi: 10.1080/10584587.2011.616425.

[430] Davide Staedler, Thibaud Magouroux, Rachid Hadji, Cécile Joulaud, Jérôme Extermann, Sebastian Schwung, Solène Passemard, Christelle Kasparian, Gareth Clarke, Mathias Gerrmann, Ronan Le Dantec, Yannick Mugnier, Daniel Rytz, Daniel Ciepielewski, Christine Galez, Sandrine Gerber-Lemaire, Lucienne Juillerat-Jeanneret, Luigi Bonacina, and Jean Pierre Wolf. Harmonic nanocrystals for biolabeling: A survey of optical properties and biocompatibility. *ACS Nano*, 6(3):2542–2549, 2012. doi: 10.1021/nn204990n.

[431] Miaomiao Yuan, Li Cheng, Qi Xu, Weiwei Wu, Suo Bai, Long Gu, Zhe Wang, Jun Lu, Huanping Li, Yong Qin, Tao Jing, and Zhong Lin Wang. Biocompatible nanogenerators through high piezoelectric coefficient $0.5Ba(Zr_{0.2}Ti_{0.8})O_3$-$0.5(Ba_{0.7}Ca_{0.3})TiO_3$ nanowires for in-vivo applications. *Advanced Materials*, 26(44):7432–7437, 2014. doi: 10.1002/adma.201402868.

[432] Jordan P. Ball, Brittnee A. Mound, Juan C. Nino, and Josephine B. Allen. Biocompatible evaluation of barium titanate foamed ceramic structures for orthopedic applications. *Journal of Biomedical Materials Research - Part A*, 102(7):2089–2095, 2014. doi: 10.1002/jbm.a.34879.

[433] Márcio M. Beloti, Paulo T. de Oliveira, Rossano Gimenes, Maria A. Zaghete, Márcio J. Bertolini, and Adalberto L. Rosa. In vitro biocompatibility of a novel membrane of the composite poly(vinylidene-trifluoroethylene)/ barium titanate. *Journal of Biomedical Materials Research Part A*, 79(2):282–288, 2006. doi: 10.1002/jbm.a.

[434] Giada Graziana Genchi, Luca Ceseracciu, Attilio Marino, Massimiliano Labardi, Sergio Marras, Francesca Pignatelli, Luca Bruschini, Virgilio Mattoli, and Gianni Ciofani. P(VDF-TrFE)/$BaTiO_3$ Nanoparticle Composite Films Mediate Piezoelectric Stimulation and Promote Differentiation of SH-SY5Y Neuroblastoma Cells. *Advanced Healthcare Materials*, 5(14):1808–1820, 2016. doi: 10.1002/adhm.201600245.

[435] Tae Ho Lee, Hyun Gyu Hwang, Seonghoon Jang, Gunuk Wang, Seongbeom Han, Dong Hwee Kim, Chong Yun Kang, and Sahn Nahm. Low-Temprature-Grown $KNbO_3$ Thin Films and Their Application to Piezoelectric Nanogenerators and Self-Powered ReRAM Device. *ACS Applied Materials and Interfaces*, 9(49):43220–43229, 2017. doi: 10.1021/acsami.7b11519.

[436] Yuwei Zhao, Huiqing Fan, Xiaohu Ren, Changbai Long, Guocai Liu, and Zhiyong Liu. Lead-free $Bi_{5-x}La_xTi_3FeO_{15}$ (x = 0, 1) nanofibers toward wool keratin-based biocompatible piezoelectric nanogenerators. *Journal of Materials Chemistry C*, 4(30):7324–7331, 2016. doi: 10.1039/c6tc01828a.

[437] Q. Wang, Jun Yang, W. Zhang, Roxanne Khoie, Yi Ming Li, Jian Guo Zhu, and Zhi Qing Chen. Manufacture and cytotoxicity of a lead-free piezoelectric ceramic as a bone substitute-consolidation of porous lithium sodium potassium niobate by cold isostatic pressing. *International journal of oral science*, 1(2):99–104, 2009. doi: 10.4248/ijos.09005.

[438] Sheng-Wen Yu, Shu-Ting Kuo, Wei-Hsing Tuan, Yu-Yu Tsai, and Ching-Hua Su. Ion release from three lead-free piezoelectric ceramics and their physical and cytotoxicity characteristics. *Materials Letters*, 65(23-24):3522–3524, dec 2011. doi: 10.1016/j.matlet.2011.07.098.

[439] Sheng-wen Yu, Shu-ting Kuo, Wei-hsing Tuan, Yu-yu Tsai, and Sea-fu Wang. Cytotoxicity and degradation behavior of potassium sodium niobate piezoelectric ceramics. *Ceramics International*, 38(4):2845–2850, 2012. doi: 10.1016/j.ceramint.2011.11.056.

[440] A. K. Dubey, K. Kakimoto, A. Obata, and T. Kasuga. Enhanced polarization of hydroxyapatite using the design concept of functionally graded materials with sodium potassium niobate. *RSC Advances*, 4(47):24601–24611, 2014. doi: 10.1039/c4ra02329c.

[441] Guoxin Tan, Shuangying Wang, Ye Zhu, Lei Zhou, Peng Yu, Xiaolan Wang, Tianrui He, Junqi Chen, Chuanbin Mao, and Chengyun Ning. Surface-Selective Preferential Production of Reactive Oxygen Species on Piezoelectric Ceramics for Bacterial Killing. *ACS Applied Materials and Interfaces*, 8(37):24306–24309, 2016. doi: 10.1021/acsami.6b07440.

[442] Bo Yun Kim, Woong Hee Lee, Hyun Gyu Hwang, Dong Ha Kim, Jeong Hun Kim, Sang Hoon Lee, and Sahn Nahm. Resistive Switching Memory Integrated with Nanogenerator for Self-Powered Bioimplantable Devices. *Advanced Functional Materials*, 26(29):5211–5221, 2016. doi: 10.1002/adfm.201505569.

[443] Wei Chen, Zunxiong Yu, Jinshan Pang, Peng Yu, Guoxin Tan, and Chengyun Ning. Fabrication of Biocompatible Potassium Sodium Niobate Piezoelectric Ceramic as an Electroactive Implant. *Materials*, 10:345, 2017. doi: 10.3390/ma10040345.

[444] Ozcan Ozmen, Cigdem Ozsoy-Keskinbora, and Ender Suvaci. Chemical stability of $KNbO_3$, $NaNbO_3$, and $K_{0.5}Na_{0.5}NbO_3$ in aqueous medium. *Journal of the American Ceramic Society*, 101:1074–1086, 2017. doi: 10.1111/jace.15291.

[445] Tiantian Yao, Junqi Chen, Zhengao Wang, Jinxia Zhai, Yangfan Li, Jun Xing, Shiqian Hu, Guoxin Tan, Suijian Qi, Yunbing Chang, Peng Yu, and Chengyun Ning. The antibacterial effect of potassium-sodium niobate ceramics based on controlling piezoelectric properties. *Colloids and Surfaces B: Biointerfaces*, 175:463–468, 2019. doi: 10.1016/j.colsurfb.2018.12.022.

[446] Marija Kosec, Barbara Malič, W. W. Wolny, A. S. James, C. Alemany, and L. Pardo. Effect of a chemically aggressive environment on the electromechanical behaviour of modified lead titanate ceramics. *Journal of the Korean Physical Society*, 32(1):S1163–S1166, 1998. ISSN 03744884.

[447] Jinxia Zhai, Yahong Zhou, Zhengao Wang, Lei Fan, Cairong Xiao, Xiaolan Wang, Yangfan Li, Zhengnan Zhou, Yian Luo, Changhao Li, Suijian Qi, Guoxin Tan, Lei Zhou, Peng Yu, and Chengyun Ning. Endogenous electric field as a bridge for antibacterial ion transport from implant to bacteria. *Science China Materials*, (June):1–11, 2020. doi: 10.1007/s40843-020-1329-8.

[448] T. M. Raeder, K. Bakken, J. Glaum, M. A. Einarsrud, and T. Grande. Enhanced in-plane ferroelectricity in $BaTiO_3$ thin films fabricated by aqueous chemical solution deposition. *AIP Advances*, 8(10):105228, 2018. doi: 10.1063/1.5059549.

[449] Kristine Bakken. *In situ Characterization of Ferroelectric Oxide Thin Films during Aqueous Chemical Solution Deposition*. PhD thesis, Norwegian University of Science and Technology, 2020.

[450] Astri Bjørnetun Haugen, Gerhard Henning Olsen, Francesco Madaro, Maxim I Morozov, Goknur Tutuncu, Jacob L Jones, Tor Grande, and Mari-ann Einarsrud. Piezoelectric $K_{0.5}Na_{0.5}NbO_3$ Ceramics Textured Using Needlelike $K_{0.5}Na_{0.5}NbO_3$ Templates. *Journal of the American Ceramic Society*, 97(12):3818–3825, 2014. doi: 10.1111/jace.13223.

[451] Monica Lundberg and Margareta Sundberg. Studies of phases in the $KNbO_3$-Nb_2O_5 system by high-resolution electron microscopy and X-ray powder diffraction. *Journal of Solid State Chemistry*, 63(2):216–230, 1986. doi: 10.1016/0022-4596(86)90172-6.

[452] Francesco Madaro, Ragnhild Sæterli, Julian R Tolchard, Mari-ann Einarsrud, Randi Holmestad, and Tor Grande. Molten salt synthesis of $K_4Nb_6O_{17}$, $K_2Nb_4O_{11}$ and KNb_3O_8 crystals with needle- or plate-like morphology. *CrystEngComm*, 13:1304–1313, 2011. doi: 10.1039/c0ce00413h.

[453] Nikolai Helth Gaukås, Silje Marie Dale, Trygve Magnus Ræder, Andreas Toresen, Randi Holmestad, Julia Glaum, Mari-ann Einarsrud, and Tor Grande. Controlling phase purity and texture of $K_{0.5}Na_{0.5}NbO_3$ thin films by aqueous chemical solution deposition. *Materials*, 12: 2042, 2019. doi: 10.3390/ma12132042.

[454] Nikolai Helth Gaukås, Julia Glaum, Mari-Ann Einarsrud, and Tor Grande. Ferroelectric and dielectric properties of Ca^{2+}-doped and Ca^{2+}-Ti^{4+} co-doped $K_{0.5}Na_{0.5}NbO_3$ thin films. *Journal of Materials Chemistry C*, 8:5102–5111, 2020. doi: 10.1039/d0tc00276c.

[455] Hwi-Yeol Park, Kyung-Hoon Cho, Dong-Soo Paik, Sahn Nahm, Hyeung-Gyu Lee, and Duk-Hee Kim. Microstructure and piezoelectric properties of lead-free (1-x)($Na_{0.5}K_{0.5}$)NbO_3-x$CaTiO_3$ ceramics. *Journal of Applied Physics*, 102:124101, 2007. doi: 10.1063/1.2822334.

[456] L Ramajo, R Parra, and M S Castro. Electrical and microstructural properties of $CaTiO_3$-doped $K_{1/2}Na_{1/2}NbO_3$-lead free ceramics. *Bulletin of Materials Science*, 34(6):1213–1217, 2011. doi: 10.1007/s12034-011-0241-y.

[457] Jiagang Wu, Dingquan Xiao, Yuanyu Wang, Wenjuan Wu, Bin Zhang, and Jianguo Zhu. Improved temperature stability of CaTiO3-modified $[(K_{0.5}Na_{0.5})_{0.96}Li_{0.04}](Nb_{0.91}Sb_{0.05}Ta_{0.04})O3$ lead-free piezoelectric ceramics. *Journal of Applied Physics*, 104:024102, 2008. doi: 10.1063/1.2956390.

[458] Yunfei Chang, Zupei Yang, Xiaolian Chao, Rui Zhang, and Xiaorui Li. Dielectric and piezoelectric properties of alkaline-earth titanate doped ($K_{0.5}Na_{0.5}$)NbO_3 ceramics. *Materials Letters*, 61(3):785–789, 2007. doi: 10.1016/j.matlet.2006.05.065.

[459] Hong Chen and Peng Liu. Electrical properties of 0.98($K_{0.5}Na_{0.5}$)NbO_3-0.02A$ETiO_3$ piezoceramics doped with Li_2CO_3. *Ferroelectrics*, 551(1):53–59, 2019. doi: 10.1080/00150193.2019.1658029.

[460] Nazanin Bassiri-Gharb, Ichiro Fujii, Eunki Hong, Susan Trolier-Mckinstry, David V. Taylor, and Dragan Damjanovic. Domain wall contributions to the properties of piezoelectric thin films. *Journal of Electroceramics*, 19(1):47–65, 2007. doi: 10.1007/s10832-007-9001-1.

[461] F. Xu, S. Trolier-McKinstry, W. Ren, Baomin Xu, Z. L. Xie, and K. J. Hemker. Domain wall motion and its contribution to the dielectric and piezoelectric properties of lead zirconate titanate films. *Journal of Applied Physics*, 89(2):1336–1348, 2001. doi: 10.1063/1.1325005.

[462] Haksung Lee, Teruyasu Mizoguchi, Takahisa Yamamoto, and Yuichi Ikuhara. First principles study on intrinsic vacancies in cubic and orthorhombic $CaTiO_3$. *Materials Transactions*, 50(5): 977–983, 2009. doi: 10.2320/matertrans.MC200813.

[463] Akio Shigemi and Takahiro Wada. Evaluations of phases and vacancy formation energies in $KNbO_3$ by first-principles calculation. *Japanese Journal of Applied Physics*, 44(11):8048–8054, 2005. doi: 10.1143/JJAP.44.8048.

[464] Ubong Eduok, Omar Faye, and Jerzy Szpunar. Recent developments and applications of protective silicone coatings: A review of PDMS functional materials. *Progress in Organic Coatings*, 111(June):124–163, 2017. doi: 10.1016/j.porgcoat.2017.05.012.

[465] K. Van Werde, D. Mondelaers, G. Vanhoyland, D. Nelis, M. K. Van Bael, J. Mullens, L. C. Van Poucke, B. Van Der Veken, and H. O. Desseyn. Thermal decomposition of the ammonium zinc acetate citrate precursor for aqueous chemical solution deposition of ZnO. *Journal of Materials Science*, 37(1):81–88, 2002. doi: 10.1023/A:1013141723764.

[466] L. N. Ji, J. B. Li, J. Luo, J. K. Liang, J. Y. Zhang, Y. H. Liu, and G. H. Rao. Phase relations and flux research for zinc oxide crystal growth in the ZnO-Na_2O-P_2O_5 system. *Journal of Alloys and Compounds*, 465(1-2):436–441, 2008. doi: 10.1016/j.jallcom.2007.10.112.

[467] L. N. Ji, J. B. Li, J. Luo, J. K. Liang, Y. H. Liu, J. Y. Zhang, and G. H. Rao. Phase relations and flux research for zinc oxide crystal growth in the ZnO-K_2O-P_2O_5 system. *Journal of Alloys and Compounds*, 470(1-2):336–339, 2009. doi: 10.1016/j.jallcom.2008.02.057.

[468] Yasumasa Okada and Yozo Tokumaru. Precise determination of lattice parameter and thermal expansion coefficient of silicon between 300 and 1500 K. *Journal of Applied Physics*, 56(2):314–320, 1984. doi: 10.1063/1.333965.

[469] Atsuto Seko, Fumiyasu Oba, Akihide Kuwabara, and Isao Tanaka. Pressure-induced phase transition in ZnO and ZnO-MgO pseudobinary system: A first-principles lattice dynamics study. *Physical Review B*, 72(2):024107, 2005. doi: 10.1103/PhysRevB.72.024107.

[470] Yi He. Heat capacity, thermal conductivity, and thermal expansion of barium titanate-based ceramics. *Thermochimica Acta*, 419(1-2):135–141, 2004. doi: 10.1016/j.tca.2004.02.008.

[471] Mads Christensen, Mari Ann Einarsrud, and Tor Grande. Fabrication of lead-free $Bi_{0.5}Na_{0.5}TiO_3$ thin films by aqueous chemical solution deposition. *Materials*, 10(2):213, 2017. doi: 10.3390/ma10020213.

[472] Tor Olav Løveng Sunde, Edita Garskaite, Benjamin Otter, Helle Ervik Fossheim, Ragnhild Sæterli, Randi Holmestad, Mari-Ann Einarsrud, and Tor Grande. Transparent and conducting ITO thin films by spin coating of an aqueous precursor solution. *Journal of Materials Chemistry*, 22(31):15740, 2012. doi: 10.1039/c2jm32000b.

[473] Tor Olav Løveng Sunde, Mari Ann Einarsrud, and Tor Grande. Optimisation of chemical solution deposition of indium tin oxide thin films. *Thin Solid Films*, 573(3):48–55, 2014. doi: 10.1016/j.tsf.2014.10.093.

[474] Edita Garskaite, Mikael Lindgren, Mari Ann Einarsrud, and Tor Grande. Luminescent properties of rare earth (Er, Yb) doped yttrium aluminium garnet thin films and bulk samples synthesised by an aqueous sol-gel technique. *Journal of the European Ceramic Society*, 30(7): 1707–1715, 2010. doi: 10.1016/j.jeurceramsoc.2010.01.001.

[475] W. Mark Saltzman, Patricia Parsons-Wingerter, Kam W. Leong, and Shin Lin. Fibroblast and hepatocyte behavior on synthetic polymer surfaces. *Journal of Biomedical Materials Research*, 25(6):741–759, 1991. doi: 10.1002/jbm.820250605.

[476] Carmen Lia A M Vleggeert-Lankamp, Ana P. Pêgo, Egbert A J F Lakke, Marga Deenen, Enrico Marani, and Ralph T W M Thomeer. Adhesion and proliferation of human Schwann cells on adhesive coatings. *Biomaterials*, 25(14):2741–2751, 2004. doi: 10.1016/j.biomaterials.2003.09.067.

[477] Ying Yuan, Peiyun Zhang, Yuming Yang, Xiaodong Wang, and Xiaosong Gu. The interaction of Schwann cells with chitosan membranes and fibers in vitro. *Biomaterials*, 25(18):4273–4278, 2004. doi: 10.1016/j.biomaterials.2003.11.029.

[478] Jiagang Wu. Perovskite lead-free piezoelectric ceramics. *Journal of Applied Physics*, 127(19): 190901, 2020. doi: 10.1063/5.0006261.

[479] Kenji Shibata, Ruiping Wang, Tonshaku Tou, and Jurij Koruza. Applications of lead-free piezoelectric materials. *MRS Bulletin*, 43(8):612–616, 2018. doi: 10.1557/mrs.2018.180.

[480] Google patents search engine, accessed 21.06.2020. URL https://patents.google.com/.

Appended papers

Paper I

Paper II

Manuscript I

Manuscript II

Paper I

Controlling phase purity and texture of $K_{0.5}Na_{0.5}NbO_3$ thin films by aqueous chemical solution deposition

Reprinted from *Materials*, N. H. Gaukås, S. M. Dale, T. M. Ræder, A. Toresen, R. Holmestad, J. Glaum, M.-A. Einarsrud, T. Grande, Controlling Phase Purity and Texture of $K_{0.5}Na_{0.5}NbO_3$ Thin Films by Aqueous Chemical Solution Deposition, 12, 2042, **2019**.

materials

MDPI

Article

Controlling Phase Purity and Texture of $K_{0.5}Na_{0.5}NbO_3$ Thin Films by Aqueous Chemical Solution Deposition

Nikolai Helth Gaukås [1], Silje Marie Dale [1], Trygve Magnus Ræder [1], Andreas Toresen [2], Randi Holmestad [2], Julia Glaum [1], Mari-Ann Einarsrud [1] and Tor Grande [1,*]

[1] Department of Materials Science and Engineering, NTNU Norwegian University of Science and Technology, NO-7491 Trondheim, Norway
[2] Department of Physics, NTNU Norwegian University of Science and Technology, NO-7491 Trondheim, Norway
* Correspondence: grande@ntnu.no; Tel.: +47-976-169-18

Received: 14 May 2019; Accepted: 20 June 2019; Published: 26 June 2019

Abstract: Aqueous chemical solution deposition (CSD) of lead-free ferroelectric $K_{0.5}Na_{0.5}NbO_3$ (KNN) thin films has a great potential for cost-effective and environmentally friendly components in microelectronics. Phase purity of KNN is, however, a persistent challenge due to the volatility of alkali metal oxides, usually countered by using excess alkali metals in the precursor solutions. Here, we report on the development of two different aqueous precursor solutions for CSD of KNN films, and we demonstrate that the decomposition process during thermal processing of the films is of detrimental importance for promoting nucleation of KNN and suppressing the formation of secondary phases. Based on thermal analysis, X-ray diffraction and IR spectroscopy of films as well as powders prepared from the solutions, it was revealed that the decomposition temperature can be controlled by chemistry resulting in phase pure KNN films. A columnar microstructure with out-of-plane texturing was observed in the phase pure KNN films, demonstrating that the microstructure is directly coupled to the thermal processing of the films.

Keywords: KNN; thin film; aqueous chemical solution deposition

1. Introduction

Piezoelectric $K_{0.5}Na_{0.5}NbO_3$-based (KNN) ceramics have been extensively studied the last decade to replace the state-of-the-art piezoelectric materials based on $PbZr_xTi_{1-x}O_3$ (PZT) [1–3]. In addition to the environmental advantage of being lead-free, KNN-based ceramics benefit from having relatively high piezoelectric coefficients [4] and high Curie temperatures [1]. Moreover, KNN has shown promising results with respect to ion release and cytotoxicity tests [5,6], which make KNN a potential candidate for biomedical applications. Investigations on bulk KNN have been dominated by compositional engineering to enhance piezoelectric performance. Fabrication of KNN thin films for incorporation in electronic devices has also been investigated [7–9]. Preparation of thin films of KNN has successfully been performed by physical vapor deposition (PVD) [10,11] and chemical vapor deposition (CVD) [12,13]. Fabrication of KNN thin films by chemical solution deposition (CSD) has also been targeted, and 2-methoxyethanol based solutions with cation ethoxides and acetates are by far the most used, giving KNN thin films with varying degree of texture [7,14–25]. Aqueous CSD of KNN opens for more environmentally friendly precursors and chemistry [16,22,26]. A persistent challenge in CSD synthesis of KNN thin films is the formation of alkali metal deficient secondary phases, most notably $K_4Nb_6O_{17}$. Measures to avoid formation of such parasitic phases are usually

Materials **2019**, *12*, 2042

implemented by using an excess amount of alkali metal in the precursor solution and by optimization of the synthesis temperature [14,20,21,23].

The ferroelectric performance of thin films is strongly correlated with the microstructure. Of special interest is the ability to tailor the degree of texturing in ferroelectric thin films, since the ferroelectric performance is coupled directly to the microstructural orientation [27]. Both polycrystalline and epitaxial KNN thin films have been prepared by CSD by tailoring the thermal processing to favor either homogeneous or heterogeneous nucleation, respectively [25]. The crystallization kinetics can also be controlled chemically by altering the nucleation temperature through modification of the precursor chemistry [16,28,29].

An aqueous niobium(V) precursor solution has recently been applied in aqueous based synthesis of KNN ceramics [30–32]. This precursor solution has further been used to prepare KNN thin films by CSD [26]. Both polycrystalline and highly epitaxial KNN thin films were prepared on $SrTiO_3$ (STO) substrates. Two distinct regions of were observed in KNN thin films on (100) oriented STO, where the majority of the films was polycrystalline with a thin epitaxial layer close to the substrate. A secondary $K_2Nb_4O_{11}$ phase was observed, particularly at the surface of the films. NaCl/KCl was included in the precursor solution to form a salt flux, which suppressed the formation of $K_2Nb_4O_{11}$ although it was not completely eliminated in films deposited on (100) STO. The epitaxial layer was obtained through a thermal treatment avoiding nucleation during pyrolysis (400 °C) and using a rapid heating rate up to the annealing temperature (40 K s^{-1}, 800 °C).

Here, we report on developments of the aqueous CSD route to phase pure KNN thin films. A new solution based on malic acid [33] was developed, and it was demonstrated that phase purity and microstructure can be controlled by modification of the sol-gel chemistry and the thermal processing, which alter the decomposition and crystallization kinetics during pyrolysis of the films. Finally, the in-plane ferroelectric properties of the films were characterized by using interdigitated Pt electrodes.

2. Materials and Methods

2.1. Materials Synthesis

The oxalic acid-complexed solution, referred to as KNN-Ox in the following, was prepared based on the synthesis reported by Pham et al. [26]. $NH_4NbO(C_2O_4)_2{\cdot}xH_2O$ (99.99%, Sigma-Aldrich, St. Louis, MO, USA) was dissolved in distilled water, and dried $NaNO_3$ (99%, Sigma-Aldrich) and KNO_3 (99%, Alfa Aesar, Haverhill, MA, USA) were added to the niobium solution in a molar ratio of 1:0.525:0.525 (Nb:Na:K), giving 5 mol% excess of alkali metals. The solution was stirred on a hotplate at 70 °C for 2 h. The concentration of the final solution was 0.25 M with respect to Nb.

The malic acid-complexed solution, referred to as KNN-MA in the following, was prepared based on the synthesis described by Madaro [32]. A niobic acid precipitate was dissolved in distilled water with 0.33 M DL-malic acid (99%, Sigma-Aldrich) with a molar ratio of 1:2 (Nb:malic acid) during vigorous stirring at 70 °C, and the pH of the solution was finally adjusted to 7–8 by addition of NH_3 solution. Finally, dried $NaNO_3$ (99%, Sigma-Aldrich) and KNO_3 (99%, Alfa Aesar) were added to the malic acid-complexed niobium solution in a ratio of 1:0.525:0.525 (Nb:Na:K), giving 5 mol% excess of alkali metals. The final solution had a Nb concentration of 0.14 M.

KNN thin films were deposited on (100) oriented $SrTiO_3$ single crystal (Crystal GmbH, Berlin, Germany) substrates. Prior to deposition, the substrates were rinsed with ethanol (96%), heat-treated at 550 °C for 5 min in a rapid thermal processing (RTP) oven (RTP-1, Jipelec Jetfirst 200 mm, Semco Technologies, Montpellier, France) to remove any organic residues, before the substrate surface was activated in an oxygen plasma cleaner (Femto, Diener Electronics, Ebhausen, Germany), improving the wettability. The KNN precursor solutions were then deposited on the substrates, using a spin coater (WS-400B-6NPP-LITE/AS, Laurell Technologies, Montgomery, PA, USA) at 3500 rpm for 40 s, followed by drying on a hotplate at 200 °C for 3 min. The films were then pyrolyzed at 550 °C for 5 min in either flowing O_2 (RTP-1) or in air using a rapid heating plate (RTP-2) as described by Blichfeld et al. [34] at a heating rate of 100 K min^{-1}. Deposition was repeated until a desired film thickness was obtained

(15 layers deposited if not otherwise specified). Finally, the thin films were annealed at 700 °C for 10 min in O_2 (RTP-1) or air (RTP-2), at a heating rate of 100 K min^{-1}.

Powders from the two precursor solutions were prepared by drying the KNN-Ox and KNN-MA precursor solutions at 100 °C and 200 °C, respectively, for 24 h, followed by hand milling. The powders were heat-treated at various temperatures for further characterization.

2.2. Characterization

The thermal decomposition of the gel powders was analyzed with thermogravimetric analysis combined with mass spectroscopy (TGA-MS, TGA: STA 449C, Netzsch, MS: QMS 403C, Netzsch, Selb, Germany) up to 725 °C in flowing synthetic air and O_2, using a heating rate of 10 K min^{-1}. Fourier-transform infrared spectroscopy (FTIR, Vertex 80v, Bruker, Billerica, MA, USA), using an attenuated total reflection (ATR) cell, was performed of the gel powders heat-treated in air at various temperatures. The phase composition of the powders was determined using X-ray diffraction (XRD, D8 Advance, Bruker). The phase composition of the prepared KNN films was studied using gracing incidence X-ray diffraction (GI-XRD, D8 A25 Advance, Bruker) with an incidence angle of 2°, and the average microstructure of the films was analyzed using regular X-ray diffraction (θ–2θ XRD, D5005, Siemens, Karlsruhe, Germany) with scanning geometry parallel to the (100) direction of the substrate. The film thickness and local microstructure were studied using scanning electron microscopy (SEM, Ultra 55, Carl Zeiss AG, Oberkochen, Germany) and transmission electron microscopy (TEM, JEM-2100 and JEM-2100F, Jeol, Tokyo, Japan, both operated at 200 kV). Cross-sectional SEM samples were prepared by scribing and breaking the films using a diamond tip scriber (DX-III, Dynatex International, Santa Rosa, CA, USA). The SEM imaging was performed using an in-lens detector and an acceleration voltage of 10 kV. The TEM samples were prepared using focused ion beam (FIB, Helios Nanolab DualBeam, FEI Company, Hillsboro, OR, USA) using a standard lift-out technique. TEM imaging was performed in both bright field imaging (BFI) and high resolution (HR) mode. Fast Fourier transforms (FFTs) were applied to selected areas in the high resolution TEM (HRTEM) images to obtain information on the local crystal structure of the substrate, the thin film and the interface. Crystal orientation maps were obtained by performing scanning precession electron diffraction (SPED). The recorded data was used to calculate misorientation in the film relative to the substrate. Nanomegas ASTAR hardware and software were used for acquisition and template matching of the precession electron diffraction (PED) patterns. The template used for KNN was based on a pseudo-cubic crystal structure (data in Table A1, Appendix A). The in-plane ferroelectric response of the films was analyzed by measuring polarization-electric field (P-E) hysteresis loops, using a piezoelectric evaluation system (PES, aixPES, aixACCT, Aachen, Germany), and interdigitated Pt electrodes (electrode dimensions described in Table A2, Appendix A) deposited on top of the films. The measurements were performed at 0.1 and 0.3 Hz, using an electric field bias of 4 kV cm^{-1}.

3. Results

3.1. Deposition of KNN Thin Films

KNN thin films were successfully prepared by spin coating using both precursor solutions. The solutions wetted the substrates well, resulting in dense films with uniform thickness as evident from the SEM images shown in Figure 1. The final film thickness per deposition was ~23 and ~17 nm for the KNN-Ox and KNN-MA films, respectively. The main shrinkage of the deposited films took place during pyrolysis, while the thickness remained relatively constant during the final annealing step. The grain size of the annealed films, determined from the surface images (Figure 1), varied from 30 to 170 nm, with average values of 110 and 105 nm for the KNN-Ox and KNN-MA films, respectively. Good adhesion of the films to the substrate was observed as no delamination occurred during film handling and characterization or sample preparation for TEM.

GI-XRD patterns of KNN-Ox and KNN-MA films are shown in Figure 2, demonstrating the presence of Bragg reflections of KNN for films pyrolized at 550 °C and annealed at 700 °C. The diffraction

Materials **2019**, *12*, 2042

lines of the films become sharper by annealing at 700 °C. It is important to note that secondary phases ($K_4Nb_6O_{17}$, $K_2Nb_4O_{11}$) are present in the two KNN-Ox films and the KNN-MA film prepared in O_2 (RTP-1), while the KNN-MA film prepared in air (RTP-2) is phase pure according to GI-XRD. The secondary phases were also present in KNN-Ox films prepared in air (RTP-2) and pyrolized at 450 °C (Figure A1, Appendix A).

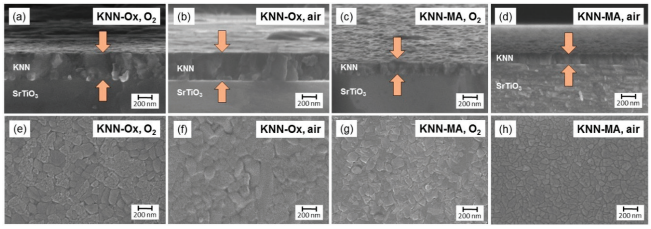

Figure 1. SEM micrographs of KNN films prepared by spin coating of the two precursor solutions (**a**,**b**,**e**,**f**) KNN-Ox (15 depositions) and (**c**,**d**,**g**,**h**) KNN-MA (10 depositions). (**a**–**d**) are cross-sectional images of the thin films. (**e**–**h**) are top-view images of the surface of the films.

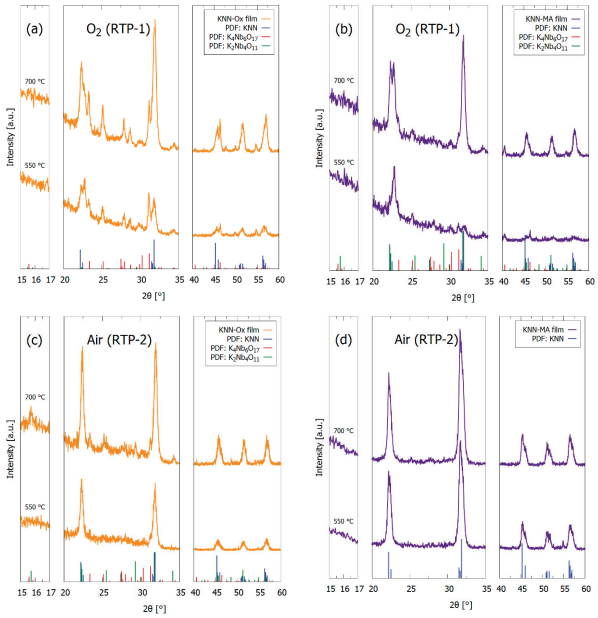

Figure 2. GI-XRD patterns of pyrolyzed (550 °C) and annealed (700 °C) 15-layer thick films from the precursor solutions (**a**), (**c**) KNN-Ox and (**b**), (**d**) KNN-MA. (**a**,**b**) are films thermally processed in O_2 (RTP-1) and (**c**,**d**) are films prepared in air (RTP-2). An incident angle of 2° was used. Reference patterns for $K_{0.5}Na_{0.5}NbO_3$ (blue, PDF card 00-061-0315), $K_4Nb_6O_{17}$ (red, PDF card 04-009-6408) and $K_2Nb_4O_{11}$ (green, from Madaro et al. [35]) are included in the figure.

Materials **2019**, *12*, 2042 5 of 16

θ–2θ X-ray diffraction patterns of the KNN-MA film prepared in air is presented in Figure 3, including the diffraction pattern of the STO substrate. The patterns confirm the phase purity of KNN prepared from the KNN-Ma solution and thermal treatment in air. The insets in Figure 3 highlight the (100) and (200) Bragg reflections of the KNN films. The pseudo-cubic (100), (110) and (200) reflections of KNN are clearly present for the KNN-MA film, and the relative intensity of the pseudo-cubic (100) and (110) reflections demonstrate substantial texturing. The (100):(110) intensity ratio of the KNN-MA film annealed at 700 °C is approximately 5.2, compared to the theoretical ratio of 0.67 for KNN powders.

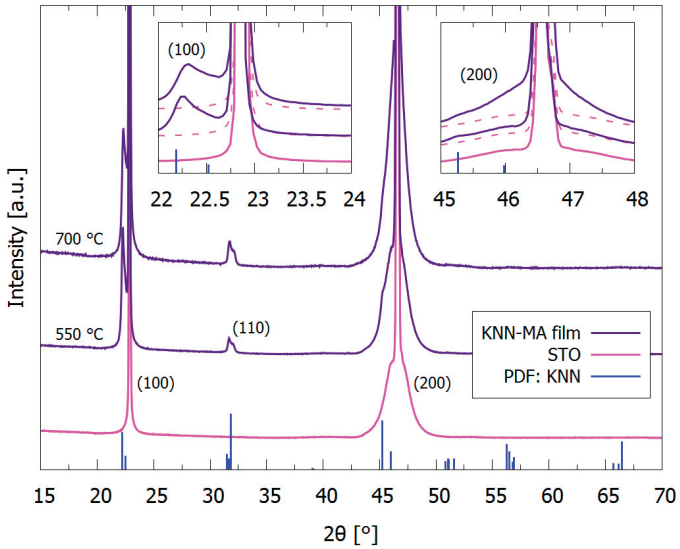

Figure 3. θ–2θ XRD patterns of pyrolyzed (550 °C) and annealed (700 °C) 15 layer thick KNN films prepared from the precursor solution KNN-MA and thermally processed in air (RTP-2). The insets highlight the pseudo-cubic (100) and (200) KNN reflections close to the corresponding STO reflections. The diffraction pattern of the (100) STO substrate is included. Reference pattern for $K_{0.5}Na_{0.5}NbO_3$ (blue, PDF card 00-061-0315) is included.

The microstructure of the KNN-MA film annealed at 700 °C in air (RTP-2) is shown in Figure 4. The phase purity of the films was confirmed by electron microscopy and electron diffraction. The microstructure is dominated by continuous columnar KNN grains through the film. The average thickness for each deposition was 17 ± 1 nm based on electron microscopy (SEM and TEM). A thin interfacial layer of 1–3 nm was observed between the substrate and the KNN-MA film (Figure 4a). An orientation map with reconstructed grains is presented in Figure 5a. The coloring gives the misorientation relative to the substrate (blue-yellow, low-high), demonstrating a polycrystalline microstructure. This is supported by the figures presented in Figure 5b, showing no in-plane texturing in the calculated orientation distribution function (ODF) probability plot and only some clustering of crystal coordinates originating from the substrate in the pole figures.

Materials **2019**, *12*, 2042 6 of 16

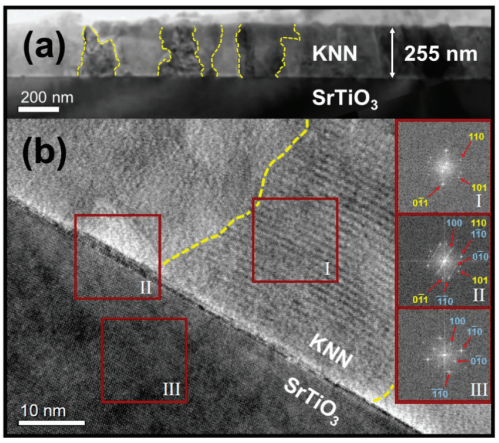

Figure 4. TEM images of the KNN film from the KNN-MA precursor solution prepared in air (RTP-2). (**a**) Bright field image (BFI) of the thin film cross section. Grain boundaries are highlighted with yellow lines. (**b**) High resolution TEM image (HRTEM) from the cross section with electron diffraction patterns from three selected areas (I–III). The electron diffraction pattern from Area II also contained the diffraction spots from Areas I and III.

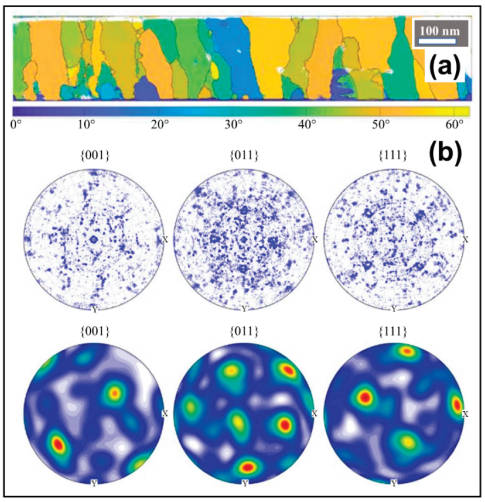

Figure 5. Misorientation mapping of 15-layer thick KNN film pyrolyzed at 550 °C and annealed at 700 °C in air (RTP-2), from the KNN-MA precursor solution; (**a**) Map of misorientation relative to the mean orientation of the substrate, with reconstructed grain boundaries. The substrate is located at the bottom; (**b**) Oriented pole figures of crystal coordinates (**top**), and calculated ODFs with colors indicating the probability density (**bottom**).

Materials **2019**, *12*, 2042 7 of 16

P-E hysteresis loops of the KNN-MA film prepared in air (RTP-2) at 0.1 and 0.3 Hz are presented in Figure 6a with the current flow for these measurements in Figure 6b. Ferroelectric polarization switching is present at both frequencies, indicated by current spikes at the coercive field (~2.2–2.7 kV cm^{-1}) in Figure 6b. The ferroelectric switching is obscured by leakage current. At higher frequencies (<10 HZ) ferroelectric switching was not observed, also when the applied field was increased to 120 kV cm^{-1} (Figure A2, Appendix A).

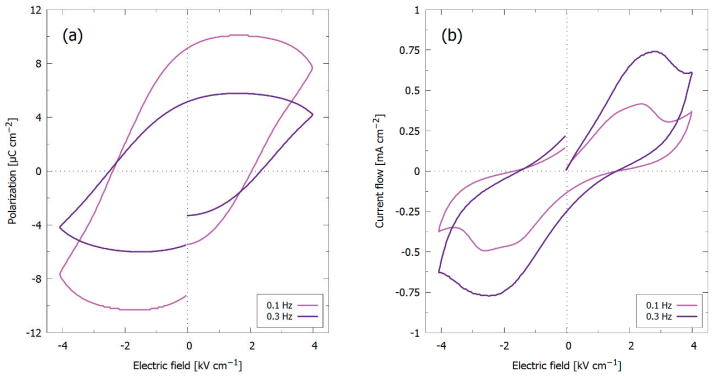

Figure 6. (**a**) P-E hysteresis loops of KNN-MA films prepared in air (RTP-2) at 0.1 and 0.3 Hz, using an electric field bias of 4 kV cm^{-1}; (**b**) The correspond current flows during the measurements.

3.2. *Preparation of KNN Powders*

Powders prepared from the precursor solutions were investigated to give additional information concerning the decomposition/crystallization kinetics. XRD patterns of the two heat-treated powders from the precursor solutions (KNN-Ox and KNN-MA) are given in Figure 7. Crystallization of the KNN perovskite phase appeared at 450 °C in both powders, although the crystallinity is more prominent in the KNN-Ox powder at this temperature. Phase pure KNN powders were obtained from 500 °C and 550 °C for KNN-Ox and KNN-MA, respectively. Notably, $K_4Nb_6O_{17}$ was formed at 450 °C in the KNN-Ox powder, but this phase vanished after heat treatment at 500 °C.

The thermal decomposition of the powders from the precursor solutions was further studied by TGA-MS in synthetic air and O_2, and the data are shown in Figure 8. The KNN-Ox precursor (Figure 8a) decomposes in the temperature interval 200 to 400 °C, compared to the two-step decomposition of the KNN-MA precursor at 200 to 400 °C and 500 to 550 °C, Figure 8b. The mass loss in the KNN-Ox precursor powder before 200 °C is mainly assigned to evaporation of water, followed by an endothermic decomposition between 200 °C and 300 °C. The mass loss observed at 350–400 °C is mostly due to combustion of carbon species and decomposition of nitrates, as evident from the MS-signatures and the exothermic dip at this temperature interval. The thermogravimetric (TG) data for the KNN-Ox powders in air and O_2 are more or less identical from 400 °C and above. The overall mass loss in the KNN-Ox precursor is ~55 wt.%. The first decomposition step (200 to 400 °C) of the KNN-MA precursor powder is analogous to the decomposition of the KNN-Ox powder between 200 and 300 °C, although the overall energy flux is exothermic in this step. The second decomposition step is an exothermic combustion of carbon and decomposition of nitrates, shifted up in temperature to 500–550 °C compared to the same decomposition in the KNN-Ox gel (350–400 °C). This decomposition step is notably steeper for the KNN-MA powder in oxygen atmosphere (500–515 °C) than in synthetic air (500–550 °C). The overall mass loss of the KNN-MA precursor is ~65 wt.%, where ~20 wt.% is lost in the second decomposition step.

Materials **2019**, *12*, 2042

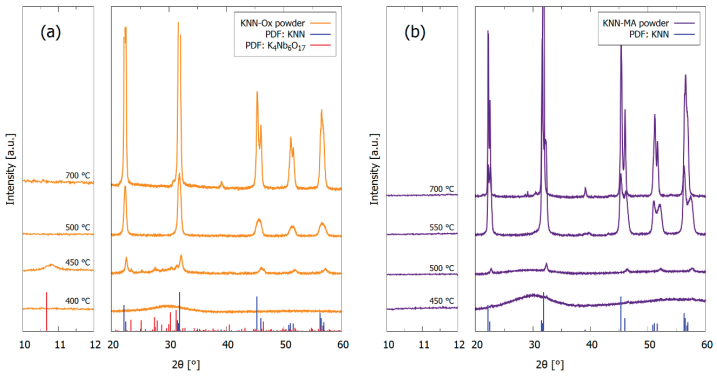

Figure 7. Powder X-ray diffraction patterns of heat-treated powder from the precursor solutions (**a**) KNN-Ox and (**b**) KNN-MA. Reference patterns for $K_{0.5}Na_{0.5}NbO_3$ (blue, PDF card 00-061-0315) and $K_4Nb_6O_{17}$ (red, PDF card 04-009-6408) are included.

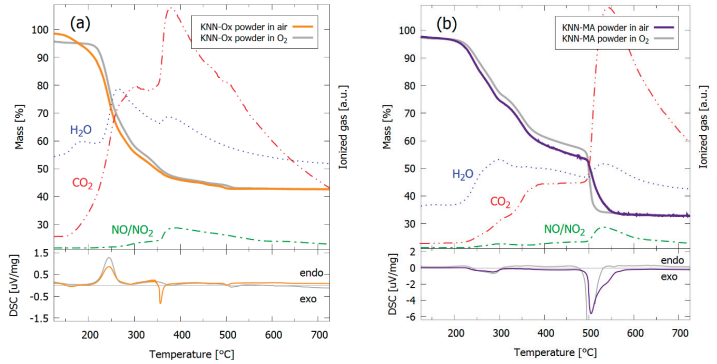

Figure 8. Thermogravimetric analyses of powders from the precursor solutions (**a**) KNN-Ox and (**b**) KNN-MA. The top panels contain mass loss curves (solid) from the TG and gas signatures (dotted) from the MS. The gas signatures are from the measurements in synthetic air. The lower panels contain the differential scanning calorimetry (DSC) signals from the measurements.

Fourier-transform infrared spectra of the powders heat-treated at different temperatures, presented in Figure 9, suggest no precursor decomposition at 200 °C as the vibrational modes are mostly resembling the modes of the complexing agents, i.e., oxalic and malic acid for KNN-Ox and KNN-MA, respectively. The IR spectra show diminished and shifted vibrational modes of the initial bands for both powders after heat treatment at 300 °C. At 400 °C, only bands corresponding to Nb-O (~525 cm^{-1}) are observed in the KNN-Ox powder in addition to C–O/O–C=O (~1300 cm^{-1}) and C=O (~1600 cm^{-1}), corresponding to carbonates. A broad band at 1100–1700 cm^{-1} in the temperature range 400–500 °C is observed in the KNN-MA powder, marked with horizontal arrows in Figure 9b. This band is confirming the presence of residuals of organics in line with the second mass loss in the TGA data (Figure 8b) and an amorphous phase at 450 °C in the powder XRD (Figure 7b). This is in coherence with the powder going from a brown to white color between 500 and 550 °C. The characteristic perovskite band at ~525 cm^{-1}

Materials **2019**, *12*, 2042

show the formation of crystalline KNN after heat treatment at 500 and 550 °C for the KNN-Ox powder and KNN-MA powder, respectively.

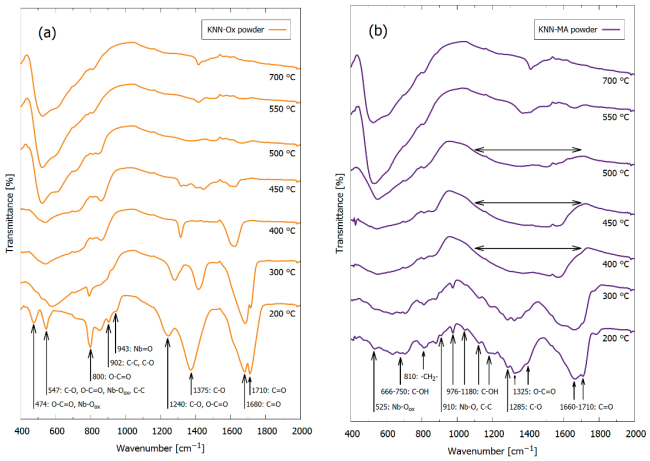

Figure 9. FTIR spectra of heat-treated powders from the precursor solutions (**a**) KNN-Ox and (**b**) KNN-MA. Characteristic vibrational modes are assigned. The horizontal arrows in (**b**) highlight the broad band at 1100–1700 cm^{-1}, corresponding to residuals of organic species.

4. Discussion

4.1. Phase Purity

Both precursor solutions yielded phase pure KNN by thermal treatment of powders from the solutions (Figure 7), which is in accordance with previous work [30,32]. However, only the KNN-MA solution heat-treated in air gave phase pure KNN thin films, as evident from the GI-XRD patterns in Figure 2. Alkali metal deficient secondary phases ($K_4Nb_6O_{17}$, $K_2Nb_4O_{11}$) formed in the films synthesized from the KNN-Ox and the KNN-MA solution in O_2. Both these secondary phases have been reported previously in relation to KNN synthesis [36], however, for KNN thin film synthesis $K_4Nb_6O_{17}$ is the most frequently reported due to the low nucleation temperature [20,37] and the instability of $K_2Nb_4O_{11}$ at lower temperatures [35,38]. Previous work using a similar oxalic acid-complexed niobium precursor solution reported formation of the $K_2Nb_4O_{11}$ secondary phase in ceramics sintered at 1100 °C [31] and in thin films heat-treated at 800 °C [26]. $K_4Nb_6O_{17}$ was also observed in the 450 °C in heat-treated KNN-Ox powder (Figure 7a), but the phase was eliminated by further heat treatment at 500 °C or higher. The presence of $K_4Nb_6O_{17}$ in both the KNN-Ox powder and KNN-Ox films, and the elimination of this phase in the powder and not in the films, can be explained by two phenomena: (i) Nucleation kinetics of the crystalline phases and (ii) volatilization of alkali metals. The results presented here demonstrate that both phenomena are dependent on the precursor chemistry and atmosphere during thermal treatment. More specific, the nucleation kinetics and evolution of secondary phases are dependent on the precursor decomposition temperature relative to the nucleation temperature. In general, the precursor decomposition is observed to be completed before the nucleation of KNN in the KNN-Ox system, whereas the decomposition is not yet completed when nucleation of KNN takes place in the KNN-MA system.

Materials **2019**, *12*, 2042

4.1.1. Nucleation Kinetics

Nucleation of the targeted KNN phase occurred at around 450 °C in both the KNN-Ox and KNN-MA powders (Figure 7), although the crystallinity was higher in the KNN-Ox powder. Phase pure KNN was obtained at 500 °C and 550 °C in the KNN-Ox and KNN-MA powders, respectively. However, $K_4Nb_6O_{17}$ was also formed at 450 °C in the KNN-Ox powder. At the temperature when KNN was first formed (450 °C), the KNN-Ox powder mostly consists of amorphous niobium oxide and alkali metal carbonates in addition to KNN, whereas the thermal decomposition of the organic residuals in the KNN-MA powder was not completed, as evident from the TGA and FTIR data (Figure 8; Figure 9, respectively). In the KNN-MA powder, the nucleation of crystalline phases was affected by the delayed decomposition process, thus shifting the nucleation temperature upwards and suppressing the formation of the $K_4Nb_6O_{17}$ secondary phase. In case of the KNN-Ox powder, the nucleation of the $K_4Nb_6O_{17}$ secondary phase was not suppressed in the same manner and nucleation of both KNN and $K_4Nb_6O_{17}$ occurred at 450 °C. These observations from the KNN powders are in line with the GI-XRD patterns in Figure 3, as alkali metal poor secondary phases are formed in the films from the KNN-Ox precursor solution. Reduction of the pyrolysis temperature during processing of the KNN-Ox films was also attempted (Figure A1, Appendix A), but this did not affect the phase composition of the films compared to the films pyrolyzed at 550 °C. Traces of a secondary phase are also observed in the films from the KNN-MA precursor solution heat-treated in oxygen. This is expected due to a more efficient decomposition of the residual mass in the system around 500 °C, as observed in the TGA measurement (Figure 8), thus enabling nucleation of $K_4Nb_6O_{17}$ during pyrolysis in oxygen. In short, elevation of the nucleation temperature, e.g., by engineering of the decomposition mechanisms of the precursor solution, is crucial to avoid nucleation of secondary phases during synthesis of KNN from solutions.

4.1.2. Alkali Metal Volatility

The absence of alkali metal poor phases in the KNN-MA powder at 450 °C was rationalized by the presence of residuals of organics. The volatility of alkali metals oxides must also be taken into consideration to explain the evolution of the secondary phases in the KNN-Ox powder and thin films. As evident from the XRD in Figure 7a, the secondary phase formed at 450 °C in the KNN-Ox powder could be removed by further heat treatment at 500 °C. The disappearance of this secondary phase at higher temperatures in the powder suggests that $K_4Nb_6O_{17}$ is metastable and will react with residual alkali carbonates in the powder to form KNN when the reaction kinetics (temperature) is increased. Alkali metal carbonates are present in the KNN-Ox powder at 450 °C, as seen in the KNN-Ox IR-spectrum (Figure 9a) at 400 °C where C–O/O–C=O and C=O modes are observed. The reaction involving the secondary phase can be formulated as

$$K_4Nb_6O_{17}\ (s) + K_2CO_3\ (s) \rightarrow 6\ KNbO_3\ (s) + CO_2\ (g) \quad (1)$$

where the presence of Na is neglected for simplicity.

In the case of KNN films, the surface area is significantly higher than for the powder, and diffusion of volatile species away from a flat surface with purging furnace atmosphere is higher compared to evaporation from a porous powder compact. Alkali metal carbonates are volatile and pose a constant challenge in KNN synthesis due to loss through evaporation [1–3]. Therefore, loss of alkali metal carbonates due to evaporation during the heat treatment of the thin films will result in irreversible changes in the cation stoichiometry, and $K_4Nb_6O_{17}$ cannot react to form KNN according to Reaction (1). This demonstrates that once $K_4Nb_6O_{17}$ is formed during film pyrolysis, it cannot be removed by Reaction (1) by further thermal treatment if irreversible changes in the alkali metal to niobium stoichiometry has taken place due to evaporation of alkali metal carbonates. Similar observations have been reported by Wang et al. [39], where the loss of alkali metals was suppressed by addition of organic stabilizing agents (MEA, DEA and EDTA) to the precursor solution.

4.2. Texture and Microstructure

The TEM characterization of the KNN-MA film synthesized in air (Figures 4 and 5) revealed a 1–3 nm thick epitaxial interface layer between the substrate and the KNN film, followed by a columnar microstructure throughout the film thickness. Fast Fourier transform of the interface area (Inset II in Figure 4) give information from the combination of Areas I and III, but the TEM misorientation mapping (Figure 5a) demonstrate that this layer is epitaxial KNN (thin blue area at the bottom). The thin epitaxial layer corresponds to the inner part of the first deposited layer (17 nm). The θ–2θ diffractions of the KNN-MA films demonstrated that the films have out-of-plane texturing (Figure 3. This is due to preferential orientation of the columnar grains, despite that the PED pattern mapping indicate a local in-plane polycrystalline microstructure. No symmetry pointing towards texturing can be observed in the pole figures (Figure 5b). This is further supported by plotting misorientation of PED patterns relative to the substrate (Figure A3, Appendix A), where the misorientation follows the Mackenzie distribution of polycrystalline materials [40]. This suggests a mixed heteroepitaxial and somewhat oriented homogeneous nucleation and growth in the first deposited layer [41]. The crystallization mechanism of the subsequent layers is dominated by heterogeneous nucleation, forming a thin epitaxial interface and columnar grains with out-of-plane preferential orientation. Using a thermal treatment program with a low pyrolysis temperature (400 °C) and a high heating rate and annealing temperature (40 K s^{-1}, 800 °C), Pham et al. [26] obtained highly textured KNN films using an oxalic acid-complexed niobium precursor (KNN-Ox) similar to the one presented in this work. Pyrolysis at 400 °C prevents nucleation of KNN until the final annealing, and combined with the use of a salt flux, strongly textured growth of the film was promoted. Therefore, the thermal processing during synthesis dictates the degree of texturing/epitaxy of the final films, which is in line with Yu et al. [25]. This suggests that phase pure epitaxial KNN films should be obtainable from the KNN-MA precursor solution by altering the thermal processing during synthesis

4.3. In-Plane Ferroelectric Strain

A ferroelectric response in the polarization-electric field measurements (Figure 6) of the KNN-MA film was only obtained at low frequencies (0.1 and 0.3 Hz) and field (4 kV cm^{-1}). At higher frequencies, the film exhibited a capacitive behavior (Figure A2, Appendix A). However, at the conditions presented in Figure 6 (0.1 and 0.3 Hz, 4 kV cm^{-1}), a leakage current is clearly present. The polarization observed in these measurements are expected to be due to (i) strain-induced out-of-plane preferential polarization, which is normal to the in-plane electric field used in this study and (ii) a parasitic contribution from the leakage current.

(i) Strain-induced preferential polarization: Synthesis of a thin film on a dissimilar substrate will cause misfit strain in the film due to different lattice parameters and thermal expansion coefficients in the two materials. The lattice parameter of bulk STO is smaller than the pseudo-cubic lattice parameter of KNN [42,43], and the thermal expansion coefficient of STO is higher than that of KNN [44,45]. The KNN film will thus experience compressive in-plane strain promoting out-of-plane polarization [46]. Consequently, only a minor polarization switching was observed (Figure 6). Growing the KNN films on a substrate giving tensile in-plane strain (e.g., $SrRuO_3$/Pt/MgO [47], Pt/$SrTiO_3$ [48]) will promote in-plane polarization and should therefore promote polarization saturation when conducting in-plane measurements.

(ii) Leakage current: Current leakage is a persistent challenge in KNN thin films due to formation of conductive electron holes ($h^{\bullet}$) in the films [49]. It is proposed that the electron holes form due to oxidation of the KNN films, enabled by the presence of oxygen vacancies in the films that originate from loss of alkali oxides (K_2O or Na_2O) at the film surface during synthesis. Mn-doping is usually applied in KNN to reduce the leakage current [49,50]. Dopants manipulating phase boundaries in KNN to enhance the ferroelectric properties has been thoroughly investigated by others [1] and might also be necessary to observe a stronger ferroelectric behavior in KNN thin films.

5. Conclusions

An environmentally friendly synthesis route to phase pure KNN films by aqueous chemical solution deposition was successfully developed. The phase purity of KNN films from two different precursor solutions, differentiated by the complexing agent for niobium, was demonstrated to be related to the decomposition temperature of the precursors during synthesis. Phase pure, dense KNN films were obtained from the solution with malic acid as complexing agent (KNN-MA) and when processed in air due to suppressed nucleation of the secondary phase due incomplete thermal decomposition of the deposited film. The decomposition of the precursors during thermal treatment of the KNN-MA films was completed at 550 °C (air) and 515 °C (O_2), and ~20 wt.% of undecomposed mass remained at the nucleation temperature. The phase pure KNN-MA films were shown to have an out-of-plane textured columnar microstructure and to have ferroelectric properties. Finally, KNN films containing secondary phases ($K_4Nb_6O_{17}$, $K_2Nb_4O_{11}$) was obtained from the solution with oxalic acid as complexing agent (KNN-Ox) due to limited suppression of nucleation of the secondary phase due to a lower thermal decomposition temperature in this case. The work demonstrates the importance of chemistry for nucleation and growth and phase purity of thin films prepared by chemical solution deposition.

Author Contributions: N.H.G., M.-A.E. and T.G. conceived and designed the experiments; N.H.G. and S.M.D. synthesized the powders and thin films and performed SEM and XRD on the thin films; N.H.G. performed XRD, TGA-MS and FTIR on the powders; A.T. and R.H. performed TEM; N.H.G. and T.M.R. performed the ferroelectric measurements; N.H.G., A.T., R.H., J.G., M.-A.E. and T.G. analyzed the data; N.H.G. and T.G. wrote the paper with inputs from all the authors. All authors gave final approval for publication.

Funding: Financial support from the Research Council of Norway through NANO2021 project PIEZOMED project number 250184 is acknowledged. The Research Council of Norway is acknowledged for the support to the Norwegian Micro-and Nano-Fabrication Facility, NorFab, project number 245963/F50.

Acknowledgments: Anders B. Blichfeld is acknowledged for the help and advice concerning the use of the RTP-2 unit.

Conflicts of Interest: The authors declare no conflicts of interest.

Appendix A

Details of the pseudo-cubic crystal structure for KNN used for template matching of PED patterns are given in Table A1.

Table A1. Lattice position of atoms, lattice parameters and unit cell angles in pseudo-cubic KNN used as template for precession electron diffraction (PED) pattern matching.

Element	X	Y	Z	Occ.
K	0.0	0.0	0.0	0.5
Na	0.0	0.0	0.0	0.5
Nb	0.5	0.5	0.5	1.0
O	0.0	0.5	0.5	1.0
Lattice parameters and angles	a = b = c = 3.983 Å		α = β = γ = 90°	

Details of the interdigitated Pt electrodes used for P-E measurements are given in Table A2.

Table A2. Dimensions of interdigitated Pt electrodes.

Dimension	Size
Finger length	900 µm
Finger width	3.311 µm
Finger distance	6.689 µm
Number of fingers	100

Figure A1 shows GI-XRD patterns of pyrolyzed (450 °C) and annealed (700 °C) KNN-Ox films.

Materials **2019**, *12*, 2042 13 of 16

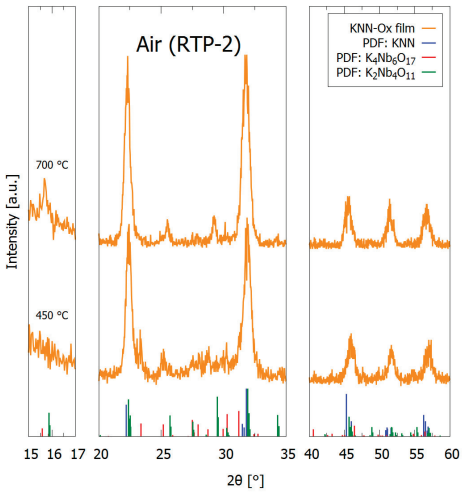

Figure A1. GI-XRD pattern of pyrolyzed (450 °C) and annealed (700 °C) KNN-Ox films (5 depositions) prepared in air (RTP-2). An incident angle of 2° was used. Reference patterns for $K_{0.5}Na_{0.5}NbO_3$ (blue, PDF card 00-061-0315), $K_4Nb_6O_{17}$ (red, PDF card 04-009-6408) and $K_2Nb_4O_{11}$ (green, from Madaro et al. [35]) are included in the figure.

P-E hysteresis loops of the KNN-MA film prepared in air (RTP-2) at different frequencies and electric fields is shown in Figure A2.

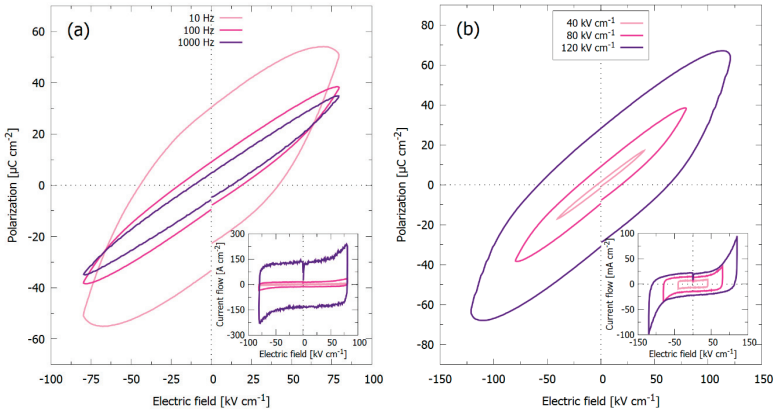

Figure A2. P-E hysteresis loops of the KNN-MA film prepared in air (RTP-2) (**a**) at 10, 100 and 1000 Hz, using an electric field bias of 80 kV cm^{-1} and (**b**) at 40, 80 and 120 kV cm^{-1}, using a frequency of 100 Hz. Insets: Current flows during the measurements.

Figure A3 illustrates misorientation of PED patterns relative to the substrate, based on results presented in Figure 5a.

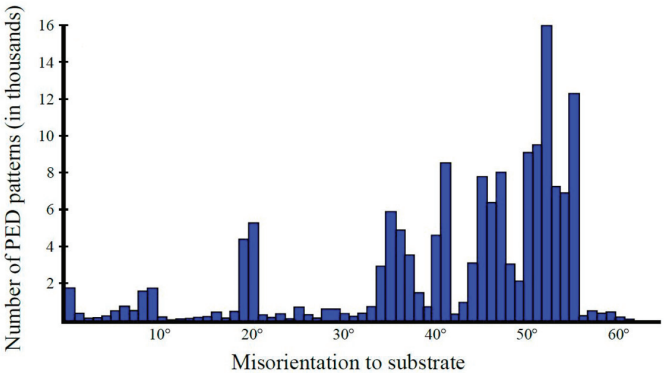

Figure A3. Misorientation of PED patterns relative to the substrate of 15 layer thick KNN film pyrolyzed in air (RTP-2) at 550 °C and annealed at 700 °C, from the KNN-MA precursor solution.

References

1. Wu, J.; Xiao, D.; Zhu, J. Potassium−sodium niobate lead-free piezoelectric materials: Past, present, and future of phase boundaries. *Chem. Rev.* **2015**, *115*, 2559–2595. [CrossRef] [PubMed]
2. Safari, A.; Abazari, M. Lead-free piezoelectric ceramics and thin films. *Ultrason. Ferroelectr. Freq. Control* **2010**, *57*, 2165–2176. [CrossRef] [PubMed]
3. Rödel, J.; Jo, W.; Seifert, K.T.P.; Anton, E.M.; Granzow, T.; Damjanovic, D. Perspective on the development of lead-free piezoceramics. *J. Am. Ceram. Soc.* **2009**, *92*, 1153–1177. [CrossRef]
4. Xu, K.; Li, J.; Lv, X.; Wu, J.; Zhang, X.; Xiao, D.; Zhu, J. Superior piezoelectric properties in potassium-sodium niobate lead-free ceramics. *Adv. Mater.* **2016**, *28*, 8519–8523. [CrossRef] [PubMed]
5. Yu, S.-W.; Kuo, S.-T.; Tuan, W.-H.; Tsai, Y.-Y.; Su, C.-H. Ion release from three lead-free piezoelectric ceramics and their physical and cytotoxicity characteristics. *Mater. Lett.* **2011**, *65*, 3522–3524. [CrossRef]
6. Yu, S.; Kuo, S.; Tuan, W.; Tsai, Y.; Wang, S. Cytotoxicity and degradation behavior of potassium sodium niobate piezoelectric ceramics. *Ceram. Int.* **2012**, *38*, 2845–2850. [CrossRef]
7. Kwak, J.; Kingon, A.I.; Kim, S.H. Lead-free $(Na_{0.5},K_{0.5})NbO_3$ thin films for the implantable piezoelectric medical sensor applications. *Mater. Lett.* **2012**, *82*, 130–132. [CrossRef]
8. Won, S.S.; Lee, J.; Venugopal, V.; Kim, D.-J.; Lee, J.; Kim, I.W.; Kingon, A.I.; Kim, S.-h. Lead-free Mn-doped $(K_{0.5},Na_{0.5})NbO_3$ piezoelectric thin films for MEMS-based vibrational energy harvester applications. *Appl. Phys. Lett.* **2016**, *108*, 232908. [CrossRef]
9. Jeong, C.K.; Han, J.H.; Palneedi, H.; Park, H.; Hwang, G.-T.; Joung, B.; Kim, S.-G.; Shin, H.J.; Kang, I.-S.; Ryu, J.; et al. Comprehensive biocompatibility of nontoxic and high-output flexible energy harvester using lead-free piezoceramic thin film. *Appl. Mater.* **2017**, *5*, 74102. [CrossRef]
10. Shibata, K.; Oka, F.; Nomoto, A.; Mishima, T.; Kanno, I. Crystalline structure of highly piezoelectric $(K,Na)NbO_3$ films deposited by RF magnetron sputtering. *Jpn. J. Appl. Phys.* **2008**, *47*, 8909–8913. [CrossRef]
11. Saito, T.; Wada, T.; Adachi, H.; Kanno, I. Pulsed laser deposition of high-quality $(K,Na)NbO_3$ thin films on $SrTiO_3$ substrate using high-density ceramic targets. *Jpn. J. Appl. Phys.* **2004**, *43*, 6627–6631. [CrossRef]
12. Cho, C. c-Axis oriented $(Na,K)NbO_3$ thin films on Si substrates using metalorganic chemical vapor deposition. *Mater. Lett.* **2002**, *57*, 781–786. [CrossRef]
13. Sønsteby, H.H.; Nilsen, O.; Fjellvåg, H. Atomic layer deposition of $(K,Na)(Nb,Ta)O_3$ thin films. *J. Vaccuum Sci. Technol. A* **2016**, *34*. [CrossRef]
14. Yan, X.; Ren, W.; Wu, X.; Shi, P.; Yao, X. Lead-free $(K,Na)NbO_3$ ferroelectric thin films: Preparation, structure and electrical properties. *J. Alloys Compd.* **2010**, *508*, 129–132. [CrossRef]
15. Chowdhury, A.; Bould, J.; Londesborough, M.G.S.; Milne, S.J. Fundamental issues in the synthesis of ferroelectric $Na_{0.5}K_{0.5}NbO_3$ thin films by sol−gel processing. *Chem. Mater.* **2010**, *22*, 3862–3874. [CrossRef]

16. Zhang, D.; Zheng, F.; Yang, X.; Liu, H.; Cao, M. Preparation and ferroelectric properties of $K_{0.5}Na_{0.5}NbO_3$ thin films derived from non- alcohol niobium salt sol-gel process. *Integr. Ferroelectr.* **2014**, *154*, 673–678. [CrossRef]
17. Lai, F.; Li, J.-F.; Zhu, Z.-X.; Xu, Y. Influence of Li content on electrical properties of highly piezoelectric $(Li,K,Na)NbO_3$ thin films prepared by sol-gel processing. *J. Appl. Phys.* **2009**, *106*, 64101. [CrossRef]
18. Kang, C.; Dongna, J.P. Growth and characterization of $(K_{0.5}Na_{0.5})NbO_3$ thin films by a sol–gel method. *J. Sol-Gel Sci. Technol.* **2011**, *58*, 85–90. [CrossRef]
19. Wu, X.Q.; Wang, L.Y.; Ren, W.; Yan, X.; Shi, P.; Chen, X.F.; Yao, X. Preparation and properties of (110) oriented lead-free sodium potassium niobate thin films by MOD method. *Ferroelectrics* **2008**, *367*, 61–66. [CrossRef]
20. Nakashima, Y.; Sakamoto, W.; Maiwa, H.; Shimura, T.; Yogo, T. Lead-free piezoelectric $(K,Na)NbO_3$ thin films derived from metal alkoxide precursors. *Jpn. Soc. Appl. Phys.* **2007**, *46*, L311–L313. [CrossRef]
21. Ahn, C.W.; Lee, S.Y.; Lee, H.J.; Ullah, A.; Bae, J.S.; Jeong, E.D.; Choi, J.S.; Park, B.H.; Kim, I.W. The effect of K and Na excess on the ferroelectric and piezoelectric properties of $K_{0.5}Na_{0.5}NbO_3$ thin films. *J. Phys. D Appl. Phys.* **2009**, *42*, 215304. [CrossRef]
22. Lu, T.; Zhu, K.; Liu, J.; Wang, J.; Qiu, J. Lead-free $(K,Na)NbO_3$ thin films derived from chemical solution deposition modified with EDTA. *J. Mater. Sci.* **2014**, *25*, 1112–1116. [CrossRef]
23. Vendrell, X.; Raymond, O.; Ochoa, D.A.; García, J.E.; Mestres, L. Growth and physical properties of highly oriented La-doped $(K,Na)NbO_3$ ferroelectric thin films. *Thin Solid Films* **2015**, *577*, 35–41. [CrossRef]
24. Luo, J.; Sun, W.; Zhou, Z.; Bai, Y.; Wang, Z.J.; Tian, G.; Chen, D.; Gao, X.; Zhu, F.; Li, J.-f. Domain evolution and piezoelectric response across thermotropic phase boundary in $(K,Na)NbO_3$-based epitaxial thin films. *Appl. Mater. Interfaces* **2017**, *9*, 13315–13322. [CrossRef] [PubMed]
25. Yu, Q.; Li, J.; Chen, Y.; Cheng, L.-Q.; Sun, W.; Zhou, Z.; Wang, Z. Effect of pyrolysis temperature on sol-gel synthesis of lead-free piezoelectric $(K,Na)NbO_3$ films on $Nb:SrTiO_3$ substrates. *J. Am. Ceram. Soc.* **2014**, *97*, 107–113. [CrossRef]
26. Pham, K.-N.; Gaukås, N.H.; Morozov, M.; Tybell, T.; Vullum, P.E.; Grande, T.; Einarsrud, M.-A. Epitaxial $K_{0.5}Na_{0.5}NbO_3$ thin films by aqueous chemical solution deposition. *R. Soc. Open Sci.* **2019**, *6*, 180989. [CrossRef] [PubMed]
27. Malič, B.; Kupec, A.; Vojisavljević, K.; Pečnik, T. Lead-free Ferroelectric Thin Films. In *Handbook of Sol-Gel Science and Technology*; Springer International Publishing: New York City, NY, USA, 2018; pp. 667–694.
28. Wang, L.; Yao, K.; Ren, W. Piezoelectric $K_{0.5}Na_{0.5}NbO_3$ thick films derived from polyvinylpyrrolidone-modified chemical solution deposition. *Appl. Phys. Lett.* **2008**, *93*, 92903. [CrossRef]
29. Yao, L.; Zhu, K.; Wang, J.; Liu, J.; Qiu, J.; Cheng, M.; Gu, Q. Annealing temperature effects on the electrical properties of $(K,Na)NbO_3$ thin film fabricated by a sol-gel process with a citrate precursor solution. *Ferroelectrics* **2016**, *493*, 47–53. [CrossRef]
30. Haugen, A.B.; Olsen, G.H.; Madaro, F.; Morozov, M.I.; Tutuncu, G.; Jones, J.L.; Grande, T.; Einarsrud, M.-A. Piezoelectric $K_{0.5}Na_{0.5}NbO_3$ ceramics textured using needlelike $K_{0.5}Na_{0.5}NbO_3$ templates. *J. Am. Ceram. Soc.* **2014**, *97*, 3818–3825. [CrossRef]
31. Haugen, A.B.; Madaro, F.; Bjørkeng, L.; Grande, T.; Einarsrud, M.-A. Sintering of sub-micron $K_{0.5}Na_{0.5}NbO_3$ powders fabricated by spray pyrolysis. *J. Eur. Ceram. Soc.* **2015**, *35*, 1449–1457. [CrossRef]
32. Madaro, F. Synthesis of Textured $K_xNa_{1-x}NbO_3$ Materials. Ph.D. Thesis, Norwegian University of Science and Technology (NTNU), Trondheim, Norway, 2010.
33. Fairbrother, B.F.; Taylor, B. Water-soluble complexes of niobium (columbium) and tantalum. Part I. Complexes with α-hydroxy-acids and (2-hydroxyethyl)-amines. *J. Chem. Soc.* **1956**, 4946–4954. [CrossRef]
34. Blichfeld, A.B.; Bakken, K.; Chernyshov, D.; Glaum, J.; Grande, T.; Einarsrud, M.-A. Development of an experimental setup for high-temperature in situ studies of crystallization of thin films with atmosphere control. **2019**, in preparation.
35. Madaro, F.; Sæterli, R.; Tolchard, J.R.; Einarsrud, M.-A.; Holmestad, R.; Grande, T. Molten salt synthesis of $K_4Nb_6O_{17}$, $K_2Nb_4O_{11}$ and KNb_3O_8 crystals with needle- or plate-like morphology. *CrystEngComm* **2011**, *13*, 1304–1313. [CrossRef]
36. Malič, B.; Koruza, J.; Hreščak, J.; Bernard, J.; Wang, K.; Fisher, J.G.; Benčan, A. Sintering of lead-free piezoelectric sodium potassium niobate ceramics. *Materials* **2015**, *8*, 8117–8146. [CrossRef] [PubMed]
37. Tanaka, K.; Kakimoto, K.; Wang, C.; Wang, J.-J.; Ryu, H.; Kim, J.-H. Effect of (Na,K)-excess precursor solutions on alkoxy-derived $(Na,K)NbO_3$ powders and thin films. *Jpn. J. Appl. Phys.* **2007**, *46*, 6964–6970. [CrossRef]

38. Madaro, F.; Tolchard, J.R.; Yu, Y.; Einarsrud, M.-A.; Grande, T. Synthesis of anisometric $KNbO_3$ and $K_{0.5}Na_{0.5}NbO_3$ single crystals by chemical conversion of non-perovskite templates. *CrystEngComm* **2011**, *13*, 1350–1359. [CrossRef]
39. Wang, Y.; Yao, K.; Mirshekarloo, M.S.; Eng, F.; Tay, H. Effects and mechanism of combinational chemical agents on solution-derived $K_{0.5}Na_{0.5}NbO_3$ piezoelectric thin films. *J. Am. Ceram. Soc.* **2016**, *99*, 1631–1636. [CrossRef]
40. Mason, J.K.; Schuh, C.A. The generalized Mackenzie distribution: Disorientation angle distributions for arbitrary textures. *Acta Mater.* **2009**, *57*, 4186–4197. [CrossRef]
41. Queraltó, A.; Mata, M. De.; Arbiol, J.; Obradors, X.; Puig, T. Disentangling epitaxial growth mechanisms of solution derived functional oxide thin films. *Adv. Mater. Interfaces.* **2016**, *3*, 1600392. [CrossRef]
42. Tellier, J.; Malič, B.; Dkhil, B.; Jenko, D.; Cilensek, J.; Kosec, M. Crystal structure and phase transitions of sodium potassium niobite perovskites. *Solid State Sci.* **2009**, *11*, 320–324. [CrossRef]
43. Schmidbauer, M.; Kwasniewski, A.; Schwarzkopf, J. High-precition absolute lattice parameter determination of $SrTiO_3$, $DyScO_3$ and $NdGaO_3$ single crystals. *Acta Crystallogr. B* **2012**, *68*, 8–14. [CrossRef]
44. De Ligny, D.; Richet, P. High-temperature heat capacity and thermal expansion of $SrTiO_3$ and $SrZrO_3$ perovskites. *Phys. Rev. B* **1996**, *53*, 3013. [CrossRef] [PubMed]
45. Malic, B.; Razpotnik, H.; Koruza, J.; Kokalj, S.; Cilensek, J.; Kosec, M. Linear thermal expansion of lead-free piezoelectric $K_{0.5}Na_{0.5}NbO_3$ ceramics in a wide temperature range. *J. Am. Ceram. Soc.* **2011**, *8*, 2273–2275. [CrossRef]
46. Wu, J.; Wang, J. Phase transitions and electrical behavior of lead-free $(K_{0.50}Na_{0.50})NbO_3$ thin film. *J. Appl. Phys.* **2009**, *106*, 66101. [CrossRef]
47. Kanno, I.; Mino, T.; Kuwajima, S.; Suzuki, T.; Kotera, H.; Wasa, K. Piezoelectric properties of (K,Na)NbO_3 thin films deposited on (001) $SrRuO_3$/Pt/MgO. *IEEE Trans. Ultrason. Ferroelectr. Freq. Control* **2007**, *54*, 2562–2566. [CrossRef] [PubMed]
48. Tkach, A.; Santos, A.; Zlotnik, S.; Serrazina, R.; Okhay, O.; Bdikin, I.; Costa, M.E.; Vilarinho, P.M. Strain-mediated substrate effect on the dielectric and ferroelectric response of potassium sodium niobate thin films. *Coatings* **2018**, *8*, 449. [CrossRef]
49. Kondo, N.; Sakamoto, W.; Lee, B.-Y.; Iijima, T.; Kumagai, J.; Moriya, M.; Yogo, T. Improvement in ferroelectric properties of chemically synthesized lead-free piezoelectric (K,Na)(Nb,Ta)O_3 thin films by Mn doping. *Jpn. J. Appl. Phys.* **2010**, *49*, 09MA04. [CrossRef]
50. Zhao, C.; Meng, X.; Wen, W.; Zhou, Y. Energy storage of (K, Na)NbO_3 ferroelectric thin films with Mn-Ta and Mn-Ti co-doping. *Ceram. Int.* **2019**, *45*, 13772–13779. [CrossRef]

Paper II

Ferroelectric and dielectric properties of Ca^{2+}-doped and Ca^{2+}–Ti^{4+} co-doped $K_{0.5}Na_{0.5}NbO_3$ thin films

Reprinted from *J. Mater. Chem. C*, N. H. Gaukås, J. Glaum, M.-A. Einarsrud, T. Grande, Ferroelectric and dielectric properties of Ca^{2+}-doped and Ca^{2+}–Ti^{4+} co-doped $K_{0.5}Na_{0.5}NbO_3$ thin films, 8, 5102-5111, **2020**, with permission from The Royal Society of Chemistry.

Journal of Materials Chemistry C

ROYAL SOCIETY OF CHEMISTRY

PAPER

View Article Online
View Journal | View Issue

Cite this: *J. Mater. Chem. C*, 2020, **8**, 5102

Ferroelectric and dielectric properties of Ca^{2+}-doped and Ca^{2+}–Ti^{4+} co-doped $K_{0.5}Na_{0.5}NbO_3$ thin films†

Nikolai Helth Gaukås, Julia Glaum, Mari-Ann Einarsrud and Tor Grande *

Received 15th January 2020,
Accepted 5th March 2020

DOI: 10.1039/d0tc00276c

rsc.li/materials-c

Chemical solution deposition (CSD) of $K_{0.5}Na_{0.5}NbO_3$ (KNN) thin films on silicon-based substrates is an interesting technology for fabrication of lead-free ferroelectric thin films. Here, we report on improved ferroelectric and dielectric properties of KNN thin films prepared by CSD through Ca^{2+}-doping and Ca^{2+}–Ti^{4+} ($CaTiO_3$) co-doping. Undoped KNN, 0.5 mol% Ca^{2+}-doped and 0.5 mol% $CaTiO_3$-doped KNN films were deposited on platinized silicon substrates by aqueous CSD. X-ray diffraction of the films as well as powders, prepared from the precursor solutions, confirmed that the three KNN materials were single phase solid solutions. A smaller grain size was observed for the doped relative to undoped KNN films. In contrast to the pure KNN films, the Ca^{2+}- and $CaTiO_3$-doping was observed to promote ferroelectric switching, with a low leakage current and remnant polarization of 6.37 ± 0.47 and 7.40 ± 0.09 μC cm^{-2} of the Ca^{2+}- and $CaTiO_3$-doped films, respectively. The dielectric constants of the films were among the highest measured for KNN films from CSD and span from 1800 to 3200 at 1 kHz.

Introduction

Potassium sodium niobate-based ($K_{0.5}Na_{0.5}NbO_3$, KNN) piezoelectric ceramics have received considerable attention as an environmentally friendly alternative to lead zirconate titanate-based materials ($PbZr_xTi_{1-x}O_3$, PZT).[1–4] Lead-free, non-toxic and biocompatible alternatives to PZT are especially important for *in vivo* biomedical applications,[5] and KNN has shown promising results in biocompatibility tests.[6–13] Materials in form of thin films are desired in many of these applications and there has been a considerable focus on development of KNN thin films.[14–16] To bring lead-free piezoelectric ceramics to the marked, economically viable large-scale industrial fabrication routes are required.[2] Chemical solution deposition (CSD) is a cheap and reliable synthesis technique capable of high-volume production of oxide thin films.[17] Synthesis of KNN thin films by CSD is usually performed using niobium ethoxide and alkali ethoxides or acetates as precursors, and 2-methoxyethanol as the solvent.[18–49] In only a few studies other solvents have been used, *e.g.* propionic acid,[50] ethanol,[51] water[52–57] and other.[58,59] Due to low cost and the ubiquity of Si in electronics, platinized silicon (SiPt, $Pt/TiO_2/SiO_2/Si$) is by far the most used substrate in ferroelectric oxide thin film CSD synthesis.[17] KNN thin film synthesis is no exception, and the majority of studies of KNN thin films are based on using SiPt substrates,[19–24,28–36,40–43,46–48,52,53] while a few other studies are reported using other substrates like SiO_2/Si,[38,58,59] ZrO_2/Si,[44,45] $LaNiO_3$/Si,[57] Pt/MgO,[39] Pt/Al_2O_3,[49,58] metals[50,51,54] and $SrTiO_3$ (STO).[18,25–27,37,55,56]

Compositional engineering is readily used to improve the functional properties of bulk KNN ceramics.[1,4] Compositional engineering is typically applied to reduce the leakage current in KNN thin films by doping with Mn^{2+} [18–20,25,28–30,34,36,37,42,43,48] or Co^{2+},[35,36] or to improve the ferroelectric properties by altering phase boundaries using Li^+,[22,27,28,31,32] Ta^{5+},[19,21] Li^+ and Ta^{5+} [20,34] or Li^+, Ta^{5+} and Sb^{5+}.[33] Except for Ta^{5+}, these dopants are toxic, and alternative dopants are required when developing KNN-based ceramics for certain technologies, *e.g. in vivo* biomedical applications.[60] Ca^{2+} and Ti^{4+} are both non-toxic, and therefore suitable for *in vivo* applications.[61,62] Ca^{2+} doping is reported to have a softening effect on the ferroelectric properties of bulk KNN,[63] improve dielectric properties[64] and to increase the piezoelectric coefficient (d_{33} or d_{33}*) compared to undoped KNN.[63–66] Enhanced ferroelectric performance has been reported for bulk KNN doped with 0.55, 1 and 5 mol% $CaTiO_3$.[67–71] These dopants have also been reported to increase the densification[65–67,70] and to reduce ion-release from KNN in aqueous media.[66] Finally, Ikeuchi *et al.*[72] demonstrated improved piezoelectric properties in RF magnetron sputtered KNN films doped with 0–6.5 mol% $CaTiO_3$.

Here, we report on improved ferroelectric and dielectric properties of KNN thin films doped with Ca^{2+} and co-doping with stoichiometric amount of Ca^{2+} and Ti^{4+} corresponding to $CaTiO_3$. KNN films doped with 0.5 mol% Ca^{2+} and 0.5 mol%

Department of Materials Science and Engineering, NTNU Norwegian University of Science and Technology, N-7491 Trondheim, Norway. E-mail: grande@ntnu.no

† Electronic supplementary information (ESI) available. See DOI: 10.1039/d0tc00276c

View Article Online
Paper Journal of Materials Chemistry C

$CaTiO_3$ were prepared on SiPt substrates by aqueous CSD, previously applied to fabricate KNN thin films on STO substrates.[56] Powders were also prepared from the same solutions to provide information concerning crystal structure and coarsening during thermal annealing. We demonstrate that this doping of the KNN films significantly improves the ferroelectric properties, which is discussed in relation to microstructure, dielectric properties and possible point defects in the doped KNN materials.

Experimental

Materials synthesis

Precursor solutions for the materials with the acronyms KNN, KNN-Ca^{2+} and KNN-$CaTiO_3$, summarized in Table 1, were prepared using an aqueous malic acid-complexed niobium solution as described previously.[56] The niobium solution was prepared by first precipitating niobic acid by adding an ammonia solution (25 wt%, VWR Chemicals, Radnor, PA, USA) to an aqueous solution of $NH_4NbO(C_2O_4)_2{\cdot}xH_2O$ (99.99%, Sigma-Aldrich, St. Louis, MO, USA). The niobic acid precipitate was dissolved in a solution of deionized water and DL-malic acid (99%, Sigma-Aldrich) with a molar ratio corresponding to 1 : 2 (Nb : malic acid). Pre-dried $NaNO_3$ (99%, Sigma-Aldrich) and KNO_3 (99%, Alfa Aesar, Haverhill, MA, USA) were dissolved in the niobium solution, and the pH was adjusted to ~7 using ammonia solution. 5 mol% excess of Na^+ and K^+ was used in all the solutions, and the concentration of the Nb in the final solutions was ~0.09 M. The KNN-Ca^{2+} and KNN-$CaTiO_3$ precursor solutions were prepared by adding solutions of Ca^{2+} and Ti^{4+} to the KNN solution. $Ca(NO_3)_2{\cdot}4H_2O$ (99%, Sigma Aldrich) was dissolved in deionized water using ethylenediaminetetraacetic acid (EDTA, 99%, Sigma Aldrich) as complexing agent in the ratio of 1 : 2 (Ca^{2+} : EDTA). The pH was adjusted to 8 using ammonia solution, and the final concentration of the Ca^{2+}-solution was 3.23×10^{-2} M. Ti-4-isopropoxide (97%, Sigma-Aldrich) was dissolved in deionized water at 80 °C using citric acid (CA, 99%, Sigma Aldrich) as complexing agent with a ratio of 1 : 3 (Ti^{4+} : CA). The pH was adjusted to 8 using ammonia solution, and the final concentration of the Ti^{4+}-solution was determined by thermogravimetric analysis to be 7.52×10^{-1} M.

The solutions were deposited on platinized silicon (SiPt, Pt(111)/TiO_2/SiO_2/Si(100), SINTEF MiNaLab, Oslo, Norway) substrates. Prior to the deposition, the substrates were activated in an oxygen plasma cleaner (Femto, Diener Electronics, Ebhausen, Germany) to increase the wettability. The deposition was performed using a spin coater (WS-400A-6NPP/C-1, Laurell Technologies, Montgomery, PA, USA), operating at 3500 rpm for 40 s. The deposited films were dried on a hotplate at 200 °C for 3 min and pyrolyzed on a rapid heating plate (descried in[56]) at 550 °C for 5 min using a heating rate of 100 °C min^{-1}. The deposition and heat treatment were repeated 15 and 30 times. The films were post-annealed at 700 °C for 10 min using a heating rate of 100 °C min^{-1}.

KNN powders were prepared by drying the precursor solutions at 160 °C for 8 h. The dried precursor solutions were calcined and coarsened in air at 700 and 850 °C, respectively, for 4 h (LT 15/12/P330, Nabertherm, Lilienthal, Germany).

Characterization

X-ray diffraction (XRD) patterns of the powders were recorded using Cu Kα radiation (D8 Advance, Bruker, Billerica, MA, USA). Gracing incidence X-ray diffraction (GIXRD, D8 Advance, Bruker) of the films were recorded using Cu Kα radiation and a 2° incidence angle, while conventional Bragg–Brentano XRD of the films were measured using monochromatic Cu Kα radiation (D5005, Siemens, Karlsruhe, Germany). Scanning electron microscopy (SEM, Ultra 55, Carl Zeiss AG, Oberkochen, Germany) of the thin films was performed using an in-lens detector and acceleration voltage of 10 kV. For electric characterization of the films, Pt top electrodes (thickness 100 nm) with diameters of 0.5 and 1.0 mm were deposited by e-beam evaporation (Custom ATC-2200V, AJA International Inc., Scituate, MA, USA) through a shadow mask. Prior to the measurements, the films with the electrodes were heat treated at 400 °C for 2.5 h in flowing oxygen (AccuThermo AW-610, Allwin21, Morgan Hill, CA, USA). Film polarization and capacitance as a function of electric field at room temperature were analyzed with a piezoelectric evaluation system (aixACCT, Aachen, Germany). Relative permittivity as a function of temperature and frequency was studied using AC impedance spectroscopy (Alpha-A High Performance Frequency Analyzer, Novocontrol Technologies, Montabaur, Germany) with a rapid heating plate as temperature controller.[56]

Results

The powders calcined at 700 and 850 °C were phase pure based on the diffraction patterns shown in Fig. 1. All the Bragg reflections can be assigned to monoclinic KNN, and Pawley fits of the diffraction patterns are summarized in Table S1 in ESI.† A coarsening was observed for the powders going from 700 to 850 °C especially for undoped KNN (Table S1, ESI†), while no major changes in the unit cell parameters were observed by increasing the calcination temperature. A minor contraction of the unit cell volume and the *c* lattice parameter, and an increase in β-distortion of the unit cell, were observed due to the doping (Table S1, ESI†), but no apparent change in symmetry by doping can be inferred from the diffraction patterns.

Table 1 Overview of the chemical compositions and acronyms of the KNN-based thin films prepared in this work

Acronym	Chemical formula	Doping
KNN	$(K_{0.5}Na_{0.5})NbO_3$	—
KNN-Ca^{2+}	$(K_{0.495}Na_{0.495}Ca_{0.005})NbO_3$	0.5 mol% Ca^{2+}
KNN-$CaTiO_3$	$(K_{0.4975}Na_{0.4975}Ca_{0.005})Nb_{0.995}Ti_{0.005}O_3$	0.5 mol% Ca^{2+} and 0.5 mol% Ti^{4+}

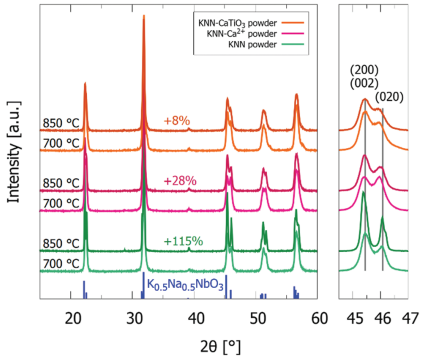

Fig. 1 XRD patterns of powders from precursor solutions calcined at 700 and 850 °C, respectively, for 4 h. Percent increase in crystallite size from 700 to 850 °C is marked in the figure above each composition. Reference pattern for $K_{0.5}Na_{0.5}NbO_3$ (blue, PDF card 00-061-0315[73]) is included.

Electron micrographs of cross sections and the top surfaces of the three different KNN films are shown in Fig. 2. Dense and uniform films were successfully deposited on the SiPt substrates. An average thickness of ~11 nm per deposition was inferred from the SEM images. The top surface of the films (insets Fig. 2) demonstrate coarser grains in the undoped KNN film (~85 nm) compared to the films doped with Ca^{2+} and $CaTiO_3$ (~70 and ~60 nm respectively). No evidence for columnar growth was observed in the cross sections, in agreement with the polycrystalline nature of the films as discussed below.

GIXRD patterns of the films after pyrolysis (550 °C) and annealing (700 °C) presented in Fig. 3 show only reflections indexed to KNN and the films appeared phase pure and polycrystalline. The low degree of texture and polycrystalline nature of the films was confirmed by conventional XRD for the undoped KNN film, shown in Fig. S3 (ESI†).

The ferroelectric behaviour of the films was analysed by measuring polarization as a function of electric field. Polarization–electric field loops measured using a frequency of 10 Hz and an electric field bias of 100 kV cm^{-1} are given in Fig. 4. Ferroelectric polarization switching is observed for the doped films (KNN-Ca^{2+}, KNN-$CaTiO_3$), demonstrated by the onset of polarization saturation at increasing field and switching current spikes in the current flux shown in the inset in Fig. 4. Ferroelectric polarization switching was not observed for the undoped KNN film regardless of the frequency and field applied.

The frequency dependency of polarization–electric field hysteresis loops of the doped KNN films between 50 and 5000 Hz is presented in Fig. 5. Electric field biases of 125 and 142 kV cm^{-1} were used for the KNN-Ca^{2+} and KNN-$CaTiO_3$ films, respectively. A decrease in polarization is observed with increasing frequency. The remnant polarization (P_r) at 50 and 1000 Hz is 6.37 ± 0.47 and 4.67 ± 0.04 μC cm^{-2} for the KNN-Ca^{2+} film and 7.40 ± 0.09 and 6.20 ± 0.51 μC cm^{-2} for the KNN-$CaTiO_3$ film. A complete list of remnant polarization (P_r), maximum polarization (P_{max}) and coercive field (E_c) from Fig. 4 and 5 is given in Table S2 in the ESI.†

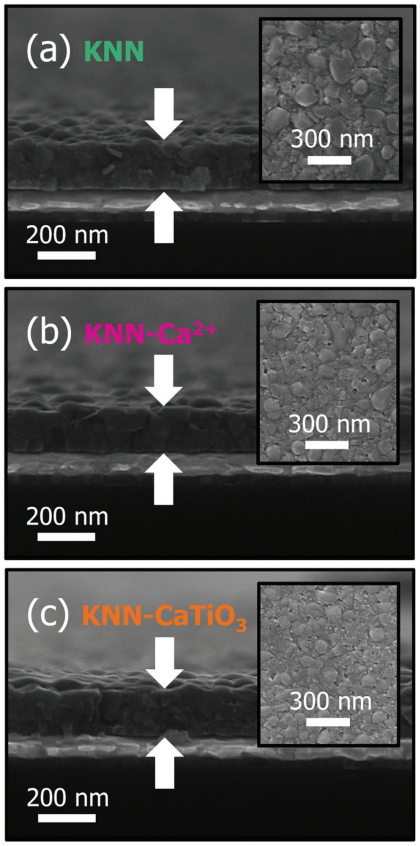

Fig. 2 Cross section and top-view SEM micrographs of KNN films prepared by 15 layers. (a) undoped (KNN), (b) 0.5 mol% Ca^{2+} doped (KNN-Ca^{2+}) and (c) 0.5 mol% $CaTiO_3$ doped (KNN-$CaTiO_3$).

The capacitances of the films as a function of electric field, displayed in Fig. 6, were measured using an electric (DC) field of 100 kV cm^{-1}, a frequency of 500 Hz and an AC amplitude of 50 mV. The highest overall capacitance is observed in the film doped with $CaTiO_3$, followed by the film doped with Ca^{2+}. Capacitance peaks at the coercive fields are modest and most predominant in the $CaTiO_3$-doped film. The dielectric loss

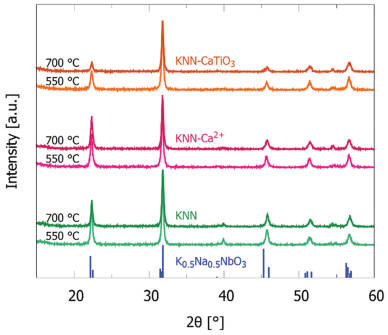

Fig. 3 GIXRD patterns of pyrolyzed (550 °C) and annealed (700 °C) KNN films on SiPt. Reference pattern for $K_{0.5}Na_{0.5}NbO_3$ (blue, PDF card 00-061-0315[73]) is included. The films were prepared by 30 repeating spin coatings.

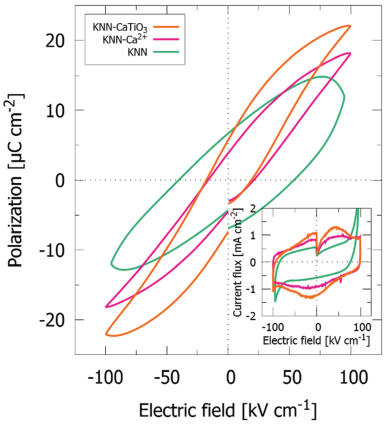

Fig. 4 Polarization as a function of electric field for the KNN films. Ferroelectric polarization switching is observed for the doped films. The current fluxes during the measurements are included in the figure. A frequency of 10 Hz and an electric field bias of 100 kV cm^{-1} was used.

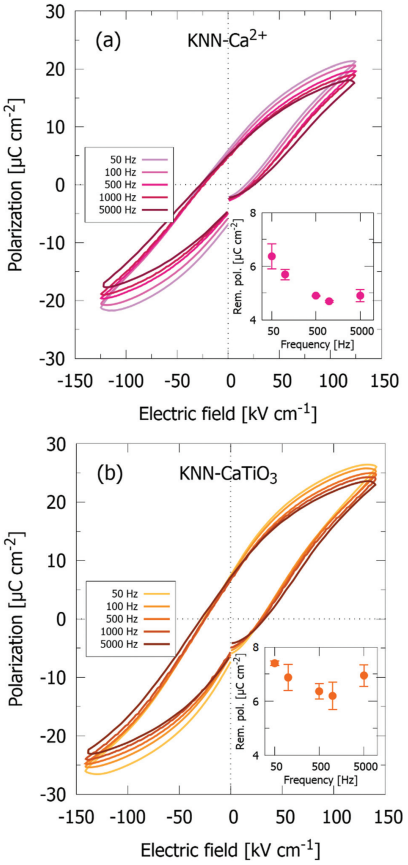

Fig. 5 Polarization as a function of electric field measured at different frequencies for (a) Ca^{2+}-doped and (b) $CaTiO_3$-doped KNN films. The measured remnant polarization plotted against frequency is provided as insets. Electric field biases of 125 kV cm^{-1} (KNN-Ca^{2+}) and 142 kV cm^{-1} (KNN-$CaTiO_3$) were used for the measurements.

tangent ($\tan\delta$) for the measurement is included in the insert of Fig. 6, demonstrating low losses in all the three films.

The dielectric permittivity (ε') of the films as a function of temperature from 150 to 420 °C is presented in Fig. 7. The data are shown for 1 kHz and an AC amplitude of 50 mV. A shallow maximum around ~210 °C and more pronounced maximum at 375 °C were observed for all the three compositions. The temperature at the maxima is not significantly shifted by doping KNN, indicating no major shift in the phase transition temperatures of KNN by the minor doping used in this study. Reproducible data below 150 °C could not be obtained and are therefore not shown. Frequency dependency of the permittivity at 150 °C is plotted in Fig. S4 in the ESI.†

Discussion

This study has demonstrated that both undoped and doped KNN films can be fabricated on SiPt substrates by aqueous CSD.

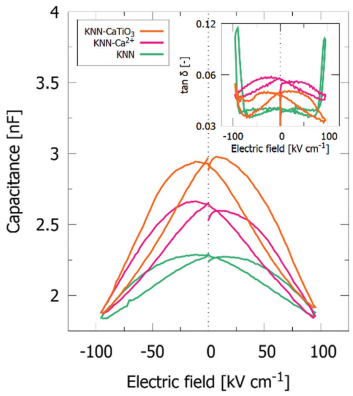

Fig. 6 Capacitance as a function of electric field for the KNN films. The loss tangent is included as inset. An electric field of 100 kV cm^{-1}, a frequency of 500 Hz and an AC amplitude of 50 mV was used for the measurements.

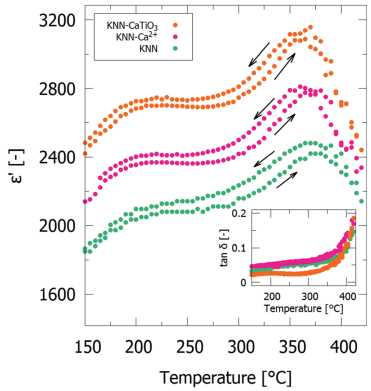

Fig. 7 Real part of the dielectric permittivity at 1 kHz as a function of temperature of the three KNN films. Arrows indicate heating/cooling. Insert: The loss tangent measured at the same frequency. An AC amplitude of 50 mV was used in the measurements.

The KNN films were homogenous, dense and phase pure as demonstrated by the scanning electron micrographs (Fig. 2) and the GIXRD patterns (Fig. 3). This is in line with our previous work on KNN films using (100) oriented $SrTiO_3$ (STO) single crystal substrates[56] and demonstrates that the aqueous precursor solution developed is suitable for fabricating high-quality KNN films on several types of substrates. Moreover, it was demonstrated that the aqueous precursor solution can be chemically modified to allow for compositional engineering of the KNN films. In this work complexes of Ca^{2+} and Ti^{4+} dissolved in water were used as dopants, but further doping with alkaline earth and rare earth elements should be possible. We have shown previously that aqueous precursor solutions can be applied to fabricate thin films of a whole range of different functional materials ranging from ferroelectric,[74,75] transparent conducting[76,77] and optical active materials.[78]

Based on their ionic radii[79] and charge, Ca^{2+} and Ti^{4+} are proposed to be incorporated in the KNN lattice on the A- and B-site, respectively. Incorporation of the dopants in the KNN perovskite lattice was confirmed since no additional reflections in the diffraction patterns were observed for the powders from the precursor solutions (Fig. 1) or the thin films (Fig. 3 and Fig. S2, ESI†). A decrease in the *c* lattice parameter and the unit cell volume, and an increase in the monoclinic β-distortion of the unit cell, were also observed in the doped KNN powders (Fig. S1 and Table S1, ESI†), supporting the formation of solid solutions. The decrease in unit cell volume is expected due to the smaller sizes of the dopant cations compared to the inherent cations of KNN. The increase in crystallite size was much more prominent for the undoped KNN powder after heat treatment at 850 °C (Fig. 1), suggesting that the doping strongly influences the mobility of the cations and reduces the grain growth in the doped KNN thin films (Fig. 2). Suppressed grain growth has been observed in bulk samples doped with Ca^{2+} and $CaTiO_3$,[66] and in thin films doped with $CaZrO_3$ [29] and $SrTiO_3$.[46] The coarsening is also influenced by the alkali excess, which has been shown to strongly promote grain growth in KNN.[80] The alkali excess cannot however explain the difference in grain growth observed for the two doped materials since all three solutions used contained a considerable alkali excess.

The XRD patterns (Fig. 3 and Fig. S3, ESI†) demonstrated that the KNN films were polycrystalline in nature with no preferential orientation or crystallographic texture. Textured films can possibly be obtained by tuning the processing conditions. We have previously reported on KNN films with (100) texture using (100) oriented single crystal STO substrates and the same precursor solution as used in this work.[56] Promoting texture in KNN films on SiPt substrates has also been reported for both 2-methoxyethanol- and water-based CSD syntheses by tuning the processing temperature or atmosphere.[34,57]

Ferroelectric switching was clearly observed for the doped KNN films (Fig. 4). A ferroelectric response was not observed for the undoped KNN film at any electric fields or frequencies, which is in line with our previous work using the same precursor solution, where only a weak ferroelectric response was obtained for undoped KNN films on STO substrates.[56] Moreover, the hysteresis loops were also conducted at higher electric fields without breakdown for the $CaTiO_3$-doped films compared to the Ca^{2+}-doped films, resulting in higher remnant polarizations for these two compositions (Fig. 5). The maximum remnant polarization measured for the KNN-$CaTiO_3$ film (7.40 ± 0.09 μC cm^{-2}) is comparable with previous reports on KNN thin films.[19,23,25,29,36,40,47,48]

Doping increases the capacitance of the KNN films by ~14.3% (Ca^{2+}-doping) and ~29.1% ($CaTiO_3$-doping) at zero

View Article Online
Paper Journal of Materials Chemistry C

DC field, according to the data presented in Fig. 6. This is in accordance with the permittivity shown in Fig. 7, where the increases in permittivity were 15.4% (Ca^{2+}-doping) and 32.0% ($CaTiO_3$-doping) at 150 °C. The values of the dielectric permittivity of the films as a function of temperature (Fig. 7) are among the highest reported for KNN films from CSD.[20,21,26–28,30,31,33,34,36,42,46,47,51,53,54] The dielectric loss of the three films (insets in Fig. 6 and 7) showed only minor variations and were low for all three compositions.

0.5% doping with Ca^{2+} and $CaTiO_3$ only induced minor changes in the leakage current (inset Fig. 4). The round-shaped P–E loop measured for undoped KNN (Fig. 4) is a strong indication of high leakage currents, however the leakage was initiated at around 70 kV cm^{-1}, which is well above the coercive field of KNN. This demonstrates that the absence of ferroelectric switching is not due to low resistivity of the undoped KNN film. Hagh *et al.*[81] reported an increase in resistivity by doping with 0.5–1.5 mol% Ba^{2+} in bulk KNN, implying that Ba^{2+} acts as a donor dopant in KNN. A similar effect might be expected for doping with other alkali earth metals, such as Ca^{2+}, but this was not observed in the present work or in literature on bulk KNN.[63–65]

Only negligible changes due to doping were observed for the phase transitions induced from the permittivity (Fig. 7). $CaTiO_3$-doping has been reported to decrease and diffuse/blur out the onset temperatures for the monoclinic to tetragonal (T_{M-T}) and tetragonal to cubic (T_C) phase transitions in bulk KNN and thereby improve ferroelectric polarization.[67–71] This was not observed in this work as evident from the permittivity measurements shown in Fig. 7.

Despite a low doping concentration (0.5 mol%), a significant effect was observed in the ferroelectric response. The origin is suggested to be related to the dopants' influence on the concentration of point defects in the crystal lattice although a difference in the dielectric loss could not be correlated with the doping. Charged defects like oxygen vacancies are associated with domain wall pinning and dampening of the ferroelectric properties,[82,83] and doping may influence on the concentration of oxygen vacancies. For co-doping with Ca^{2+}/Ti^{4+} ($CaTiO_3$-doping), this can possibly be explained in terms of increased energy of formation for lattice defects, as defects like oxygen vacancies have a higher energy of formation in $CaTiO_3$ than in $KNbO_3$.[84,85] For Ca^{2+}-doping, a reduction in defect concentration can be explained in terms of charge compensation. As mentioned above, Ca^{2+} cations enter on the A-site in KNN. We propose three possible point defect equilibria for the incorporation of Ca^{2+}, leading to A-site deficiency (A < B), stoichiometric A : B ratio (A = B) or A-site excess (A > B) in ABO_3. In all cases Ca^{2+} on the A-site, $Ca_A^{\bullet}$, will have a formal charge of +1, which needs to be charge compensated.

(1) A < B, $(K,Na)_{1-2x}Ca_xNbO_3$:

When incorporated into the lattice, Ca^{2+} can form A-site deficiency according to eqn (1). Here the Ca^{2+} is charge compensated by the formation of an A-site vacancy, changing the A : B stoichiometry corresponding to $(K,Na)_{1-2x}Ca_xNbO_3$, as proposed by Malic *et al.*[65]

$$CaO(s) + 2A_A^x \rightarrow A_2O(s) + Ca_A^{\bullet} + V'_A \quad (1)$$

(2) A = B, $(K,Na)_{1-x}Ca_xNbO_{3+x/2}$:

Alternatively, Ca_{2+} can be incorporated in KNN according to eqn (2), where Ca^{2+} is charge compensated by removal of oxygen vacancies in the lattice. In this case, the A : B stoichiometry is maintained (A : B = 1 : 1).

$$2CaO(s) + Nb_2O_5(s) + V_O^{\bullet\bullet} \rightarrow 2Ca_A^{\bullet} + 2Nb_{Nb}^x + 7O_O^x \quad (2)$$

(3) A > B, $(K,Na)Ca_xNbO_{3+x}$:

The third possibility involves charge compensation by removal of both an A-site vacancy and an oxygen vacancy as shown in eqn (3). This will form an excess on A-site (A > B) corresponding to $(K,Na)Ca_xNbO_{3+x}$.

$$CaO(s) + V'_A + V_O^{\bullet\bullet} \rightarrow Ca_A^{\bullet} + O_O^x \quad (3)$$

During electrical characterization, no effect from Ca^{2+}-doping was observed for the current flux (Fig. 4) or the dielectric losses (insets in Fig. 6 and 7), compared to undoped and $CaTiO_3$-doped KNN. This suggests that the overall concentration of mobile point defects like electron holes ($h^{\bullet}$) is not affected by Ca^{2+}-doping, and that the minor variations in the dielectric losses cannot be explained by the defect equilibria presented here. However, the ferroelectric properties (Fig. 4) are improved with Ca^{2+}-doping, and one explanation for this could be elimination of charged defects like oxygen and alkali vacancies, $V_O^{\bullet\bullet}$ and V'_A. As mentioned, such defects can pin ferroelectric domain walls and thereby reduce the ferroelectric response.[82,83] In eqn (1), an alkali vacancy is formed, while in eqn (2) and (3) an oxygen vacancy is removed, suggesting that the latter mechanisms could reduce domain wall pinning. The number of A-site and oxygen vacancies increases at elevated temperatures due to increased evaporation of alkali metals,[86] which means that eqn (1) is most relevant for high-temperature processing of KNN. For low-temperature processing of KNN, or when using high amounts of excess alkali metals, eqn (2) and (3) are more likely. In this work, a low processing temperature (700 °C, 10 min) and an alkali excess (5 mol% Na^+ and K^+) was used, making eqn (2) and (3) the most plausible point defect equilibria for Ca^{2+} incorporation. Following this, Ca^{2+}-doping is proposed to have a positive influence on reduction of domain wall pinning in KNN, as reflected in the improved ferroelectric properties presented in this work (Fig. 4 and 5).

Conclusions

Phase pure KNN thin films with three different compositions (undoped KNN, 0.5 mol% Ca^{2+}-doped KNN, 0.5 mol% Ca^{2+}–Ti^{4+} co-doped KNN) were successfully fabricated on platinized silicon substrates by aqueous CSD. Reduced grain growth was observed in the doped films and powders prepared from the precursor solutions, suggesting that the dopants reduce cation mobility. A reduction in unit cell volume was observed in the doped KNN powders. The effect of 0.5 mol% Ca^{2+}-doping and 0.5 mol% Ca^{2+}–Ti^{4+} co-doping on the ferroelectric and dielectric properties of the KNN films was measured using Pt top electrodes. Polarization switching was observed in the doped KNN films in the frequency range 10 to 5000 Hz, with peak remnant

polarization of 6.37 ± 0.47 and 7.40 ± 0.09 μC cm^{-2} for Ca^{2+}- and $CaTiO_3$-doping, respectively. Polarization switching was not observed in the undoped KNN films. All films had exceptionally high dielectric constants, ranging from 1800 to 3200, measured at 1 kHz in the temperature range 150 to 420 °C. The capacitance of the doped films was ∼15% (Ca^{2+}-doping) and ∼30% ($CaTiO_3$-doping) higher than the undoped KNN films. No significant difference in leakage currents or phase transition temperatures was observed between the films. The improved ferroelectric properties from doping is suggested to be linked to reduced defect concentration due to higher energies of formation ($CaTiO_3$-doping) or shifted defect equilibrium (Ca^{2+}-doping).

Conflicts of interest

There are no conflicts to declare.

Acknowledgements

Financial support from the Research Council of Norway through NANO2021 project PIEZOMED project number 250184 is acknowledged. Dr Magnus Rotan is acknowledged for the support regarding X-ray diffractogram fitting using the Pawley method.

References

1 J. Wu, D. Xiao and J. Zhu, Potassium–Sodium Niobate Lead-Free Piezoelectric Materials: Past, Present, and Future of Phase Boundaries, *Chem. Rev.*, 2015, **115**, 2559–2595.
2 J. Rödel, K. G. Webber, R. Dittmer, W. Jo, M. Kimura and D. Damjanovic, Transferring lead-free piezoelectric ceramics into application, *J. Eur. Ceram. Soc.*, 2015, **35**(6), 1659–1681.
3 A. M. Manjón-sanz and M. R. Dolgos, Applications of Piezoelectrics: Old and New, *Chem. Mater.*, 2018, **30**(24), 8718–8726.
4 Y. Zhang and J. F. Li, Review of chemical modification on potassium sodium niobate lead-free piezoelectrics, *J. Mater. Chem. C*, 2019, **7**(15), 4284–4303.
5 Y.-H. Joung, Development of Implantable Medical Devices: From an Engineering Perspective, *Int. Neurourol. J.*, 2013, **17**, 98–106.
6 S.-W. Yu, S.-T. Kuo, W.-H. Tuan, Y.-Y. Tsai and C.-H. Su, Ion release from three lead-free piezoelectric ceramics and their physical and cytotoxicity characteristics, *Mater. Lett.*, 2011, **65**(23–24), 3522–3524.
7 S. Yu, S. Kuo, W. Tuan, Y. Tsai and S. Wang, Cytotoxicity and degradation behavior of potassium sodium niobate piezoelectric ceramics, *Ceram. Int.*, 2012, **38**(4), 2845–2850.
8 W. Chen, Z. Yu, J. Pang, P. Yu, G. Tan and C. Ning, Fabrication of Biocompatible Potassium Sodium Niobate Piezoelectric Ceramic as an Electroactive Implant, *Materials*, 2017, **10**, 345.
9 T. Yao, J. Chen, Z. Wang, J. Zhai, Y. Li, J. Xing, S. Hu, G. Tan, S. Qi, Y. Chang, P. Yu and C. Ning, The antibacterial effect of potassium–sodium niobate ceramics based on controlling piezoelectric properties, *Colloids Surf., B*, 2018, **175**, 463–468.
10 C. K. Jeong, J. H. Han, H. Palneedi, H. Park, G. Hwang, B. Joung, S. G. Kim, H. J. Shin, I. S. Kang, J. Ryu and K. J. Lee, Comprehensive biocompatibility of nontoxic and high-output flexible energy harvester using lead-free piezoceramic thin film, *Appl. Mater.*, 2017, **5**, 74102.
11 Q. Wang, J. Yang, W. Zhang, R. Khoie, Y. M. Li, J. G. Zhu and Z. Q. Chen, Manufacture and cytotoxicity of a lead-free piezoelectric ceramic as a bone substitute-consolidation of porous lithium sodium potassium niobate by cold isostatic pressing, *Int. J. Oral Sci.*, 2009, **1**(2), 99–104.
12 B. Y. Kim, W. H. Lee, H. G. Hwang, D. H. Kim, J. H. Kim, S. H. Lee and S. Nahm, *Adv. Funct. Mater.*, 2016, **26**(29), 5211–5221.
13 G. Tan, S. Wang, Y. Zhu, L. Zhou, P. Yu, X. Wang, T. He, J. Chen, C. Mao and C. Ning, Surface-Selective Preferential Production of Reactive Oxygen Species on Piezoelectric Ceramics for Bacterial Killing, *ACS Appl. Mater. Interfaces*, 2016, **8**(37), 24306–24309.
14 H. J. Seog, S. Y. Lee and J. Park, Recent Progress in Potassium Sodium Niobate Lead-free Thin Films, *J. Korean Phys. Soc.*, 2018, **72**(12), 1467–1483.
15 S. W. Zhang, Z. Zhou, J. Luo and J. F. Li, Potassium–Sodium–Niobate-Based Thin Films: Lead Free for Micro-Piezoelectrics, *Ann. Phys.*, 2019, **531**(7), 1800525.
16 H. C. Thong, C. Zhao, Z. Zhou, C. F. Wu, Y. X. Liu and Z. Z. Du, *et al.*, Technology transfer of lead-free (K, Na)NbO_3-based piezoelectric ceramics, *Mater. Today*, 2019, **29**, 37–48.
17 N. Bassiri-Gharb, Y. Bastani and A. Bernal, Chemical solution growth of ferroelectric oxide thin films and nanostructures, *Chem. Soc. Rev.*, 2014, **43**, 2125–2140.
18 Q. Yu, J.-F. Li, W. Sun, Z. Zhou, Y. Xu, Z.-K. Xie, F. P. Lai and Q. M. Wang, Electrical properties of $K_{0.5}Na_{0.5}NbO_3$ thin films grown on Nb:$SrTiO_3$ single-crystalline substrates with different crystallographic orientations, *J. Appl. Phys.*, 2013, **113**, 24101.
19 N. Kondo, W. Sakamoto, B. Lee, T. Iijima, J. Kumagai, M. Moriya and T. Yogo, Improvement in Ferroelectric Properties of Chemically Synthesized Lead-Free Piezoelectric (K,Na)-(Nb,Ta)O_3 Thin Films by Mn Doping, *Jpn. J. Appl. Phys.*, 2010, **49**, 09MA04.
20 C. W. Ahn, H. J. Seog, A. Ullah, S. Y. Lee, J. W. Kim, S. S. Kim, M. Park, K. No and I. W. Kim, Effect of Ta content on the phase transition and piezoelectric properties of lead-free $(K_{0.48}Na_{0.48}Li_{0.04})$ $(Nb_{0.995-x}Mn_{0.005}Ta_x)O_3$ thin film, *J. Appl. Phys.*, 2012, **111**, 24110.
21 S. Y. Lee, C. W. Ahn, J. S. Kim, A. Ullah, H. J. Lee, H.-I. Hwang, J. S. Choi, B. H. Park and I. W. Kim, Enhanced piezoelectric properties of Ta substituted-$(K_{0.5}Na_{0.5})NbO_3$ films: A candidate for lead-free piezoelectric thin films, *J. Alloys Compd.*, 2011, **509**(20), L194–L198.
22 F. Lai, J.-F. Li, Z.-X. Zhu and Y. Xu, Influence of Li content on electrical properties of highly piezoelectric (Li,K,Na)NbO_3 thin films prepared by sol–gel processing, *J. Appl. Phys.*, 2009, **106**(6), 64101.
23 Y. Nakashima, W. Sakamoto, H. Maiwa, T. Shimura and T. Yogo, Lead-Free Piezoelectric (K,Na)NbO_3 Thin Films

Derived from Metal Alkoxide Precursors, *Jpn. Soc. Appl. Phys.*, 2007, **46**(14), L311–L313.

24 Y. Wang, K. Yao, M. S. Mirshekarloo, F. Eng and H. Tay, Effects and Mechanism of Combinational Chemical Agents on Solution-Derived $K_{0.5}Na_{0.5}NbO_3$ Piezoelectric Thin Films, *J. Am. Ceram. Soc.*, 2016, **99**(5), 1631–1636.

25 Q. Yu, J. Li, Y. Chen, L. Cheng, W. Sun, Z. Zhou and Z. Wang, Effect of Pyrolysis Temperature on Sol–Gel Synthesis of Lead-free Piezoelectric (K,Na)NbO_3 Films on Nb:$SrTiO_3$ Substrates, *J. Am. Ceram. Soc.*, 2014, **97**, 107–113.

26 X. Vendrell, O. Raymond, D. A. Ochoa, J. E. García and L. Mestres, Growth and physical properties of highly oriented La-doped (K,Na)NbO_3 ferroelectric thin films, *Thin Solid Films*, 2015, **577**, 35–41.

27 J. Luo, W. Sun, Z. Zhou, Y. Bai, Z. J. Wang, G. Tian, D. Chen, X. Gao, F. Zhu and J. F. Li, Domain Evolution and Piezoelectric Response across Thermotropic Phase Boundary in (K,Na)NbO_3-Based Epitaxial Thin Films, *Appl. Mater. Interfaces*, 2017, **9**, 13315–13322.

28 X. Zhang, J. Liu, K. Zhu, J. Wang and Z. Li, Effects of Mn doping on dielectric and ferroelectric characteristics of lead-free (K,Na,Li)NbO_3 thin films grown by chemical solution deposition, *J. Mater. Sci.: Mater. Electron.*, 2017, **28**(1), 487–492.

29 T. Matsuda, W. Sakamoto, B. L. Takashi, I. Jun, K. Makoto and M. Toshinobu, Electrical Properties of Lead-Free Ferroelectric Mn-Doped $K_{0.5}Na_{0.5}NbO_3$–$CaZrO_3$ Thin Films Prepared by Chemical Solution Deposition, *Jpn. J. Appl. Phys.*, 2012, **51**, 09LA03.

30 S. Y. Lee, C. W. Ahn, A. Ullah, H. J. Seog, J. S. Kim, S. H. Bae and I. W. Kim, Effect of Mn substitution on ferroelectric and leakage current characteristics of lead-free $(K_{0.5}Na_{0.5})(Mn_xNb_{1-x})O_3$ thin films, *Curr. Appl. Phys.*, 2011, **11**(3), S266–S269.

31 P. C. Goh, K. Yao and Z. Chen, Lithium diffusion in (Li,K,Na)NbO_3 piezoeletric thin films and the resulting approach for enhanced performance properties, *Appl. Phys. Lett.*, 2011, **99**, 92902.

32 C. W. Ahn, E. D. Jeong, S. Y. Lee, H. J. Lee, S. H. Kang and I. W. Kim, Enhanced ferroelectric properties of $LiNbO_3$ substituted $Na_{0.5}K_{0.5}NbO_3$ thin films grown by chemical solution deposition, *Appl. Phys. Lett.*, 2008, **93**, 212905.

33 L. Wang, R. Zuo, L. Liu, H. Su, M. Shi, X. Chu, X. Wang and L. Li, Preparation and characterization of sol–gel derived (Li,Ta,Sb) modified (K,Na)NbO_3 lead-free ferroelectric thin films, *Mater. Chem. Phys.*, 2011, **130**(1–2), 165–169.

34 S. W. Zhang, J. Luo, Z. Zhou and J. F. Li, Sol–gel processed highly (100)-textured (K, Na)NbO_3-based lead-free thin films: Effect of pyrolysis temperature, *J. Am. Ceram. Soc.*, 2019, **102**(5), 2696–2705.

35 L. Wang, W. Ren, P. Shi and X. Wu, Cobalt doping effects on structures and electrical properties of lead-free ferroelectric $K_{0.5}Na_{0.5}NbO_3$ films, *J. Alloys Compd.*, 2014, **608**, 202–206.

36 L. Wang, W. Ren, P. C. Goh, K. Yao, P. Shi, X. Wu and X. Yao, Structures and electrical properties of Mn- and Co-doped lead-free ferroelectric $K_{0.5}Na_{0.5}NbO_3$ films prepared by a chemical solution deposition method, *Thin Solid Films*, 2013, **537**, 65–69.

37 J. Luo, S. Zhang, Z. Zhou, Y. Zhang, H. Y. Lee, Z. Yue and J. F. Li, Phase transition and piezoelectricity of $BaZrO_3$-modified (K,Na)NbO_3 lead-free piezoelectric thin films, *J. Am. Ceram. Soc.*, 2019, **102**(5), 2770–2780.

38 K. Tanaka, K. Kakimoto and H. Ohsato, Fabrication of highly oriented lead-free (Na, K)NbO_3 thin films at low temperature by Sol–Gel process, *J. Cryst. Growth*, 2006, **294**(2), 209–213.

39 Y. Nakashima, W. Sakamoto and T. Yogo, Processing of highly oriented (K,Na)NbO_3 thin films using a tailored metal–alkoxide precursor solution, *J. Eur. Ceram. Soc.*, 2011, **31**(14), 2497–2503.

40 A. Kupec, B. Malic, J. Tellier, E. Tchernychova, S. Glinsek and M. Kosec, Lead-Free Ferroelectric Potassium Sodium Niobate Thin Films from Solution: Composition and Structure, *J. Am. Ceram. Soc.*, 2012, **95**(2), 515–523.

41 A. Kupec, H. Uršič, R. C. Frunză, E. Tchernychova and B. Malič, Microstructure-dependent leakage-current properties of solution-derived $(K_{0.5}Na_{0.5})NbO_3$ thin films, *J. Eur. Ceram. Soc.*, 2015, **35**(13), 3507–3511.

42 S. Y. Lee, H. J. Seog, C. W. Ahn, A. Ullah and I. W. Kim, Interfacial Dead Layers on Lead Free Ferroelectric $(K_{0.5}Na_{0.5})(Mn_{0.005}Nb_{0.995})O_3$ Thin Films, *Jpn. J. Appl. Phys.*, 2012, **51**, 09MD03.

43 C. Zhao, X. Meng, W. Wang and Y. Zhou, Energy storage performance of (K, Na)NbO_3 ferroelectric thin films with Mn–Ta and Mn–Ti co-doping, *Ceram. Int.*, 2019, **45**(11), 13772–13779.

44 F. Lai and J. F. Li, Sol–gel processing and characterization of (Na,K)NbO_3 lead-free ferroelectric films, *Ferroelectrics*, 2007, **358**, 181–187.

45 F. Lai and J. F. Li, Sol–gel processing of lead-free (Na,K)NbO_3 ferroelectric films, *J. Sol-Gel Sci. Technol.*, 2007, **42**(3), 287–292.

46 A. Kupec and B. Malič, Structural and dielectric properties of the lead-free $(1-x)K_{0.5}Na_{0.5}NbO_{3-x}SrTiO_3$ thin films from solutions, *J. Alloys Compd.*, 2014, **596**, 32–38.

47 S. Y. Lee, J. S. Kim, C. W. Ahn, H. In Hwang and W. Kim, Impedance spectroscopy and relaxation phenomena of (Na,K) excess $Na_{0.5}K_{0.5}NbO_3$ thin films grown by chemical solution deposition, *Thin Solid Films*, 2010, **519**(2), 947–951.

48 L. Wang, W. Ren, P. Shi, X. Chen, X. Wu and X. Yao, Enhanced ferroelectric properties in Mn-doped $K_{0.5}Na_{0.5}NbO_3$ thin films derived from chemical solution deposition, *Appl. Phys. Lett.*, 2010, **97**(7), 72902.

49 A. Tkach, A. Santos, S. Zlotnik, R. Serrazina, O. Okhay, I. Bdikin, M. E. Costa and P. M. Vilarinho, Effect of solution conditions on the properties of sol–gel derived potassium sodium niobate thin films on platinized sapphire substrates, *Nanomaterials*, 2019, **9**(11), 1600.

50 J. Grivel, K. Thydén, J. R. Bowen and A. B. Haugen, Deposition of highly oriented (K,Na)NbO_3 films on flexible metal substrates, *Thin Solid Films*, 2018, **650**(December 2017), 7–10.

51 J. Kwak, A. I. Kingon and S. H. Kim, Lead-free $(Na_{0.5},K_{0.5})NbO_3$ thin films for the implantable piezoelectric medical sensor applications, *Mater. Lett.*, 2012, **82**, 130–132.

52 T. Lu, K. Zhu, J. Liu, J. Wang and J. Qiu, Lead-free (K,Na)NbO_3 thin films derived from chemical solution deposition modified with EDTA, *J. Mater. Sci.*, 2014, **25**, 1112–1116.

53 D. Zhang, F. Zheng, X. Yang, H. Liu and M. Cao, Preparation and ferroelectric properties of $K_{0.5}Na_{0.5}NbO_3$ thin films derived from non-alcohol niobium salt sol–gel process, *Integr. Ferroelectr.*, 2014, **4587**(September 2016), 673–678.

54 L. Yao, K. Zhu, J. Wang, J. Liu, J. Qiu, M. Cheng and Q. Gu, Annealing temperature effects on the electrical properties of (K,Na)NbO_3 thin film fabricated by a sol–gel process with a citrate precursor solution, *Ferroelectrics*, 2016, **493**, 47–53.

55 K. Pham, N. H. Gaukås, M. Morozov, T. Tybell, P. E. Vullum, T. Grande and M.-A. Einarsrud, Epitaxial $K_{0.5}Na_{0.5}NbO_3$ thin films by aqueous chemical solution deposition, *R. Soc. Open Sci.*, 2019, **6**, 180989.

56 N. H. Gaukås, S. M. Dale, T. M. Ræder, A. Toresen, R. Holmestad, J. Glaum, M.-A. Einarsrud and T. Grande, Controlling phase purity and texture of $K_{0.5}Na_{0.5}NbO_3$ thin films by aqueous chemical solution deposition, *Materials*, 2019, **12**, 2042.

57 W. Zhang, H. Zhu, X. Zhang, H. Wu, J. Bao and F. Hu, Structural and electrical study of highly (100)-oriented KNN films fabricated by a sol–gel non-alkoxide process, *Ceram. Int.*, 2019, **14**(17), 22156–22162.

58 H. Bruncková, L. Medvecký and P. Hvizdoš, Effect of substrate on microstructure and mechanical properties of sol–gel prepared (K, Na)NbO_3 thin films, *Mater. Sci. Eng., B*, 2013, **178**(4), 254–262.

59 H. Bruncková, L. Medvecký, P. Hvizdoš and J. Ďurišin, Structural and nanomechanical properties of sol–gel prepared (K, Na)NbO_3 thin films, *Surf. Interface Anal.*, 2015, **47**(11), 1063–1071.

60 J. Rödel, W. Jo, K. T. P. Seifert, E. M. Anton, T. Granzow and D. Damjanovic, Perspective on the development of lead-free piezoceramics, *J. Am. Ceram. Soc.*, 2009, **92**(6), 1153–1177.

61 D. A. Puleo and W. W. Huh, Acute toxicity of metal ions in cultures of osteogenic cells derived from bone marrow stromal cells, *J. Appl. Biomater.*, 1995, **6**(2), 109–116.

62 C. G. Fraga, Relevance, essentiality and toxicity of trace elements in human health, *Mol. Aspects Med.*, 2005, **26**(4–5), 235–244.

63 J. Taub, L. Ramajo and M. S. Castro, Phase structure and piezoelectric properties of Ca- and Ba-doped $K_{0.5}Na_{0.5}NbO_3$ lead-free ceramics, *Ceram. Int.*, 2013, **39**(4), 3555–3561.

64 L. Tang, T. Liu, J. Ma, X. Zhang, L. An and K. Chen, Ca^{2+} doping effects in (K, Na, Li)$(Nb_{0.8}Ta_{0.2})O_3$ lead-free piezoelectric ceramics. Front, *Mater. Sci.*, 2019, **13**, 431–438.

65 B. Malic, J. Bernard, J. Holc, D. Jenko and M. Kosec, Alkaline-earth doping in (K,Na)NbO_3 based piezoceramics, *J. Eur. Ceram. Soc.*, 2005, **25**, 2707–2711.

66 M. Zhuk, M. A. Einarsrud and J. Glaum, in preparation.

67 H. Park, K. Cho, D. Paik, S. Nahm, H. Lee and D. Kim, Microstructure and piezoelectric properties of lead-free $(1-x)(Na_{0.5}K_{0.5})NbO_{3-x}CaTiO_3$ ceramics, *J. Appl. Phys.*, 2007, **102**, 124101.

68 L. Ramajo, R. Parra and M. S. Castro, Electrical and microstructural properties of $CaTiO_3$-doped $K_{0.5}Na_{0.5}NbO_3$-lead free ceramics, *Bull. Mater. Sci.*, 2011, **34**(6), 1213–1217.

69 J. Wu, D. Xiao, Y. Wang, W. Wu, B. Zhang and J. Zhu, Improved temperature stability of $CaTiO_3$-modified $[(K_{0.5}Na_{0.5})0.96Li_{0.04}](Nb_{0.91}Sb_{0.05}Ta_{0.04})O_3$ lead-free piezoelectric ceramics, *J. Appl. Phys.*, 2008, **104**, 24102.

70 Y. Chang, Z. Yang, X. Chao, R. Zhang and X. Li, Dielectric and piezoelectric properties of alkaline-earth titanate doped $(K_{0.5}Na_{0.5})NbO_3$ ceramics, *Mater. Lett.*, 2007, **61**, 785–789.

71 H. Chen and P. Liu, Electrical properties of $0.98(K_{0.5}Na_{0.5})$-NbO_3-$0.02AETiO_3$ piezoceramics doped with Li_2CO_3, *Ferroelectrics*, 2019, **551**(1), 53–59.

72 S. Ikeuchi, T. Yoneda, Y. Matsuki, N. Endo, Y. Takeshima, H. Horiuchi, Y. Kishimoto, K. Yamamoto and K. Fujimoto, Preparation of (K,Na)NbO_3–$CaTiO_3$ film by RF magnetron sputtering, In: 2014 IEEE International Ultrasonics Symposium Proceedings, IEEE, 2014, pp. 1578–1581.

73 J. Tellier, B. Malic, B. Dkhil, D. Jenko, J. Cilensek and M. Kosec, Crystal structure and phase transitions of sodium potassium niobate perovskites, *Solid State Sci.*, 2009, **11**(2), 320–324.

74 M. Christensen, M. A. Einarsrud and T. Grande, Fabrication of lead-free $Bi_{0.5}Na_{0.5}TiO_3$ thin films by aqueous chemical solution deposition, *Materials*, 2017, **10**(2), 213.

75 T. M. Raeder, K. Bakken, J. Glaum, M. A. Einarsrud and T. Grande, Enhanced in-plane ferroelectricity in $BaTiO_3$ thin films fabricated by aqueous chemical solution deposition, *AIP Adv.*, 2018, **8**(10), 105228.

76 T. O. L. Sunde, E. Garskaite, B. Otter, H. E. Fossheim, R. Sæterli, R. Holmestad, M.-A. Einarsrud and T. Grande, Transparent and conducting ITO thin films by spin coating of an aqueous precursor solution, *J. Mater. Chem.*, 2012, **22**(31), 15740.

77 T. O. L. Sunde, M. A. Einarsrud and T. Grande, Optimisation of chemical solution deposition of indium tin oxide thin films, *Thin Solid Films*, 2014, **573**(3), 48–55.

78 E. Garskaite, M. Lindgren, M. A. Einarsrud and T. Grande, Luminescent properties of rare earth (Er, Yb) doped yttrium aluminium garnet thin films and bulk samples synthesised by an aqueous sol–gel technique, *J. Eur. Ceram. Soc.*, 2010, **30**(7), 1707–1715.

79 R. D. Shannon, Revised Effective Ionic Radii and Systematic Studies of Interatomie Distances in Halides and Chaleogenides, *Acta Crystallogr., Sect. A: Cryst. Phys., Diffr., Theor. Gen. Crystallogr.*, 1976, **32**(5), 751–767.

80 P. Bomlai, P. Wichianrat, S. Muensit and S. J. Milne, Effect of Calcination Conditions and Excess Alkali Carbonate on the Phase Formation and Particle Morphology of $Na_{0.5}K_{0.5}NbO_3$ Powders, *J. Am. Ceram. Soc.*, 2007, **90**(5), 1650–1655.

81 N. M. Hagh, B. Jadidian, E. Ashbahian and A. Safari, Lead-Free piezoelectric ceramic transducer in the donor-doped $K_{1/2}Na_{1/2}NbO_3$ solid solution system, *IEEE Trans. Ultrason. Ferroelectr. Freq. Control*, 2008, **55**(1), 214–224.

82 N. Bassiri-Gharb, I. Fujii, E. Hong, S. Trolier-Mckinstry, D. V. Taylor and D. Damjanovic, Domain wall contributions to the properties of piezoelectric thin films, *J. Electroceram.*, 2007, **19**(1), 47–65.

83 F. Xu, S. Trolier-McKinstry, W. Ren, B. Xu, Z. L. Xie and K. J. Hemker, Domain wall motion and its contribution to the dielectric and piezoelectric properties of lead zirconate titanate films, *J. Appl. Phys.*, 2001, **89**(2), 1336–1348.

84 H. Lee, T. Mizoguchi, T. Yamamoto and Y. Ikuhara, First principles study on intrinsic vacancies in cubic and orthorhombic $CaTiO_3$, *Mater. Trans.*, 2009, **50**(5), 977–983.

85 A. Shigemi and T. Wada, Evaluations of phases and vacancy formation energies in $KNbO_3$ by first-principles calculation, *Jpn. J. Appl. Phys., Part 1*, 2005, **44**(11), 8048–8054.

86 A. Popovič, L. Bencze, J. Koruza and B. Malič, Vapour pressure and mixing thermodynamic properties of the $KNbO_3$–$NaNbO_3$ system, *RSC Adv.*, 2015, **5**(93), 76249–76256.

Electronic Supplementary Information

Ferroelectric and dielectric properties of Ca^{2+}-doped and Ca^{2+}-Ti^{4+} co-doped $K_{0.5}Na_{0.5}NbO_3$ thin films

Nikolai Helth Gaukås[a], Julia Glaum[a], Mari-Ann Einarsrud[a], Tor Grande[a]*

a: Department of Materials Science and Engineering, Norwegian University of Science and Technology (NTNU), N-7491 Trondheim, Norway.

*Corresponding author. E-mail: grande@ntnu.no

XRD curve fitting using the Pawley method

The Pawley method was used for curve fitting of the X-ray diffractograms from powders calcined at 700 and 850 °C for 4 h after calcination. The patterns were fitted to the monoclinic space group Pm, using a=c=4.000 Å, b=3.950 and β=90.33° as starting parameters. Calculated unit cell parameters and unit cell volumes from the Pawley fitting are presented in Table S.1 and plotted in Figure S.1. Pawley method fitted curves to powder X-ray diffractograms are given in Figure S.2.

Table S.1: Lattice parameters, unit cell volumes, crystallite sizes and weighted profile R-factors from Pawley method fitting of X-ray diffractograms from the KNN powders.

	a [Å]	b [Å]	c [Å]	β [°]	V [Å^3]	Crystallite size [nm]	R_{wp} [%]
KNN-700°C	4.005	3.949	3.989	90.19	63.089	26.3	10.04
KNN-850°C	4.004	3.943	3.998	90.22	63.119	56.5	13.48
KNN-Ca^{2+}-700°C	4.001	3.945	3.981	90.52	62.833	18.4	10.32
KNN-Ca^{2+}-850°C	3.997	3.944	3.981	90.42	62.755	23.6	10.66
KNN-$CaTiO_3$-700°C	4.000	3.943	3.977	90.78	62.712	21.4	14.48
KNN-$CaTiO_3$-850°C	3.998	3.945	3.979	90.53	62.755	23.1	10.76

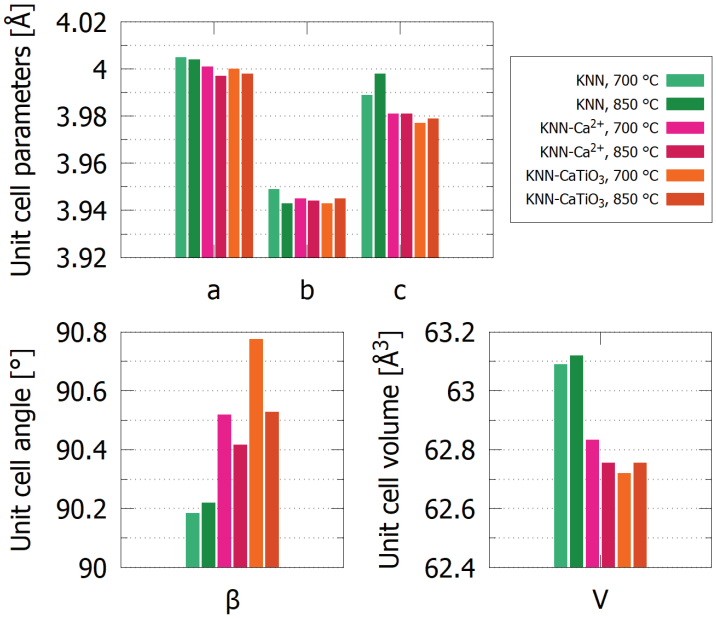

Figure S.1: Unit cell parameters and unit cell volumes from the Pawley method fitting of XRD patterns of the powder (values in Table A.1).

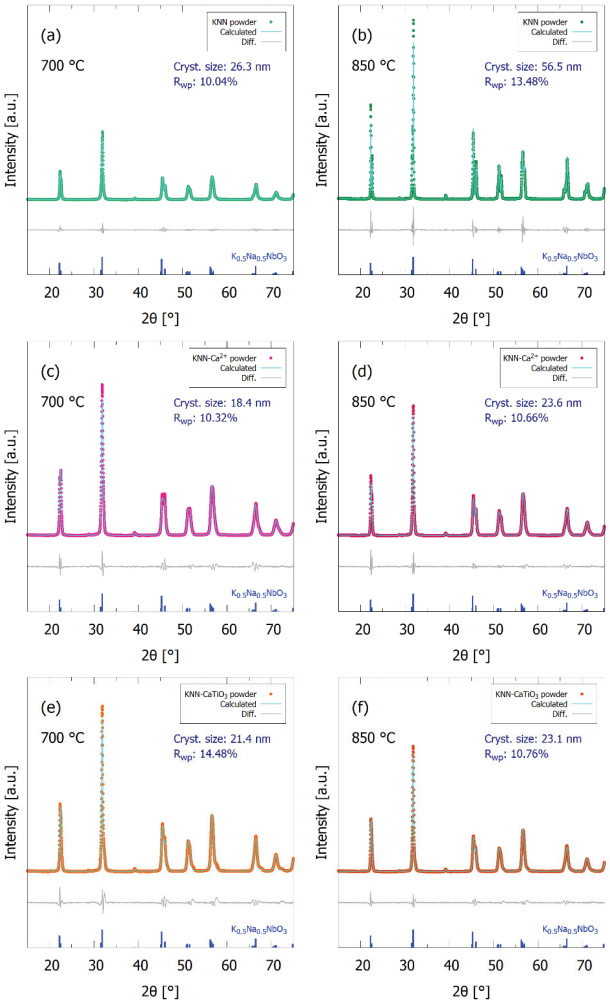

Figure S.2: Pawley method fitting of powder X-ray diffractograms from (a), (b) undoped, (c), (d) Ca^{2+}-doped and (e), (f) $CaTiO_3$-doped KNN powders. Figures (a), (c) and (e) are from powders heat treated at 700 °C and figures (b), (d) and (f) from powders heat treated at 850 °C. Crystallite sizes and weighted profile R-factors (R_{wp}) for the fits are given in each plot. Reference pattern for $K_{0.5}Na_{0.5}NbO_3$ (blue, PDF card 00-061-0315 (1)) is included.

Conventional XRD of KNN films

Conventional XRD diffraction patterns (θ-2θ mode) of the KNN films after pyrolysis (550 °C) and annealing (700 °C) are presented in Figure S.3. The intensities of the Bragg reflections of the annealed KNN films are comparable to those of the reference pattern of bulk KNN, demonstrating the films are polycrystalline and with no degree of texture. The pyrolyzed films have some (100) preferential orientation (inset) which might be caused by the film not being completely crystallized.

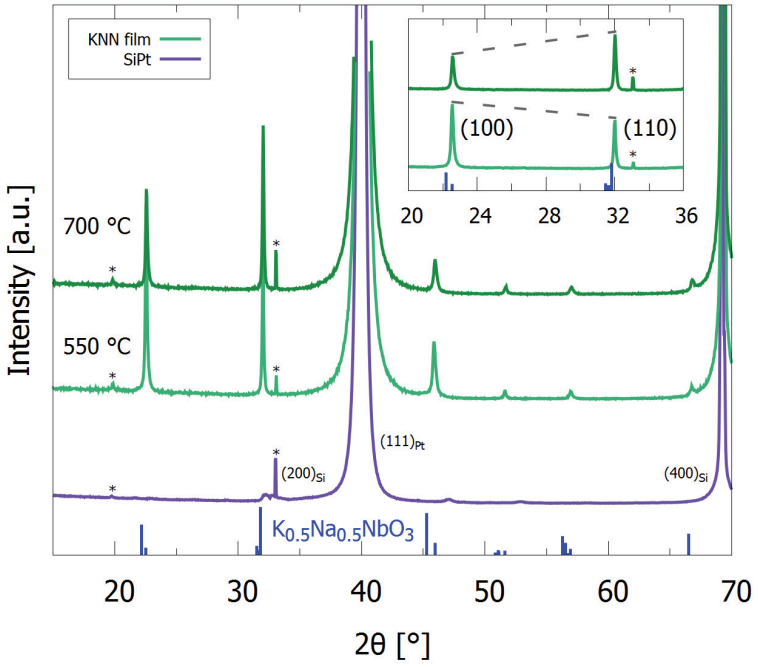

Figure S.3: Conventional XRD patterns of pyrolyzed (550 °C) and annealed (700 °C) KNN films on SiPt. The pattern of a blanc SiPt substrate is included for comparison. Reference pattern for $K_{0.5}Na_{0.5}NbO_3$ (blue, PDF card 00-061-0315 (1)) is included. The films were prepared by 30 repeating spin coatings.

P_r, P_{max} and E_c from polarization-electric field measurements

Remnant polarization (P_r), maximum polarization (P_{max}) and coercive field (E_c) from the polarization vs. electric field measurements of the films at 10 to 5000 Hz (Figure 4 and 5) are presented in Table S.2. The values at 10 Hz are measured using an electric field of 100 kV cm^{-1}. The values at 50 to 5000 Hz are measured using an electric field of 125 and 142 kV cm^{-1} for KNN-Ca^{2+} and KNN-$CaTiO_3$, respectively.

Table S.2: Remnant polarization (P_r), maximum polarization (P_{max}) and coercive field (E_c) of KNN-based films from 10 to 5000 Hz.

		10 Hz	50 Hz	100 Hz	500 Hz	1000 Hz	5000Hz
P_r [µC cm^{-2}]	KNN	5.47±2.25	-	-	-	-	-
	KNN-Ca^{2+}	4.24±0.47	6.37±0.94	5.69±0.37	4.90±0.05	4.69±0.07	4.90±0.46
	KNN-$CaTiO_3$	6.65±1.44	7.40±0.17	6.88±0.96	6.37±0.57	6.20±1.02	6.95±0.80
P_{max} [µC cm^{-2}]	KNN	13.80±2.00	-	-	-	-	-
	KNN-Ca^{2+}	18.20±0.00	21.45±0.50	20.70±0.20	19.70±0.00	19.00±0.00	17.85±0.30
	KNN-$CaTiO_3$	22.20±0.20	26.45±0.10	25.60±0.40	24.90±0.20	24.20±0.20	23.35±0.50
E_c [kV cm^{-1}]	KNN	47.08±12.83	-	-	-	-	-
	KNN-Ca^{2+}	18.42±4.17	22.00±8.67	22.58±3.50	24.08±0.17	23.00±0.67	26.58±1.83
	KNN-$CaTiO_3$	17.92±1.17	27.75±4.50	27.83±3.00	27.08±5.50	28.25±6.50	31.00±4.33

Frequency dependency of dielectric permittivity

The frequency dependency of the dielectric permittivity from 1 to 10^6 Hz is presented in Figure S.4. The measurements were performed at 150 °C (upon heating), using an AC amplitude of 50 mV. The dielectric loss tangent (tan δ) for the measurements is included in the figure.

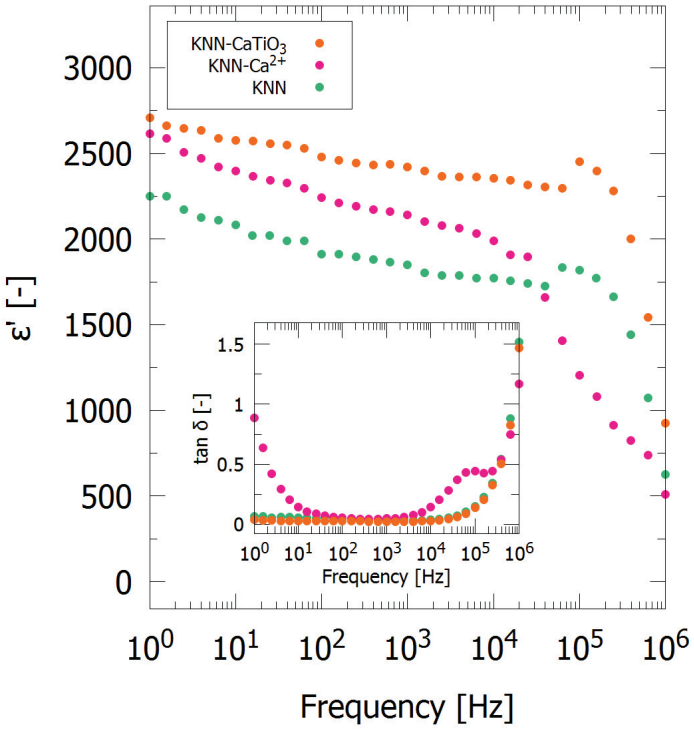

Figure S.4: Dielectric permittivity as a function of frequency for the three KNN-based films, measured at 150 °C and using an AC amplitude of 50 mV. Inset: The loss tangent recorded during the measurement.

References:

1. Tellier J, Malic B, Dkhil B, Jenko D, Cilensek J, Kosec M. Crystal structure and phase transitions of sodium potassium niobate perovskites. Solid State Sci. 2009;11(2):320–4.

Manuscript I

Preparation of flexible piezoelectric $K_{0.5}Na_{0.5}NbO_3$ thin films

N. H. Gaukås, R. H. Klaussen, E. Khomyakova, J. Glaum, M.-A. Einarsrud, T. Grande.

Not submitted.

This manuscript is awaiting publication and is not included in NTNU Open

Manuscript II

***In vitro* biocompatibility of piezoelectric $K_{0.5}Na_{0.5}NbO_3$ thin films on platinized silicon substrates**

N. H. Gaukås, Q.-S. Huynh, A. A. Pratap, M.-A. Einarsrud, T. Grande, R. M. D. Holsinger, J. Glaum.

In submission.

This manuscript is awaiting publication and is not included in NTNU Open